



HAL
open science

CFD-based numerical strategy and full-scale experiment applied to traffic air pollution in urban area: from outdoor/indoor air pollutant cartographies to mitigation through the smart placement of depolluting panel

Tsubasa Hamada

► To cite this version:

Tsubasa Hamada. CFD-based numerical strategy and full-scale experiment applied to traffic air pollution in urban area: from outdoor/indoor air pollutant cartographies to mitigation through the smart placement of depolluting panel. Fluids mechanics [physics.class-ph]. Université Gustave Eiffel, 2023. English. NNT: 2023UEFL2054 . tel-04541469

HAL Id: tel-04541469

<https://theses.hal.science/tel-04541469>

Submitted on 10 Apr 2024

HAL is a multi-disciplinary open access archive for the deposit and dissemination of scientific research documents, whether they are published or not. The documents may come from teaching and research institutions in France or abroad, or from public or private research centers.

L'archive ouverte pluridisciplinaire **HAL**, est destinée au dépôt et à la diffusion de documents scientifiques de niveau recherche, publiés ou non, émanant des établissements d'enseignement et de recherche français ou étrangers, des laboratoires publics ou privés.



CFD-based numerical strategy and full-scale experiment applied to traffic air pollution in urban area: from outdoor/indoor air pollutant cartographies to mitigation through the smart placement of depolluting panel

Thèse de doctorat de l'Université Gustave Eiffel

Ecole doctorale Sciences, Ingénierie et Environnement (SIE)
Spécialité de doctorat: Sciences de l'Ingénieur

Tsubasa HAMADA

Nadège BLOND

Chargée de recherche, CNRS, Université de Strasbourg

Rapporteure

Lionel SOULHAC

Professeur, INSA Lyon, Université Lyon I

Rapporteur

Yoshihide TOMINAGA

Professor, Niigata Institute of Technology

Examineur

Isabelle COLL

Professeure, Université Paris Est Créteil

Présidente

Tarik BOUROUINA

Professeur, ESIEE-Paris

Examineur

Olivier SANCHEZ

Ingénieur, Airparif

Examineur

Delphine LEJRI

Chargée de recherche, Ecole Nationale des Travaux Publics de l'Etat

Examinatrice

Julien WAEYTENS

Directeur de recherche, Université Gustave Eiffel

Directeur de thèse

Acknowledgment

I would like to sincerely thank my supervisor, Julien Waeytens, for his unwavering guidance and support during the three years of my doctoral thesis. His invaluable advice across various research aspects played a pivotal role in completing my Ph.D. Moreover, his warm welcome and willingness to provide support beyond the research realm significantly contributed to creating a conducive environment for me as a Japanese. I want to convey my most profound appreciation here. I also express my gratitude to my co-supervisor, Delphine Lejri. Her advice and guidance during our meetings brought fresh perspectives to my research. Her expertise proved to be immensely beneficial to the progress of my research. Furthermore, I extend my heartfelt appreciation to Rachida Chakir and Fatiha Chabi, with whom I co-authored an article. In addition, I'd like to acknowledge Airparif for providing essential data and insights that were pivotal for my research, particularly Fabrice Dugay and Olivier Sanchez. I would like to express my gratitude to Yan Ulanowski, who consistently assisted with our experiments in Sense-City. My gratitude also extends to all the members of the IMSE laboratory for their support and collaboration, and special thanks are due to Nacer Sellila and Solaine Hachem. I would also like to thank the administrative staff assisting with this academic journey. Lastly, my heartfelt thanks go to my family in Japan. With their support throughout my extensive academic journey, I reached this point.

Abstract

Air pollution is a major issue regarding health and environmental concerns. In fact, outdoor air pollution in urban areas is responsible for millions of deaths worldwide. One of the main outdoor pollutant sources is vehicle emissions. Moreover, there is a transfer of outdoor air pollution to indoor environments, which results in the deterioration of indoor air quality by traffic pollution. To tackle air pollution issues, today, there is growing interest in the use of panels incorporating photocatalytic technology (depolluting panels).

In my Ph.D. research, I have developed a novel approach aimed at efficiently placing depolluting panels in urban districts, with the goal of minimizing human exposure to outdoor and indoor air pollutants. My works aim to propose a practical methodology and its numerical implementation. The proposed method encompasses a comprehensive series of steps; from the automatic creation of 3D urban geometry, the computation of detailed outdoor and indoor pollutant cartography using CFD to the generation of sensitivity indicator maps that pinpoint relevant placement for depolluting panel installation through adjoint-based sensitivity analysis.

The proposed method was applied to a full-scale experimental district, "Sense-City" in controlled condition scenarios and a real urban area in Paris. Concerning pollution maps, the interaction between outdoor and indoor air quality was investigated using CFD and validated by measurement campaigns. According to the numerical and experimental results, indoor pollutant concentrations reach the same level as outdoors within 15 minutes after opening windows (natural ventilation). At the district scale, thanks to the proposed sensitivity indicator, I show that depolluting panels should be placed on part of the sidewalks, roads and lower floors of building facades in order to mitigate human exposure to outdoor air pollution and to prevent outdoor air pollutants from entering indoors.

Despite various simplifications, the numerical strategy was able to distinguish between non-effective and relevant depolluting panel placement areas as regards of urban airflow. This methodology can potentially serve as a valuable decision-making tool for reducing pollutant exposure during urban planning processes for both new and existing urban areas and buildings.

Résumé

La pollution de l'air est un problème majeur pour la santé et l'environnement. En effet, la pollution de l'air extérieur dans les zones urbaines est responsable de millions de décès dans le monde. Les émissions des véhicules constituent l'une des principales sources de pollution extérieure. De surcroît, la pollution de l'air extérieur liée au trafic est transférée vers l'intérieur des bâtiments, entraînant ainsi une détérioration de la qualité de l'air intérieur. Pour atténuer les problèmes de pollution de l'air, l'utilisation de panneaux dépolluants par photocatalyse suscite aujourd'hui un intérêt croissant.

Dans ma thèse, j'ai proposé une nouvelle approche visant à placer efficacement des panneaux dépolluants en environnement urbain, dans le but de réduire l'exposition humaine aux polluants de l'air extérieur et intérieur. Mes travaux concernent le développement d'une méthodologie pratique et son implémentation numérique. Ma démarche englobe l'ensemble des étapes : depuis la création automatique d'une géométrie urbaine en 3D, la simulation d'une cartographie détaillée des polluants extérieurs et intérieurs à l'aide de la CFD, jusqu'à la génération de cartes d'indicateurs de sensibilité permettant de sélectionner les emplacements pertinents pour le déploiement de panneaux dépolluants.

La stratégie numérique a été appliquée au quartier laboratoire "Sense-City" en conditions contrôlées et à un quartier réel de Paris. Concernant les cartographies de pollution liées au trafic, l'interaction entre la qualité de l'air extérieur et intérieur a été étudiée à l'aide de la CFD et validée par des campagnes de mesure. D'après les résultats numériques et expérimentaux, les concentrations de polluants à l'intérieur atteignent le même niveau qu'à l'extérieur dans les 15 minutes qui suivent l'ouverture des fenêtres (ventilation naturelle). À l'échelle du quartier, grâce à l'indicateur de sensibilité proposé, j'ai montré que des panneaux dépolluants devraient être positionnés sur une partie des trottoirs, des routes et sur la partie inférieure des façades des bâtiments afin d'atténuer l'exposition humaine à la pollution de l'air extérieur et d'empêcher les polluants de l'air extérieur de pénétrer dans les bâtiments.

Malgré diverses simplifications, cette stratégie numérique prenant en compte l'aérodynamique urbaine permet de distinguer les zones non-efficaces et pertinentes pour le placement de panneaux dépolluants. Cette méthodologie peut être utile comme outil d'aide à la décision pour les collectivités locales lors de la planification urbaine sur des quartiers existants ou nouveaux (et également les bâtiments) dans le but de réduire l'exposition aux polluants.

Contents

List of Figures	12
List of Tables	14
Introduction	15
1 Air Quality	19
1.1 Introduction to air quality	19
1.1.1 Outdoor environment	20
1.1.2 Indoor environment	21
1.1.3 Overview of typical monitored pollutants	21
1.2 Air quality standard and regulation	29
1.2.1 Outdoor standard and regulation	30
1.2.2 Indoor standard and regulation	30
1.3 Measurement of Air Quality	33
1.3.1 Reference and low-cost sensor for gas and particle	34
1.4 Conclusion	37
2 Air Pollutant Dispersion: Measurement and Modeling	39
2.1 Spatial scale in urban pollutant dispersion	39
2.2 Methodology to study air pollutant dispersion: measurement and prediction	41
2.2.1 Experimental way	41
2.2.2 Semi-empirical modeling	43
2.2.3 CFD modeling	46
2.3 Data Assimilation	50
2.4 Specific modeling for indoor air quality	51
2.4.1 Single/Multizone model	51
2.4.2 Fast Fluid Dynamics	51
2.4.3 Low-Dimensional Linear Ventilation Model	52

2.5	Conclusion	52
3	Development of a numerical strategy: from making outdoor/indoor pollutant cartography to smart placement of depolluting panel	54
3.1	Interaction between outdoor and indoor air quality	54
3.1.1	Literature review on the interaction between outdoor and indoor air quality	55
3.1.2	CFD for the interaction between outdoor and indoor air quality	60
3.2	Mitigation strategies for air pollution in urban area	64
3.2.1	Source term	64
3.2.2	Advection and diffusion term	65
3.2.3	Chemical reaction term	67
3.3	Developing methodology for smart placement of depolluting panel . .	70
3.3.1	Outline of methodology for smart placement of depolluting panel	72
3.3.2	Technical description	75
3.3.3	Derivation of the backward advection-diffusion equation	79
3.3.4	Limitations of the considered pollutant dispersion modeling .	86
3.4	Conclusion	88
4	Application to controlled conditions in Sense-City	89
4.1	Description of Sense-City	89
4.2	Numerical study of pollutant dispersion in controlled condition: from making pollutant cartography to smart placement of depolluting panel	92
4.2.1	Numerical mock-up of Sense-City	92
4.2.2	Diagnosis stage: making outdoor pollutant cartography	93
4.2.3	Remediation stage: smart placement of depolluting panel . . .	110
4.3	Study of the interaction between outdoor and indoor air quality through simulation and experiment	117
4.3.1	Airflow validation	117
4.3.2	CO ₂ dispersion validation	130
4.4	Conclusion	147
5	Application to real conditions in Paris 8 district	149
5.1	Description of Paris 8 arrondissement	150
5.2	Study on the interaction between outdoor and indoor air quality in natural conditions in Paris via measurement and simulation	150
5.2.1	Indoor NO ₂ measurement in an apartment in Paris	150
5.2.2	CFD modeling for outdoor air pollutant dispersion	159
5.2.3	CFD modeling of outdoor/indoor pollutant transfer	176

5.2.4	Summary on the interaction between outdoor and indoor air quality in the apartment in Paris	185
5.3	Numerical study for smart placement of depolluting panel in Paris 8 district	186
5.3.1	Wind direction and target dates	186
5.3.2	Diagnosis stage: making pollutant cartography	187
5.3.3	Remediation stage: smart placement of depolluting panel . . .	192
5.4	Conclusion	203
	Conclusion and Perspectives	205
	Appendix	210
	A NO2 measurements in Paris apartment - 2021&2022 campaigns	211
	Bibliography	211

List of Figures

1	NOx emissions emitted by different sectors in Île-de-France.	17
1.2	Graphic abstract of the photochemical cycle of O ₃ -NO-NO ₂	25
1.3	Graphic abstract of secondary Ozone production processes.	26
1.4	EU urban population exposed to air pollutant concentrations above WHO and EU air quality standards, EU-27.	32
2.1	Three scales used to distinguish atmospheric processes in urban area and the atmospheric layers	40
2.2	Schematic representation of relevant spatial scales in pollutant dispersion from neighborhood to body scale.	41
2.3	Monitoring stations of field measurement (Airparif): in Paris (left) and next to a highway.	42
2.4	(a) wind tunnel testing and (b) PIV.	43
2.5	Schematic figure of a Gaussian plume.	44
2.6	Schematic figure of Box model	45
2.7	Comparison between DNS, LES and RANS: (a) concept of the DNS, LES, URANS and SRANS approaches on the typical time evolution of the velocity behind a building and (b) turbulent jet with each turbulence model.	48
2.9	Example layout of the house in Multizone model application	52
2.10	The pollutant concentration distribution inside the ventilation enclosure obtained (a1, a2) using a high-dimensional representation (RANS) and (b1, b2) using a LLVM	53
3.1	Source and pathways of indoor air pollutants.	55
3.2	Distribution of I/O ratios of PM _{2.5} in the large-scale studies (larger than 20 homes) in different cites. The numbers in () represent the number of sample homes. ”*” shows indoor smoking	57
3.3	Pollutant dispersion in a general street canyon	58
3.4	Classification of street canyon flow	59

3.5	CFD simulation to study the interaction between outdoor and indoor air quality: (a) coupled and (b) decoupled approach	60
3.6	Velocity vectors on a building: PIV (left) coupled (center) decoupled (right)	62
3.7	Schematic procedure for the decoupled approach using pressure boundary condition; (a) outdoor airflow simulation, (b) extracting and imposing pressure and (c) indoor airflow simulation by pressure boundary condition.	63
3.8	The comparison of velocity through different urban demolition patterns.	66
3.9	Pedestrian ventilation system.	68
3.10	ZnO depolluting panel in Sense-city experimental.	70
3.11	Emissions of main air pollutants in Île-de-France 2018 (Airparif, 2020)	71
3.12	ZnO nanostructures based innovative photocatalytic road in Sense-City experiment: (a)Depolluting road infrastructures, (b)experimental campaign, (c)Pollutant evolution under solar light with and without ZnO (Plots of pollutant concentration evolution as function of photocatalysis time under artificial solar light with and without the presence of ZnO	73
3.13	Selecting highly polluted areas in diagnosis stage.	74
3.14	Definition of the quantity of interest: (a) Concentration cartography, (b) area of interest and (c) time of interest.	77
4.1	Sense-City: (a) overview of Mini-city 1 and Mini-city 2 and (b) Mini-city 1 within the climatic chamber.	90
4.2	Concrete building in Mini-city 1: (a) overview, (b) main room, (c) side room and (d) plan view of the 1st floor.	91
4.3	Partial view of the chamber ventilation system: sets of fans extraction ducts and forced-air ducts.	92
4.4	Position of the pollutant source and the mast sensors in Sense-City district.	93
4.5	Numerical mock-up of the mini-city 1 within the climatic chamber of Sense-city.	94
4.6	Mesh configuration of numerical mock-up of Sense-City: (a) overview of mesh, (b) local mesh for extraction duct, (c) local mesh for fan and forced-air duct, and (d) overview from the top.	100
4.9	Pollutant concentration from the simulation at the masts of Sense-City district as a function of time - no depolluting panels.	104
4.10	Geometry of indoor region: (a) picture of Sense-City, (b) mock-up indoor geometry.	105

4.11	Mesh configuration for the indoor simulation: (a) overview, (b) horizontal view.	106
4.12	Average velocity field in the 1st floor of the concrete building obtained by the decoupled approach: (a) overview view, (b) horizontal view.	107
4.13	Time evolution of pollutant dispersion obtained by the decoupled approach: (a) $t=4s$, (b) $t=60s$, (c) $t=100s$	107
4.14	Time history of pollutant concentration on the probe points: (a) locations of probe points and (b) time history of the pollutant concentration.	108
4.15	Selected QoIs: (i) sidewalk (red color) and (ii) window (green color).	112
4.16	Adjoint solution represented at the surfaces of Sense-City district - Quantity of interest \mathcal{J}_2 associated to the pollutant concentration at the vicinity of the window building.	113
4.17	Sensitivity indicator maps I_1 associated to the pollutant concentration at the building sidewalk \mathcal{J}_1 (at left) and I_2 associated to the pollutant concentration at the building window \mathcal{J}_2	114
4.18	Smart placement of depolluting panels, indicated by black rectangles, in Sense-City district on the road and the sidewalk (at left) and on the building facade (at right) to improve the quantities of interest \mathcal{J}_1 and \mathcal{J}_2 - White rectangular denotes the window position.	115
4.19	3D anemometer set-up: (a) virtual geometry of Sense-City with the indoor environment at the 1st floor of the concrete building, (b) Picture of 3D anemometer and (c) Location of 3D anemometer for airflow measurement.	119
4.20	Numerical mock-up: (a) coupled approach and (b) decoupled approach.	120
4.21	Indoor geometry: (a) actual geometry (picture) and (b) numerical mock-up.	121
4.22	Surface mesh: (a) coupled approach and (b) decoupled approach.	122
4.23	Time history of the pressure difference between inlet and outlet (inlet pressure - outlet pressure).	123
4.24	Average velocity comparison between coupled and decoupled approach: (a) vertical section at the front window ($x = -2.9m$), (b) vertical section at the rear window ($x = -3.9m$) and (C) horizontal section at a height of 1.55 m.	124
4.25	Time history of U_x , U_y , U_z with $\Delta t = 0.1s$ at P1 of experiment and URANS simulation. The red lines show the average of each velocity component. The moving average is applied to the measurement data on a length of 0.1s.	126
4.26	Velocity and TKE comparison at 14 points between the experiment and the coupled approach inside the concrete building in Sense-City.	128

4.27	Gas dispersion device.	131
4.28	Position of the pollutant source and CO ₂ sensor in the CO ₂ controlled dispersion experiment.	131
4.29	Diagram for connection of the gas emission device and gas bottles in Sense-City.	132
4.30	ETHERA CO ₂ sensor.	133
4.31	CO ₂ sensor arrangement; (a) ~ (b) around the gas dispersion device from the 1st floor and (c) inside the 1st floor.	134
4.32	Picture of the calibration (a) overview and (b) CO ₂ sensors in the calibration box.	135
4.33	Mapped boundary conditions for the inside of the climatic chamber's ventilation systems: (a) extraction duct, (b) fan and (c) forced-air duct.	138
4.34	Time history of the pollutant concentration (CO ₂ for the experiment and passive scalar for the simulations) in long-term simulation for 3 min.	140
4.35	Time history of the pollutant concentration (CO ₂ for the experiment and passive scalar for the simulations) in long-term simulation for 55 min.	142
4.36	Time evolution of pollutant dispersion of URANS using instantaneous velocity in Sense-City at $t = 55, 80, 90$ s: (left) pollutant concentrations in the vertical cross-section at the front window at $x = 2$ m and (right) contour surface at $C = 501$ ppm. Background concentration is 490 ppm.	146
5.1	Paris 8 district: (a) overview of Paris and (b) studied domain in Paris 8 arrondissement.	151
5.2	Floor map of the 1st floor of the target apartment and NO ₂ microsensor location.	153
5.3	Cairsens NO ₂ microsensor.	154
5.4	Picture of the NO ₂ analyzer and NO ₂ microsensors for sensors' validation.	155
5.5	Time history of NO ₂ concentration for the analyzer and microsensors for 9 days in February 2023.	156
5.6	Measurement results in the Paris apartment: (a) NO ₂ concentration at each sensor, (b) Normal and horizontal tangential velocity at the road-side window, (c) vertical velocity at the road-side window.	158
5.7	Measurement station of Airparif in Av des Champs-Élysées.	160
5.8	Proposition of a dedicated software chain for making numerical mock-ups of urban districts.	162
5.9	Computational domain: (a) overview and (b) detailed view.	163

5.10	Position of NO _x pollutant source on the 44 main roads in Paris 8 district.	166
5.11	Mesh configuration: (a) vertical section, (b) horizontal section at $z = 1.5$ m, (c) mesh near the pollutant sources and (d) overview.	168
5.12	Image of the horizontal average velocity (U_x, U_y) at a height of 1.5 m. $\textcircled{1}$ is the vertical average velocity (U_x, U_z).	171
5.13	Image of average NO _x concentration at a height of 1.5 m.	173
5.14	NO ₂ mobile measurement route in Paris 8: starting from Rue de Naples.	175
5.15	NO ₂ concentration in the mobile measurement campaign in Paris 8.	175
5.16	Numerical mock-up for the pressure-driven and additional domain approaches.	178
5.17	Mesh configuration of the apartment from top view at a height = 1.33 m from the floor of the rooms: (a) pressure-driven approach and (b) additional domain approach.	179
5.18	Comparison of averaged velocity at height of 1.5m (measurement height of the 3D anemometer): (a) pressure-driven approach, (b) additional domain approach and (c) floor plan and the average velocity components of 3D anemometer.	181
5.19	Time evolution of NO ₂ concentration at a height of 1.33 m (corresponds to the center of the road-side window): (a) $t = 5$ s, (b) $t = 10$ s, (c) $t = 25$ s, (d) $t = 45$ s (e) $t = 300$ s (5min) and (f) $t = 900$ s (15min).	183
5.20	Time evolution of NO ₂ concentration: comparison between the simulation (a) and measurement (b). Note that (b) is the same figure as Fig. 5.6 (a).	184
5.21	Window frame in the passage between the living room and the kids' room.	184
5.22	Wind rose obtained at CDG airport in 2021.	187
5.23	Overview of the numerical Paris 8 district mock-ups for (a) SW case and (b) NE case.	189
5.24	Mean velocity and mean NO _x concentration on 1 hour-interval at 1.5 m height: SW case (top) and NE case (bottom) in Paris 8 district.	191
5.25	Average NO _x concentration and wind direction on the vertical direction in SW case at 58 Bd Malesherbes.	193
5.26	Selected areas of interest in the Paris district where air quality should be improved: (a) the south-west sidewalk in red and the lower floors of the building facade in blue from 69 to 81 Bd Malesherbes, (b) sidewalks at the intersection of Rue de Miromesnil and Rue de Boétie, (c) the north-east sidewalk from 48 to 60 Bd Malesherbes.	195

5.27	Pictures of the selected areas of interest in the Paris district: (a) 58 Bd Malesherbes and (b) 43 Rue de Miromesnil.	196
5.28	Direct concentration, adjoint concentration, and sensitivity indicator associated with each quantity of interest: (a) \mathcal{J}_1 , the south-west sidewalk from 69 to 85 Bd Malesherbes, (b) \mathcal{J}_2 , the building facade at the lower floor on south-west side from 69 to 81 Bd Malesherbes, (c) \mathcal{J}_3 , the subway station and shops at the intersection of Rue de Miromesnil and Rue la Boétie, (d) \mathcal{J}_4 , the north-east sidewalk from 48 to 60 Bd Malesherbes.	197
5.29	Vertical velocity and wind direction on the southwest sidewalk at Bd Malesherbes at 1m height.	198
5.30	Definition of the position for the sidewalk and road in Bd Malesherbes (on the sensitivity map of Fig. 5.28 (a)).	199
5.31	Recommended depolluting panel placement as regards of urban air-flow in Paris 8 district	201
A.1	Results of other NO_2 measurement in the Paris apartment: (a) 19th October 2021, (b) 22nd October 2021, (c) 8th November 2022 and (d) 14th November 2022. Results of first 30 min. U_n denotes the normal velocity component at the window.	212

List of Tables

1.1	Indoor air pollutants and sources.	22
1.3	Features of Reference sensor (RS) and Low-cost sensor (LCS).	35
2.1	Summary on the applicability of each method for outdoor- and indoor-scale pollutant dispersion prediction.	53
3.1	Performance comparison between coupled and decoupled approach.	63
4.1	Volumetric airflow rates of the ventilation systems in the climatic chamber.	98
4.2	Boundary condition for pollutant concentration of the ventilation systems in the climatic chamber.	99
4.3	Cells size of meshes used for pollutant dispersion study.	100
4.4	Indicator of direct sensitivity analysis: I_{dif} , I_{ref} , I_i at three points.	110
4.5	Numerical values of the quantities of interest in different urban planning configurations for Sense-City district, k denotes the reaction rate of the depolluting panels.	117
4.6	Coordinates of Points for 3D anemometer position.	118
4.7	Comparison of average velocity, TKE, and standard deviation at P1 (front side window).	127
4.8	Statistical metrics comparing the simulation with the experiment at 14 points in the concrete building of Sense-City.	129
4.9	Coordinates of CO ₂ sensor position.	133
4.10	Calibration factor determined in laboratory.	136
4.11	Accuracy validation: slope α of the linear regression line of the pollutant concentration and statistical metrics (BIAS and RMSE) comparing the simulated and measured pollutant dispersion at Sensor 1, 4, 6 in Sense-City.	143
4.12	Velocity comparison at Sensor 9 between the experiment and the long-term simulation with the insider modeling of the ventilation systems.	144

5.1	Sensor numbers and placement in indoor measurement campaign. . .	155
5.2	Validation metrics in ppb for the NO ₂ microsensors in comparison with NO ₂ analyzer (reference sensor) in Sense-City: BIAS, MAE and RMSE.	157
5.3	Average velocity at the road-side window for the first 15min.	159
5.4	Magnitude of NO _x pollutant sources on the roads ($\mu\text{g}/\text{m}^3/\text{s}$) on 15th November 2022 8 AM \sim 9 AM.	167
5.5	Mesh size of the Paris 8 domain discretization when wind direction at 180° (south direction).	167
5.6	Comparison of NO _x concentration between CFD and the measurement station at Av des Champs-Élysées. Note that the total NO ₂ simulated concentration is deduced from Derwent and Middleton formula.	172
5.7	Comparison of NO ₂ concentration between CFD and the measurement from the indoor NO ₂ experiment at 15 Rue de Naples. Note that, for CFD simulations, total NO ₂ concentration is deduced from Derwent and Middleton formula.	174
5.8	Comparison of NO ₂ concentration on 15th November 2022 between the mobile measurement and the CFD using Derwent and Middleton formula at 8 points marked by the red circles in Fig. 5.14.	176
5.9	Boundary conditions for the additional domain approach.	180
5.10	Magnitude of NO _x emission on 44 main roads for NE and SW case. .	188
5.11	Mesh size of the Paris 8 domain for the study on the smart placement of depolluting panels.	189
5.12	Comparison of NO _x concentration between CFD and measurement station.	192
5.13	Area of depolluting panel enclosed by $I_1(x) = 0.1$, $I_2(x) = 0.1$, $I_3(x) = 0.2$ and $I_4(x) = 0.003$	202

Introduction

Clean air is a fundamental human right. However, air pollution causes 7 million premature deaths annually due to outdoor and indoor pollutants according to WHO [1]. In fact, approximately 90% of the world's population lives in areas where air pollutant levels exceed WHO standards. Considering air pollution issues, people often understand the health risks associated with outdoor pollutants, but there is often a lack of common understanding regarding indoor air quality [2]. Some outdoor pollutant sources, such as transportation emissions, can be transferred into indoor environments, thus deteriorating indoor air quality. There is a wide variety of air pollutants, e.g., NO_x, SO₂, O₃, CO, COV, and PM, and a wide range of pollution sources such as fossil fuel combustion, transportation, industry, and household activities. Many of these sources are associated with essential daily activities, therefore making the rapid reduction of air pollutants by removing these pollutant sources challenging. Consequently, we need strategies to mitigate pollutants after they have been released.

Various mitigation strategies have been proposed for improving air quality. The most straightforward and best approach is to reduce pollutant generation through technological advances in various industrial sectors (such as fuel-efficient vehicles and industrial turbines) and political emission control (such as low emission zone). Nevertheless, in this thesis, I will focus on mitigation measures for already emitted air pollution. The first approach would be to enhance the ventilation capacity of cities by modifying the building density, layout and heterogeneity to generate airflow favorable to pollutant dispersion. For instance, cities with lower densities can prevent the accumulation of air pollutants [3]. In extreme cases, creating district-scale wind corridors by demolishing some urban neighborhoods can also enhance urban ventilation [4]. It is also important to consider aspect ratios in street canyons during the urban design phase [5]. In addition, modifications to building geometry can also lead to pollutant removal. Strategies such as building separation [6] and introducing permeability (large openings in buildings) [7] have been successfully implemented in Hong Kong. Besides urban and building shape modifications, the installation of roadside barriers [4] to prevent pollutants on the road from reaching the sidewalks

is another option. Ventilation ducts connecting pedestrian pavements to the sky above buildings are also proposed to remove air pollutants at the pedestrian level [8]. Overall, these methods are convincing and can improve air quality. However, solutions like modification of urban geometry and building shape are challenging to apply to existing cities and buildings. It is an expensive and long-term solution. The roadside barriers and pedestrian ventilation ducts can be effective but can spoil the urban landscape. Hence, there's a need for feasible and aesthetically compatible approaches to air quality improvement.

In recent years, UV photocatalytic oxidation (PCO) has received significant attention as a technology for cleaning air pollutants. Its advantages include high removal efficiency, a wide range of applications, easy installation, and no secondary pollution [9, 10]. With sufficient light and under the presence of photocatalyst (ZnO or TiO₂), a catalytic oxidation effect is triggered, degrading certain pollutants [11, 12]. Notably, at Université Gustave Eiffel, photocatalyst nanostructures ZnO grown on construction materials (tiling, rock aggregates) were developed, named "depolluting panels" [13]. Their experiments have demonstrated the effectiveness of removing pollutants from vehicles. Overall, depolluting panels are very practical in removing outdoor and indoor pollutants because they can be conveniently placed on roads and building surfaces. However, the efficient use of depolluting panels in practice is complex [14], as it depends on several parameters, such as sunlight intensity, pollutant concentration, airflow, temperature, humidity, etc. Additionally, considering the cost associated with panel deployment and maintenance, installing panels throughout the entire city is unrealistic. Hence, strategic and efficient panel placement is crucial.

Several aspects need to be considered when placing depolluting panels. It is particularly important to place panels in areas where pollutant concentrations are frequently high. Hence, making detailed pollutant concentration maps at the district scale is the first important step. There are several methods for obtaining the spatial distribution of pollution concentrations; field measurements and CFD are currently the most commonly used. Nonetheless, in many cases, the number and density of air quality monitoring sensors are mostly insufficient, casting doubt about the spatial representativeness and accuracy of spatial variation of pollutant concentrations using only field measurements. In contrast, CFD has the capability to generate detailed pollutant maps encompassing entire regions, although some uncertainty exists in computational parameters.

Depolluting panels are currently being developed and improved, which involve multidisciplinary works in the fields of chemistry, materials and environmental sciences. While these works aim to enhance the panels' efficiency, the study of the panels' optimal placement in urban areas is also essential. Accordingly, the objec-

tive of my Ph.D. is twofold: to develop a numerical strategy for determining the smart placement of depolluting panels using detailed outdoor and indoor simulations and to validate the effectiveness of this approach through its application in real urban settings.

The numerical strategy encompasses a comprehensive series of steps; from the automatic creation of 3D urban geometry, the computation of detailed outdoor and indoor pollutant cartography through CFD to the generation of sensitivity indicator maps that pinpoint the relevant placement for depolluting panels' installation through adjoint-based sensitivity analysis. My works aim to propose a practical methodology and its numerical implementation. Although the pollutant removal efficiency of the panels is sensitive to many factors, herein the optimization of panel placement is only done as regards of airflow pollutant dispersion.

Among many pollutant sources, vehicle exhaust is a main source of pollutants in daily life. Car emissions occur on every road in cities close to us and are directly linked to our air quality outdoors and indoors. Fig. 1 shows that the traffic sector is the main contributor to NO_x in the region Ile de France. Due to high health risks, it is very important to reduce NO_x concentration. Therefore, my Ph.D. considers the numerical strategy to reduce NO_x concentration from traffic in urban areas.

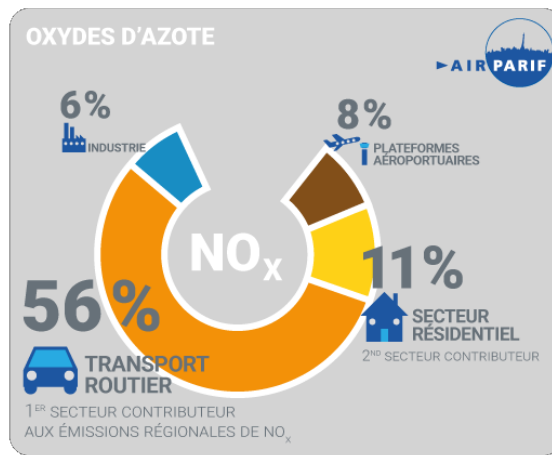


Figure 1: NO_x emissions emitted by different sectors in Île-de-France [15].

My Ph.D. work is interdisciplinary and includes many research fields such as fluid dynamics, measurement engineering, chemistry, computational science, applied mathematics and city planning. In my Ph.D. manuscript, I describe the research background, the theoretical aspects of the numerical strategy and the results of its application to cities. Chapter 1 provides essential background knowledge on air quality, as well as regulations and standards. Additionally, the principles of sensor

monitoring for air quality are briefly described. This is crucial for comparing and validating the results of CFD with sensor measurements. Chapter 2 focuses on several methodologies to get pollutant concentrations: experimental, semi-empirical, and numerical approaches. Chapter 3 first provides literature reviews on the interaction between outdoor and indoor air quality and on numerical techniques to simulate them. Subsequently, a novel numerical strategy and its limitation for the smart placement of depolluting panels for mitigating outdoor and indoor pollutant concentrations is presented. In Chapter 4, the numerical strategy is applied to an experimental full-scale district, Sense-City under controlled atmospheric condition scenarios. In Chapter 5, it is applied to a real district in Paris. In Chapters 4 and 5, comparisons between CFD results with measurement values of airflow and pollutant concentrations are also performed. Lastly, I give the conclusions of my Ph.D. work and future perspectives.

Chapter 1

Air Quality

1.1 Introduction to air quality

Air pollution refers to the release of air components, including those of biological origin and particles containing harmful chemicals, into the air. When they exist in the atmosphere with concentrations high enough adversely to affect the health of humans (also animals, plants, and buildings), it is called "air pollution" in general.

According to WHO [1], air pollution is one of the most severe environmental problems of our time. According to the WHO, nearly 7 million people die each year due to outdoor and indoor air pollution. In addition, approximately 90% of the world's population lives in areas with air pollution exceeding WHO standards, making it a major global problem rather than a problem of a specific country or region. It has become important to address this environmental challenge while at the same time achieving sustainable economic development. However, this is challenging. A large part of air pollution is caused by the combustion of fuels from automobiles, industry, and households, but almost all countries still need them to enhance their lives. Although regulations, laws, and technological innovations have been proposed to decrease air pollution, significant improvement has not yet been achieved. Especially in developing countries, the situation is more difficult due to rapid urbanization and population growth. As pollutants move across international borders, the problem is tackled by several countries in the same region, not by a single country.

1.1.1 Outdoor environment

According to WHO, outdoor air pollution causes about 4 million deaths yearly and has received significant attention in the last few decades because of its health risks [16]. It is now relatively commonplace to take steps to mitigate it in almost every country. Even today, however, the adverse effects of outdoor air pollution are still observed especially in developing countries in Asia and Africa, where rapid economic development occurs [17]. Even in developed countries, cities tend to have many pollutant sources. In urban areas, high-density building arrangements inhibit the dispersion of pollutants from traffic and power plants, etc., making them accumulate in cities.

Outdoor air contains a variety of primary and secondary air pollutants; for example, nitrogen oxides (NO_x), sulfur oxides (SO₂), ground-level ozone (O₃) from chemical reactions, carbon monoxide (CO), particle matter (PM), ammonia (NH₃) and volatile organic compounds (VOCs) are the typical pollutants. Air pollutants can be broadly classified into anthropogenic and natural sources. The anthropogenic source is the so-called man-made source, including:

- burning of fossil fuels in electricity generation, transport, industry and households;
- industrial processes and solvent use, for example, in the chemical and mining industries;
- agriculture;
- waste treatment.

On the other hand, wildfires and volcanic activities are examples of naturally occurring pollutants. It is thereby called natural sources. However, they are often not treated as common pollutants because they rarely occur.

As seen from the pollution sources above, we are constantly exposed to outdoor pollutants. Many outdoor pollutant sources are an integral part of our lives, and it is difficult to remove them easily. Mitigation measures are required for these. Developing mitigation measures to remove human exposure to outdoor air quality is an important aspect throughout all of my Ph.D.

1.1.2 Indoor environment

As the majority of people spend 80% of their time in the indoor environment, indoor air quality is essential for occupants' health. In fact, about 3 million deaths each year are attributed to indoor air pollution [18]. This is contrary to popular beliefs expecting that indoor air quality is relatively better than outdoor air quality thanks to the shielding effect of buildings. This is why public awareness and understanding of indoor air pollution lag far behind outdoor air pollution [2, 19]. Indoor air quality also contributes to occupants' comfort and work efficiency. My Ph.D. will focus on indoor air quality along with outdoor air quality and their interaction, especially outdoor pollutant transfer into indoor spaces. They will be discussed in detail in future chapters.

Many indoor air pollutants exist: some pollutants such as NO_x, SO₂, O₃, and CO are common, and other pollutants are, for example, VOCs, PM, radon, formaldehyde and microorganisms. [20] summarizes the sources for each indoor pollutant (see Table 1.1). It is worth noting that outdoor air is also a source of many pollutants. Outdoor air pollution significantly impacts indoor air quality [20]. It enters indoor spaces through natural or mechanical ventilation openings mainly. Due to the many pollutants of indoor and outdoor origin, human exposure to indoor air can also cause severe health problems. Therefore, to address indoor air quality issues effectively, it is crucial to consider both outdoor and indoor air pollution and their interaction.

In developing countries, indoor air quality is often a serious problem due to poorly ventilated homes and severe outdoor air pollution. In developed countries, homes are often airtight to save energy, making it easier for air pollutants to stay indoors for extended periods. Regardless of short- or long-term exposure, they affect various body parts, including the circulatory, respiratory, and reproductive systems. During the pollen season, allergic reactions indoors, despite pollen from outdoors, are precisely the result of the interaction between outdoor and indoor air pollution. In addition, sick building syndrome, a common problem in newly built homes, is also a common problem [21].

1.1.3 Overview of typical monitored pollutants

In general, chemicals that lower air quality are called air pollutants. Air pollutants significantly affect our health, reduce our quality of life, and shorten our lives. Due to the nature of air pollutants, they affect many people over a long period and a wide area, resulting in problems such as the urgent need for national health care. According to Department of the Environment and Energy (DCCEEW, Australia),

Type of indoor air pollutant	Sources
PM	Cooking stoves; fireplaces; smoking; outdoor air
SO ₂	Cooking stoves; fireplaces; outdoor air
NO ₂	Cooking stoves; fireplaces; outdoor air
CO	Cooking stoves; fireplaces; water heater; outdoor air
Ozone	Air cleaning device with high voltage; outdoor air
VOCs (such as formaldehyde, turpenes)	Building materials including carpet, plywood (emit formaldehyde); Paint and solvents; Clothing (after dry cleaning) (emits tetrachloroethylene, or other dry cleaning fluids); air fresheners, incense, other scented items; certain plants (emit turpenes)
Radon	Exuded from earth and rocks such as granite and gneiss in certain locations with low ventilated air and trapped inside houses
Biological air pollutants (gasses and airborne particulates)	Pets (dander), human (dust from minute skin flakes and decomposed hair), dust mites (enzymes and μ m-sized fecal droppings), inhabitants (methane), wall and air-duct (mold)

Table 1.1: indoor air pollutants and sources [20].

pollutants are broadly classified into three categories [22]:

- criteria pollutants;
- air toxics;
- biological pollutants.

Internationally, the term "criteria air pollutants" describes air pollutants that have undergone regulation and serve as air quality indicators. DCCEEW and The U.S. Environmental Protection Agency (EPA) defined the term "criteria pollutants" to six air pollutants: NO_x, SO₂, O₃, CO, PM and Lead, as having significant impacts on human health and the environment. These six pollutants can be observed over the countries. In the U.S., these pollutants have national ambient air quality standards (NAAQS) established by the EPA based on specific criteria related to their effects on public health and the environment. These standards are put in place to safeguard the general public's well-being, susceptible people such as children, the

elderly, and those with respiratory or cardiovascular illnesses. Their health risks depend on many factors, e.g., the concentration in the air, duration of exposure, toxicity, and age [23]. In particular, children and the elderly, who have weak immune systems, tend to be more vulnerable to health hazards from pollutants.

[24] examined trends of the concentrations of critical pollutants in New Jersey (USA) over the past few decades, and he confirmed that air quality has improved over the past few decades (Fig. 1.1). Such trends of pollutant concentration im-

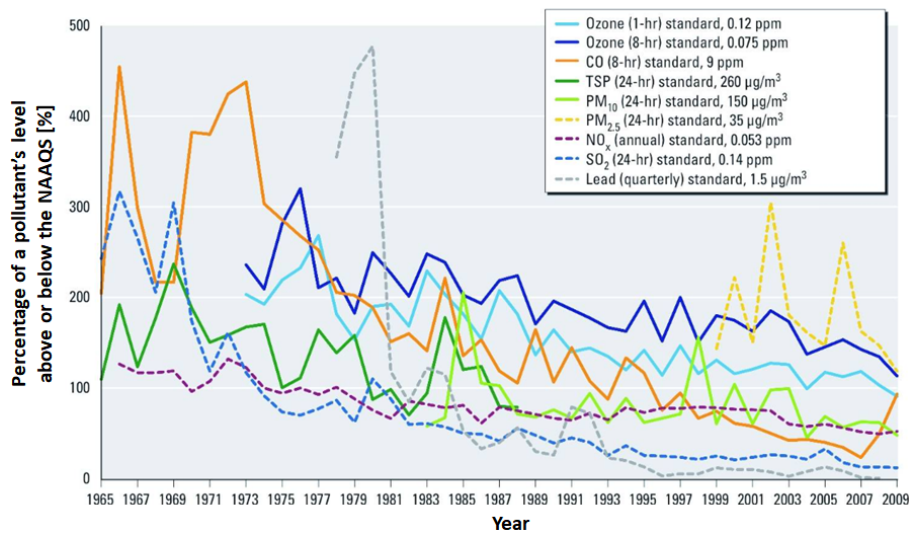


Figure 1.1: Overall trend for all the criteria air pollutants in New Jersey over the last few decades for the annual maximum measured at all monitoring sites in the state shown as a percentage of a pollutant's level above or below the NAAQS [24]. (NAAQS is National Ambient Air Quality Standards in the U.S.)

provement are also reported, e.g., [25]. Nevertheless, [24] [25] point out that many people are still exposed to at least one or more pollutants that exceed concentration standards and emphasize the need for further improvement in air quality, especially for vulnerable populations such as children elderly, and also for areas near roadways where pollution levels tend to be high.

In the following, some pollutants (CO, NO_x, O₃, PM, SO₂, NH₃ and VOCs) will be described in detail concerning their properties, sources and health hazards.

- Carbon Monoxide (CO)

CO is a substance produced by the incomplete combustion of fuels. It is a colorless, tasteless, odorless gas that does not irritate skin or mucous membranes.

The primary outdoor source of CO is automobiles, and the indoor environment has a variety of sources, such as stoves and furnaces. They release CO when materials do not burn completely. Incomplete combustion happens when engines are not tuned properly or when boilers are not adjusted correctly, leading to significant amounts of CO in the air. However, ambient concentration is improving yearly due to the progress of automobile source control measures [26].

CO binds to hemoglobin in the blood and inhibits the oxygen-carrying function, causing symptoms of central and peripheral nerve paralysis. [27] assessed the association between short-term exposure to atmospheric CO and daily mortality in a multiethnic and multinational setting, collecting daily data on air pollution, weather, and total mortality from 337 cities in 18 countries or regions from 1979 to 2016. The authors report that an increase in average CO concentration on the previous day leads to an increase in total mortality.

- Nitrogen Oxides (NO_x)

NO_x is the general term for oxides of nitrogen. In the atmosphere, NO, NO₂, N₂O, and N₂O₃, for example, are present. In environmental science, NO_x often refers collectively to NO and NO₂. NO_x is generated when nitrogen compounds in fuel or nitrogen in air are oxidized at high temperatures during combustion processes such as those in automobiles, industries, residential heating, and cooking. In urban areas, most NO_x is emitted from automobiles, accounting for more than half of all emissions. Factories and businesses have established NO_x emission standards and address this issue by implementing total emission controls (i.e., regulating the total amount of pollutants emitted). NO_x is usually generated as primary NO at first in combustion processes at high temperatures and released into the air. Then, it is oxidized to NO₂ in the atmosphere as a secondary pollutant. During this process, e.g., photochemical smog and secondary Ozone are produced with reactions with UV radiation. Fig. 1.2 shows the photochemical cycle of O₃-NO-NO₂ in which NO₂ reverts to NO via NO and UV radiation. NO_x is the source of ground-level Ozone, so the management of NO_x is very important to reduce Ozone.

Regarding health impact, NO_x is a neutral, reddish-brown gas or liquid easily absorbed by the lungs. Intracellularly, NO₂ has a strong oxidizing effect that can damage cells and irritate mucous membranes, causing bronchitis and pulmonary edema. Higher levels of NO_x are associated with an elevated risk of coughing, sputum production, and respiratory diseases. In particular, NO₂ is a respiratory irritant gas. A high concentration of NO₂ adversely affects the respiratory tract. Animal experiments have shown that NO₂ is more insoluble

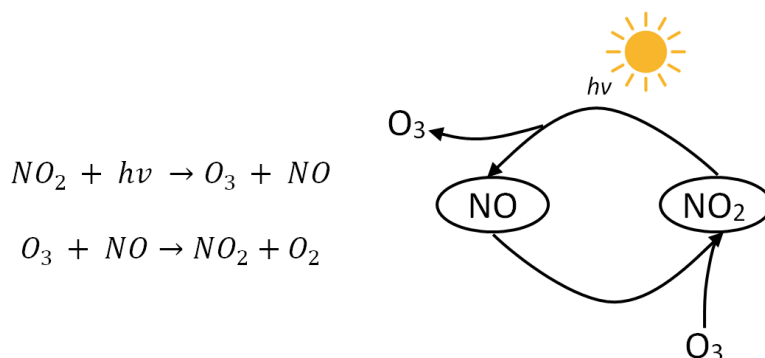


Figure 1.2: Graphic abstract of the photochemical cycle of O_3 -NO- NO_2 [28].

than SO_2 , so the uptake rate of NO_2 in the airways is lower than that of SO_2 . Thus, the rate of penetration into the lungs is high.

- Ozone (ground-level O_3)

Ozone is a faint blue gas with a characteristic odor used for disinfection, sterilization, and bleaching. There are two types of Ozone: stratospheric and tropospheric Ozone. Stratospheric Ozone occurs naturally in the upper atmosphere. This Ozone is beneficial because it forms a protective layer against the sun's harmful UV radiation. On the other hand, tropospheric Ozone is detrimental to our health. This is also called "ground-level" ozone. This Ozone is not produced directly in the air but is created by a photochemical reaction between the sun, NO_x and VOCs from cars, power plants, refineries, and so on (see Fig. 1.3); it is thereby called "secondary" Ozone. Most of the ground-level Ozone is a secondary pollutant. Photochemical reactions are more active when ultraviolet rays are intense, so they are more likely to form seasonally from spring to summer. Still, even during colder months, Ozone levels can reach high concentrations. Ozone constitutes the primary component of "smog."

The consensus among WHO and other national agencies (e.g., EPA and the European Environment Agency (EEA)) is that a low concentration of Ozone is not considered to be harmful to human health. However, high concentrations of Ozone are detrimental to the human body. When concentrations exceed 0.1 ppm, it affects the human body by irritating the eyes, nasal passages, and throat. The main effect of high Ozone concentrations on the human body is damage to the respiratory system. Ozone gas that enters the respiratory system can cause bronchitis and other problems.

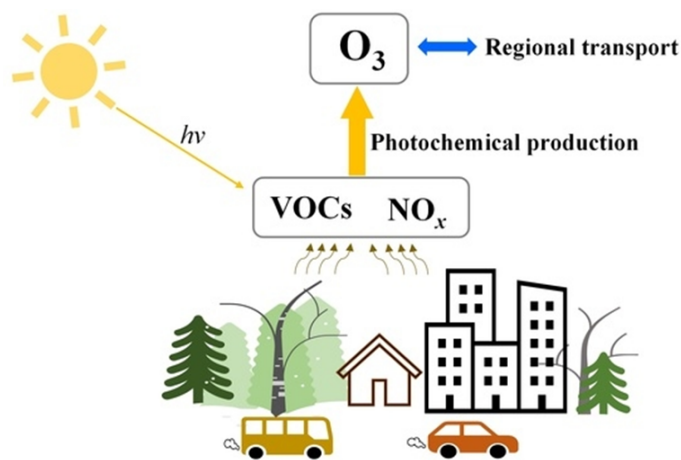


Figure 1.3: Graphic abstract of secondary ozone production processes [29].

- Particle matter (PM)

PM refers to micrometer (μm) sized solid and liquid particles. It consists of soil particles blown up by the wind (e.g., yellow sand), dust from factories and construction sites, soot and emissions from combustion, and particles formed when volatile components from oil are transformed in the atmosphere. It can be classified into primary and secondary particles according to the particle formation process. Primary PM is emitted directly by, for example, the combustion of materials. Secondary PM is formed by, for example, chemical reactions in the ambient air of gaseous air pollutants such as sulfur oxides (SO_x), NO_x and VOCs. PM is present in the atmosphere in large quantities as both primary and secondary substances. An even smaller size is the PM₁. The smaller the size, the easier it is to penetrate the body. PM₁ has recently come to attention. Anthropogenic factors cause PM₁, but its actual nature is not fully known. There are numerous PM sources indoors and outdoors: boilers, incinerators, and other facilities that generate soot, coke ovens, mineral deposition sites, and other facilities that generate dust, automobiles, ships, aircraft, and other anthropogenic sources, as well as natural sources such as soil, oceans, and volcanoes.

While some developed countries and areas have succeeded in reducing PM₁₀ to levels close to WHO guideline values, its level in developing countries is more severe due to the increased use of cars in urban areas in addition to the use of firewood in homes, leading to higher average annual concentration in developing countries than developed countries [30].

PM affects health primarily through deposition in the human respiratory sys-

tem. Depending on the size of the particles, they behave differently in the body and have different health effects. To estimate the degree of health impact, indicators such as PM10 and PM2.5 classified according to size have been developed. Epidemiologically, there are robust reports that higher PM concentration is associated with higher mortality rates from respiratory and cardiac diseases [31]. PM10 is inhalable and can enter our lungs, causing local and systemic inflammation of the respiratory system and heart and cardiovascular and respiratory diseases such as asthma and bronchitis. PM2.5 can also be inhaled. However, its small particle size allows it to enter the lungs and deeper into our bodies. It can enter the bloodstream and be carried to various organ systems beyond the respiratory and cardiovascular systems, posing a threat to health.

- Sulfur dioxide (SO₂)

Sulfur oxide (SO_x) in air pollution refers to sulfur compounds present in the atmosphere, primarily to SO₂. They are released into the atmosphere primarily through the combustion of fossil fuels. Thus, it is a primary pollutant. SO₂ chemically reacts in the atmosphere to form acidic components such as sulfuric acid and sulfates, which attach to PM in the air and contribute to acid rain and smog formation. Acid rain and smog can lead to health hazards and environmental pollution in densely populated areas such as urban areas. SO₂ can be transported long distances by wind, making them a global environmental problem.

During combustion, SO₂ is mainly generated from coal, oil, natural gas, fuel oil, and wood. These fuels are used in industrial processes and transportation. In particular, thermal power plants, factories, and vehicle and ship exhaust are significant sources of atmospheric SO₂. SO₂ is also emitted from natural phenomena, volcanic activity, and the oceans. Natural emission, mainly from the oceans, is tiny compared to anthropogenic activities.

SO₂ in the air can cause health problems. The primary health hazard is their effect on the respiratory system. Short-term exposure can cause sore eyes and throat, coughing, bronchitis, and breathing difficulties. In particular, people with respiratory problems and those with weakened immune systems are more susceptible to health problems from short-term exposure. Long-term exposure can cause chronic bronchitis, chronic obstructive pulmonary disease (COPD), and lung cancer. Smokers and people living in areas with chronic air pollution are particularly vulnerable to health problems from long-term exposure. SO₂ can also affect the cardiovascular system, increasing the risk of hypertension and coronary artery disease. In particular, the elderly and people with heart

disease are at increased risk of adverse health effects from SO_2 .

- Volatile organic compounds (VOCs)

VOCs refer to volatile organic compounds. This is a generic term for organic compounds that evaporate easily and become gaseous in the atmosphere when released into the air. Specifically, The most well-known are, for example: Formaldehyde, Benzene, Acetone, Ethanol and Butane. VOCs are generated in many places, including indoors and outdoors. Many industrial and daily activities emit VOCs. Typical sources of VOCs are the exhaust of automobiles and industry. They are released into the atmosphere by fuel evaporation and incomplete combustion processes. When VOCs are released into the atmosphere, they cause photochemical reactions contributing to air pollution, such as photochemical smog and Ozone formation. Building materials such as paints and adhesives contain VOCs, which cause sick building syndrome [32]. In the printing, painting, and cleaning industries, VOCs exist in printing inks, paints, and cleaning agents. Chemical industries release VOCs during the manufacturing process of raw materials and products. Daily commodities such as hair sprays and deodorant sprays may also contain VOCs. Indoor environments often exhibit consistently higher concentrations of various VOCs.

VOCs themselves can also be hazardous substances, and long-term exposure can cause health problems; inhalation of VOCs can cause symptoms such as coughing, sore throats, and breathing difficulties. Prolonged exposure to VOCs can cause respiratory problems such as bronchitis and asthma. They can also affect the central nervous system, causing headaches, dizziness, and nausea. Long-term exposure is also known to cause nerve damage and cognitive decline. Some VOCs can cause liver dysfunction if inhaled or ingested through drinking water or food. Some VOCs are also known to be carcinogenic. In particular, long-term exposure can cause chronic inflammation and cell mutations.

- Ammonia (NH_3)

NH_3 is a colorless gas with a pungent odor and can be noticeable at concentrations above 50 ppm. Livestock waste treatment and fertilizer production are famous for NH_3 origin, but it is also known that car exhaust emissions emit a lot. NH_3 also contributes to the formation of harmful PM. NH_3 reacts with acidic pollutants such as SO_2 and NO_x to form aerosols containing fine ammonium (NH_4^+). These have long lifetimes and travel long distances, thus polluting the atmosphere on local and international scales.

High ammonia concentrations can irritate the eyes, nose, throat and skin. Long-term health concerns associated with ammonia exposure include severe

cardiovascular and respiratory effects, decreased lung function, worsening of asthma and premature death.

1.2 Air quality standard and regulation

Air quality standards and regulations are considered to safeguard human health and preserve the natural environment. Some air pollutants naturally occur, while others are anthropogenic, emitted by human activities like industry and traffic. Excessive emissions into the atmosphere can cause air pollution, leading to health problems such as respiratory diseases and lung cancer and adversely affecting the ecosystems of forests and water bodies. Therefore, many countries and regions establish standard values and regulations for air pollutants to minimize health hazards and environmental impacts by limiting emissions. They are determined on a scientific basis, taking into account the impact of air pollutants on human health and the environment.

According to [33], to determine the appropriate values for each air pollutant in the guidelines, WHO follows a standardized and transparent process that involves several steps:

Step 1 Identification of the health effects

WHO first identifies the health effects associated with exposure to each air pollutant. This is done by reviewing and analyzing the scientific literature on the topic.

Step 2 Assessment of the evidence

WHO assesses the strength and quality of the scientific evidence on the health effects of each air pollutant. This includes evaluating the consistency and coherence of the findings across different studies and populations.

Step 3 Estimation of the health risk

Based on the evidence, WHO estimates the health risks associated with exposure to each air pollutant. This involves quantifying the level of exposure that would cause a given level of risk for a specific health effect.

Step 4 Development of guideline values

Finally, WHO develops guidelines for each air pollutant based on the health risk estimates. The guideline values represent the maximum levels of each air pollutant considered safe for human health.

The development of the guidelines involves a multidisciplinary group of experts from different fields, including epidemiology, toxicology, environmental science, and public health. The process is also subject to extensive peer review and consultation with stakeholders to ensure that the guidelines are scientifically sound, transparent, and relevant to the needs of member countries.

1.2.1 Outdoor standard and regulation

The first guidelines on air pollution were developed by WHO in 1987 and have been updated several times since then. Originally developed as a guideline for the European region, it was subsequently expanded in 2005 to encompass all regions [30], ensuring their global applicability. EU developed "Directive 2004/107/EC" in 2004 [34] and "Directive 2008/50/EC" in 2008 [35]. Table 1.2 compares standard values of both WHO (Air quality guidelines, 2006 [30]) and EU (Directives (2004/107/EC [34], 2008/50/EC [35]). As health problems depend on the time of exposure to pollutants, standard values have been established for various duration. WHO guidelines are generally more strict than EU ones, aiming to provide the highest possible protection for public health. In contrast, EU guidelines have to consider not only health effects but also environmental and economic considerations. Hence, the standard values are lower than those of WHO. WHO guidelines are voluntary and provide recommendations for member states to follow, while EU guidelines have legal status and are implemented in member states.

Air quality has been improved over the past twenty years thanks to the improvement of combustion technology and advances in household appliances. Fig. 1.4 shows the percentage of people in the EU exposed to pollutant concentrations above the standard values of WHO and EU over the past 20 years. While a significant portion of the population is still exposed to air pollutant concentrations exceeding WHO guidelines, a lower percentage of people face concentrations above EU standards. However, this does not imply fewer health hazards in the EU. As mentioned, WHO has adopted stricter standards because preventing health risks is their top priority. In conclusion, improvements in air quality are still required outdoors.

1.2.2 Indoor standard and regulation

Whereas outdoor air pollution has long been the focus of attention and regulation, the issue of indoor air pollution has lagged behind. It can be due to the difficulty of setting indoor air pollution standards. Unlike outdoor air pollution, it is difficult to monitor indoor air quality in each household regularly. Furthermore, dwelling

Pollutant	Averaging period	EU Air Quality Directives				WHO Air Quality Guidelines				
		objective	Concentration	Comments	Concentration				Comments	
					Interim targets	AQG level				
					1	2	3	4		
PM2.5	24-hour	Target value			75	50	37.5	25	15 $\mu\text{g}/\text{m}^3$	99th percentile (i.e. 3-4 exc.Days/year)
PM2.5	Annual	Limit value	25 $\mu\text{g}/\text{m}^3$		35	25	15	10	5 $\mu\text{g}/\text{m}^3$	
PM2.5	Annual	Indicative value	20 $\mu\text{g}/\text{m}^3$							
PM10	24-hour	Limit value	50 $\mu\text{g}/\text{m}^3$	Not to be exceeded on more than 35 days/year	150	100	75	50	45 $\mu\text{g}/\text{m}^3$	99th percentile (i.e. 3-4 exc.Days/year)
PM10	Annual	Limit value	40 $\mu\text{g}/\text{m}^3$		70	50	30	20	15 $\mu\text{g}/\text{m}^3$	
O ₃	Max. daily 8-hour mean	Target value	120 $\mu\text{g}/\text{m}^3$	Not to be exceeded on more than 25 days/year						
O ₃	Max. daily 8-hour mean	Long-term objective	120 $\mu\text{g}/\text{m}^3$							
O ₃	8-hour	Target value			160	120	-	-	100 $\mu\text{g}/\text{m}^3$	99th percentile (i.e. 3-4 exc.Days/year)
O ₃	Peak season	Target value			100	70	-	-	60 $\mu\text{g}/\text{m}^3$	
NO ₂	Hourly	Limit value	200 $\mu\text{g}/\text{m}^3$	Not to be exceeded on more than 18 hours/year					200 $\mu\text{g}/\text{m}^3$	
NO ₂	Annual	Limit value	40 $\mu\text{g}/\text{m}^3$		40	30	20	-	10 $\mu\text{g}/\text{m}^3$	
NO ₂	24-hour	Target value			120	50	-	-	25 $\mu\text{g}/\text{m}^3$	99th percentile (i.e. 3-4 exc.Days/year)
SO ₂	Hourly	Limit value	350 $\mu\text{g}/\text{m}^3$	Not to be exceeded on more than 24 hours/year						
SO ₂	24-hour	Limit value	125 $\mu\text{g}/\text{m}^3$	Not to be exceeded on more than 3 days/year	125	50	-	-	40 $\mu\text{g}/\text{m}^3$	99th percentile (i.e. 3-4 exc.Days/year)
CO	Max. daily 8-hour mean	Limit value	10 mg/m ³						10 $\mu\text{g}/\text{m}^3$	
CO	24-hour	Limit value			7	-	-	-	4 $\mu\text{g}/\text{m}^3$	99th percentile (i.e. 3-4 exc.Days/year)

Table 1.2: Comparison EU (Directives (2004/107/EC, 2008/50/EC) and WHO (Air quality guidelines: global update 2005) standard values [36].

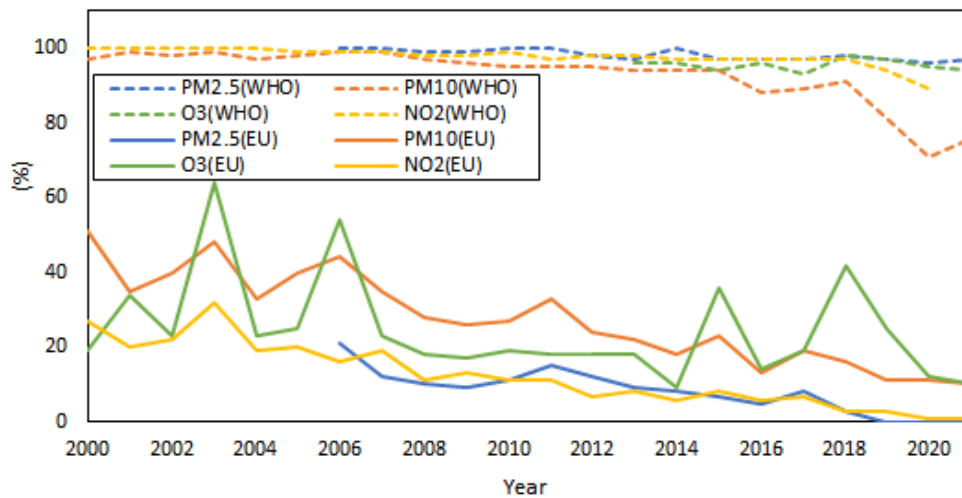


Figure 1.4: EU urban population exposed to air pollutant concentrations above WHO and EU air quality standards, EU-27 [37].

types and ventilation levels vary considerably from country to country and region to region, and health risks also vary. Therefore, it is difficult to establish uniform standards worldwide.

WHO had stressed in the 1st edition of guidelines for outdoor air quality in 1987 that standards should also apply to indoor air quality [38], and further emphasized the importance of this when it was updated in 2005 [30]. A total of 9 indoor pollutants: benzene, carbon monoxide, formaldehyde, naphthalene, nitrogen dioxide, polycyclic aromatic hydrocarbons (especially benzo[a]pyrene), radon, trichloroethylene, and tetrachloroethylene were added to the guidelines. In France, for example, Agence Nationale Sécurité Sanitaire Alimentaire Nationale (ANSES) has set standards for 13 indoor air pollutants [39]. Although WHO has set them only as recommended values, the French standards have to be followed in some indoor environments (e.g., schools and kindergartens).

WHO and France have different standard values. For example, concerning benzene, WHO sets no standard value, just recommendation values and says that the generation of benzene itself should be removed or controlled, given its hazardous nature. On the other hand, France has set short-term exposure, intermediate-term exposure, and life-long exposure.

1.3 Measurement of Air Quality

In this part, I discuss monitoring of air quality using gas sensors. Modeling and mitigation strategies will be presented in Chapters 2 and 3 respectively. Monitoring air quality is of great importance to individuals, public administration, and science. Air quality fluctuates widely over time and space. Local high concentrations generated from traffic or industry affect not only the local area but also the surrounding areas. By monitoring air quality correctly, the source of pollution can be identified, and countermeasures can be taken to ensure that people enjoy clean air. Air quality monitoring is essential for the following reasons:

- Continuous monitoring allows local authorities to identify deviations and excessive emissions, enabling them to take necessary actions to mitigate the impact on the environment and public health.
- Monitoring air quality helps to identify areas and sources of poor air quality, enabling local authorities and the general public to make informed decisions and take necessary precautions to minimize exposure to pollutants and maintain their well-being.
- Long-term observations can identify and assess both short- and long-term diseases and disorders caused by air pollution, facilitating the development of appropriate air quality management and countermeasures.
- Air quality monitoring provides valuable data to create pollutant concentration cartography, offering visually accessible information to local authorities for decision-making, such as urban planning strategies. (However, it is worth mentioning that people generally do not have a sufficient number of sensors; therefore, in practice, sensor measurements are often combined with physical models, which is discussed in a future chapter;
- Identifying areas and causes of poor air quality through monitoring enables the implementation of effective countermeasures to improve air quality.
- Public awareness raised by pollutant maps and air quality information encourages appropriate actions against poor air quality, fostering the motivation of local authorities, researchers, and industries to develop new technologies and strategies to address the problem.

The accuracy of monitoring depends to a large extent on sensor technology. There are many different types of sensors, depending on their accuracy, measurement methods, and purpose. The following subsections concern the different types of sensors.

1.3.1 Reference and low-cost sensor for gas and particle

Although it has long been clear that air pollution is a major health hazard, obtaining information on the concentration of the numerous pollutants that have spatiotemporal variations is still challenging. Historically, air pollution has been monitored by deploying precise but expensive reference sensors (RS) at low densities. RS provides high-quality data and is essential for scientific research and regulatory compliance. This has prevented widespread individual use of sensors. Those who can access the information from these sensors are limited to, e.g., government agencies, researchers and air quality monitoring agencies (i.e., Airparif agency). However, this situation has changed drastically in recent years with the emergence of low-cost sensors (LCS) suitable. LCSs are inexpensive. Therefore, LCS is more accessible to individuals and communities, allowing them to monitor air quality in their immediate surroundings. Also, they can be used in a wide range of arrangements at high densities, useful to identify locally high concentrations and create maps of inhomogeneous pollutant concentration in real-time. Nevertheless, it has been noted that the accuracy of LCS sensors is highly questionable, and the use of their data should be used with caution. Both types of sensors have their own place to be used in air pollution monitoring. They can also be used together to provide a more comprehensive understanding of air quality. The features and performance of both sensors are highlighted in Table 1.3.

Both have various advantages and disadvantages, but recent developments in microsensor technology have contributed significantly to the rapid introduction of LCS [40]. Considering the potential for further development and the ease of use for individuals, private companies and local authorities, it is likely that LCS will become even more popular in the future. Accordingly, the following subsection explains LCS sensor's principles.

There are primarily two types of sensors for air pollutants: one that measures the concentration of gaseous substances and the other the mass concentrations of PM or different characteristics of particles, such as absorption or scattering. In air quality monitoring, the fundamental principle of sensor technology lies in converting the detection of gases or particles into an electrical signal. The magnitude of this signal is related to the concentration of the target gas or particle in the atmosphere.

	RS	LCS
Performance and Accuracy	<ul style="list-style-type: none"> ✓ High-precision instruments that are designed to meet specific performance standards × Require specialized training to operate 	<ul style="list-style-type: none"> ✓ Small and portable × Not meet the same performance standards as RS × Depending on the type of sensor and the environment
Cost	<ul style="list-style-type: none"> × Expensive ranging from thousands to tens of thousands of dollars × High expenditure for maintenance 	<ul style="list-style-type: none"> ✓ Typically cost between 50 to 1000 EURO ✓ Affordable and accessible for the general public
Application	<ul style="list-style-type: none"> ✓ Used as reference values to calibrate and validate LCS ✓ Provides accurate and reliable data 	<ul style="list-style-type: none"> ✓ Best suited for community-based monitoring and citizen science projects ✓ Used in large numbers to create a dense monitoring network
Maintenance	<ul style="list-style-type: none"> ✓ Low-frequently maintenance and calibration × Often operated by trained professionals × Difficult to make in-situ calibration 	<ul style="list-style-type: none"> × Need regular calibration × Require some maintenance such as cleaning and replacing filters

Table 1.3: Features of Reference sensor (RS) and Low-cost sensor (LCS).

1.3.1.1 Gas sensor

Gas sensors typically measure gaseous air pollutants: NO, NO₂, O₃, SO₂, CO and VOC. These gases are of particular interest as they can cause direct or indirect harm to human health and ecosystems, or such that they can react and produce secondary pollutants like O₃. Let me introduce some typical sensors: electrochemical (EC) sensor, metal-oxide-semiconductor (MOS) sensor, miniature photoionization detector (PIDs), and non-dispersive infrared (NDIR) sensor are often utilized to detect air pollutants and reactive gases.

EC sensors use electrochemical reactions between the target gas and an electrolyte to produce a current corresponding to the gas concentration. These sensors typically consist of three electrodes and have lower detection limits and lower sensitivity to changes in environmental conditions and interfering gases than MOS sensors. The response of EC sensors is either linear or logarithmic, and they typically require slightly more power than MOS sensors. They are also more expensive and they can interfere with relative humidity and temperature, requiring additional measurements for reliable results.

MOS utilizes a metal oxide film that changes its electrical resistance when exposed to a target gas, allowing for easy measurement and detection of the gas concentration. These sensors are small, lightweight, and inexpensive, with low detection limits and quick response times. However, they have a non-linear response curve and can be sensitive to changes in environmental conditions and interference from other gases.

PIDs are the most frequently used on-site detection instruments for VOCs using ultraviolet light to break organic molecules apart. Once they are ionized, they induce a small current which can be detected by sensors. PIDs can be applied to a broad range of VOCs, including those that are not easily detected by other gas sensors. However, PIDs have limitations in detecting certain VOCs and their accuracy can be affected by factors such as humidity and temperature. Moreover, PIDs have variable efficiency in ionizing different VOCs, which leads to variations in their detection levels. Therefore, PID-based sensors provide measurements for the total ambient VOCs that are influenced by the specific mixture of VOCs present.

NDIR sensor is widely used in various industries, particularly to measure CO₂ concentration. The operational principle of NDIR sensors is to employ an infrared (IR) lamp to project infrared light through an air-filled chamber. The emitted light passes an optical filter before reaching an IR detector, which quantifies the light's

intensity. The disparity between anticipated and measured intensity is attributed to light absorption by CO₂. This principle faces some interference from fluctuations due to the light absorption by water vapor and gases and variation of the light source.

1.3.1.2 PM sensor

Particle measurement is a challenging task that involves categorizing particles based on their sizes. The complexity arises due to various factors that differ across measurement methodologies and particle types, such as their chemical composition, density, relative humidity, refractive index, shape, and size distribution. Besides, particles can also be highly reactive, and sampling biases can affect the accuracy of reported mass concentrations when particles are transferred across significant gradients of temperature or humidity during sampling.

There are various techniques to determine the PM concentration in the air, including the filter-based gravimetric method, β -attenuation method, and optical method. Among these, the optical method is preferred for low-cost sensing due to its affordability, low power consumption, and fast response time. This method involves illuminating the particles with a light source and measuring the scattered light using a photometer. The amount of scattered light is directly proportional to the mass or number concentration of particles.

1.4 Conclusion

Since my Ph.D. work is interdisciplinary, in this chapter, I provided an overview of air quality issues, health risks, air quality standards and guidelines, and sensor monitoring principles, which are essential information hereafter.

The general public often focuses on outdoor pollutants, but indoor pollutants are equally concerning. For indoor environments, it is worth noting that polluted outdoor air is a major pollutant source. Many standards and guidelines have been established for outdoor pollutants, but indoor air quality is delayed. Thanks to low-cost sensors, access to air quality information has become easier for the general public, but its accuracy has limitations. Therefore, achieving fundamental improvement in air quality is of utmost importance. Since outdoor pollutants significantly impact indoor air quality, there is a growing need to understand the interaction between indoor and outdoor air quality and develop appropriate mitigation measures

to consider this interaction. The next chapter will describe methodologies for the pollutant dispersion prediction and study.

Chapter 2

Air Pollutant Dispersion: Measurement and Modeling

To date, many methods for measuring or predicting pollutant concentrations have been developed and used. Whether it is a measurement, modeling or other methods, the ultimate aim is to obtain accurately predicted values. Each method has different accuracy, scope and use, so understanding them is important in air pollution research. I conveniently divided methods for studying air pollution into three broad categories: experiment (including field measurement and wind tunnel testing), semi-empirical modeling, and CFD modeling. This chapter provides a brief description of each type of method.

2.1 Spatial scale in urban pollutant dispersion

Before describing each method in detail, this section explains the spatial scale of pollutant dispersion because appropriate methods are different according to spatial scales of pollutant dispersion.

Pollutant dispersion is mainly caused by atmospheric dynamics. As the major sources of pollution (e.g., emissions from traffic and industry) and production of pollution (e.g., secondary pollutants produced by chemical reactions) generally occur close to the ground surface, the atmospheric dynamics near the ground surface is an essential parameter in urban pollutant dispersion. As shown in Fig. 2.1, the layer of the atmosphere near the ground surface is called urban boundary layer (UBL). UBL consists of turbulent flows and has a strong vertical mixing of physical quantities such as velocity, temperature, humidity, and pollutants. Within UBL, the layer

particularly affected by buildings near the ground surface is called surface layer (SL), below which there are roughness sub-layer (RSL) where airflow is directly affected by buildings, and urban canopy layer (UCL) where individual elements (e.g., human, building, tree and road) creates its own microclimate. Within RSL and UCL, airflow disturbed by cities' elements generates complex flows locally. These complex flows highly influence pollutant dispersion characteristics in urban areas.

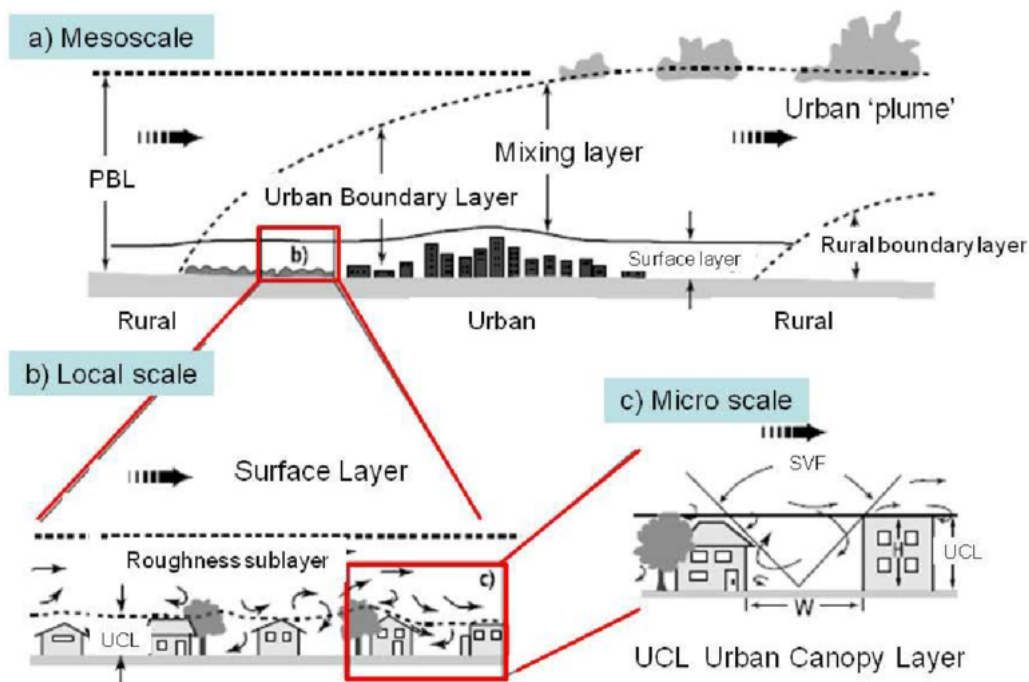


Figure 2.1: Three scales used to distinguish atmospheric processes in urban area and the atmospheric layers [41].

The scale, where pollutant dispersion is affected by urban areas, is smaller than phenomena occurring at meteorological scales. [42] provides a detailed classification of scales smaller than RSL. Many studies have been conducted for each different scale: neighborhood scale (e.g., [43]), street scale (e.g., [44]), and building and indoor scale (e.g., [45]). Depending on the scale and objective, one has to select appropriate approaches. In the following, some typical methods to observe or predict air pollution are described.

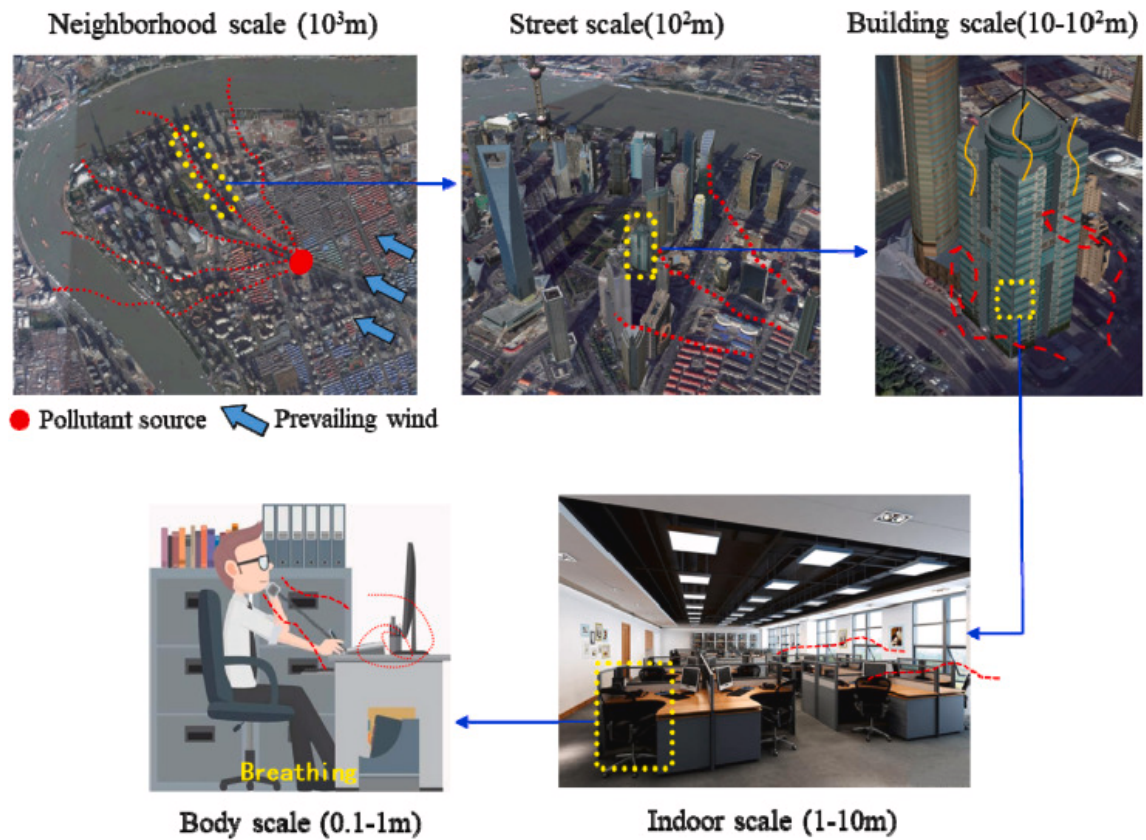


Figure 2.2: Schematic representation of relevant spatial scales in pollutant dispersion from neighborhood to body scale [42].

2.2 Methodology to study air pollutant dispersion: measurement and prediction

2.2.1 Experimental way

- Field measurement

The first method to study air pollution is field measurements. As the name suggests, field measurements directly measure pollutant concentrations in urban areas using sensors (Fig. 2.3). A significant advantage of field measurement is that if the sensor works correctly, the measured value precisely and reliably represents the pollutant concentration at that point. These values take into account all the complexity of the flow, traffic conditions, weather fluctuations, etc.



Figure 2.3: Monitoring stations of field measurement (Airparif): in Paris (left) and next to a highway [46].

Many countries, regions and institutions have issued guidelines on air pollution (e.g., Directive/2008/50/EC in EU). These guidelines assume sensor-based field measurements. However, one major disadvantage of field measurements is that the number and density of sensors are mostly insufficient. The values measured by each sensor only indicate the value at that point and cannot capture spatial variation or gradients of pollutant concentrations in whole regions. In general, the distribution of pollutant concentration is non-uniform in urban areas. In order to get high spatial information, sensors need to be placed in appropriate locations with high densities. In the case of measurements in real environments, it is difficult to govern fluctuations in the measurement conditions during the measurement intervals and to ascertain all the factors that influence pollutant concentrations, such as wind direction, wind speed, temperature, traffic volume and construction working in the vicinity. They cause difficulty in interpreting the measured values. To address these shortcomings, data assimilation combining sensor measurements and simulations has attracted attention recently [47].

- Wind tunnel testing

The second method is wind tunnel testing (reduced-scale measurement) (Fig. 2.4 (a)). In wind tunnel testing, flow and pollution are measured using, for example, hot-wire. Wind tunnel testing offers a significant advantage by allowing precise control of boundary conditions like wind speed and direction, which are uncontrollable in field measurements. This control enables researchers to tailor these conditions to their specific objectives, thereby reducing uncertainties in the measured data and making an interpretation of the results easy. Nev-

ertheless, like field measurements, wind tunnel testing provides pointwise information. In such a case, hybridizing with Particle Image Velocimetry (PIV) method using tracer gases provides a visual understanding of airflow and dispersion of whole areas (Fig. 2.4 (b)). However, wind tunnel testing and PIV require some specialized equipment, which is not always accessible to everybody. Moreover, wind tunnel testing always suffers from the similarity law that must be satisfied. Making a geometry of reduced-scale models is also a time-consuming task. Nevertheless, it is worth noting that wind tunnel testing is used to study and understand pollutant dispersion rather than predict it.

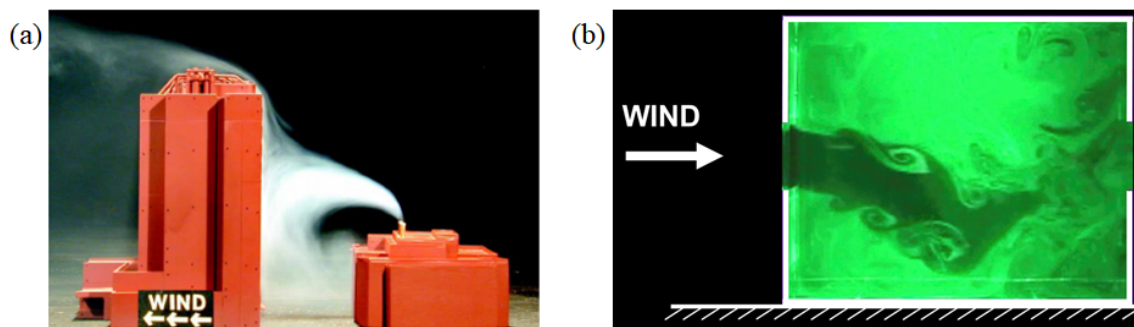


Figure 2.4: (a) wind tunnel testing [48] and (b) PIV [49].

2.2.2 Semi-empirical modeling

There are many semi-empirical models to predict pollutant dispersion. In this subsection, three common models are presented: Gaussian plume model, Box model and chemistry-transport model.

- Gaussian plume model

Gaussian plume model is a simple method often used by local authorities to predict pollutant dispersion. This model assumes that pollutant dispersion spreads downwind as Gaussian distribution. This process applies to both horizontal and vertical dispersion (Fig. 2.5). The magnitude of pollutant concentration is proportional to the emission ratio of the source, and the dispersion is determined by some parameters:

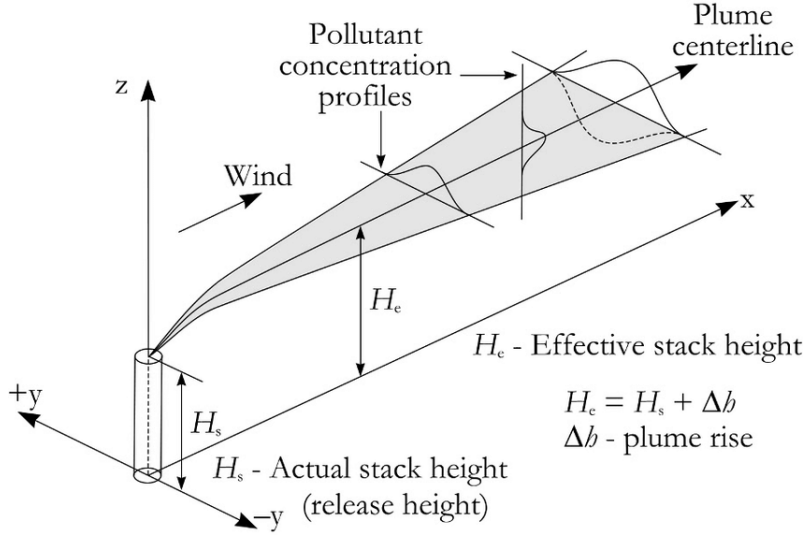


Figure 2.5: Schematic figure of a Gaussian plume [50].

$$C(x, y, z) = \frac{Q}{2\pi u \sigma_y \sigma_z} \exp\left(\frac{-y^2}{2\sigma_y^2}\right) \left\{ \exp\left(\frac{-(z-h)^2}{2\sigma_z^2}\right) + \exp\left(\frac{-(z+h)^2}{2\sigma_z^2}\right) \right\} \quad (2.1)$$

where $C(\mu g/m^3)$ is the time-averaged pollutant concentration, $Q(\mu g/s)$ is the pollutant emission rate at location (x, y, z) , $u(m/s)$ is the time-averaged wind speed, $\sigma_y(m)$ and $\sigma_z(m)$ are the horizontal and vertical standard deviation of the emission distribution that are influenced by atmospheric stability, $h(m)$ is the height at pollutant source, $y(m)$ is the distance from the emission centerline and $z(m)$ is the distance from the ground. In this modeling, many assumptions and simplifications are made, for example,

- $u(m/s)$ is the constant average wind speed and constant wind direction;
- $Q(\mu g/s)$ is the continuous constant pollutant emission rate;
- Diffusion to the upwind side is neglected;
- Pollutants are stable and not reactive;
- The terrain is not complex.

These assumptions are often not correct in reality, but they are easy and fast to use. To improve the prediction accuracy, many modified Gaussian

plume models have been developed, e.g., AERMOD [51] developed by the US Environmental Protection Agency.

- Box model

Box model method is a computationally light and easy-to-use model. This is also known as the simplest model. The concept of Box model is shown in Fig. 2.6. The area for which the pollutant concentration is to be determined is box-shaped. The mass balance equation is constructed on the assumption that the conservation of mass is preserved within the box. The model is represented with the following equation:

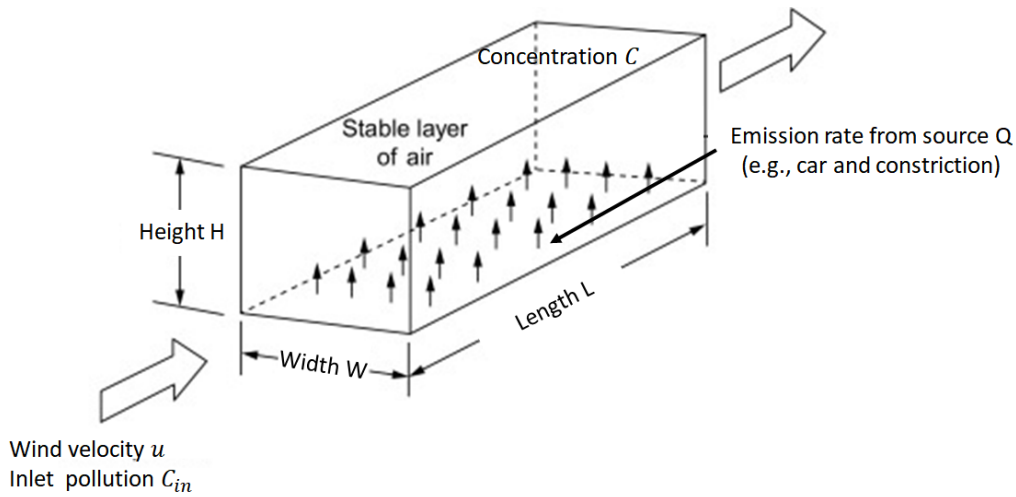


Figure 2.6: Schematic figure of Box model [52].

$$\frac{dCV}{dt} = QA + uC_{in}WH - uCWH \quad (2.2)$$

where $C(\mu\text{g}/\text{m}^3)$ is pollutant concentration throughout the box, $V(\text{m}^3)$ is the Volume of the box, $Q(\mu\text{g}/(\text{m}^2 \cdot \text{s}))$ is pollutant source emission rate, $A(\text{m}^2)$ is area of the box (box length $L(\text{m}) \times$ box width $W(\text{m})$), $u(\text{m}/\text{s})$ is wind velocity normal to the box, $C_{in}(\mu\text{g}/\text{m}^3)$ is inlet pollutant concentration, $H(\text{m})$ is box height. The dimensions of the box are determined based on average wind speed, terrain condition, pollution source location, etc. For this box, some assumptions are made:

- Wind enters perpendicularly on one side;

- Incoming air pollutants are instantly mixed in the area inside the box;
- Pollutant concentration is uniform throughout the box.

Chemical reactions can also be incorporated into Eq. (2.2). However, the prediction accuracy of this model is limited due to big simplifications, e.g., homogeneous pollutant concentrations throughout the box.

- **Chemistry-transport model**

This model solves equations for pollutant transport and chemical reactions from urban to continental scales. It can determine three-dimensional pollutant concentrations. The grid resolution spans 1 km to 100 km, allowing simulations to extend into the troposphere. Calculations can be performed for a wide range of pollutants, including over 100 gaseous and particulate substances such as O₃, NO_x, PM, CO, and SO₂, which are major pollutants. Moreover, various sources, both anthropogenic and natural, can be considered, and factors such as transport, turbulent diffusion, chemical reactions and deposition can be taken into account. This model, like CHIMERE [53], is used in numerous research and practical applications, such as daily air quality predictions across France by Airparif agency [54]. The model is highly reliable for simulations on a broad scale but is not designed to make detailed air pollutant cartography at high resolution, e.g., 1 ~ 5 m.

2.2.3 CFD modeling

Nowadays, CFD is the most used modeling for air pollutant dispersion prediction. When CFD is applied to urban and building scales, the advection-diffusion reaction equation (2.3) for pollutant concentrations is discretized in space and time and solved by computers;

$$\frac{\partial C}{\partial t} + \underbrace{\mathbf{v} \cdot \nabla C}_{\text{Advection}} - \underbrace{\text{div}(D\nabla C)}_{\text{Diffusion}} + \underbrace{R(C)}_{\text{Reaction}} = S \quad (2.3)$$

where $C(\mu\text{g}/\text{m}^3)$ is the pollutant concentration, $\mathbf{v}(m/s)$ is wind velocity, $D(m^2/s)$ is the diffusion coefficient (total of molecular and turbulent diffusivity), $R(C)$ represents the chemical reaction term and S is the source term. It is generally discretized using finite volume, finite difference or finite element methods. A significant advantage of CFD is to provide high spatiotemporal pollutant concentration information throughout a computational domain. This detailed and precise space-time cartography could not be obtained with field measurements, wind tunnel testings, and

semi-empirical modelings. In CFD, numerical mock-up (geometry of building, city and terrain) can be performed on the real scale, so there is no need to consider similarity law. CFD can also deal with detailed building geometries and boundary conditions, which semi-empirical modeling could not consider. However, the big disadvantage is the computation cost, e.g., when simulating neighborhood scale simulations. Moreover, computational parameters significantly affect prediction accuracy and include many uncertainties, which should be dealt with carefully. For these reasons, it may be difficult for local authorities to use them easily. Some guidelines have been published to encourage their adoption in industry practice and administrative contexts [55, 56].

The choice of turbulence model is of significance for prediction accuracy. There are three major turbulence models commonly used: Reynolds-Averaged Navier-Stokes (RANS) model, Large Eddy Simulation (LES) model and Direct numerical simulation (DNS). RANS is categorized into steady RANS (SRANS) and unsteady RANS (URANS) according to whether the unsteady components can be considered or not. Each turbulence model operates eddies at different scales: DNS computes all eddies in space, LES directly computes eddies larger than the grid size and models smaller eddies, while RANS models all eddies. The accuracy of the models increases as more eddies are resolved (i.e., less reliance on turbulence model), allowing for capturing finer spatial variations. However, this also leads to a higher computational burden. Fig. 2.7 (a) illustrates an example time history of velocity for each model. DNS can reproduce the high-frequency components that exist in reality. LES removes and models these high-frequency components by applying a spatial filter, while URANS exhibits a smoother time history than LES but can reproduce major fluctuations. Lastly, SRANS only provides time-averaged results. For example, the simulation results for turbulent jet clearly demonstrate the difference (Fig. 2.7 (b)). Typically, airflow in cities is very complex and has high Reynolds numbers, making it computationally prohibitive to solve them with DNS. Instead, DNS is often employed for fundamental studies focusing on turbulence characteristics, e.g., [59]. In practical applications such as urban design, designers and local authorities generally prioritize statistical values like averages over peak values obtained through simulation that DNS captures. As a result, LES and RANS are currently the most practical turbulence models for microclimate scales, including urban and building scales.

Numerous studies have examined the accuracy of RANS and LES in predicting pollutant concentration compared with wind tunnel testings, e.g., [44, 60]. These studies generally demonstrate that LES exhibits better agreement with experimen-

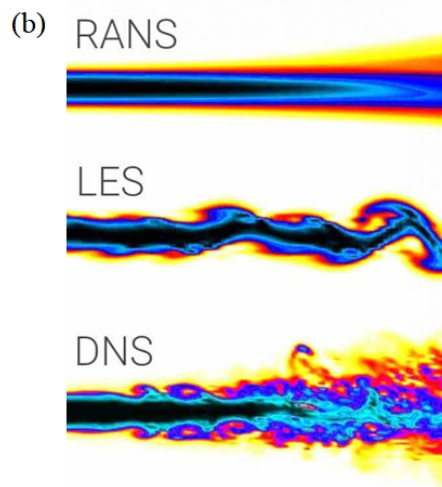
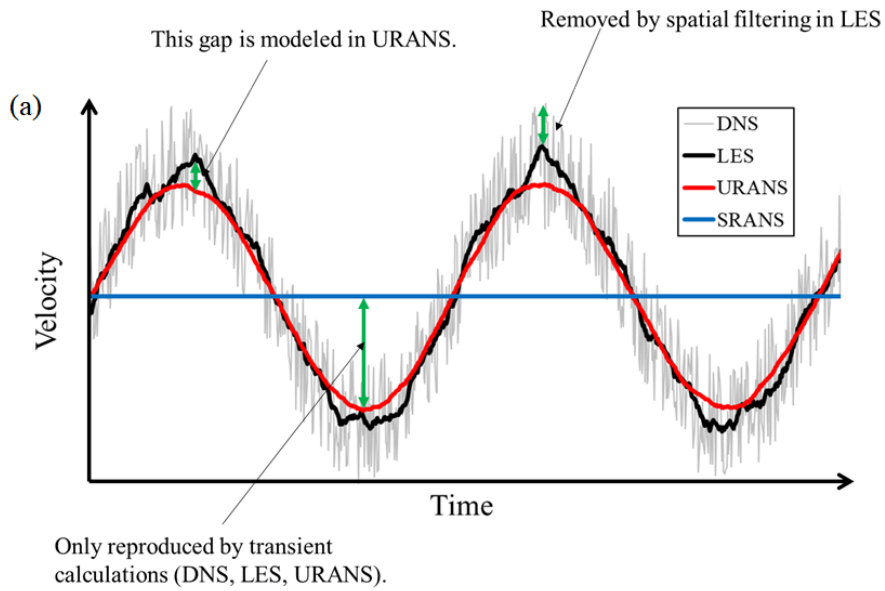


Figure 2.7: Comparison between DNS, LES and RANS: (a) concept of the DNS, LES, URANS and SRANS approaches on the typical time evolution of the velocity behind a building [57] and (b) turbulent jet with each turbulence model [58].

tal values. This can be attributed to the fact that LES more accurately captures airflow fluctuations, which plays an important role in pollutant dispersion. Fig. 2.8 compares velocity distributions inside a simple building between RANS, LES and experiment. Standard $k-\epsilon$ (SKE) and SST $k-\omega$ (SST) overestimate or underestimate the velocity sometimes, and LES provides the closest match to the experimental values. Here, k is turbulence kinetic energy, ϵ is turbulent dissipation rate, and ω is specific turbulent dissipation rate, which are detailed in the next chapter. However, while LES is computationally efficient than DNS, its computational cost is still too expensive for practical applications. In this context, it is worth noting, as depicted in Fig. 2.8, that RANS (SKE and SST) is capable of accurately predicting trends of velocity distribution. [44] also pointed out the advantage of RANS that captures trends of velocity and pollutant concentration with lower computational cost. Therefore, RANS still remains beneficial in practice. In many practical applications, the main focus often lies on average values, trends, and statistical representation, making RANS a suitable approach in practice.

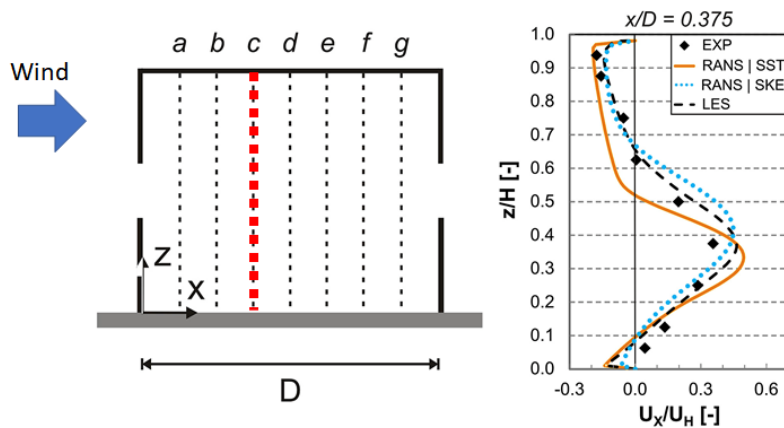


Figure 2.8: Comparison of dimensionless mean x-velocity (U_X/U_H) obtained in the vertical center plane of the inside at $x/D = 0.375$ between SKE, SST, LES and experiment [61].

Many improved RANS models have been proposed. Since turbulence models of RANS impact the prediction accuracy of pollutant concentration, many studies have compared velocity and pollutant concentration using various turbulence models, e.g., [61, 62]. It was noted that model selection is critical because pollutant concentrations around buildings can vary over an extensive range depending on the model selection. Two-equation $k-\epsilon$ model is the most used, and also two-equation $k-\omega$ model is commonly utilized in many engineering fields. Both method has its advantage and

disadvantage. Two-equation $k - \epsilon$ model has good prediction accuracy in free-shear layer flow but struggles to accurately predict turbulence near walls, often necessitating wall functions [63]. On the other hand, two-equation $k - \omega$ model exhibits enhanced accuracy and provides more precise results within boundary layers near walls, compared to two-equation $k - \epsilon$ model, but its accuracy diminishes as it moves away from the wall surface. To address their disadvantage and use their advantages, [64] developed $k - \omega$ SST model, which incorporates $k - \omega$ formulation near the wall and $k - \epsilon$ formulation elsewhere. Two-equation $k - \omega$ SST model has gained significant popularity in many engineering fields. In my Ph.D., I will employ $k - \omega$ SST model for the numerical prediction of air pollutant dispersion in future applications (Chapter 4 and 5).

2.3 Data Assimilation

As discussed in the previous section, simulations offer high-resolution space-time analysis. However, it still involves some uncertainties, e.g., boundary conditions and numerical parameters. On the other hand, field measurements provide accurate values that take into account all fluctuations and uncertainties in reality, but the number of measurement points is often not sufficient to make pollutant cartography. In this context, data assimilation (DA) has attracted much attention in recent years to utilize both simulations' and measurements' advantages. Combining numerical simulations and measured data can significantly improve the overall accuracy and reliability of both approaches. DA has two main objectives:

- Enhancing the accuracy and performance of numerical simulations by incorporating measured data;
- Using simulation models to compensate for missing observations or correct observation errors.

In practical applications, DA is very commonly used for weather forecasting and prediction. Weather forecast models generally require estimating the correct initial values to get good predictions. In weather forecasting, data assimilation with new and past data is used to predict more plausible initial values. As a result, forecast performance improves. In DA, several methodologies are utilized: Nudging methods, Least Square method, Three-dimensional variational method, Ensemble Kalman Filter, Four-Dimensional Variational method, etc.

2.4 Specific modeling for indoor air quality

As with outdoor airflow and air pollutant dispersion prediction, CFD modeling is a promising tool for analyzing indoor airflow and indoor pollutant dispersion. Although the computational cost for indoors is generally cheaper than outdoors, CFD is still sometimes computationally demanding. For indoor air quality, for example, real-time air quality monitoring and online ventilation control are often required. Therefore, computationally efficient indoor air quality modelings are usually preferred. Accordingly, some semi-empirical modelings have been developed to study indoor environments, especially semi-empirical modelings. This subsection focuses on them. Regarding other modelings, for example, [65] reviewed some methods and proposed a new modeling for indoor air quality.

2.4.1 Single/Multizone model

Single/Multizone model is a computationally efficient approach as it has to solve just ordinary differential equations. The target indoor environment is modeled by some zones connected to each other through designated flow paths (see Fig. 2.9). The underlying principle of this method is the network model method, which is to construct equations representing the airflow paths in a building. The airflow between zones driven by wind pressure differences at window surfaces, buoyancy effects due to temperature, and pressure differences due to mechanical ventilation can be calculated. Airflow and pollutant concentrations within all zones are considered uniform. Flow patterns and pollutant concentrations are predicted based on factors such as airflow, pollutant infiltration, indoor ventilation conditions, and weather conditions in each zone. Interactions with the outdoors are modeled by connecting zones that represent outdoor conditions. The method provides good insights given that correct parameters are imposed and the appropriate ventilation environment is assumed. Although it is suitable for providing spatially averaged airflow and pollutant concentrations, other methods, such as CFD, are required to obtain more detailed information on airflow and air quality.

2.4.2 Fast Fluid Dynamics

Fast fluid dynamics (FFD) has recently been used for indoor airflow and air quality since the 2000s, mainly by Zuo and Chen et al. [67]. FFD is an intermediate method between CFD and semi-empirical models. The aim is to obtain more information, like CFD, with less computation time as in Single/Multizone model. This method solves Navier–Stokes equations and the continuity equation assuming laminar flow.

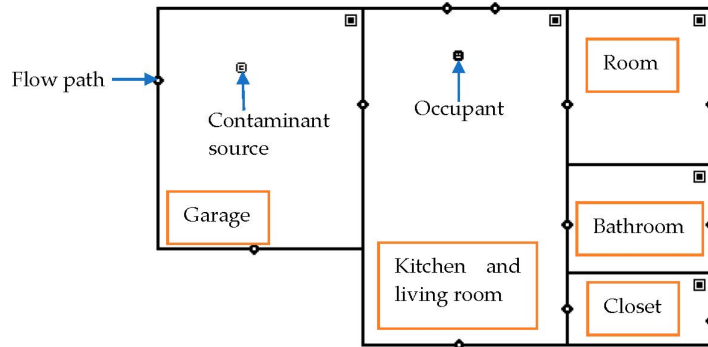


Figure 2.9: Example layout of the house in Single/Multizone model application [66].

By ignoring turbulence effects, the calculations can be performed significantly faster than normal CFD.

2.4.3 Low-Dimensional Linear Ventilation Model

[68] proposed Low-Dimensional Linear Ventilation Model (LLVM) model, which is similar to Box model in Subsection 2.2.2, It calculates indoor airflow and air quality on the basis of linear low-dimensional equations derived directly from NS equation and the advection-diffusion equation. Unlike FFD, the results include the effects of turbulence. Fig. 2.10 shows the pollutant concentrations obtained with the RANS and LLVM models, showing that LLVM model can roughly estimate pollutant concentrations in comparison with CFD.

2.5 Conclusion

This chapter has described measurements and modelings used in research and industry to obtain pollutant dispersion cartography. Each method has advantages and disadvantages for outdoor-scale and indoor-scale pollutant dispersion, summarised in Table 2.1. Field measurement and wind tunnel testing are available for both outdoor and indoor, and their accuracy is high if used correctly. However, they generally require equipment investment, maintenance and specialized facilities. Also, their representativeness is not enough. Those developed specifically for outdoor or indoor scale predictions respectively are often not suitable for the other scales' prediction. In this context, CFD is a promising tool. CFD provides numerical predictions with good accuracy for both outdoors and indoors. Therefore, the following

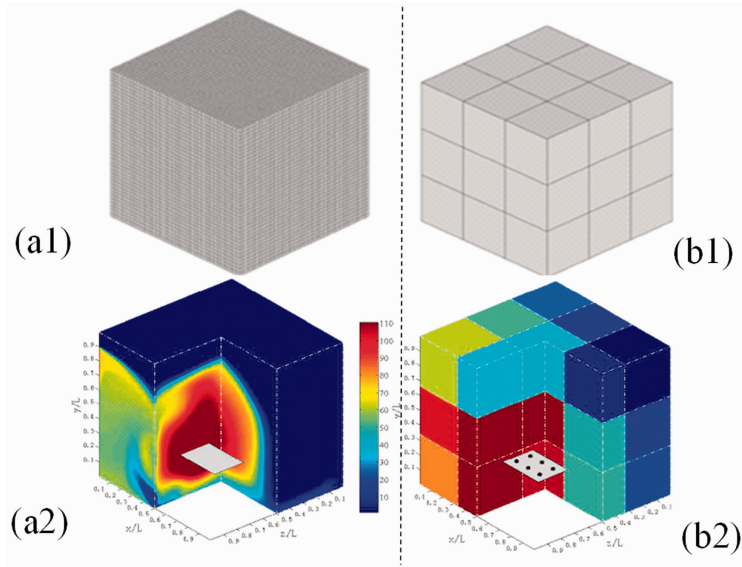


Figure 2.10: The pollutant concentration distribution inside the ventilation enclosure obtained (a1, a2) using a high-dimensional representation (RANS) and (b1, b2) using a LLVM [68].

chapters will mainly discuss a novel methodology based on CFD for improving air quality.

	Outdoor		Indoor	
	Accuracy	practicality	Accuracy	practicality
Field measurement	++	-	++	+
Wind tunnel testing	++	+	++	+
Gaussian plume model	+	++	NA	NA
Box model	-	++	NA	NA
CHIMERE	++	++	NA	NA
CFD model	++	+	++	++
Single/Multizeon model	NA	NA	+	++
FFD	NA	NA	+	++
LLVM	NA	NA	+	++

Table 2.1: Summary on the applicability of each method for outdoor- and indoor-scale pollutant dispersion prediction.

Chapter 3

Development of a numerical strategy: from making outdoor/indoor pollutant cartography to smart placement of depolluting panel

Based upon the earlier discussion of outdoor and indoor air quality separately in Chapter 1, this section focuses on the interaction between outdoor and indoor air quality. Mitigation strategies for air pollution are also reviewed. Given the usefulness of CFD as a tool for predicting pollutant dispersion in urban areas as discussed in Chapter 2, I will finally propose a novel numerical strategy to mitigate air pollution for outdoor/indoor air quality and their interactions.

3.1 Interaction between outdoor and indoor air quality

As mentioned in Chapter 1, many pollutants exist in outdoor and indoor environments. Although people often emphasize their exposure to outdoor pollutants, indoor air quality is equally crucial. One significant source of indoor pollution is outdoor pollutants, namely outdoor pollutant transport to indoor spaces. The progressive trend of enhancing energy-efficient homes through increased airtightness has inadvertently led to reduced indoor air ventilation, thereby contributing to the decline in indoor air quality. These trends have resulted in an emphasis on the

significance of indoor air quality today. There are three primary pathways through which outdoor air pollutants can enter indoor environments (see Fig. 3.1): natural ventilation, mechanical ventilation and infiltration [20]. Natural ventilation uses the stacking effect caused by differences in wind pressure and temperature to drive air-flow. Opening windows is the most common way of natural ventilation. Mechanical ventilation, as the name suggests, employs fans and ducts to encourage ventilation forcefully. One notable advantage of mechanical ventilation is its ability to incorporate filters and other equipment within the ventilation system, allowing for the intake of fresh air while effectively limiting the entry of outdoor air pollutants. A disadvantage, however, is the difficulty of installing mechanical ventilation systems in older or traditional homes. Infiltration is the unintended inflow through gaps in walls, doors and windows. Depending on building designs e.g., for poorly sealed buildings, it impacts indoor air quality significantly [20, 69]. Nevertheless, in my Ph.D., infiltration is considered neglected with respect to natural and mechanical ventilation. Among the three options, natural ventilation is the most feasible choice for every house despite its vulnerability to the influence of outdoor pollutant transfer into indoor spaces. Therefore, solutions are required to ensure good indoor air quality while using natural ventilation.

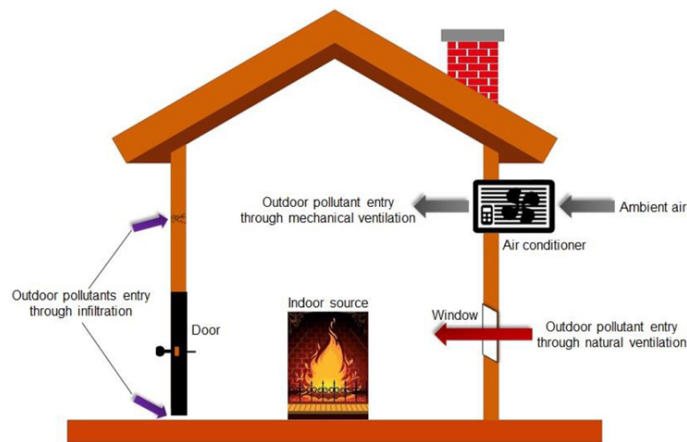


Figure 3.1: Source and pathways of indoor air pollutants [20].

3.1.1 Literature review on the interaction between outdoor and indoor air quality

Numerous field measurements have examined the interaction between outdoor and indoor air quality. [70] has observed that indoor concentrations of some fine parti-

cles are often comparable to outdoors. [71] has reported that correlations between outdoor and indoor particle concentrations vary widely, depending on many factors (e.g., indoor combustion process and building tightness). Regarding NO₂ concentration, [72] concludes that the relationship between outdoor and indoor NO₂ concentrations varies between countries and regions because of different building styles, ventilation methods, indoor behavior, and cultural practices. This variation is one of the reasons why there is no worldwide standardized regulation of indoor air quality. Nevertheless, both studies ([71, 72]) commonly point out that outdoor air quality impacts indoor air quality, which is evident when there are few indoor sources. Numerous other studies on outdoor/indoor air quality interactions have been conducted; however, the findings vary significantly depending on measurement conditions and environments, etc. These results make it difficult to draw general conclusions and recommendations about how to deal with the interaction between outdoor and indoor air quality, implying that more studies on the interaction between outdoor and indoor air quality are required.

Indoor/outdoor (I/O) ratio serves as an important indicator of the relationship between outdoor and indoor concentrations in environmental studies. Despite extensive research into I/O ratio, no consistent conclusions have been reached due to the complex and variable nature of factors influencing outdoor and indoor concentrations, such as particle and gaseous sources, ventilation system, season, occupant behavior, and outdoor environment. [71] reviewed many large-scale previous studies and summarized PM_{2.5} I/O ratios. As shown in Fig. 3.2, I/O ratios are distributed over an extensive range, with a maximum value of 3.35 in Portage (USA) and a minimum value of less than 1. Concerning the wide range of these values, the authors explain that this is due to differences in the measurement environment. In areas with high values (e.g., Portage (USA) and Indianapolis (USA)), measurements were conducted when indoor pollutant sources (e.g., fireplaces) were present. On the other hand, areas with low values (e.g., Riverside (USA)) were measured during the evening hours when there were fewer indoor pollution sources or in winter when filtration was active. These measurements were not made under identical conditioning. Also, [73] showed the variations of I/O ratio for NO₂ in many studies. Therefore, some researchers [45, 71] have concluded that I/O ratio may not be a reliable indicator for direct comparison between outdoor and indoor air quality since the differences mentioned above pose challenges for simple comparisons.

Urban geometry (including building geometry) has been extensively researched because it directly influences pollutant dispersion in urban areas. In particular, street canyon is a common feature of urban geometry in dense urban environments,

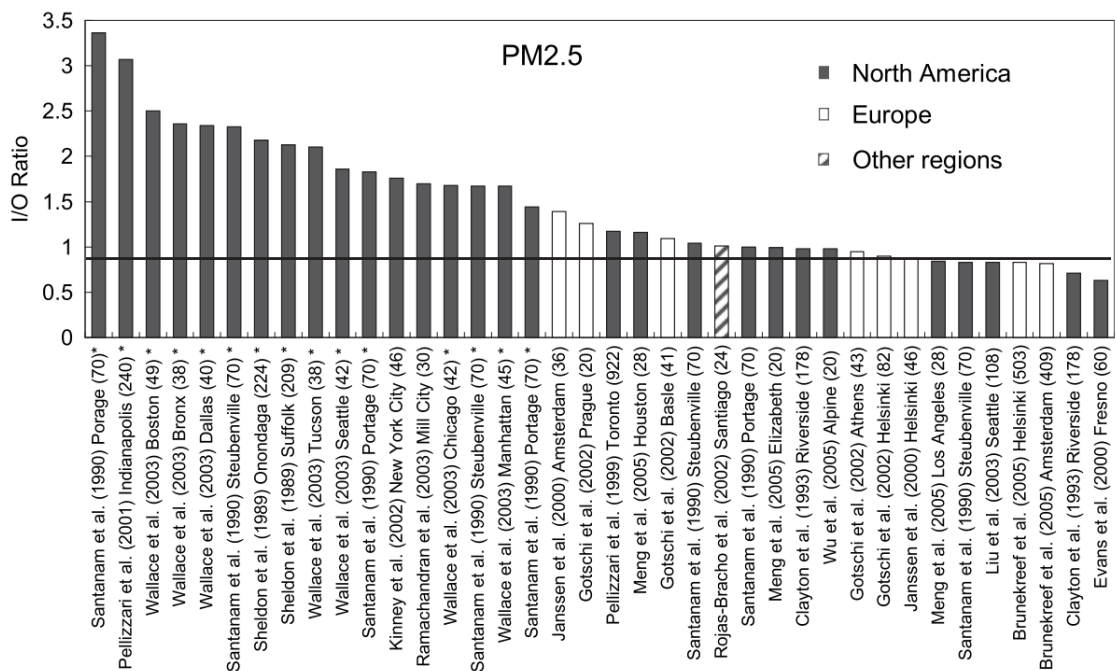


Figure 3.2: Distribution of I/O ratios of PM2.5 in the large-scale studies (larger than 20 homes) in different cities. The numbers in () represent the number of sample homes. "*" shows indoor smoking [71].

which have narrow streets with buildings on both sides. Hence, understanding pollutant dispersion in street canyons can provide valuable insights into how to mitigate people's exposure to pollutants. Fig. 3.3 shows a schematic of a typical street canyon. Wind flowing over the buildings creates a circulation within a street canyon, which carries traffic-derived pollutants generated on the road to the leeward side. Buildings on both sides inhibit pollutant dispersion; therefore, pedestrians, cyclists, drivers, and people inside buildings, especially on the leeward side, are exposed to high concentrations of pollutants. Within street canyons, the aspect ratio H/W (H : building height and W : road width) is an important parameter for pollutant dispersion. The higher the aspect ratio, the deeper the street canyon and the more inhibited the removal of pollutants. Nevertheless, to accommodate population growth in many cities, the building height limit tends to be increased in many cities, e.g., Manhattan [74] and Kyoto [75], causing more air quality problems. Therefore, air quality problems can be severe in urban areas in the future. As a well-known flow classification in the street canyon, [76] classified three characteristic flows according to aspect ratio (H/W): (a) isolated roughness flow, (b) wake interference flow, and (c) skimming flow (Fig. 3.4). Isolated roughness flow occurs when ($H/W < 0.3$). In

this case, airflow disturbed by upwind buildings does not reach leeward buildings, thereby which can be treated as an isolated building. Wake interference flow occurs at ($H/W \simeq 0.5$), where windward disturbed airflow and the downwind buildings interfere with each other. Skimming flow occurs at ($H/W \simeq 1$) and constantly forms a circulation within street canyons. There have been many studies on airflow and pollutant dispersion with varying aspect ratios, e.g., [77, 78].

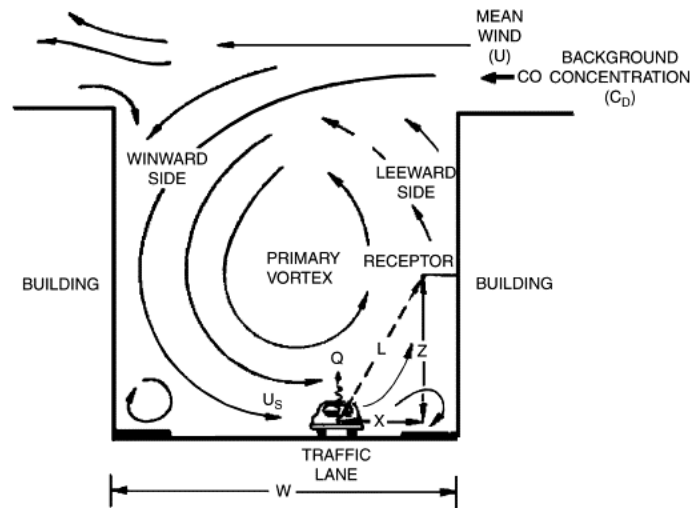


Figure 3.3: Pollutant dispersion in a general street canyon [79].

To comply with air quality guidelines (e.g., WHO [17] or EU (Directive 2008 50 EC)), people's exposure is often calculated using values from air quality monitoring stations. However, these monitoring stations are often installed to measure ambient concentration in cities, not local high concentrations in cities. Thus, even if the concentrations at those limited measurement points meet the guideline values, they are not sufficient to evaluate pollutant concentrations in urban areas where high pollution occurs locally. Complicated urban geometry and local pollutant sources in urban areas can produce severe pollutant concentrations locally. This is evidenced by the fact that I/O ratio is not a good indicator of the air quality correlation between outdoor and indoor air quality with the limited number of sensors. Sometimes, outdoor air pollution has been calculated by mesoscale studies, e.g., [80]. These scale simulations are beneficial for estimating, for example, long-term exposure to contaminants. However, in that way, the concentrations can be obtained on each large cell (e.g., resolutions on the kilometer scale). Therefore, as well as sensor measurements, mesoscale simulations cannot capture rapid gradients of pollutant concentrations in urban areas, and the spatial representativeness of results is

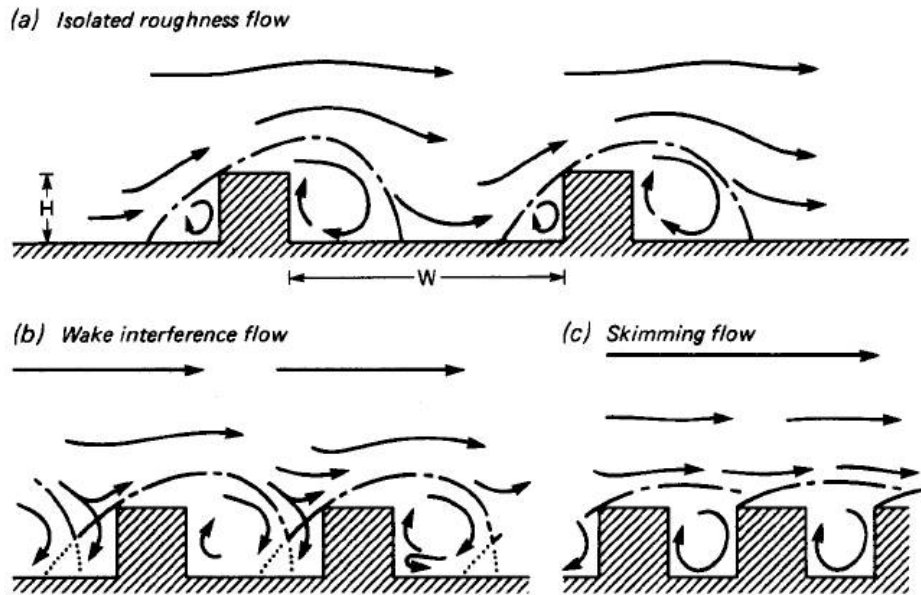


Figure 3.4: Classification of street canyon flow [76].

limited. Such a low-resolution assessment leads to an underestimation of pollutant concentrations.

In this situation, the usefulness of CFD modeling to assess pollutant concentrations in urban areas has been recognized. CFD can provide detailed cartography of pollutant concentrations over an entire area. However, even in previous studies using CFD, there is limited research on the interaction between outdoor and indoor air quality. Even when considering the interaction, many studies often considered it in simplified urban geometries and buildings. The reasons for this may be due to the fact that it is often difficult to analyze air quality for both indoor scales to outdoor scales at the same time with sufficient resolution due to operational reasons such as computational cost. However, recent developments in computer power have made this possible.

In summary, more studies are required to get a better understanding of the interaction between outdoor and indoor air quality. Field measurement and mesoscale simulations are not promising tools because they do not have sufficient resolution. Also, as discussed in the previous chapter, some semi-empirical models may be applicable for simplified terrain and urban areas but may introduce significant errors in complex urban areas and building geometries [81]. Therefore, as of now,

CFD stands out as one of the most efficient approaches to evaluate the interaction between outdoor and indoor air quality by accurately estimating pollutant concentrations throughout a given area although there are some disadvantages e.g., time and cost consuming. The following subsection provides detailed reviews on how to apply CFD to study the interaction between outdoor and indoor air quality.

3.1.2 CFD for the interaction between outdoor and indoor air quality

There are two approaches to simulate the interaction between outdoor and indoor air quality using CFD. The first one is the coupled approach (Fig. 3.5 (a)). This method reproduces both outdoor and indoor spaces in the same computational domain. The interaction between outdoor and indoor environments can be effectively simulated and captured within a single simulation. The second one is the decoupled approach (Fig. 3.5 (b)), in which the outdoor and indoor simulations are performed separately. Firstly, only outdoor simulations are carried out. Here, openings like windows and doors of buildings are represented as wall surfaces. Once outdoor simulations are finished, some variables (velocity, flow rate or pressures, etc.) at these openings are extracted and imposed as boundary conditions for the indoor simulation. Each approach has its advantages and disadvantages, as follows.

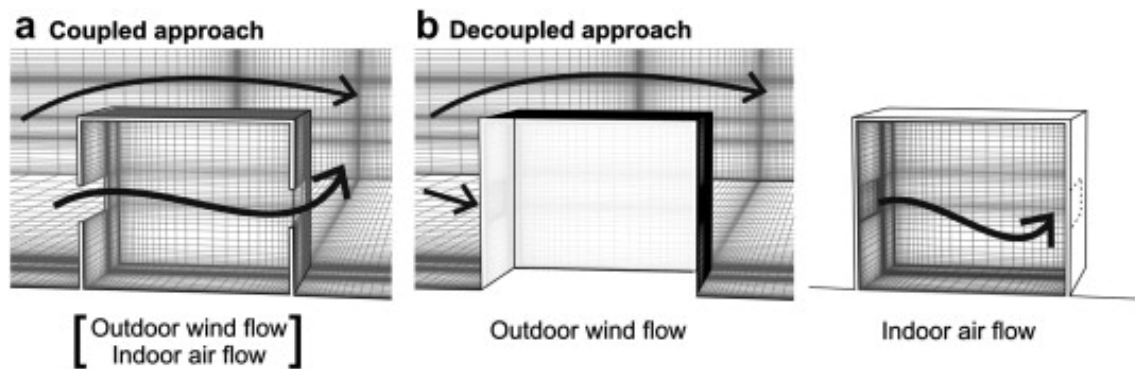


Figure 3.5: CFD simulation to study the interaction between outdoor and indoor air quality: (a) coupled and (b) decoupled approach [82].

Regarding mesh, in the coupled approach, it is necessary to make appropriate meshes in a computational domain for both outdoor and indoor scales in the same mesh. When studying transient indoor pollutant dispersion, indoor simulations need fine meshes. Therefore, the coupled approach requires many meshes. In contrast, since the decoupled approach can separate outdoor and indoor computational do-

mains, one can save mesh for both outdoor and indoor simulations.

Concerning the repetition of simulations, it is a tough task for the coupled approach. For the coupled approach, one has to make geometries of the whole domain including outdoor and indoor areas, which is a time-consuming task in the case of large urban areas. When one wants to add another indoor domain to be calculated, new geometry and mesh have to be re-generated again and additional simulations have to be performed. From this point of view, the coupled approach is not suited for operational purposes. On the other hand, in the decoupled approach, there is no need to run an additional outdoor simulation once an outdoor simulation is carried out. When one wants to analyze additional indoor of a building, it can be done by extracting variables (e.g., pressure, temperature and velocity) on window surfaces modeled as walls from the first outdoor simulation and imposing them to a new indoor geometry as boundary conditions.

In terms of accuracy, the coupled approach is better. The coupled approach can directly analyze the interaction between outdoor and indoor areas. It can reproduce the influence of outdoor air quality on indoor well. In the decoupled approach, outdoor airflow is detached as some variable (e.g., velocity and temperature) or converted into static pressure on surfaces, and then they are imposed again as boundary conditions for indoor simulations. However, in any way, various characteristics of the original outdoor airflow, i.e., momentum and wind directions, may not be well taken into account. Therefore, the decoupled approach can cause some errors in indoor simulations. For instance, extracting correct wind velocity at windows modeled as walls is difficult as velocity can be zero on walls. Regarding wind direction, when only pressure is given as boundary conditions to generate indoor airflow (this is called pressure-drive flow), the outdoor airflow direction is disregarded. Pressure-drive flow produces only airflow directions normal to the inlet boundary. [83] pointed out that airflow travels along surfaces of the building before it enters indoors from openings, meaning that airflow has not only normal components of velocity to openings but also tangential components.

Nevertheless, in terms of reducing computational cost and time and of operational use in practice, the decoupled approach is likely to be significantly beneficial given appropriate boundary conditions. In fact, [84] compared the decoupled and coupled approaches for a single building and verified a high degree of accuracy of the decoupled approach (Fig. 3.6). [85] applied the decoupled approach using pressure boundary conditions obtained from the measurement and showed good agreement with the full-scale measurements. Table 3.1 summarises performances of the cou-

pled and decoupled approaches from several perspectives. Overall, the decoupled approach is more suitable for operational purposes. However, the applicability of the decoupled approach has yet to be fully revealed due to the lack of previous studies. The decoupled approach is inferior in terms of accuracy, which is an important aspect of industry practice, but there is a possibility that the accuracy of the decoupled approach can be improved by providing appropriate boundary conditions. It is, therefore, important to continue to study and compare the accuracy of the coupled and decoupled approaches. In Chapter 4, I will discuss the accuracy and limitations by comparing the coupled and decoupled approach results. The decoupled approach has different ways to impose boundary conditions, but in my study, I will mainly consider pressure boundary conditions (pressure-driven flow). This is because wind speed and airflow rate are difficult to extract at buildings' surface from outdoor simulations where the window surface is modeled as walls. Fig. 3.7 illustrates the procedure for the decoupled approach when using Dirichlet pressure boundary conditions.

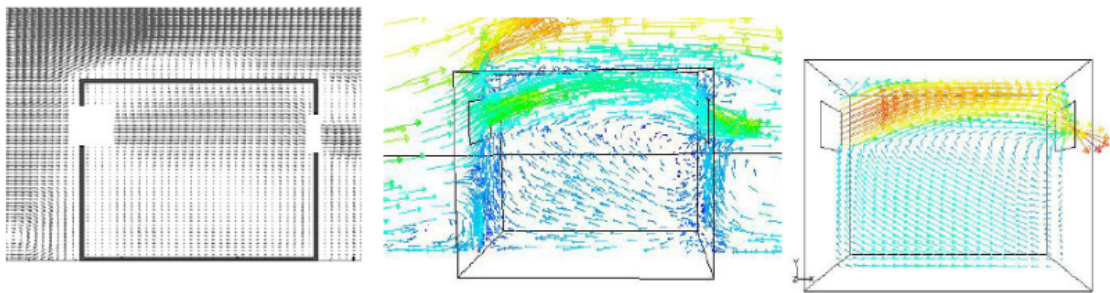


Figure 3.6: Velocity vectors on a building: PIV (left) coupled (center) decoupled (right) [84].

	Coupled approach	Decoupled approach
Making geometry	-	++
Computational time	+	++
Repetition of simulation	-	++
Accuracy of result	++	+
Number of previous study	++	+
Total practicality	+	++

Table 3.1: Performance comparison between coupled and decoupled approach.

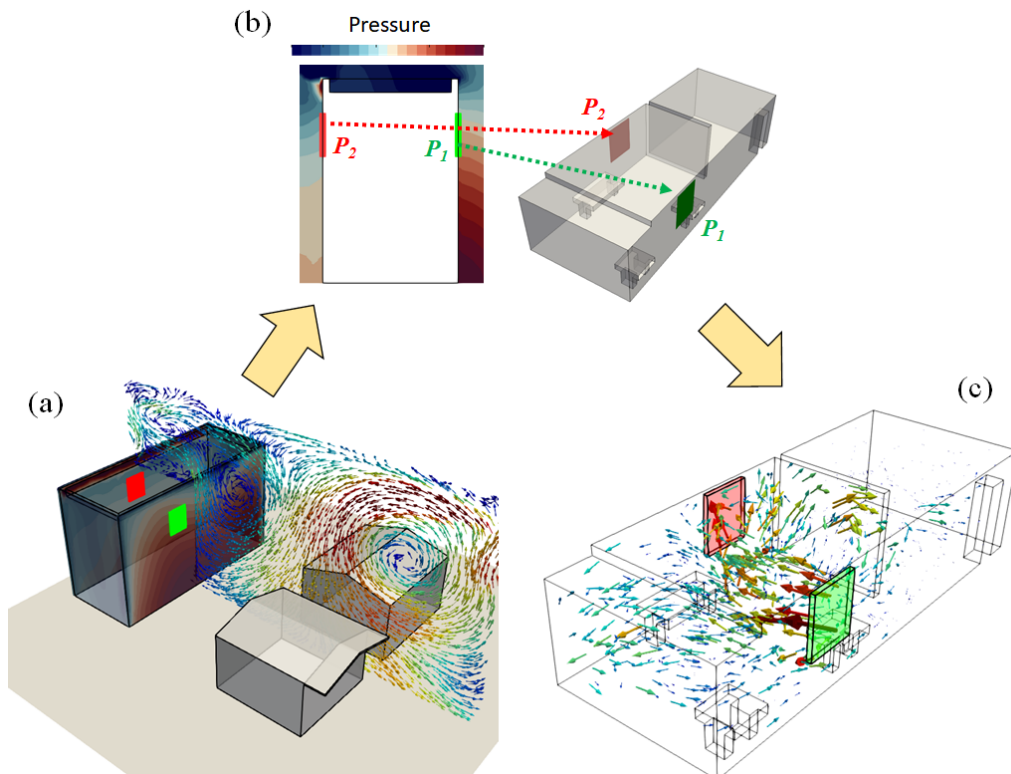


Figure 3.7: Schematic procedure for the decoupled approach using pressure boundary condition; (a) outdoor airflow simulation, (b) extracting and imposing pressure and (c) indoor airflow simulation by pressure boundary condition.

3.2 Mitigation strategies for air pollution in urban area

The interaction between outdoor and indoor air quality occurs mainly when pollutants of outdoor origin enter the indoor environment and deteriorate indoor air quality. There is less airflow indoors than outdoors, and pollutants can accumulate unless conscious ventilation is provided. As the airtightness of houses increases, the impact of outdoor air quality on indoors' will become even more significant as outdoor pollutants can accumulate and stay indoors more easily once they enter indoors. Therefore, to reduce human exposure to pollutants in critical areas, actions have to be carried out. The different types of mitigation strategies can be categorized based on the partial differential equation (3.1) representing transport-diffusion-reaction phenomena of pollutants:

$$\frac{\partial C}{\partial t} + \underbrace{\mathbf{v} \cdot \nabla C - \text{div}(D\nabla C)}_{II} + \underbrace{R(C)}_{III} = \underbrace{S}_I \quad (3.1)$$

where $C(\mu\text{g}/\text{m}^3)$ is the pollutant concentration, $\mathbf{v}(m/s)$ and $D(m^2/s)$ are velocity and the diffusion parameter, $R(C)$ represents chemical reaction of species and S is associated to source emissions. The subsequent sections present various mitigation strategies based on the different terms in Eq. (3.1): source term (“I”), advection-diffusion term (“II”) and chemical reaction term (“III”). Hereafter, among many pollutant sources, I mainly focus on traffic pollution as it is the most typical pollutant source in cities [86, 87].

3.2.1 Source term

As shown in Eq. (3.1), the pollutant concentration C can be decreased by reducing the source emission S . This strategy “I” is often employed by municipalities and regional authorities via air quality planning e.g., traffic restrictions. For example, even if heavy-duty vehicles account for only 5% of the car population in the world, they are responsible for a large proportion of pollutants on roads [88]. Similarly, vehicles with older emission standards and longer mileage also emit more emissions, so replacing these with hybrid or electric vehicles can effectively reduce emissions. Also, It is important to implement programs to change people’s mobility and transport behavior at a municipal scale. An example of this is Low Emission Zone (LEZ) introduced in Europe, where the traffic volume of vehicles emitting high pollutant concentrations, especially PM and NOx, is restricted. A good knowledge of the local traffic characteristics and virtual testings of different scenarios via

simulations is recommended to efficiently design LEZ [89, 90]. In addition, encouraging individual citizens to use public transport (buses, trams, metros, and trains), walking and cycling should be employed to help reduce emissions. There are other pollutant-emitting sectors (e.g., industry, agriculture, food, shipping), and as in the automotive industry, introducing advanced technologies is expected to lead to improvements [91].

3.2.2 Advection and diffusion term

Strategy "II" corresponds to the advection and diffusion terms in Eq. (3.1). Reducing air pollution via strategy "II" mainly aims at improving the ventilation capacity of cities and facilitating the dispersion of pollutants. As mentioned, urban planning plays one of the biggest roles in pollutant dispersion [92].

- Urban and building geometry modification

Several improvement measures at the city scale have been proposed. Improvements in urban-scale ventilation capacity can be achieved by changing building clusters and urban morphology. Building density has a significant impact on pollutant dispersion. Urban density generally refers to the planar urban density, often defined by Building Coverage Ratio (BCR): the ratio of the base area of buildings to the urban area under consideration. [93] found that wind speeds at the pedestrian level decrease as the BCR increases. Vertical building density is another important indicator of urban ventilation capacity. This is often defined by Frontal Area Density (FAD): the ratio of the frontal area to the total surface area of the building. In street canyons, the importance of density in the vertical direction can easily be inferred from the fact that deeper street canyons lead to more severe air quality problems.

In addition to building density, building layout also significantly impacts pollutant dispersion. When the building layout is non-uniform, the flow pattern will be more complex, and diffusivity can be stronger. Many studies have reported that horizontal urban heterogeneity, e.g., [94] and vertical urban heterogeneity, e.g., [95] can improve the ventilation capacity of cities. Moreover, in literature, numerous researches have shown the effects of the urban morphology at the building, street and district scales on the air quality [96, 97]. At the district scale, the mitigation of air pollution through the planning of urban morphology can be performed by, e.g., demolition of old buildings to create wind corridors leading to the improvement of air quality and thermal comfort (see Fig. 3.8). However, the biggest drawback is that changing urban layout can only be applied to new districts or local urban renewal, not to existing urban areas.

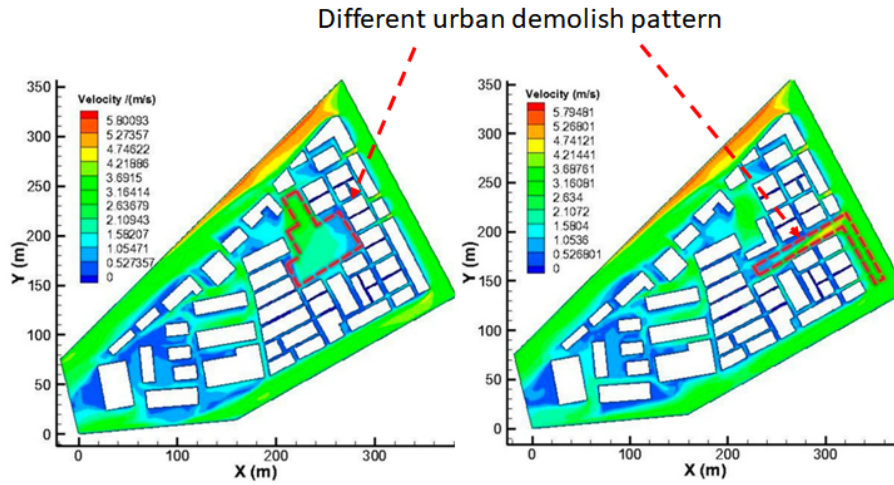


Figure 3.8: The comparison of velocity through different urban demolition patterns [4].

- Urban and building design

As noted in the previous section on street canyons, buildings along roads inhibit the dispersion of pollutants. This is expected to become a more severe problem as deeper street canyons are formed due to recent urbanization. To prevent the air quality issue in the street canyon, it needs to be designed with the aspect ratio in mind. Small aspect ratios are important in urban design to improve air quality. The shape of the roof of a building can also help with ventilation in street canyons because they create vortex structures that promote pollutant dispersion [98].

In addition, building separation is being promoted in Hong Kong [6] to improve air quality at the street canyon scale. By separating the groups of buildings that form the street canyons, fresh air can be taken in urban areas. Corners of the separated buildings produce a lateral vortex (double-eddy circulation [5]), which promotes the mixing of air within the street canyons. [99] investigated the effect of the degree of building separation on wind speed at the pedestrian level. The results showed that when the ratio of separation distance to street length is equal to 10%, wind speed at the pedestrian level increases and helps pollutant dispersion. [7] points out that building permeability improves the ventilation capacity of street canyons.

- Local mitigation actions

Apart from reducing exposure to pollutants by improving the ventilation capacity of cities, several methods have been proposed to prevent pollutants generated on roads from flowing into human living spaces by limiting dispersion capacity. Concerning nature-based solutions, vegetation can also contribute to improving air quality. Nevertheless, contrary to popular belief, the reduction of air pollution by vegetation in urban areas is not so evident [100]. On the one hand, the pollutant concentrations can be reduced *via* the deposition on leaves. On the other hand, the presence of trees can modify the pollutant dispersion by obstructing the urban airflow. Studies point out that trees can increase traffic concentrations on the sidewalk in street canyons but show a beneficial decrease of concentrations in open terrain configurations, which are mainly found outside city center [101]. In summary, trees in streets and more generally in urban parks have a positive global impact on city air pollution but they can be locally deteriorated

Barriers can be installed just next to traffic roads in order to reduce the air pollution on the sidewalk especially in street canyon [102, 103]. The studies show that barriers must be continuous, high (more than 2 meters height) and impermeable, *e.g.* solid walls or green barriers with very low porosity/permeability. Cars parked on the road shoulder themselves act as barriers [104].

In addition, street canyon-scale ventilation systems, which modify urban airflow, can be installed to remove pollution using passive or active ventilation strategies. In [8], the authors proposed a pedestrian ventilation system in order to enhance the air quality and thermal comfort in pedestrian areas (Fig. 3.9). The controlled air movement is ensured by ventilation mechanisms. The updraft movement of air can also be achieved using a passive solar strategy. Hence, in [105], the author developed a solar chimney street-lighting pole where the inner part of the lamp structure is employed for air pollutant removal.

3.2.3 Chemical reaction term

Strategy "III" entails utilizing chemical reactions to degrade pollutant concentration, which corresponds to the chemical reaction term in Eq. (3.1). This method is easier to implement in existing buildings, cities and indoors than the methods described above. [106] reviews air purification methods using physicochemical reactions *e.g.*, filtration (mechanical and electronic), adsorption, UV photocatalytic oxidation, which are described below.

- Filtration

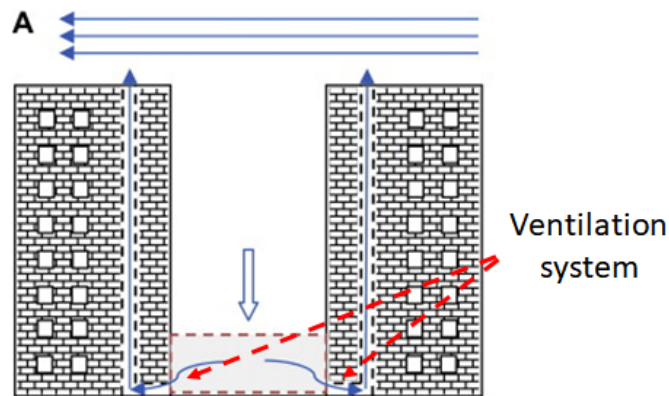


Figure 3.9: Pedestrian ventilation system [8].

Filtration is most often used to remove PM from the air. Filtration methods can be classified as mechanical or electronic methods. The principle of mechanical filtration is very simple. Depending on the desired PM size, materials of various sizes and densities are used as media for PM removal. Filters can be combined with other materials such as adsorption to remove organic and inorganic chemical and gas pollutants simultaneously as PM. Filters are very efficient, especially with regard to the removal of PM. For other pollutants, future developments can be expected through new materials and combinations of other materials. However, there are some disadvantages. High maintenance is required to keep the filter functional. Filters generate a pressure drop in the air, requiring additional energy when integrated into the ventilation function.

- Adsorbent

Air purification by adsorption is the capture of pollutants on the surface of adsorbent materials. Adsorbent materials have large surface areas, suitable pore structures and strong adsorption. Adsorbent materials have the advantage of easily being incorporated into building materials. By simply placing adsorbents, e.g., on building surfaces, adsorbents can benefit air quality. Furthermore, adsorbents can be combined with various materials and methods to remove pollutants efficiently. For example, [107] used an activated carbon fiber filter, resulting in high pollutant removal rates and low-pressure drop. This demonstrated both environmental and energy advantages. The disadvantage of adsorbents is that airborne bacteria can adhere and develop on the adsorbent surface. Furthermore, correct treatment of the adsorbent is required.

- UV photocatalytic oxidation

In recent years, UV photocatalytic oxidation (PCO) has received significant attention as a technology for cleaning air pollutants. PCO is a light-mediated, redox reaction of gases and biological particles adsorbed on the surface of a solid pure or doped metal oxide semiconductor material or photocatalyst. Its advantages include high removal efficiency, a wide range of applications, easy installation, and no secondary pollution. Thus, with sufficient light and under the presence of photocatalyst (ZnO or TiO₂), a catalytic oxidation effect is triggered, degrading certain polluting particles [11, 12]. Common photocatalyst materials are TiO₂ and ZnO, which are used to remove pollutants (O₃, CO₂, NO_x, VOCs) [13, 108, 109, 110]. PCO can be incorporated into building materials, such as paints, roof tiles, wall cloth and curtains, to improve indoor air quality. Various pre-coated products exist, such as plasterboard, ceramic tiles and wallpaper [111]. These materials allow relatively flexible and practical use of the panels. Due to the harmful effects of TiO₂, recent trends are moving towards the use of other photocatalysts such as ZnO. At Université Gustave Eiffel, [13] developed "depolluting panels," which consist of photocatalyst nanostructures ZnO grown on construction materials (tiling, rock aggregates) to test their efficiency to reduce air pollution from road traffic (Fig. 3.10). Depolluting panels are very effective and practical in removing outdoor and indoor pollutants. However, the efficient use of depolluting panels in practice is complex, as it depends on several parameters, such as sunlight intensity, pollutant concentration, airflow, humidity, etc. Additionally, considering the cost associated with panels deployment and maintenance, installing panels throughout the entire city is not realistic. Consequently, selecting efficient and practical locations for depolluting panels in urban areas is one of the main objectives of my Ph.D. research, which will be discussed in subsequent sections.

To sum up, many types of mitigation strategies, e.g., from reducing outdoor pollutant sources to using photocatalytic devices, are available to reduce outdoor and indoor pollutants and, ultimately, human exposure. Strategy "I" and "II" have shown mitigation strategies related to source and advection-diffusion terms to improve air quality. However, some solutions, like changing urban geometry, are challenging to apply to existing cities and buildings. In fact, it is an expensive and long-term solution. Therefore, feasible methods for the improvement of air quality are required. Regarding the indoor environment, good air quality can often be achieved by natural ventilation, i.e., by opening windows. Furthermore, modern buildings are often equipped with efficient mechanical ventilation to remove pollutants and replace air simultaneously. Nevertheless, when the outdoor air is highly polluted and it is difficult to install new ventilation equipment, other solutions are

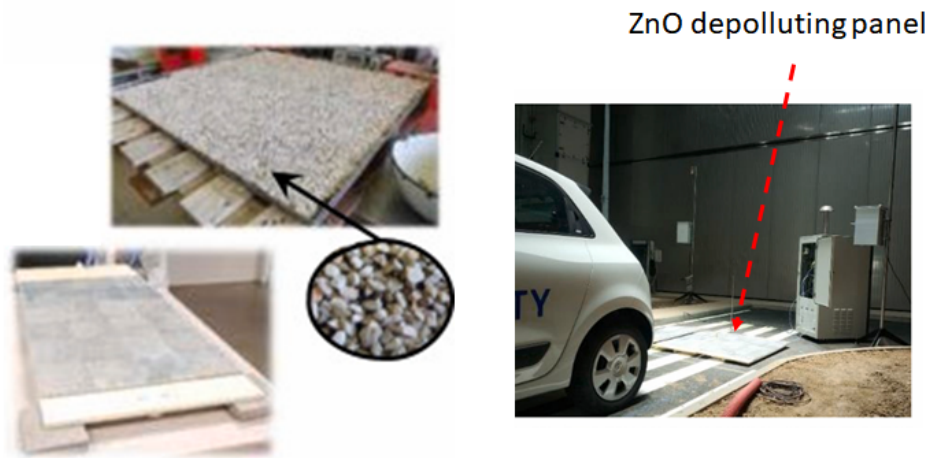


Figure 3.10: Depolluting panel in Sense-city experimental [13].

required. In this context, one practical mitigation measure is to use chemical reactions that can be easily applicable to existing buildings and cities. As discussed above, the photocatalytic panels for road pavements [13] can be extended to, e.g., building walls, sidewalks, parks and open areas. However, their efficiency depends on various conditions (airflow, pollutant concentration, temperature, humidity solar radiation), making their design difficult to determine the appropriate placement of the panels. In particular, predicting the correct pollutant concentration is essential for efficient panel placement. Accordingly, the following sections propose and validate a first novel method for smart placement of depolluting panels.

3.3 Developing methodology for smart placement of depolluting panel

The previous chapters and sections have described the various pollutants and their sources, measurements and modelings to predict their pollutant dispersion and effective mitigation measures for air pollution. Based on these discussions, this section develops a novel numerical strategy for efficiently mitigating outdoor/indoor air pollution and their interaction. This strategy involves the use of CFD and depolluting panels through photocatalytic oxidation. The mathematical derivation of the numerical strategy and its use are summarized.

To clarify subsequent discussions, I briefly outline the key points of the method: target pollutant and its sources, modeling approach and mitigation measure:

- Target pollutant: NOx emission from traffic

Many pollutant sources are present outdoors and indoors. Among them, vehicle exhaust is the major source of pollution. Car emissions occur on every road in cities close to us and are directly linked to our air quality both outdoor and indoor. Due to its high health risks, it is very important for human health to take measures to reduce and mitigate pollution from car emissions. Fig. 3.11 shows that the traffic sector contributes the most to NOx. Its contribution amounts to more than 50% of the total emissions of NOx. Therefore, my Ph.D. considers a numerical strategy for reducing NOx concentration from traffic.

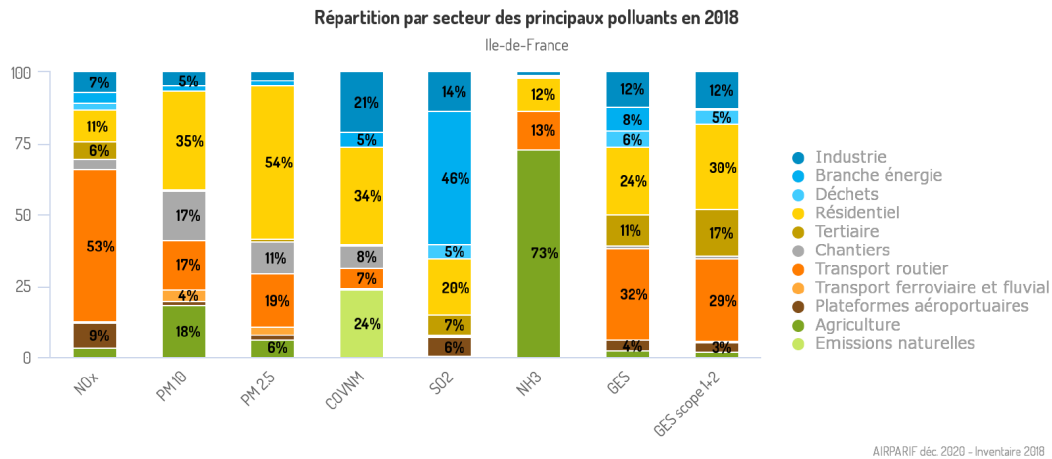


Figure 3.11: Emissions of main air pollutants in Île-de-France 2018 (Airparif, 2020) [112].

- Mitigation measure: Depolluting panel

As mentioned in the previous section, UV photocatalytic oxidation (PCO) by ZnO is a promising measure to remove pollutants in existing buildings and districts. [13] has developed depolluting panels (ZnO-based PCO panels). These panels have an area of approximately 1 m² each and therefore are easy to install and to move from one area to another. Fig. 3.12 illustrates the result of the first experiment to measure the effect of ZnO depolluting panels on car exhaust gases in Sense-City equipment. The concentration of O₃ is significantly reduced, while NOx is reduced by about 5%. Although it is not as much as O₃, this may be improved in future developments. One parameter affecting the panel's pollutant removal efficiency is the pollutant concentration

near panels that mainly depends on airflow. Therefore, my Ph.D. proposes a numerical strategy to find the optimal location of depolluting panels regarding airflow dispersion.

My Ph.D. considers only pollutants from traffic and not indoor pollution sources, meaning that the only pollutants that affect indoor air quality are those from the outdoors. Accordingly, the depolluting panels should be positioned in such a way that outdoor pollutants are prevented from entering the indoor environment.

- Pollutant dispersion modeling: CFD modeling with the decoupled approach
To maximize the efficiency of the depolluting panel, accurate and detailed cartography of the pollutant concentration is essential. As explained in Section 2.2, CFD is currently considered as the most effective way to predict non-uniform pollutant concentrations at the urban scale. Therefore, CFD is used as part of the numerical strategy. To simulate the air pollutant interaction between outdoors and indoors, the decoupled approach is used, where the outdoor and indoor areas are simulated separately.

3.3.1 Outline of methodology for smart placement of depolluting panel

In my Ph.D. I propose a numerical strategy to optimize the placement of photocatalytic panels using CFD for NO_x concentration from the traffic sector. This section details of the numerical strategy. There are two main steps: Diagnosis stage and Remediation stage. In the diagnosis stage, CFD simulation is used to get precise pollutant cartography and diagnose the level of concentration at the district scale. The remediation stage relies on the formulation of an optimization problem and a sensitivity analysis through the adjoint framework to smartly place the depolluting panels. An overview of each step is summarised below.

Diagnosis stage:

CFD is used to produce detailed cartography of urban-scale pollutant concentration. From this map, we identify critical zones where people are exposed to deteriorated air quality. As shown in Fig. 3.13, for example, high pollutant concentrations are observed on the road but should not be defined as Quantity of Interest (QoI) because people do not stay on the road for long periods. Considering the interaction between outdoor and indoor air quality, it is important to prevent air pollution from entering indoors by putting depolluting panels on the building surfaces. The general procedure is as follows:

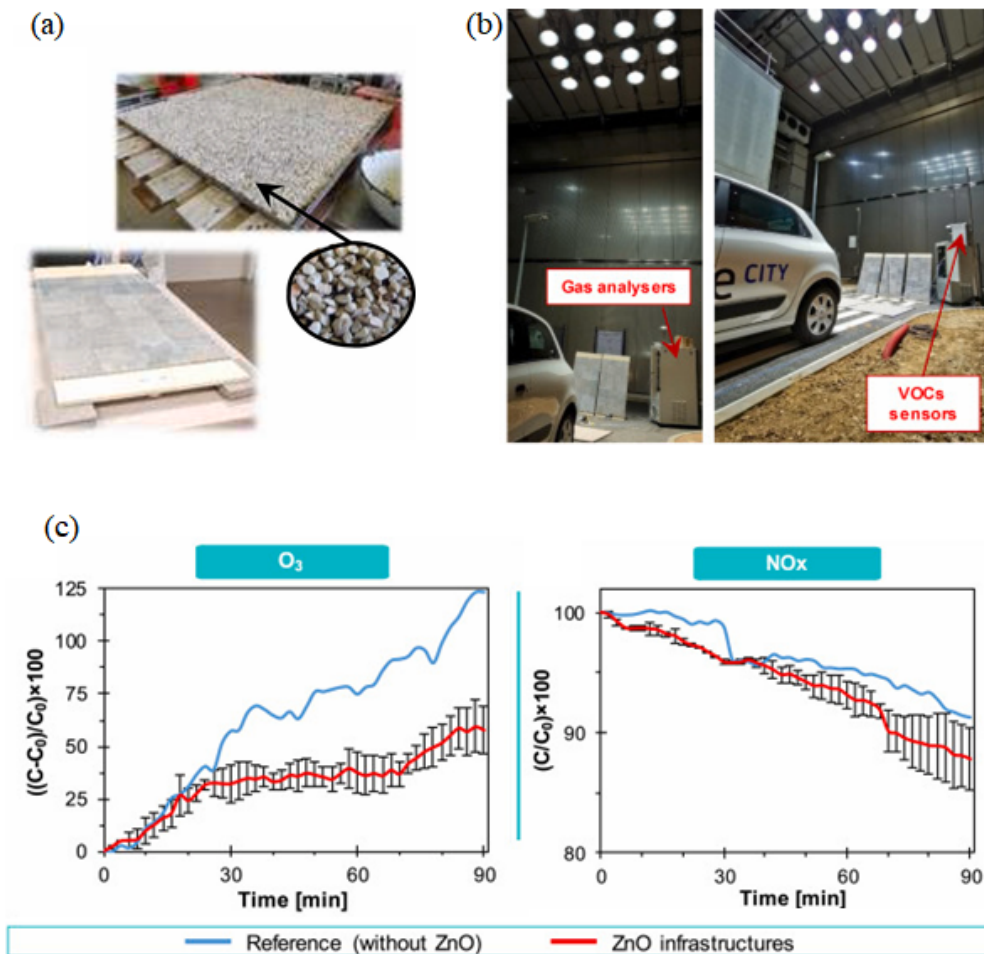


Figure 3.12: ZnO nanostructures based innovative photocatalytic road: (a) Depolluting road infrastructures production, (b) experimental campaign, (c) Pollutant evolution under solar light with and without ZnO (Plots of pollutant concentration evolution as function of photocatalysis time under artificial solar light with and without the presence of ZnO [13]).

- determine the airflow at the district scale using computational fluid dynamics;
- solve the direct advection-diffusion-reaction model to reconstruct precisely the pollution map at the district scale;
- identify from the pollution map the critical areas where people can be exposed to high level of pollutant. The pollutant concentration in these critical areas are defined as QoI.

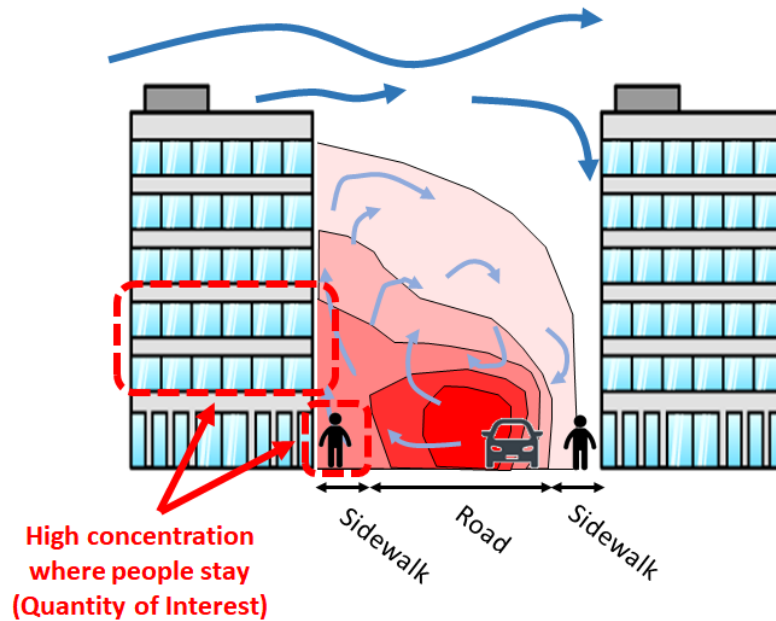


Figure 3.13: Selecting highly polluted areas in diagnosis stage.

Remediation stage:

The objective is to minimize the pollutant concentration in critical zones selected in the diagnosis stage by smartly placing depolluting panels. To achieve this, an adjoint-based sensitivity analysis is performed to calculate the sensitivity. By determining the highest sensitivity areas, one can select efficient depolluting panels' placements. As panels can only be placed on some surface of the district (e.g., surfaces of buildings and roads), only the sensitivity indicator on the surface is important. The general procedure is as follows:

- solve the adjoint advection-diffusion-reaction problem associated to the chosen quantities of interest ;
- evaluate the spatial sensitivity indicator using the numerical concentration of the direct problem determined in the diagnosis stage and the numerical solution of the adjoint problem ;
- determine a relevant position of depolluting panels given by the significant value of the sensitivity indicator.

These two steps are explained precisely in the following sections.

3.3.2 Technical description

This subsection describes the physical and mathematical background of the CFD modeling and adjoint formulation used for the optimal placement of depolluting panels.

3.3.2.1 Diagnosis: district pollutant map using CFD modeling

To determine the pollutant concentration, at first flow field must be determined by solving Navier-Stokes (NS) equation for air:

$$\frac{\partial \mathbf{v}}{\partial t} + (\mathbf{v} \cdot \nabla) \mathbf{v} = -\frac{1}{\rho} \nabla p + \nu \nabla^2 \mathbf{v} \quad (3.2)$$

When solving NS equation, the computational cost varies greatly depending on the turbulence modeling. Since the turbulence modeling must be chosen according to the designer and the target flow, this section does not explain the details of NS equation and turbulence modeling. Chapters 3 and 4, which discuss the application of the numerical strategies to real districts, provide an explanation with regard to the theoretical background of NS equation and the turbulence modeling used. For practical purposes, obtaining the averaged velocity field and its statistical representativeness is often important, so here I assume that the averaged velocity $\vec{\mathbf{v}}$ will be used to calculate pollutant dispersion.

I denote by Ω the computational domain of the district. Assuming that after simulating the averaged airflow $\vec{\mathbf{v}}$ over Ω , the detailed cartography of the pollutant concentration $C(\mathbf{x}, t)$ is obtained by solving the convection-diffusion-reaction equation:

$$\begin{cases} \frac{\partial C}{\partial t} + \vec{\mathbf{v}} \cdot \nabla C - \text{div}(D \nabla C) + R(C) = S & \text{in } \Omega \times [0, T] \\ C = C_i & \text{on } \Gamma_i \times [0, T] \\ \nabla C \cdot \vec{\mathbf{n}} = 0 & \text{on } \Gamma_o \cup \Gamma_w \times [0, T] \\ C(t=0) = C_0 & \text{in } \Omega \end{cases} \quad (3.3)$$

where C_i and C_0 denotes respectively the background concentration entering the domain Ω through the inlets Γ_i and the initial concentration in the domain. The boundaries Γ_o and Γ_w are associated to outlet and wall surfaces. The diffusion term D involved in Eq. (3.3) is the sum of the molecular diffusion and the turbulent diffusion D_t . The turbulent diffusion D_t (m^2/s) is given by the formula

$$D_t = \frac{\mu_t}{\rho Sc_t}, \quad (3.4)$$

where μ_t ($kg/(m.s)$) is the turbulent viscosity, ρ (kg/m^3) is the density of air and Sc_t is the turbulent Schmidt number. In practice, the turbulent viscosity μ_t ($kg/(m.s)$) can be obtained from the turbulent airflow simulation. In the applications in Sections 4 and 5, the turbulent Schmidt number Sc_t is set to 0.7 which is a commonly used value [113, 114]. Lastly, $R(C)$ and S in Eq.(3.3) are the reaction and the source terms. In this study, the source term S in the domain Ω is used to define the position and the amplitude of vehicle exhaust.

From the detailed pollutant concentration map $C(x, t)$ (see Fig. 3.14 (a)), the critical areas where people are exposed to high pollution levels are determined. Hence, the concentrations in these areas are defined as quantities of interest \mathcal{J} .

$$\mathcal{J} = \int_0^T \int_{\Omega} f_q(\mathbf{x})\xi(t)C(\mathbf{x}, t)d\Omega dt \quad (3.5)$$

where $f_q(\mathbf{x})$ is the space function to extract the pollution in a critical area Ω_q (Fig. 3.14 (b)) and $\xi(t)$ is the time extractor function to define the period of interest (Fig. 3.14 (c)). Herein Ω_q denotes the subdomain of Ω representing the location where we want to improve the air quality.

3.3.2.2 Remediation: Smart placement of depolluting panels solving minimization problem

To simply model the effects of depolluting panels on the district air quality, I consider in the optimization problem the advection-diffusion-reaction equation:

$$\begin{cases} \frac{\partial C}{\partial t} + \vec{v} \cdot \nabla C - div(D\nabla C) = S & \text{in } \Omega \times [0, T] \\ C = C_i & \text{on } \Gamma_i \times [0, T] \\ \nabla C \cdot \vec{n} = 0 & \text{on } \Gamma_o \cup \Gamma_n \times [0, T] \\ -D\nabla C \cdot \vec{n} = kC & \text{on } \Gamma_p \times [0, T] \\ C(t = 0) = C_0 & \text{in } \Omega \end{cases} \quad (3.6)$$

To remain simple, the degradation of the pollutant by the photocatalytic depolluting system is described using a first-order-reaction where k (m/s) denotes the reaction rate function. The reaction rate is an approximation of Langmuir-Hinshelwood kinetic model and was used in previous works [115, 116, 117]. The degradation reaction occurring at the surfaces of the depolluting panels, it is considered as a boundary condition [116, 117]. For operational reasons, the depolluting panels can not be placed on any surfaces of the district. Consequently, we limit the potential

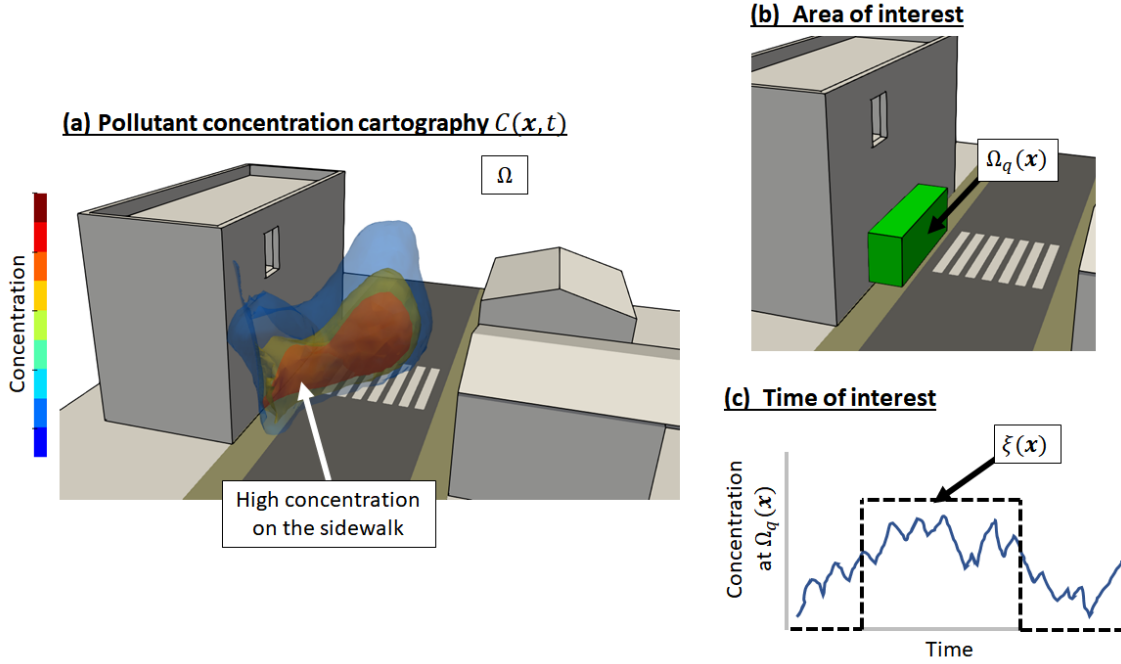


Figure 3.14: Definition of the quantity of interest: (a) Concentration cartography, (b) area of interest and (c) time of interest.

placement of depolluting panels on the boundary Γ_p which is a restricted part of the wall boundary Γ_w . The boundaries Γ_p and Γ_n are defined such that $\Gamma_w = \Gamma_p \cup \Gamma_n$.

The constrained minimization problem to be solved is:

$$\min_{k, C \in \mathcal{C}} \mathcal{J}(C, k) \quad (3.7)$$

where $C \in \mathcal{C}$, implies that the concentration C has to satisfy the direct problem equation (3.6).

The constrained minimization problem (3.7) can be rewritten using the Lagrangian \mathcal{L}

$$\begin{aligned} \mathcal{L}(C, k; \lambda) = & \mathcal{J}(C, k) - \int_0^T \int_{\Omega} \lambda_1 \left(\frac{\partial C}{\partial t} + \vec{v} \cdot \nabla C - \text{div}(D\nabla C) - S \right) d\Omega dt \\ & - \int_0^T \int_{\Gamma_i} \lambda_2 (C - C_i) dS dt - \int_0^T \int_{\Gamma_o \cup \Gamma_n} \lambda_3 \nabla C \cdot \vec{n} dS dt \\ & + \int_0^T \int_{\Gamma_p} \lambda_4 (D\nabla C \cdot \vec{n} + kC) dS dt - \int_{\Omega} \lambda_5 (C(t=0) - C_0) d\Omega \end{aligned} \quad (3.8)$$

where $\lambda_i, i \in \{1, \dots, 5\}$ are Lagrange multipliers.

The derivatives of the Lagrangian \mathcal{L} according to λ_i, C, k are summarized below.

- the Lagrange multipliers $\lambda_i, i.e. \partial\mathcal{L}/\partial\lambda_i = 0$, gives as expected the “direct problem” where the concentration C has to satisfy Eq. (3.6);
- the concentration $C, i.e. \partial\mathcal{L}/\partial C = 0$, leads to the formulation of the “adjoint problem” whose the adjoint concentration noted \tilde{C} verifies

$$\begin{cases} -\frac{\partial\tilde{C}}{\partial t} - \vec{v} \cdot \nabla\tilde{C} - \text{div}(D\nabla\tilde{C}) = f_q \xi & \text{in } \Omega \times [0, T] \\ \tilde{C} = 0 & \text{on } \Gamma_i \times [0, T] \\ \nabla\tilde{C} \cdot \vec{n} = 0 & \text{on } \Gamma_n \times [0, T] \\ -D\nabla\tilde{C} \cdot \vec{n} = k\tilde{C} & \text{on } \Gamma_p \times [0, T] \\ D\nabla\tilde{C} \cdot \vec{n} + (\vec{v} \cdot \vec{n})\tilde{C} = 0 & \text{on } \Gamma_o \times [0, T] \\ \tilde{C}(t = T) = 0 & \text{in } \Omega. \end{cases} \quad (3.9)$$

The details of the calculations to obtain the adjoint problem and the relation between the Lagrange multipliers λ_i and the adjoint field \tilde{C} are given in following Subsection 3.3.3. I notably show that the adjoint field \tilde{C} corresponds to the Lagrange multiplier $\lambda_1, i.e. \tilde{C} = \lambda_1$.

The adjoint problem corresponds to a backward advection-diffusion equation which involves a fictitious source emission located in the area of interest Ω_q . Contrary to the direct problem, it has a final condition in time. By making a change of variable $t' = T - t$, the adjoint problem can be rewritten as a forward problem that can be solved using standard codes.

The adjoint concentration field \tilde{C} corresponds to a sensitivity function associated with the considered quantity of interest \mathcal{J} . Hence, if the adjoint concentration is null in a part of the domain, it physically means that what happens in this part of the domain will not affect the chosen quantity of interest.

This type of adjoint model was previously used in [118] to study the optimal placement of air quality sensors.

- the reaction rate $k, i.e. \partial\mathcal{L}/\partial k$, produces the sensitivity of the quantity of interest (QoI) to the depolluting panels;

$$\frac{\partial\mathcal{L}}{\partial k} = \frac{\partial J}{\partial k} = \int_0^T \lambda_4 C dt = - \int_0^T \tilde{C} C dt \quad \text{on } \Gamma_p \quad (3.10)$$

Here, one has $\lambda_4 = -\tilde{C}$ on $\Gamma_p \times [0, T]$ (see Section 3.3.3). The direct concentration C and the adjoint concentration \tilde{C} being positive, it can be verified from Eq. (3.10) that an increase of the reaction rate k (increase of depolluting panels area or depolluting efficiency) will lead to a negative functional gradient $\partial\mathcal{J}/\partial k$ and thus a reduction of the pollutant concentration in the area of interest.

Accordingly, to evaluate the effectiveness of depolluting panels placed at a position \mathbf{x} , I define the positive sensitivity indicator:

$$I(\mathbf{x}) = \left| \frac{\partial J}{\partial k} \right| = \int_0^T \tilde{C}(\mathbf{x}, t) C(\mathbf{x}, t) dt \quad (3.11)$$

Let us note that the indicator $I(x)$ is significant when both direct concentration C and the adjoint concentration \tilde{C} have high values. The depolluting panels must therefore be placed in high-polluted zones ($C(x, t)$ high) which can impact the chosen quantity of interest (\tilde{C} high) due to the transport and the dispersion of the pollutant.

For an operational purpose and an objective of limiting computational cost, we solve only the direct problem (Eq. (3.6)) and the adjoint problem (Eq. (3.9)) in the pre-existing configuration, *i.e.* no depolluting panels ($k(m/s) = 0$). Thus, the optimization problem 3.7 is not fully solved via iteration processes. Then, the direct and adjoint numerical solutions are used to evaluate the sensitivity indicator 3.11. Finally, the depolluting panels are to be placed only on surfaces where the indicator $I(\mathbf{x})$ is significant.

In the following chapters, the spatial sensitivity indicator $I(\mathbf{x})$ will be used to select the smart placement of depolluting panels for two urban areas' applications based on the pre-existing configuration.

3.3.3 Derivation of the backward advection-diffusion equation

This section details the derivation of the adjoint advection-diffusion equation (3.9) from the direct advection-diffusion equation (3.6). The constrained optimization problem is rewritten using the Lagrangian:

$$\mathcal{L}(C, k; \lambda) = \mathcal{J}(C, k) - \mathcal{F}(C, k; \lambda_i) \quad (3.12)$$

where

$$\mathcal{J}(C, k) = \int_0^T \int_{\Omega} f_q(\mathbf{x}) \xi(t) C(\mathbf{x}, t) d\Omega dt \quad (3.13)$$

and

$$\begin{aligned}
\mathcal{F}(C, k; \lambda_i) &= \int_0^T \int_{\Omega} \lambda_1 \left(\frac{\partial C}{\partial t} + \vec{\nu} \cdot \nabla C - \text{div}(D\nabla C) - S \right) d\Omega dt \\
&+ \int_0^T \int_{\Gamma_i} \lambda_2 (C - C_i) dS dt \\
&+ \int_0^T \int_{\Gamma_o \cup \Gamma_n} \lambda_3 \nabla C \cdot \vec{\mathbf{n}} dS dt \\
&- \int_0^T \int_{\Gamma_p} \lambda_4 (D\nabla C \cdot \vec{\mathbf{n}} + kC) dS dt + \int_{\Omega} \lambda_5 (C(t=0) - C_0) d\Omega
\end{aligned} \tag{3.14}$$

where $\lambda_i, i \in \{1, \dots, 5\}$ are Lagrange multipliers.

From Eq. (3.12), we have

$$\begin{aligned}
\mathcal{L}(C, k; \lambda) &= \int_0^T \int_{\Omega} f_q(\mathbf{x}) \xi(t) C(\mathbf{x}, t) d\Omega dt \\
&- \int_0^T \int_{\Omega} \lambda_1 \left(\frac{\partial C}{\partial t} + \vec{\nu} \cdot \nabla C - \text{div}(D\nabla C) - S \right) d\Omega dt \\
&- \int_0^T \int_{\Gamma_i} \lambda_2 (C - C_i) dS dt - \int_0^T \int_{\Gamma_o \cup \Gamma_n} \lambda_3 \nabla C \cdot \vec{\mathbf{n}} dS dt \\
&+ \int_0^T \int_{\Gamma_p} \lambda_4 (D\nabla C \cdot \vec{\mathbf{n}} + kC) dS dt - \int_{\Omega} \lambda_5 (C(t=0) - C_0) d\Omega
\end{aligned} \tag{3.15}$$

Next, we derive \mathcal{L} with respect to the state variable C

$$\frac{\partial \mathcal{L}}{\partial C} \delta C = 0 \quad \forall \delta C \tag{3.16}$$

$$\begin{aligned}
\frac{\partial \mathcal{L}}{\partial C} \delta C &= 0 \\
&= \underbrace{\int_0^T \int_{\Omega} f_q(\mathbf{x}) \xi(t) \delta C(\mathbf{x}, t) d\Omega dt}_{(1)} \\
&\quad - \underbrace{\int_0^T \int_{\Omega} \lambda_1 \left(\frac{\partial \delta C}{\partial t} + \vec{\mathbf{v}} \cdot \nabla \delta C - \text{div}(D\nabla \delta C) \right) d\Omega dt}_{(2)} \\
&\quad - \underbrace{\int_0^T \int_{\Gamma_i} \lambda_2 \delta C dS dt}_{(3)} - \underbrace{\int_0^T \int_{\Gamma_o \cup \Gamma_n} \lambda_3 \nabla \delta C \cdot \vec{\mathbf{n}} dS dt}_{(4)} \\
&\quad + \underbrace{\int_0^T \int_{\Gamma_p} \lambda_4 (D\nabla \delta C \cdot \vec{\mathbf{n}} + k \delta C) dS dt}_{(5)} - \underbrace{\int_{\Omega} \lambda_5 \delta C(t=0) d\Omega}_{(6)}
\end{aligned} \tag{3.17}$$

The term (2) in Eq. (3.17) can be written out as

$$\underbrace{- \int_0^T \int_{\Omega} \frac{\partial \delta C}{\partial t} \lambda_1 d\Omega dt}_{\text{Term I}} - \underbrace{\int_0^T \int_{\Omega} \vec{\mathbf{v}} \cdot \nabla \delta C \lambda_1 d\Omega dt}_{\text{Term II}} + \underbrace{\int_0^T \int_{\Omega} \text{div}(D\nabla \delta C) \lambda_1 d\Omega dt}_{\text{Term III}}$$

From this point onward, I will describe the calculation of each term (Term I, II and III) separately.

- **Term I:**

We apply integration by parts to Term I:

$$\begin{aligned}
- \int_0^T \int_{\Omega} \frac{\partial \delta C}{\partial t} \lambda_1 d\Omega dt &= - \int_{\Omega} [\delta C \lambda_1]_0^T d\Omega + \int_0^T \int_{\Omega} \delta C \frac{\partial \lambda_1}{\partial t} d\Omega dt \\
&= - \underbrace{\int_{\Omega} \delta C(T) \lambda_1(T) d\Omega}_{(1)} + \underbrace{\int_{\Omega} \delta C(0) \lambda_1(0) d\Omega}_{(2)} \\
&\quad + \underbrace{\int_0^T \int_{\Omega} \delta C \frac{\partial \lambda_1}{\partial t} d\Omega dt}_{(3)}
\end{aligned} \tag{Term I}$$

- **Term II:**

Using the divergence theorem (Formule of Green-Ostrogradski), Term II becomes

$$\begin{aligned}
-\int_0^T \int_{\Omega} \nabla \delta C \cdot \vec{v} \lambda_1 d\Omega dt &= -\int_0^T \int_{\Omega} \operatorname{div}(\delta C \vec{v} \lambda_1) d\Omega dt + \int_0^T \int_{\Omega} \delta C \operatorname{div}(\vec{v} \lambda_1) d\Omega dt \\
&= \underbrace{-\int_0^T \int_{\Gamma_i} \delta C \lambda_1 \vec{v} \cdot \vec{n} dS dt}_{(1)} - \cancel{\int_0^T \int_{\Gamma_p} \delta C \lambda_1 \vec{v} \cdot \vec{n} dS dt} \\
&\quad - \underbrace{\int_0^T \int_{\Gamma_o} \delta C \lambda_1 \vec{v} \cdot \vec{n} dS dt}_{(2)} - \cancel{\int_0^T \int_{\Gamma_n} \delta C \lambda_1 \vec{v} \cdot \vec{n} dS dt} \\
&\quad + \underbrace{\int_0^T \int_{\Omega} \delta C \operatorname{div}(\vec{v} \lambda_1) d\Omega dt}_{(3)}
\end{aligned} \tag{3.18}$$

The term (3) in Eq. (3.18) can be rewritten using vector calculus formulas by

$$\int_0^T \int_{\Omega} \delta C \operatorname{div}(\vec{v} \lambda_1) d\Omega dt = \int_0^T \int_{\Omega} \delta C \vec{v} \cdot \nabla \lambda_1 d\Omega dt + \underbrace{\int_0^T \int_{\Omega} \delta C \operatorname{div}(\vec{v}) \lambda_1 d\Omega dt}_{= 0 \text{ as incompressible flow}} \tag{3.19}$$

According to Eq. (3.18) and (3.19), Term II finally becomes

$$\begin{aligned}
-\int_0^T \int_{\Omega} \nabla \delta C \cdot \vec{v} \lambda_1 d\Omega dt &= \underbrace{-\int_0^T \int_{\Gamma_i} \delta C \lambda_1 \vec{v} \cdot \vec{n} dS dt}_{(1)} - \underbrace{\int_0^T \int_{\Gamma_o} \delta C \lambda_1 \vec{v} \cdot \vec{n} dS dt}_{(2)} \\
&\quad + \underbrace{\int_0^T \int_{\Omega} \delta C \vec{v} \cdot \nabla \lambda_1 d\Omega dt}_{(3)}
\end{aligned} \tag{Term II}$$

- **Term III:**

$$\begin{aligned}
&\int_0^T \int_{\Omega} \operatorname{div}(D\nabla \delta C) \lambda_1 d\Omega dt \\
&= \underbrace{\int_0^T \int_{\Omega} \operatorname{div}(D\nabla \delta C \lambda_1) d\Omega dt}_{(1)} - \underbrace{\int_0^T \int_{\Omega} D\nabla(\lambda_1) \cdot \nabla(\delta C) d\Omega dt}_{(2)}
\end{aligned} \tag{3.20}$$

Now let us define $\partial\Omega = \{\Gamma_i \cup \Gamma_o \cup \Gamma_n \cup \Gamma_p\}$. According to the divergence theorem (Formule of Green-Ostrogradski), the term (1) in Eq. (3.20) is

$$\int_0^T \int_{\Omega} \operatorname{div}(D\nabla\delta C\lambda_1) d\Omega dt = \int_0^T \int_{\partial\Omega} (D\nabla\delta C\lambda_1) \cdot \vec{\mathbf{n}} dS dt$$

Considering vector calculus formulas, the term (2) becomes

$$\begin{aligned} - \int_0^T \int_{\Omega} D\nabla(\lambda_1) \cdot \nabla(\delta C) d\Omega dt &= - \int_0^T \int_{\Omega} \operatorname{div}(D\nabla\lambda_1\delta C) d\Omega dt \\ &\quad + \int_0^T \int_{\Omega} \operatorname{div}(D\nabla\lambda_1)\delta C d\Omega dt \\ &= - \int_0^T \int_{\partial\Omega} D\nabla\lambda_1 \cdot \vec{\mathbf{n}}\delta C dS dt \\ &\quad + \int_0^T \int_{\Omega} \operatorname{div}(D\nabla\lambda_1)\delta C d\Omega dt \end{aligned}$$

Finally, Term III is

$$\begin{aligned} \int_0^T \int_{\Omega} \operatorname{div}(D\nabla\delta C)\lambda_1 d\Omega dt &= \underbrace{\int_0^T \int_{\partial\Omega} (D\nabla\delta C\lambda_1) \cdot \vec{\mathbf{n}} dS dt}_{(1)} \\ &\quad - \underbrace{\int_0^T \int_{\partial\Omega} D\nabla\lambda_1 \cdot \vec{\mathbf{n}}\delta C dS dt}_{(2)} \quad \text{(Term III)} \\ &\quad + \underbrace{\int_0^T \int_{\Omega} \operatorname{div}(D\nabla\lambda_1)\delta C d\Omega dt}_{(3)} \end{aligned}$$

Summarizing the different terms which involve δC on the boundary Γ_i : (3) in Eq. (3.17), (1) in **Term II** and (2) in **Term III**, we have

$$- \int_0^T \int_{\Gamma_i} \lambda_2 \delta C dS dt - \int_0^T \int_{\Gamma_i} \delta C \lambda_1 \vec{\mathbf{v}} \cdot \vec{\mathbf{n}} dS dt - \int_0^T \int_{\Gamma_i} D\nabla(\lambda_1) \cdot \vec{\mathbf{n}} \delta C dS dt = 0 \quad , \forall \delta C \quad (3.21)$$

Hence the Lagrange multiplier λ_2 satisfies:

$$\boxed{\lambda_2 = -\lambda_1 \vec{\mathbf{v}} \cdot \vec{\mathbf{n}} - D\nabla\lambda_1 \cdot \vec{\mathbf{n}} \quad \text{on} \quad \Gamma_i \times [0, T]} \quad (3.22)$$

The same operations are done for the terms which involve $\nabla\delta C$ on the boundaries $\Gamma_o \cup \Gamma_n$: (4) in Eq. (3.17) and (1) in **Term III**,

$$-\int_0^T \int_{\Gamma_o \cup \Gamma_n} \lambda_3 \nabla\delta C \cdot \vec{\mathbf{n}} \, dS \, dt + \int_0^T \int_{\Gamma_o \cup \Gamma_n} (D\nabla\delta C \lambda_1) \cdot \vec{\mathbf{n}} \, dS \, dt = 0 \quad , \forall \nabla\delta C \quad (3.23)$$

Then, we get

$$\boxed{\lambda_3 = D\lambda_1 \quad \text{on} \quad \Gamma_o \cup \Gamma_n \times [0, T]} \quad (3.24)$$

Concerning the terms with $\nabla\delta C$ on Γ_p : the first term of (5) in Eq. (3.17) and (1) in **Term III**, we have

$$\int_0^T \int_{\Gamma_p} \lambda_4 (D\nabla\delta C \cdot \vec{\mathbf{n}}) \, dS \, dt + \int_0^T \int_{\Gamma_p} (D\nabla\delta C \lambda_1) \cdot \vec{\mathbf{n}} \, dS \, dt = 0 \quad , \forall \nabla\delta C \quad (3.25)$$

Then, we get

$$\boxed{\lambda_4 = -\lambda_1 \quad \text{on} \quad \Gamma_p \times [0, T]} \quad (3.26)$$

To determine the last Lagrange multiplier λ_5 , we consider the terms involving $\delta C(t=0)$: (6) in Eq. (3.17) and (2) in **Term I**,

$$-\int_{\Omega} \lambda_5 \delta C(t=0) \, d\Omega + \int_{\Omega} \delta C(t=0) \lambda_1(t=0) \, d\Omega = 0 \quad , \forall \delta C(t=0) \quad (3.27)$$

$$\boxed{\lambda_5 = \lambda_1(t=0) \quad \text{on} \quad \Omega} \quad (3.28)$$

Now let us derive the boundary conditions of the adjoint problem. From the second term of (5) in Eq. (3.17) and (2) in **Term III**, and considering $\lambda_4 = -\lambda_1$, one has

$$-\int_0^T \int_{\Gamma_p} \lambda_1 (k\delta C) \, dS \, dt - \int_0^T \int_{\Gamma_p} D\nabla\lambda_1 \cdot \vec{\mathbf{n}} \delta C \, dS \, dt = 0 \quad , \forall \delta C \quad (3.29)$$

$$\boxed{-D\nabla\lambda_1 \cdot \vec{\mathbf{n}} \delta C = \lambda_1 k \quad \text{on} \quad \Gamma_p \times [0, T]} \quad (3.30)$$

On Γ_o , from (2) in **Term II** and (2) in **Term III**, we have

$$-\int_0^T \int_{\Gamma_o} \delta C \lambda_1 \vec{\mathbf{v}} \cdot \vec{\mathbf{n}} dS dt - \int_0^T \int_{\Gamma_o} D\nabla \lambda_1 \cdot \vec{\mathbf{n}} \delta C dS dt = 0 \quad (3.31)$$

Thus

$$\boxed{\lambda_1 \vec{\mathbf{v}} \cdot \vec{\mathbf{n}} + D\nabla \lambda_1 \cdot \vec{\mathbf{n}} = 0 \quad \text{on} \quad \Gamma_o \times [0, T]} \quad (3.32)$$

On Γ_i , (1) in **Term III** gives,

$$\int_0^T \int_{\Gamma_i} (D\nabla \delta C \lambda_1) \cdot \vec{\mathbf{n}} dS dt = 0 \quad , \forall \delta C \rightarrow \boxed{\lambda_1 = 0 \quad \text{on} \quad \Gamma_i \times [0, T]} \quad (3.33)$$

On Γ_n , (2) in **Term III** gives,

$$-\int_0^T \int_{\partial\Omega} D\nabla \lambda_1 \cdot \vec{\mathbf{n}} \delta C dS dt = 0 \quad , \forall \delta C \rightarrow \boxed{\lambda_1 \cdot \vec{\mathbf{n}} = 0 \quad \text{on} \quad \Gamma_n \times [0, T]} \quad (3.34)$$

According to (1) in Eq. (3.17), we obtain the null final condition of the adjoint problem,

$$-\int_{\Omega} \delta C(T) \lambda_1(T) d\Omega = 0 \quad , \forall \delta C(T) \rightarrow \boxed{\lambda_1(t = T) = 0 \quad \text{on} \quad \Omega} \quad (3.35)$$

From all the remaining terms, (1) in Eq. (3.17), (3) in **Term I**, (3) in **Term II** and (3) in **Term III**,

$$\begin{aligned} & \int_0^T \int_{\Omega} f_q(\mathbf{x}) \xi(t) \delta C(\mathbf{x}, t) d\Omega dt + \int_0^T \int_{\Omega} \delta C \frac{\partial \lambda_1}{\partial t} d\Omega dt + \\ & \int_0^T \int_{\Omega} \delta C \vec{\mathbf{v}} \cdot \nabla \lambda_1 d\Omega dt + \int_0^T \int_{\Omega} \text{div}(D\nabla \lambda_1) \delta C d\Omega dt = 0 \quad , \forall \delta C \end{aligned} \quad (3.36)$$

This gives the adjoint advection-diffusion equation;

$$\boxed{-\frac{\partial \lambda_1}{\partial t} - \vec{\mathbf{v}} \cdot \nabla \lambda_1 - \text{div}(D\nabla \lambda_1) = f_q(\mathbf{x}) \xi(t) \quad \text{on} \quad \Omega \times [0, T]} \quad (3.37)$$

The Lagrange multiplier λ_1 corresponds to the adjoint state. In summary, we obtained the following relations between the Lagrange multipliers

$$\lambda_2 = -D\nabla\lambda_1 \cdot \mathbf{n} - (\mathbf{v} \cdot \mathbf{n})\lambda_1 \quad \text{on} \quad \Gamma_i \times [0, T] \quad (3.38)$$

$$\lambda_3 = D\lambda_1 \quad \text{on} \quad \Gamma_o \cup \Gamma_n \times [0, T] \quad (3.39)$$

$$\lambda_4 = -\lambda_1 \quad \text{on} \quad \Gamma_p \times [0, T] \quad (3.40)$$

$$\lambda_5 = \lambda_1(t=0) \quad \text{on} \quad \Omega \quad (3.41)$$

and we prove that the Lagrange multiplier λ_1 satisfies

$$\begin{cases} -\frac{\partial\lambda_1}{\partial t} - \vec{\mathbf{v}} \cdot \nabla\lambda_1 - \text{div}(D\nabla\lambda_1) = f_q \xi & \text{in} \quad \Omega \times [0, T] \\ \lambda_1 = 0 & \text{on} \quad \Gamma_i \times [0, T] \\ \nabla\lambda_1 \cdot \mathbf{n} = 0 & \text{on} \quad \Gamma_n \times [0, T] \\ -D\nabla\lambda_1 \cdot \mathbf{n} = k\lambda_1 & \text{on} \quad \Gamma_p \times [0, T] \\ D\nabla\lambda_1 \cdot \mathbf{n} + (\vec{\mathbf{v}} \cdot \mathbf{n})\lambda_1 = 0 & \text{on} \quad \Gamma_o \times [0, T] \\ \lambda_1(t=T) = 0 & \text{in} \quad \Omega. \end{cases} \quad (3.42)$$

Thus, Eq. (3.42) corresponds to the adjoint problem. By convenience, we note $\tilde{C}(= \lambda_1)$ the solution of this adjoint problem.

3.3.4 Limitations of the considered pollutant dispersion modeling

The method described in the previous subsections was formulated under the assumption that the only factor contributing to pollutant dispersion is airflow (advection and diffusion (molecular and turbulent diffusion)) induced by urban morphology to simplify the problem. In reality, however, pollutant concentrations are also sensitive to e.g., temperature, atmospheric stability and chemical reaction processes, apart from airflow. Obviously, vehicles and trees are also key factors causing turbulence diffusion. However, these parameters are not considered in this study. In the following, I discuss on the limitations of the considered modeling.

- Temperature, sunlight and atmospheric stability

The density of air varies with the air temperature of the air. Air at higher temperatures than its surroundings is lighter and therefore rises, and vice versa for lower temperatures. Sunlight and temperature cause heat to accumulate

at the ground surface. The temperature difference between the ground surface and the air causes vertical air mixing near the ground surface. As a result, it contributes to increasing turbulence on the ground and significantly impacts pollutant dispersion.

Atmospheric stability is categorized based on whether vertical air motion is encouraged or suppressed. Although there are various classifications of atmospheric stability [119], here I give three general descriptions: unstable, stable and neutral conditions. In practice, there are more detailed classifications for unstable and stable conditions.

- Unstable; On sunny days, for example, when the ground is heated by the heat from the sun, resulting in a temperature distribution with high temperatures near the surface and low temperatures in the sky above, which creates a temperature difference and convection in the vertical direction.
- Stable; During clear nights with low winds in winter, the degree of radiation from the ground (infrared radiation) increases and the area near the ground surface cools as more heat is lost (radiative cooling). The temperature is then lower near the surface and higher in the sky, vertical convection is inhibited and pollutant dispersion is reduced.
- Neutral; A state in which the air temperature reduction rate is almost equal to the dry adiabatic reduction rate, e.g., when it is cloudy or windy.

In this study, However, for simplicity, temperature and sunlight are not taken into account.

- Chemical reaction modeling

NO_x is a reactive pollutant. As stated in Section 1.1.3, when NO₂ is exposed to UV radiation, O₃ is formed via NO and VOCs; thereby O₃ is a secondary pollutant. During this process, NO is produced, and finally, O₃ is destroyed by NO itself and produces again NO₂ and O₂ (see Fig. 1.2 and 1.3). In addition to the dispersion of pollutants caused by turbulence, the involvement of chemical reaction processes significantly influences the dispersion of reactive pollutants and their associated exposure characteristics. Secondary pollutants are not taken into account in many studies as they assume that the timescale for the transport of pollutants is shorter than the occurrence of chemical reactions. Thereby, pollutants are often considered inert. In my Ph.D., NO_x emissions are used in CFD simulation to make a NO_x cartography. Then, a NO₂ concentration cartography ($\mu\text{g}/\text{m}^3$) is deduced from NO_x cartography

using the Midletom formula [120], a statistical representation of the ratio of NO_x to NO₂, NO;

$$[NO_2]_h = \left(2.166 - \frac{[NO_x]_h}{1.91} \left(1.236 - 3.348A + 1.933A^2 - 0.326A^3 \right) \right) \times 1.91 \quad (3.43)$$

where $A = \log_{10} ([NO_x]_h/1.91)$.

- Traffic- and trees-induced turbulence

Trees and vehicles can increase turbulence and air mixing in urban areas. Thereby, they may facilitate the dispersion of pollutants and reduce pollutant concentrations. On the contrary, besides the dilution effect of disrupted flows, they sometimes inhibit pollutant dispersion and reduce exposure to pedestrians. Densely arranged trees [121] and roadside parked vehicles [122] may act as permanent or temporary barriers respectively. However, for simplicity, they are not considered herein.

3.4 Conclusion

In this section, I presented a general background on the interaction between outdoor and indoor air quality and mitigation strategies for air quality issues. CFD modeling is a promising tool to investigate the air quality interaction between outdoors and indoors, and depolluting panels can be a practical solution for air pollution mitigation in urban areas. Accordingly, I proposed a numerical strategy to place depolluting panels in urban areas efficiently. As this is the first such work on optimizing depolluting panels' placement, various simplifications are included. In my research, I consider the smart placement of depolluting panels concerning urban airflow.

The proposed strategy is applied for the first time in the following Chapters 4 and 5. Chapter 4 examines the applicability of the proposed strategy to an ideal environment, and Chapter 5 considers a realistic environment. In both chapters, the interaction between outdoor and indoor air quality is also investigated.

Chapter 4

Application to controlled conditions in Sense-City

In this chapter, the methodology proposed in the previous section is implemented in an experimental real-scale urban district called "Sense-City." Sense-City offers the advantage of controllable climatic conditions, making it an ideal initial application for the verification and validation of the proposed numerical strategy from outdoor/indoor air pollutant cartography to the optimal placement of depolluting panels based on airflow considerations.

This chapter is organized as follows. Firstly, outdoor and indoor pollutant concentration maps in Sense-City are created using CFD, and the results are analyzed to identify QoIs. Subsequently, we propose an optimal placement of depolluting panels based on the sensitivity indicator. Afterward, we test different panels' deployment scenarios to investigate the reduction of pollutant concentration. By comparing the extent of pollution concentration reduction between the two panel placement scenarios, we study the effectiveness of our proposed method. Finally, we validate the accuracy of the simulation by conducting a CO₂ dispersion experiment and comparing with CO₂ measurements.

It should be noted that a post-doc, Fatiha CHABI, contributed to a part of this chapter, i.e., the direct and adjoint simulations with "FreeFem++" software.

4.1 Description of Sense-City

Sense-City is an instrumented district built in 2018 and located on the campus of Université Gustave Eiffel at Champs-sur-Marne, France [123]. This district is de-

signed for the validation of numerical physical models and innovative technologies used in the field of urban environments. It is composed of two small districts of 400 m²: "Mini-city 1" and "Mini-city 2" (see Fig. 4.1 (a)). These urban areas can be studied in natural conditions or in controlled climatic conditions using a large mobile climatic chamber of the dimension (20 m × 20 m × 10 m height). The climatic chamber provides a controlled environment and can move from Mini-city 1 to Mini-city 2, and vice versa. Thanks to the climatic chamber, weather conditions: airflow, air pollution, temperatures, humidity, rain and sunlight, can be repeated according to the purposes. More than 150 sensors (temperature sensors, gas sensors, etc.) are installed at different locations in the district. In my Ph.D., we consider controlled airflow and air pollutant conditions in Mini-city 1 within the climatic chamber.

Mini-city 1 consists of a wooden chalet, a small house made of bio-based materials and a two-story concrete building (Fig. 4.2 (a)), as well as roads and sidewalks (Fig. 4.1 (b)). To study outdoor pollutant transfer to the indoor environment, we investigate the indoor air quality of the two-story concrete building (see Fig. 4.2). As the ground floor primarily serves as technical rooms, this study focuses on the indoor air quality on the 1st floor. The area of the 1st floor is approximately 40 m² (9.6 m × 3.6 m) with the height 3.6 m, respectively. The 1st floor consists of two rooms divided by a movable wall that is 72 mm thick. The movable wall has an opening of approximately 1 m between the two rooms. The rooms are equipped with three desks and one locker.

The climatic chamber consists of twelve blocks of fans and two sets of extraction ducts for suction and of forced-air ducts, as shown in Fig. 4.3, distributed over the

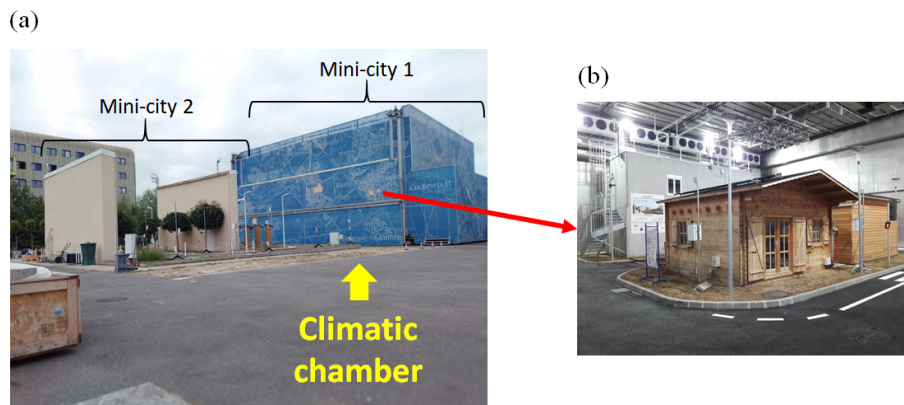


Figure 4.1: Picture of Sense-City: (a) overview of Mini-city 1 with climatic chamber (blue box) and Mini-city 2 and (b) Mini-city 1 recovered by the climatic chamber.

south and north walls of the chamber. Each block of fans is formed with three axial fans. The fans draws in air from the rear side and re-emit it from the front side into the climatic chamber. Forced-air ducts are made up of two perforated horizontal pipes that have several small holes for re-emission. Once the air is extracted from the bottom of the extraction duct, it is sent to the forced-air ducts. Therefore, in Sense-City, it is a closed-cycle airflow circulation. By imposing the same airflow setting, we can repeatedly reproduce the same airflow conditions.

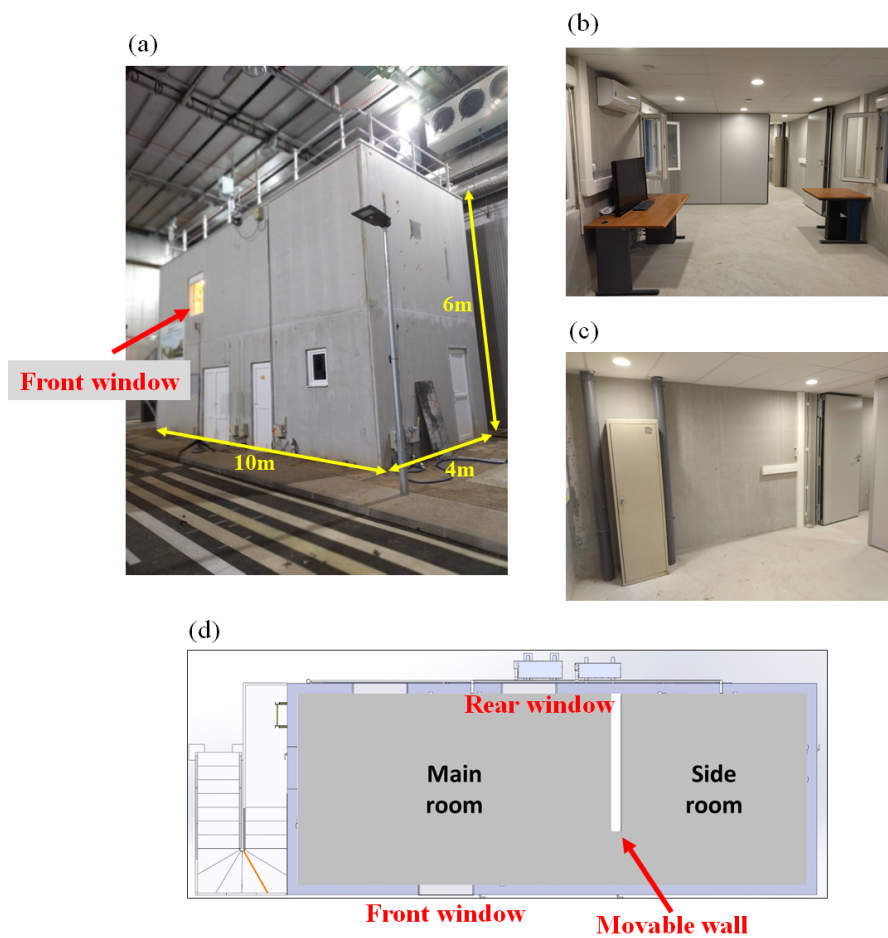


Figure 4.2: Concrete building in Mini-city 1: (a) overview, (b) main room, (c) side room and (d) plan view of the 1st floor.

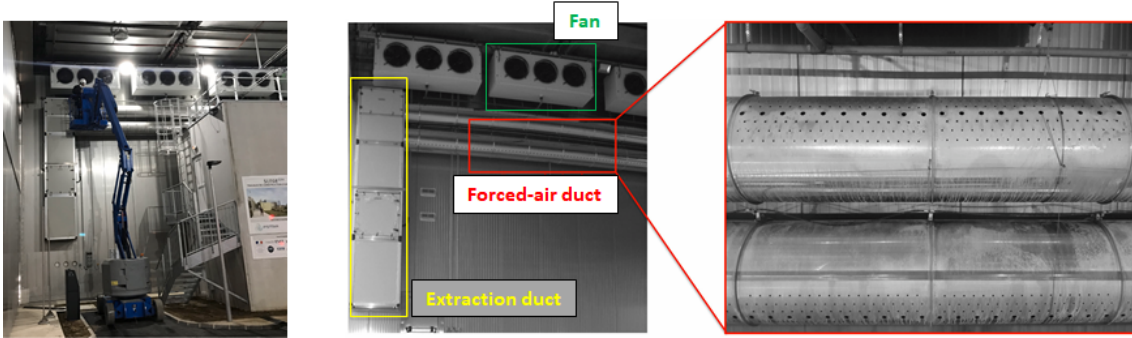


Figure 4.3: Partial view of the chamber ventilation system: sets of fans extraction ducts and forced-air ducts [124].

4.2 Numerical study of pollutant dispersion in controlled condition: from making pollutant cartography to smart placement of depolluting panel

In Sense-City application, first, we study the time evolution of the concentration under controlled conditions within the time interval $[0, 180s]$. We consider a scenario where a non-reactive pollutant tracer, allowing to study their dispersion without additional complexities introduced by chemical reactions, is continuously released from a parallelepiped volumetric source with dimensions of $0.5 \times 0.5 \times 0.5 = 0.125, \text{m}^3$ on the road. The center of the source is located in the middle of the road at the coordinates $(x = 0 \text{ m}, y = -2.5 \text{ m}, z = 1 \text{ m})$ between the concrete building and the two houses, indicated by a red rectangle in Fig. 4.4.

4.2.1 Numerical mock-up of Sense-City

The numerical mock-up of Sense-City is identical to the one employed in [124] (see Fig. 4.5). The center of the Cartesian coordinate system, represented in Fig. 4.4, is placed on the ground surface at the center of the district such that the district domain is described by $\{x \in [-11.22\text{m}, 11.22\text{m}], y \in [-11.1\text{m}, 11.1\text{m}], z \in [0\text{m}, 10\text{m}]\}$. In this computational modeling, the airflow inside the ventilation systems (inside fans, forced-air ducts and extraction ducts) is not simulated. Instead, boundary conditions, which will be described later, are applied to each surface of the ventilation system. In Fig. 4.5, the red color indicates the fan for the air discharge, green represents the fan for air intake, light blue corresponds to the extraction duct, and

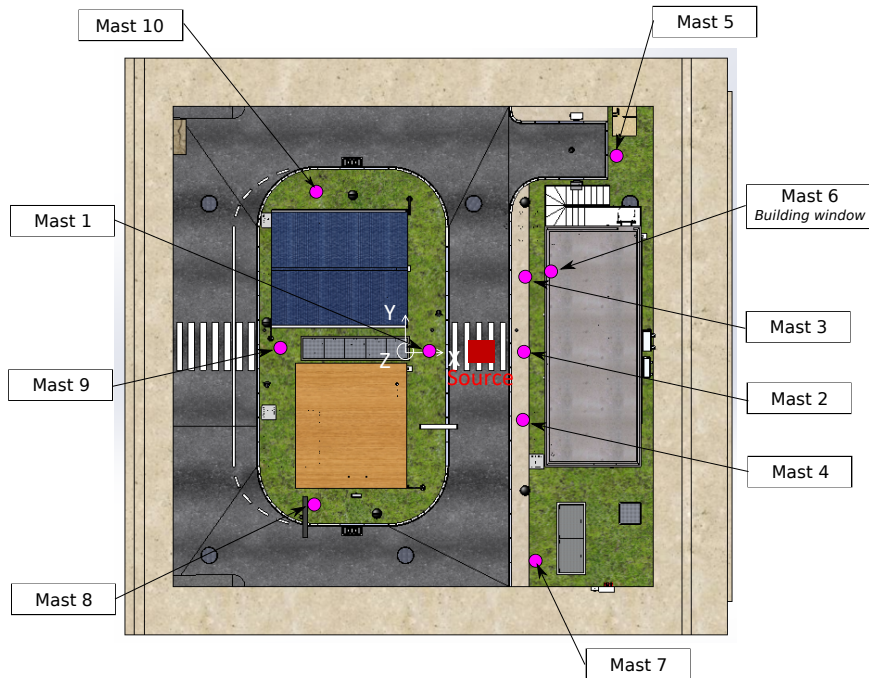


Figure 4.4: Position of the pollutant source and the mast sensors in Sense-City district.

black represents the forced-air duct. Let us note that, for practical reasons, the numerous small circular holes on the forced-air duct (see Fig. 4.3) have been simplified to rectangular-shaped slots as can be seen in Fig. 4.5. Additionally, several small details within the Mini-city 1, such as slight steps on sidewalks, traffic lights, etc., have not been considered in the numerical geometry. Moreover, at this phase, we do not consider the indoor environment of the concrete building. Therefore, window openings (the front window and rear window in Fig. 4.2 (d)) on the concrete building are modeled as walls.

4.2.2 Diagnosis stage: making outdoor pollutant cartography

4.2.2.1 Direct CFD modeling for outdoor pollutant dispersion

The direct simulations for outdoor flow and pollutant dispersion are performed with the finite-volume CFD software "Code_Saturne" [125] and finite-element based

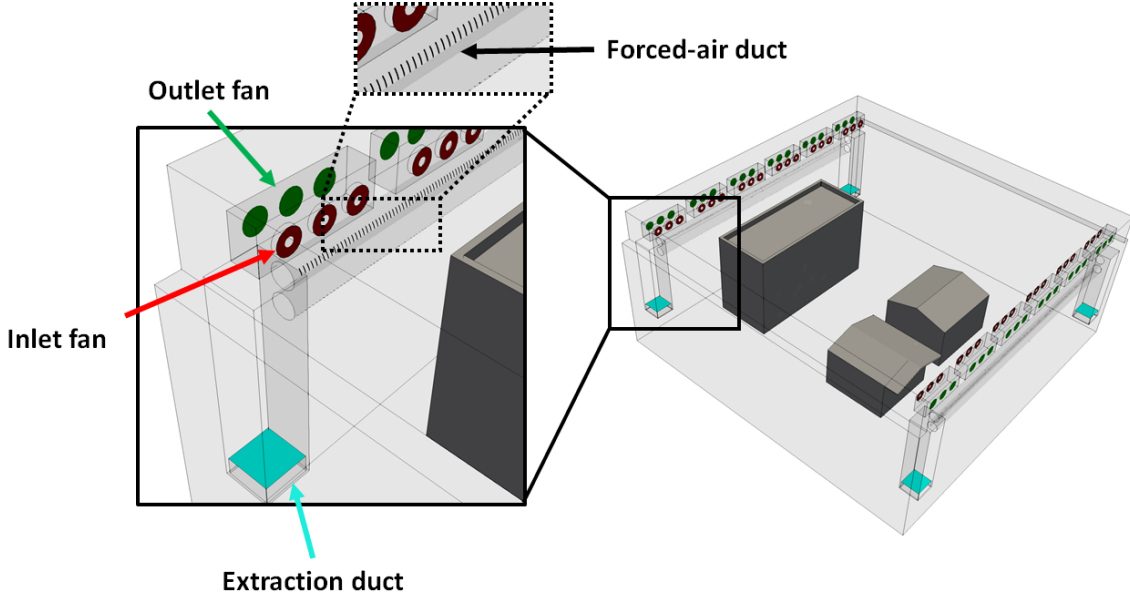


Figure 4.5: Numerical mock-up of the mini-city 1 within the climatic chamber of Sense-city.

software "FreeFem++ [126]" respectively. Note that this outdoor flow simulation in Sense-City has been previously studied in [124] during the Ph.D. of Benjamin STREICHENBERGER. Pollutant dispersion depending on the airflow, we re-use the time-averaged velocity field \vec{v} and the turbulent viscosity μ_t obtained in [124]. In the following, I summarize the characteristics of flow and scalar transport simulation. These characteristics will also be considered in the subsequent studies (Section 4.3 and Chapter 5).

- **Flow phase:**

Here, I briefly recall theoretical backgrounds from the governing equation to $k-\omega$ SST turbulence modeling that is used in my Ph.D. Hereafter, tensor notation is used for equations. First of all, the governing equations for fluid dynamics, assuming that the density and viscosity remain constant, are the continuity equation and NS equation for incompressible flow as follows:

$$\frac{\partial u_i}{\partial x_i} = 0 \quad (4.1)$$

$$\frac{\partial u_i}{\partial t} + \frac{\partial(u_i u_j)}{\partial x_j} = -\frac{1}{\rho} \frac{\partial p}{\partial x_i} + \frac{\partial}{\partial x_j} \left\{ \nu \left(\frac{\partial u_i}{\partial x_j} + \frac{\partial u_j}{\partial x_i} \right) \right\} \quad (4.2)$$

where u_i is velocity component in the i -th direction, p is pressure, ρ is density of the fluid, ν kinematic viscosity of the fluid. As mentioned in Subsection 3.3.2.1, RANS equation can be obtained by applying the ensemble average to Eq. (4.1) and Eq. (4.2), which is often used for turbulent flow field in industry practice. Here, let the ensemble average and fluctuating component of the physical quantity f denote $\langle f \rangle$ and f' . The physical quantity f can then be decomposed to the ensemble average $\langle f \rangle$ and fluctuating components f' as follows:

$$f = \langle f \rangle + f' \quad (4.3)$$

By substituting Eq. (4.3) into Eq. (4.1) and (4.2) and applying the ensemble average to them, Reynolds averaged form of Eq. (4.1) and (4.2) are obtained:

$$\frac{\partial \langle u_i \rangle}{\partial x_i} = 0 \quad (4.4)$$

$$\frac{\partial \langle u_i \rangle}{\partial t} + \frac{\partial \langle u_i \rangle \langle u_j \rangle}{\partial x_j} = -\frac{1}{\rho} \frac{\partial \langle p \rangle}{\partial x_i} + \frac{\partial}{\partial x_j} \left[\nu \left(\frac{\partial \langle u_i \rangle}{\partial x_j} + \frac{\partial \langle u_j \rangle}{\partial x_i} \right) - \langle u'_i u'_j \rangle \right] \quad (4.5)$$

where $\langle u_i \rangle$ is mean velocity component in the i -th direction, $\langle p \rangle$ is mean pressure, u'_i and u'_j are turbulent velocity fluctuations in the i -th direction. The last term $\langle u'_i u'_j \rangle$ on the right-hand side in Eq. (4.5) is called "Reynolds stress" term that is an unknown quantity. This term needs to be estimated to close the system of equations consisting of Eq. (4.4) and (4.5). This is called "turbulence closure problem". To estimate Reynolds stress $\langle u'_i u'_j \rangle$, many turbulence modelings have been developed.

The most well-known turbulence modeling is "Boussinesq eddy viscosity hypothesis" [127]. This is derived from a constitutive equation that establishes a relationship between the Reynolds stress tensor and the mean velocity gradient tensor. It introduces the eddy viscosity coefficient ν_t and estimates $\langle u'_i u'_j \rangle$ from the product of the kinematic viscosity ν_t and mean velocity gradient (mean strain tensor) as follows:

$$\langle u'_i u'_j \rangle = -\nu_t \left(\frac{\partial \langle u_i \rangle}{\partial x_j} + \frac{\partial \langle u_j \rangle}{\partial x_i} \right) + \frac{2}{3} \delta_{ij} k \quad (4.6)$$

Substituting Eq. (4.6) into Eq. (4.5), we get:

$$\frac{\partial \langle u_i \rangle}{\partial t} + \frac{\partial \langle u_i \rangle \langle u_j \rangle}{\partial x_j} = -\frac{1}{\rho} \frac{\partial \langle p \rangle}{\partial x_i} + \frac{\partial}{\partial x_j} \left[(\nu + \nu_t) \left(\frac{\partial \langle u_i \rangle}{\partial x_j} + \frac{\partial \langle u_j \rangle}{\partial x_i} \right) \right] \quad (4.7)$$

According to Eq. (4.7), provided that ν_t becomes known, the system of Eq. (4.4) and (4.5) can be closed.

At the neighborhood, street and urban scales (Fig. 2.2), Reynolds number is generally large, and thus the molecular viscosity coefficient ν is considerably smaller compared to the eddy viscosity coefficient ν_t . As mentioned in Subsection 2.2.3, to determine the eddy viscosity coefficient ν_t , in my Ph.D., I employ $k - \omega$ SST model. In $k - \omega$ SST model, the transport equation for k and ω to be solved are the followings:

$$\frac{\partial k}{\partial t} + \langle u_j \rangle \frac{\partial k}{\partial x_j} = P_k - \beta^* k \omega + \frac{\partial}{\partial x_j} \left[(\nu + \nu_T \sigma_k) \frac{\partial k}{\partial x_j} \right] \quad (4.8)$$

$$\frac{\partial \omega}{\partial t} + \langle u_j \rangle \frac{\partial \omega}{\partial x_j} = \frac{\partial}{\partial x_j} \left[(\nu + \nu_T \sigma_\omega) \frac{\partial \omega}{\partial x_j} \right] + \alpha \frac{\omega}{k} P_k - \beta \omega^2 + 2(1 - F_1) \frac{\sigma_{\omega 2}}{\omega} \frac{\partial k}{\partial x_j} \frac{\partial \omega}{\partial x_j} \quad (4.9)$$

Each constant (coefficient) is a blend of the corresponding constant of $k - \epsilon$ and $k - \omega$ model via:

$$\phi = \phi_1 F_1 + \phi_2 (1 - F_1) \quad (4.10)$$

where F_1 is a parameter that determines the mixing ratio between $k - \epsilon$ model and $k - \omega$ models; when $F_1 = 0$, $k - \epsilon$ model is employed; when $F_1 = 1$, $k - \omega$ model is utilized. For the all constants (σ_{k1} , σ_{k2} , $\sigma_{\omega 1}$, $\sigma_{\omega 2}$, α_1 , α_2 , β_1 , β_2 , β^*) please refer [128]. The eddy viscosity coefficient ν_t is calculated by

$$\nu_T = \frac{a_1 k}{\max(a_1 \omega, S F_2)} \quad (4.11)$$

where $S = \sqrt{2S_{ij}S_{ij}}$. Auxiliary relations are the following:

$$P_k = \min \left(\frac{\tau_{ij}}{\rho} \frac{\partial \langle u_j \rangle}{\partial x_j}, 10\beta^* k \omega \right) \quad (4.12)$$

$$F_1 = \tanh \left\{ \min \left[\max \left(\frac{\sqrt{k}}{\beta^* \omega y}, \frac{500\nu}{y^2 \omega} \right), \frac{4\sigma_{\omega 2} k}{CD_{k\omega} y^2} \right] \right\}^4 \quad (4.13)$$

$$F_2 = \tanh \left\{ \left[\max \left(\frac{2\sqrt{k}}{\beta^* \omega y}, \frac{500\nu}{y^2 \omega} \right) \right] \right\}^2 \quad (4.14)$$

$$CD_{k\omega} = \max \left(2\rho\sigma_{\omega 2} \frac{1}{\omega} \frac{\partial k}{\partial x_j} \frac{\partial \omega}{\partial x_j}, 10^{-10} \right) \quad (4.15)$$

Regarding numerical schemes, according to [124], the equation for velocity $\langle u_i \rangle$ was spatially discretized with second-order linear upwind schemes (SOLU). For turbulence kinetic energy k and specific turbulence dissipation ω , discretization schemes

”automatic” was chosen, which resulted in the determination of appropriate schemes by Code_Saturne. For time integration, the implicit Euler method was applied based on SIMPLE algorithm. The time step Δt was 0.1 s. The gradient calculation was performed with a least squares method over extended cell neighborhood. To solve the linear system, the ”automatic” option in “Code_Saturne” was used where an appropriate solver can be automatically chosen.

Hereafter, the mean flow velocity field obtained in [124] will be used in scalar transport calculation.

• **Scalar transport phase:**

Once the average velocity is obtained from the outdoor flow simulation, pollutant dispersion is calculated based on the average flow field. In the absence of depolluting system, to determine the time-evolution cartography of the pollutant in Sense-City district on the time interval $[0, 180 \text{ s}]$, we solve the direct advection-diffusion problem defined in Eq. (3.3). As the pollutant concentration $C(\mathbf{x}, t)$ is considered herein as a passive scalar, *i.e.* non-reactive pollutant as in the articles [129, 130], the reaction term in Eq. (3.3) is taken to 0. Therefore, Eq. (3.3) can be rewritten:

$$\frac{\partial C}{\partial t} + \langle u_i \rangle \frac{\partial C}{\partial x_i} - D \frac{\partial^2 C}{\partial x_i \partial x_i} = S \quad (4.16)$$

Let us recall that the turbulent diffusion $D_t = \mu_t / (\rho S_c h)$ is deduced from airflow simulation and Schmidt number S_c . In the present work, we consider $S_c h$ to be 0.7, which is a commonly used value [113, 114]. However, it should be noted that $S_c h$ shows big variations and no global conclusion exists [131], and it depends on many factors *e.g.*, turbulence modeling, spatial location, scenarios [132].

For the scalar transport phase in this section, we use Finite Element Method with SUPG stabilization [133, 134] in the software FreeFem++ [126] to solve the direct pollutant dispersion model Eq. (4.16). Using SUPG method, the variational formulation of the direct pollutant dispersion problem reads:

$$\begin{aligned} \int_{\Omega} \frac{\partial C}{\partial t} C^* \, d\Omega &+ \int_{\Omega} (\vec{\mathbf{v}} \cdot \nabla C) C^* \, d\Omega + \int_{\Omega} \mathcal{D}(\nabla C \cdot \nabla C^*) \, d\Omega \\ &- \int_{\partial\Omega} \mathcal{D}(\nabla C \cdot \vec{\mathbf{n}}) C^* \, d\Omega + \alpha \int_{\Omega} \frac{\partial C}{\partial t} (\vec{\mathbf{v}} \cdot \nabla C^*) \, d\Omega \\ &+ \alpha \int_{\Omega} (\vec{\mathbf{v}} \cdot \nabla C) (\vec{\mathbf{v}} \cdot \nabla C^*) \, d\Omega - \alpha \int_{\Omega} \mathcal{D} \Delta C (\vec{\mathbf{v}} \cdot \nabla C^*) \, d\Omega \\ &= \int_{\Omega} S C^* \, d\Omega + \alpha \int_{\Omega} S (\vec{\mathbf{v}} \cdot \nabla C^*) \, d\Omega \end{aligned} \quad (4.17)$$

where α represents the stabilization term, and C^* denotes the test function. Regarding the time discretization, we use Euler implicit scheme. The time step is taken to $\Delta t = 0.1$ s. For the space discretization, we consider a Lagrange-Galerkin finite element tetra mesh of the domain Ω . For the numerical resolution of the systems defined in Eq. (4.17), choices of the Finite Element spaces used for the discretization are the $P0$ Lagrange elements for the velocity and $P2$ for the pollutant concentration.

• **Boundary condition and pollutant source**

Here, I denote the computational domain as Ω , the boundary domain as Γ , Γ_i as the inlet boundaries, Γ_o as the outlet boundaries, and $\Gamma_w = \Gamma \setminus (\Gamma_i \cup \Gamma_o)$ as the wall boundaries.

In the flow simulation in Sense-City district, according to [124], the boundary conditions for the ventilation systems were determined using measurement by a 1D hot wire anemometer. Table 4.1 provides the total volumetric airflow rate (m^3/s) for each ventilation system. The two fan blocks are equipped with dehumidification functions, resulting in a lower volumetric airflow rate $5.7m^3/s$ compared to the other fan blocks. Additionally, the volumetric airflow rate in the forced-air ducts varies between the upper and lower pipes. Other surfaces are given no-slip conditions.

Table 4.2 summarize the boundary conditions of ventilation systems for the scalar tracer Dirichlet conditions are imposed at the inlet Γ_i of ventilation systems, and Neumann conditions are given the extraction ducts Γ_o and elsewhere Γ_w . The initial concentration C_i in the domain Ω is set to zero.

Ventilation system	Volumetric airflow rate
Extraction ducts (Γ_o)	-15.3 (m^3/s)
Upper forced-air ducts (Γ_i)	6.9 (m^3/s)
Lower forced-air ducts (Γ_i)	8.4 (m^3/s)
Front fans with reduced airflow (Γ_i)	5.7 (m^3/s)
Rear fans with reduced airflow (Γ_o)	-5.7 (m^3/s)
Front regular fans (Γ_i)	66.0 (m^3/s)
Rear regular fans (Γ_o)	-66.0 (m^3/s)

Table 4.1: Volumetric airflow rates of the ventilation systems in the climatic chamber [124].

As mentioned before, the pollutant source is considered here as a parallelepiped

Ventilation system	Pollutant concentration
Extraction ducts Γ_o	Neumann
Upper forced-air ducts Γ_i	Dirichlet ($C = 0$)
Lower forced-air ducts Γ_i	Dirichlet ($C = 0$)
Front fans with reduced airflow Γ_i	Dirichlet ($C = 0$)
Rear fans with reduced airflow Γ_o	Neumann
Front regular fans Γ_i	Dirichlet ($C = 0$)
Rear regular fans Γ_o	Neumann

Table 4.2: Boundary condition for pollutant emission of the ventilation systems in the climatic chamber.

volumic source ($0.5 \times 0.5 \times 0.5 = 0.125 \text{ m}^3$) placed on the road between the concrete building and two houses (see the red rectangular in Fig. 4.4) to mimic a continuous release of a passive scalar.

The parallelepiped volume of the source Ω_s is expressed by the space function f_s :

$$f_s(\mathbf{x}) = \begin{cases} 1 & \text{for } \mathbf{x} \in \Omega_s \\ 0 & \text{elsewhere} \end{cases} . \quad (4.18)$$

The emission magnitude for source term $S(x)$ [$\mu\text{g}/\text{s}$] is obtained by product of an amplitude [$\mu\text{g}/\text{m}^3/\text{s}$] $\times f_s(x)$ [m^3]. Now, the source amplitude is taken to $2000 \mu\text{g}/\text{m}^3/\text{s}$. The volume of the source being of 0.125 m^3 , the considered emission is $250 \mu\text{g}/\text{s}$. Let us note that it corresponds to the order of magnitude of NOx mean emission at $20\text{km}/\text{h}$ for EURO 6 passengers cars with small petrol engine, *i.e.* $0.039\text{g}/\text{km}$ emission factor that gives a value of $217 \mu\text{g}/\text{s}$ [135].

- **Mesh configuration for outdoor simulation**

In the previous study [124], a mesh convergence study was conducted concerning airflow characteristics to select an appropriate mesh. Unstructured mesh was generated using the open-source software SALOME [136] with the automatic mesh generator NETGEN. We further refine this mesh between the concrete building and the two houses where we defined the position of the source emission (see Fig. 4.6). The mesh has a total cell number of about 3,947,186. The size characteristics of mesh are summarized in table 4.3.

4.2.2.2 Result: outdoor pollutant concentration cartography

- **Average flow field**

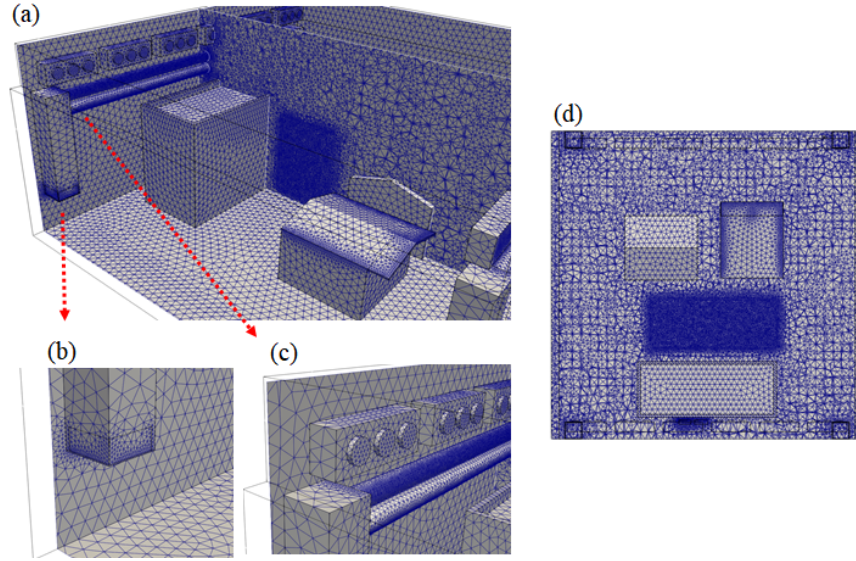


Figure 4.6: Mesh configuration of numerical mock-up of Sense-City: (a) overview of mesh, (b) local mesh for extraction duct, (c) local mesh for fan and forced-air duct, and (d) overview at 1.5m height from the top.

Maximum mesh size [m]	0.4
Local mesh size on fans [m]	0.1
Local mesh size on forced-air holes [m]	0.03
Local mesh size on extraction duct [m]	0.3
Refined area between the building and houses [m]	0.1
Total number of cells	3,947,186

Table 4.3: Cells size of meshes used for pollutant dispersion study.

Firstly, let us briefly recall the airflow characteristics in Sense-City from [124]. Fig. 4.7 illustrates the average flow field. Looking at the flow field near the pollutant source, the airflow direction is from the center of the Sense-City towards the concrete building and then separates to the left and right after colliding with the building (Fig. 4.7 (a)). Furthermore, examining the vertical section, the flow generated by the fans on both sides collides almost the upper center of the Sense-City and then moves downwards (Fig. 4.7 (c)). This is similar to street canyon flow. Nevertheless, note that in a real street canyon, airflow goes into the street canopy after separation from the top of the building, but Sense-City does not reproduce that flow properties (shear layer characteristic). Once the airflow travels downwards, it passes between

the building and houses and eventually rises along the concrete building walls (Fig. 4.7 (b)).

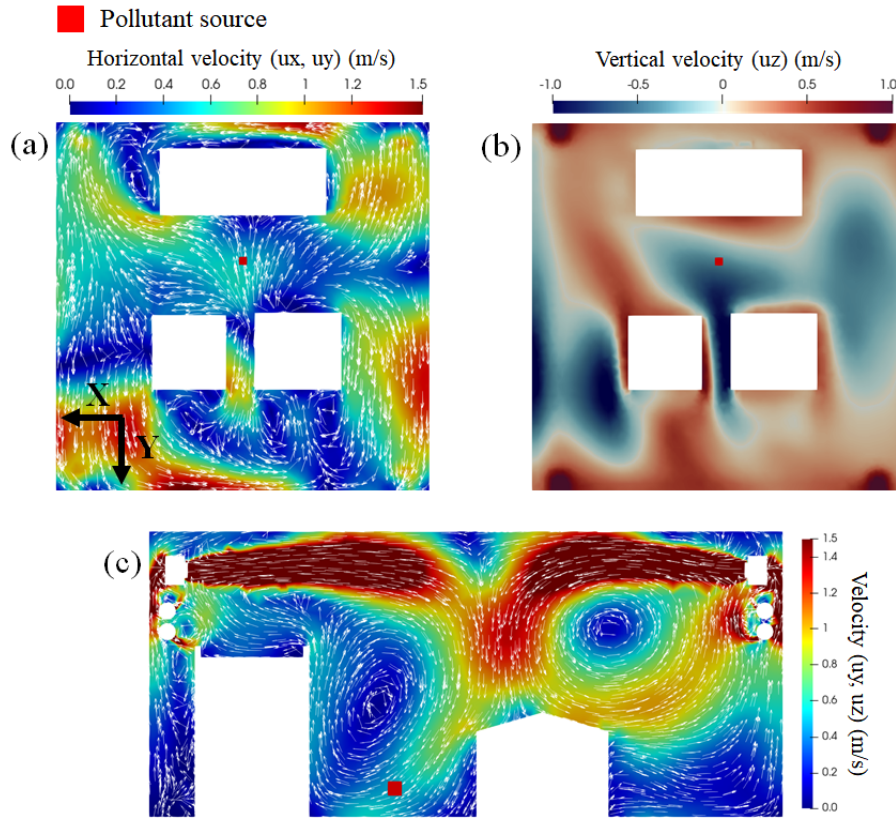


Figure 4.7: Average velocity field from [124]: (a) horizontal velocity magnitude and vector at $z = 1.5\text{ m}$, (b) vertical velocity at $z = 1.5\text{ m}$ (top right) and (c) velocity and vector on cross-section at $x = -1\text{ m}$. The red box shows the source position.

• Outdoor pollutant concentration

Fig. 4.8 shows the spatial maps of pollution in Sense-City at the pedestrian level $z = 1.5\text{ m}$ and an overview perspective for different times ($t = 5\text{ s}$; $t = 30\text{ s}$; $t = 60\text{ s}$). The blue contour surface represents $9\text{ }\mu\text{g}/\text{m}^3$. Since the concentration is almost unchanged after 60 seconds, only the pollutant maps from $t = 0\text{ s}$ to $t = 60\text{ s}$ are given (see $t = 30\text{ s}$ and $t = 60\text{ s}$).

Along the average flow path shown in Fig. 4.7, pollutants are transported from the pollution source toward the concrete building and, after hitting the building wall, propagate towards the left, right and upward directions. Regarding the horizontal

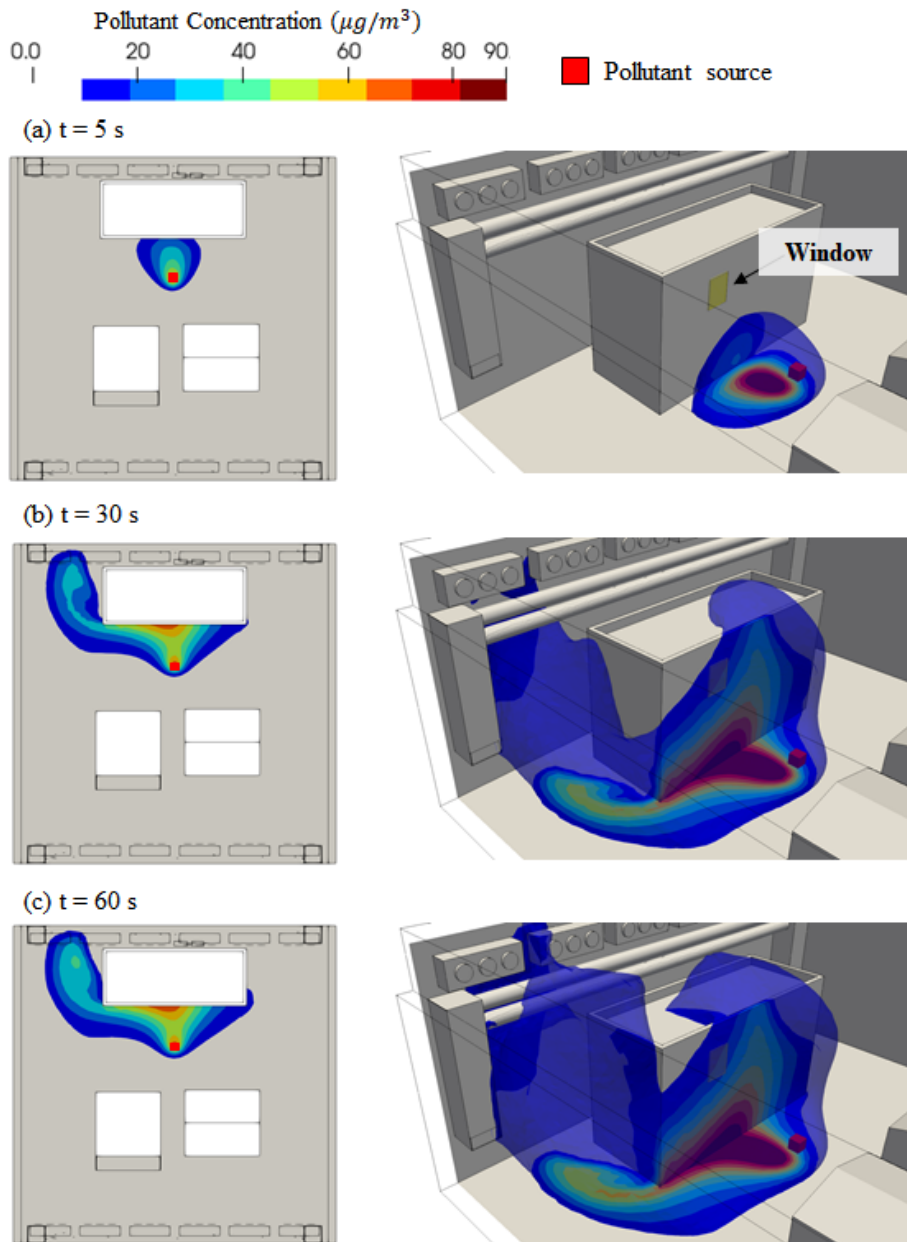


Figure 4.8: Pollutant concentration ($\mu\text{g}/\text{m}^3$) at (a) $t = 5\text{ s}$, (b) 30 s and (c) 60 s : the x-y plane at $z = 1.5\text{ m}$ (left) and 3D view (right). The blue contour surface represents $9\ \mu\text{g}/\text{m}^3$. The yellow rectangular on the building surface represents the window position of the 1st floor.

movement, the pollutants predominantly flow towards the extraction ducts on the left-hand side (see Fig. 4.8 at $t = 30\text{ s}$ and $t = 60\text{ s}$). This left-right asymmetry is due to the asymmetry airflow rates of the fans, described in Section 4.2.2.1. From Fig. 4.8, it is worth noting that a non-negligible part of the pollutant concentration, *i.e.* about $20\text{ }\mu\text{g}/\text{m}^3$, reaches Mast 6, which is placed at the front window at the 1st floor of the building, depicted by the yellow rectangular in Fig. 4.8. Therefore, it is visually evident that outdoor pollutants impact indoor air quality in Sense-City if the window is open.

To emphasize the non-homogeneous nature of the concentration level in the district, we extracted from the CFD numerical simulations the local pollutant concentration in the several mast positions defined in Fig. 4.4. The time evolution of the concentration at the masts is given in Fig. 4.9. As the concentration was negligible at Mast 7, 8, 9 and 10, they are not represented in Fig. 4.9. Since the scalar transport is calculated on the average flow, the pollution concentrations on most of the mast show a rapid increase within the first 20 seconds through the dominant average flow, followed by a gradual increase. If calculations are performed on the instantaneous flow field, the pollutant concentration is expected to exhibit a slower increase with many fluctuations. Nevertheless, even if the pollutant dispersion simulation is carried out on the average flow, the value when the pollutant concentration reaches a sufficiently stable state is deemed comparable to the value obtained through calculations on the instantaneous flow field. As a result, when considering the average airflow, the pollutant concentration can be very different from one side of the road to the other, which is a typical street canyon phenomenon. Indeed, Fig. 4.9 shows that the concentration at Mast 2 (on the building sidewalk) is 20 times higher than the one at Mast 1 (near the two houses). Even on the building sidewalk, the pollutant concentration varies significantly, *i.e.* from $10\text{ }\mu\text{g}/\text{m}^3$ to $60\text{ }\mu\text{g}/\text{m}^3$ according to the spatial position (see Masts 2, 3 and 4).

4.2.2.3 Direct CFD modeling for outdoor/indoor pollutant transfer with decoupled approach

The next step is to simulate indoor pollution due to the transfer of outdoor pollutants via natural ventilation. When using the coupled and decoupled approaches, both have advantages and disadvantages. The decoupled approach is convenient here for operational purposes: reduction of computational time and cost, separated geometry and mesh for outdoor and indoor environments that is easy to make. To simulate indoor pollutant dispersion with the decoupled approach, we use the results of the previous outdoor simulation and extract the pressure at the windows'

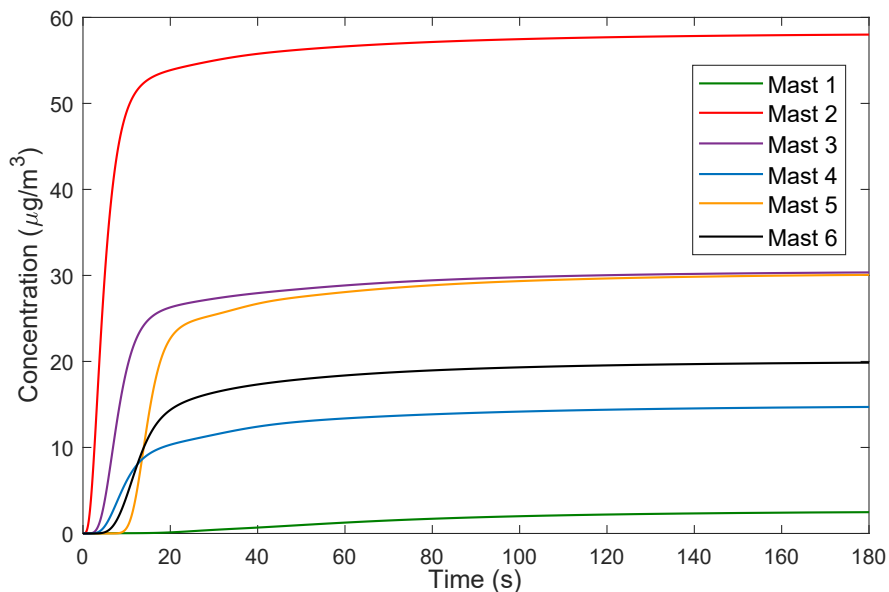


Figure 4.9: Pollutant concentration from the simulation at the masts of Sense-City district as a function of time - no depolluting panels.

surfaces. A discussion on the accuracy of the coupled and decoupled approaches will be presented in the later section. The results of this subsection were presented in [137].

- **Indoor numerical mock-up**

Fig. 4.10 illustrates the geometry of the target indoor environment located on the 1st floor of the concrete building including the three desks and one locker. The size of the room is $9.6 \text{ m} \times 3.6 \text{ m}$ and a height of 2.3 m . To simplify the geometry, no other furniture is considered. Two windows: the front and rear window, are called here inlet and outlet (see Fig. 4.10 (b)). From the previous study [124], we define a window with a higher pressure as the inlet. The floor is separated by a movable wall, and a 1 m passage is kept open between the main and next room in this case.

- **Numerical set-up for indoor airflow and scalar transport**

The governing equations are identical to that of the outdoor simulation where the spatial terms are discretized with SOLU, the time-advancement scheme is first-order, and SIMPLE algorithm is applied for pressure-velocity coupling. Time step is a constant at 0.1 s . The total simulation period is 30 min . The average velocity field

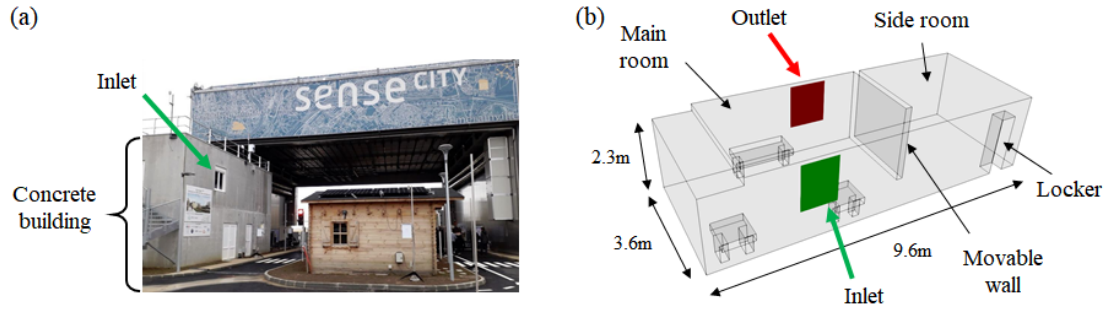


Figure 4.10: Geometry of indoor region: (a) picture of Sense-City, (b) mock-up indoor geometry.

used to solve the advection-diffusion equation is obtained from the last 20 minutes of the airflow simulation. Turbulent Schmidt number is chosen to be 0.7 which is identical to the district simulation.

• Boundary condition

At the inlet and outlet, the time-averaged pressure difference between the windows, 0.633 Pa, is imposed as Dirichlet pressure conditions, so airflow inside the room is driven only by pressure difference. Hence, simulated airflow always travels from the inlet to the outlet. At the inlet and outlet, Neumann (zero-gradient) condition is imposed for velocity. The boundary conditions for the wall, floor, ceiling and furniture are set to no-slip conditions.

Regarding the boundary condition for scalar transport, Dirichlet concentration at the constant magnitude of 1 is imposed at the inlet over the entire studied time interval. The numerical solution of this problem is called the base solution hereafter. Thanks to the linearity of the advection-diffusion equation according to the concentration according to the constant concentration magnitude, actual pollutant concentration can be calculated by multiplying the base solution by the inlet concentration magnitude obtained from the outdoor simulation. Let us note that we consider herein a time-constant concentration at the inlet, i.e. Heaviside function. At the outlet and walls, zero-gradient condition is used.

• Mesh configuration for indoor simulation

Fig. 4.11 provides the mesh generated in SALOME. Mesh density varied in each room; refined mesh in the main room and coarse mesh in the side room (for the name

of the room, see Fig. 4.2). For computational stability, hexa mesh is employed only near the inlet and outlet, and tetra mesh fills other spaces. The sizes of the mesh are 0.1 m at the inlet and outlet, 0.12 m in the main room and 0.16 m in the side room. The total number of mesh is 255,270. To determine the mesh size, a grid convergence study was conducted.

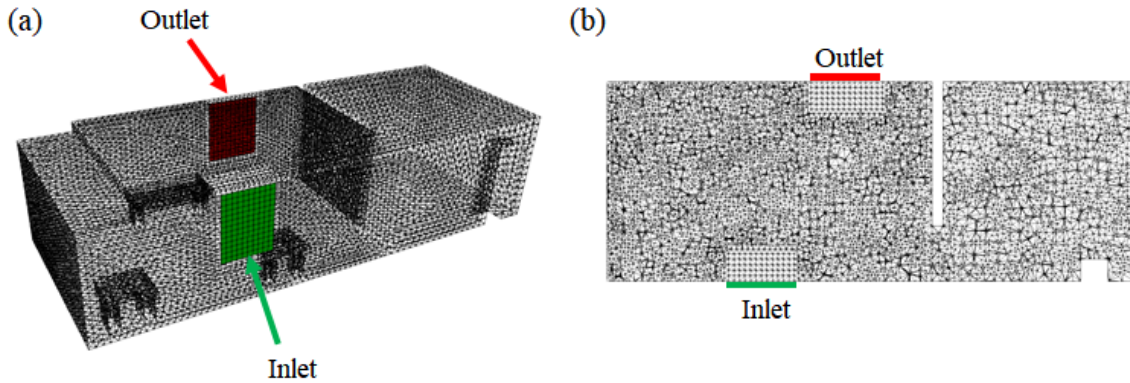


Figure 4.11: Mesh configuration for the indoor simulation: (a) overview, (b) horizontal view.

4.2.2.4 Result: indoor pollutant concentration cartography and parametric study

• Indoor flow field and pollutant concentration

Fig. 4.12 shows the average velocity vector calculated from the last 20 min of the simulation. The flow direction from the inlet window heads toward the outlet window, and then the flow is separated into two directions creating two large three-dimensional circulations in the main room. Thus, the main airflow is along the perimeter (wall) of the room. Accordingly, on the other hand, the center of the room has lower velocities compared to the perimeter. In the side room, the velocity magnitude is less than 0.3 m/s everywhere. Near the movable wall, the flow is oriented upward (z -direction) from the bottom with a magnitude of about 0.7 m/s (see Fig. 4.12 (a)) and turns into the next room through the 1 m opening between the rooms.

When considering the average flow, the pollutants are transported as can be seen in Fig. 4.13. Let me recall that as a unitary value of the concentration is imposed

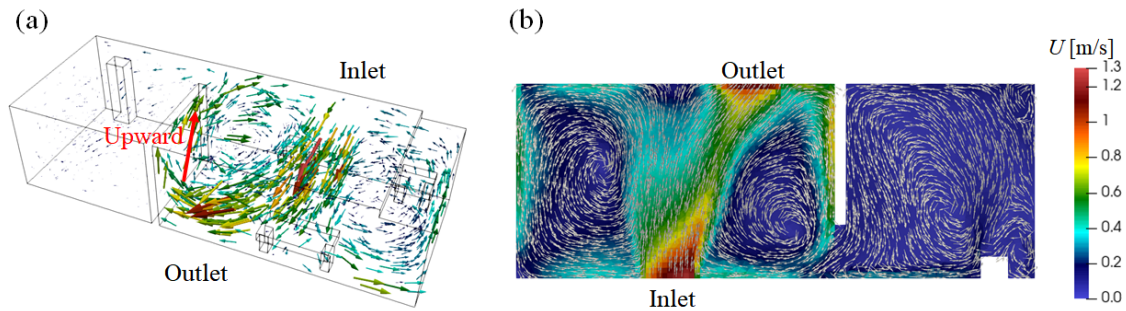


Figure 4.12: Average velocity field in the 1st floor of the concrete building obtained by the decoupled approach: (a) overview view, (b) horizontal view.

at the inlet window the figure has no unit. On the one hand, once the pollutants reach the outlet window, they propagate along the wall. On the other hand, regions far away from the wall (e.g. the center of the two three-dimensional circulations in 4.12 (a)) are not relatively contaminated at least until $t = 100$ s. Finally, they enter the side room, especially from the top of the opening pathway.

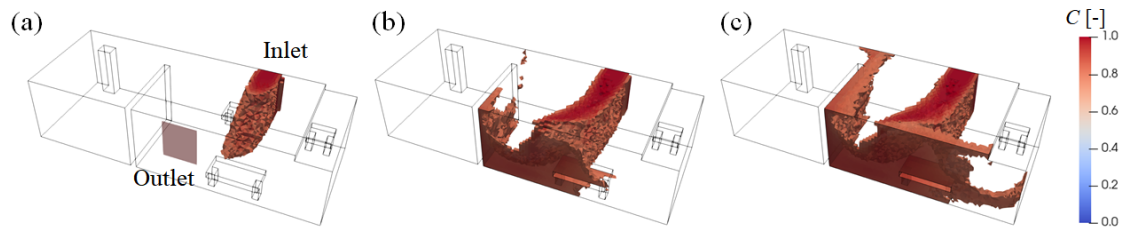


Figure 4.13: Time evolution of pollutant dispersion obtained by the decoupled approach: (a) $t=4$ s, (b) $t=60$ s, (c) $t=100$ s.

Fig. 4.14 depicts the time evolution of concentration at 4 points (see Fig. 4.14 (a)) to show the sequence of contamination, i.e., where it is contaminated firstly, secondly, etc. Point 1 is located in the center of the main room where the main flow occurs, Point 2 near the movable wall with high velocity (i.e. 0.7 m/s), Point 3 in the center of the 3D circulation in the main room, and Point 4 in the side room. Overall, at all points except for Point 4, the concentration increased significantly at first 5 ~ 10 min. Nevertheless, looking at the details, Point 1 reaches high pollution within a

few minutes as this point is in the main flow between the inlet and the outlet. Even though the positions of Point 2 and Point 3 are close to each other, their increasing trends of pollution are different from each other. Point 3 takes more time to reach a constant concentration at 1, than Point 2. Thus, I can state that air pollutants are propagated from the inlet window, the perimeter to the center of the room gradually. Point 4 rises more slowly. This is due to the time lag for the pollutant to reach Point 4. After about 30 min, every point reaches the same pollutant level. Consequently, after 30 min of the window openings, pollutant concentration may be homogeneous in the building room. when considering a time-constant concentration at the inlet.

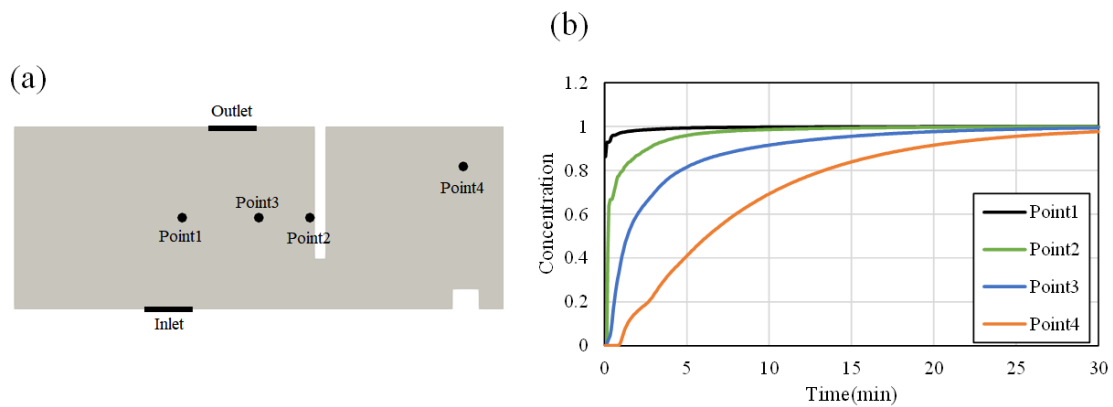


Figure 4.14: Time history of pollutant concentration on the probe points: (a) locations of probe points and (b) time history of the pollutant concentration.

- **Parametric study on indoor pollutant concentration**

From the outdoor pollutant concentration distribution, it is apparent that pollutants reach the window surfaces, meaning that pollutants can travel indoors and deteriorate indoor air quality if the window is open (natural ventilation). Supposing that there are no indoor pollutant sources and only outdoor pollutants influence indoor air quality, it can be expected that indoor air quality to be highly influenced by factors at the inlet window, which are dependent on outdoor parameters, e.g., airflow, pollutant concentration, surrounding buildings, window size and Schmidt number. To investigate the sensitivity of indoor air quality against parameters at the inlet window, a parametric study is conducted. In this context, the decoupled approach is suitable and used for the parametric study on indoor air quality.

- **Input parameter**

The input parameters considered in the sensitivity analysis are the pressure difference between the windows, which affects the indoor airflow, the pollutant concentration at the inlet and Schmidt number, which influences the pollutant diffusion. Based on the conditions used in the previous indoor simulation, the input parameters are modified by $\pm 10\%$ to create new input conditions. Thus, to limit the number of CFD calculations, I conduct a local sensitivity analysis (not a global sensitivity analysis like Morris and Sobol methods). In the previous scenario, the pressure difference was 0.633 Pa, the pollutant concentration at the inlet surface was 1, and the Schmidt number was 0.7. When each parameter is increased by +10%, the values become 0.696 Pa, 1.1, and 0.77, respectively. Conversely, decreasing each parameter by -10% results in values of 0.569 Pa, 0.9, and 0.63. To evaluate the rate of change on quantities of interest, we consider a non-dimensional indicator of pollutant level I_{dif} obtained from the first 15 min simulation by

$$I_{dif} = \frac{I_i - I_{ref}}{I_{ref}} \quad (4.19)$$

where I_{ref} and I_i are obtained by

$$I_{ref} = \frac{1}{t_s} \int_0^{t_s} C_{ref} dt \quad (4.20)$$

$$I_i = \frac{1}{t_s} \int_0^{t_s} C_i dt \quad (4.21)$$

where C_{ref} represents the reference concentration at a point of interest obtained considering the reference input parameter values: the pressure difference between the inlet and outlet is 0.633 Pa, Schmidt number is 0.7 and the inlet concentration magnitude is 1.0. C_i represents the numerical concentration at the point of interest where an input parameter has been changed by 10% compared to its reference value. For instance, Pre_{min} indicates a case with a pressure difference of 10% decrease, Sch_{max} shows a case with Schmidt number of 10% increase, and $Pre_{min} - Sch_{max}$ shows a case combining both above conditions. 15 min is now 15min, which is time duration of the simulations.

• Result and discussion

Table 4.4 shows the result of the parametric study in terms of the pressure difference and Schmidt number on the three probe points of interest: Points 1, 3, 4. As explained before, thanks to the linearity of the advection-diffusion equation, it is easy to estimate without simulations the impact of inlet pollutant concentration magnitude. Namely $\pm 10\%$ modification of time-constant pollutant concentration at the inlet window will lead to $\pm 10\%$ variation of the indicator. At Point 1, we

observe that it is not sensitive to the change of the pressure difference and Schmidt number. This can be attributed to the short time duration before reaching the high pollutant concentration even with the changed input variables. For Point 3 and Point 4, it is found that the pressure difference has a relatively large impact compared to Schmidt number. However, recalling that the change of $\pm 10\%$ of the inlet pollutant concentration gives $I_{dif} = \pm 10\%$, the inlet pollutant is the most influential parameter. Therefore, to obtain an accurate prediction of the indoor pollutant level, one needs to get relevant pollutant concentrations at the inlet opening, namely outdoor concentration at window openings by prior simulations or measurements. In addition, from the perspective of improving indoor air quality, reducing indoor pollutant concentration at windows results in improvement of the indoor air quality.

	Point 1		Point 3		Point 4	
	$I_{ref} = 1.485$		$I_{ref} = 1.194$		$I_{ref} = 0.768$	
	I_i	$I_{dif} (\%)$	I_i	$I_{dif} (\%)$	I_i	$I_{dif} (\%)$
Pre_min	1.489	0.29	1.145	4.12	0.797	3.75
Pre_max	1.479	0.39	1.226	2.65	0.761	0.87
Sch_min	1.478	0.48	1.217	1.86	0.776	1.01
Sch_max	1.487	0.11	1.189	0.42	0.772	0.56
Pre_min-Sch_min	1.489	0.26	1.174	1.68	0.730	4.95
Pre_min-Sch_max	1.492	0.45	1.170	1.99	0.733	4.57
Pre_max-Sch_min	1.481	0.28	1.242	4.00	0.716	6.74
Pre_max-Sch_max	1.485	0.03	1.235	3.4	0.721	6.10

Table 4.4: Indicator of direct sensitivity analysis: I_{dif} , I_{ref} , I_i at three points.

4.2.3 Remediation stage: smart placement of depolluting panel

4.2.3.1 Selecting quantity of interest

The next step is to select critical areas, which are highly polluted areas, from the outdoor and indoor cartography. As a reminder, the criteria for selecting such areas are twofold: it has a high pollutant concentration and it must be a location where people spend time. For instance, on a road, there are many pollutants from vehicles, but people do not usually stay longer on the road, thereby disqualifying it as a critical area. Let us note that the results of the following subsections (4.2.3.1 ~ 4.2.3.4) are presented in [138].

From the outdoor and indoor pollution maps in Sense-City, two critical polluted areas are selected:

- The first area (the red rectangular in Fig. 4.15) is located on the sidewalk near the concrete building. The area is defined by the subdomain

$$\Omega_{q1} = \{x \in [-5\text{m}, 5\text{m}], y \in [-5.5\text{m}, -4\text{m}], z \in [1\text{m}, 2\text{m}]\}$$

- The second area (the green rectangular in Fig. 4.15) corresponds to the vicinity of the front window on the 1st floor. As discussed in the parametric study, enhancing the pollutant level at the window leads to an improvement in indoor air quality. The area is defined by the subdomain

$$\Omega_{q2} = \{x \in [1.5\text{m}, 2.5\text{m}], y \in [-5.5\text{m}, -5.3\text{m}], z \in [3.7\text{m}, 5\text{m}]\}$$

For each high-polluted area, we define a quantity of interest \mathcal{J}_i , $i \in \{1, 2\}$ (see Eq. (3.5)) associated to the spatial-averaged concentration over the whole time interval $[0, 180\text{s}]$. Hence, the space function $f_{q_i}(\mathbf{x})$, $i \in \{1, 2\}$ involved in Eq. (3.5) to extract the averaged concentration in the critical areas Ω_{q_i} , $i \in \{1, 2\}$ is given by

$$f_{q_i}(\mathbf{x}) = \begin{cases} 1/\text{vol}(\Omega_{q_i}) & \text{for } \mathbf{x} \in \Omega_{q_i} \\ 0 & \text{elsewhere} \end{cases} . \quad (4.22)$$

and the time function for both quantities of interest is $\xi(t) = 1/T$ on the whole time interval $[0, T = 180\text{s}]$.

In the configuration without depolluting panels, the numerical estimation of the two quantities of interest are:

$$\begin{cases} \mathcal{J}_1 = 33.0 \mu\text{g}/\text{m}^3 \\ \mathcal{J}_2 = 17.9 \mu\text{g}/\text{m}^3 \end{cases} \quad (4.23)$$

4.2.3.2 Computational setting for adjoint modeling

After defining the QoIs, the adjoint problem (see Eq. (3.9)) needs to be solved. FreeFem++ is retained for the adjoint solver. All the numerical schemes are identical to the direction simulation (see Subsection 4.2.2.1).

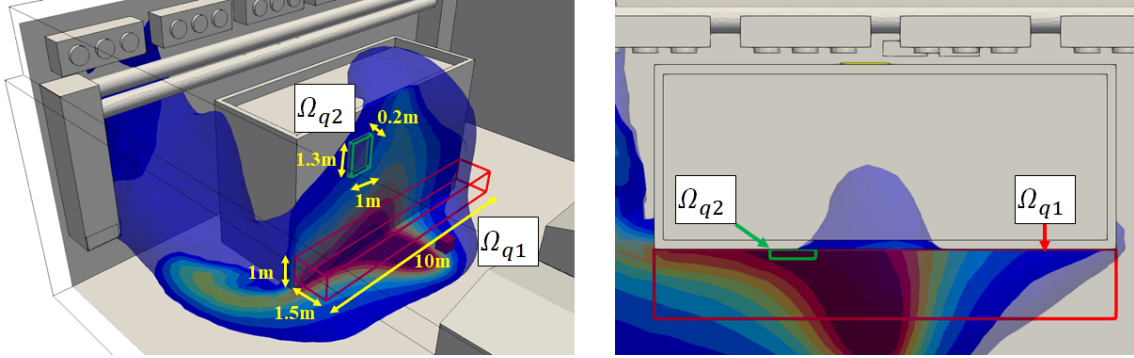


Figure 4.15: Selected QoIs: (i) sidewalk (red color) and (ii) window (green color).

4.2.3.3 Adjoint sensitivity indicator and smart placement of depolluting panel

Fig. 4.16 shows the adjoint concentration associated with \mathcal{J}_2 only on the surfaces of the domain. As illustrated in Fig. 4.16 for the quantity of interest \mathcal{J}_2 (*i.e.* the mean pollutant concentration at the building window (see the green area in Fig. 4.15)), the adjoint problem corresponds to a backward in time advection-diffusion problem where a virtual source is emitted in the quantity of interest's area (*i.e.* in this case, the virtual source is the green area in Fig. 4.15). Contrary to the direct problem defined in Eq. (3.6), the adjoint problem has a final condition in time. Let us note that the adjoint solution corresponds to a sensitivity function as regards of the chosen QoI. Thus, if the adjoint solution is almost null in a part of the domain, it means that actions in that part of the domain, like reducing pollutant emission or placement of depolluting panels, will have no influence on the considered QoI.

To smartly place depolluting panels for improving the chosen QoIs, the spatial sensitivity indicator defined in Eq. (3.11) is computed. It is obtained from the product of the pollutant concentration field (direct concentration) and the adjoint concentration. Hence, the depolluting panels are to be positioned in areas where both direct and adjoint concentrations are high. In Fig. 4.17, the sensitivity indicator maps are shown for the two selected QoIs: mean pollutant concentration values on the building sidewalk (\mathcal{J}_1) and at the building window (\mathcal{J}_2). The maximum value of the sensitivity indicator I_1 is about 25 whereas the value of I_2 can exceed 50. It means that placing a given surface in m^2 of depolluting panels in the most sensitive areas can have more impact for reducing the pollutant concentration at the building window (\mathcal{J}_2) than the one at the building sidewalk (\mathcal{J}_1). From Fig. 4.17, we remark

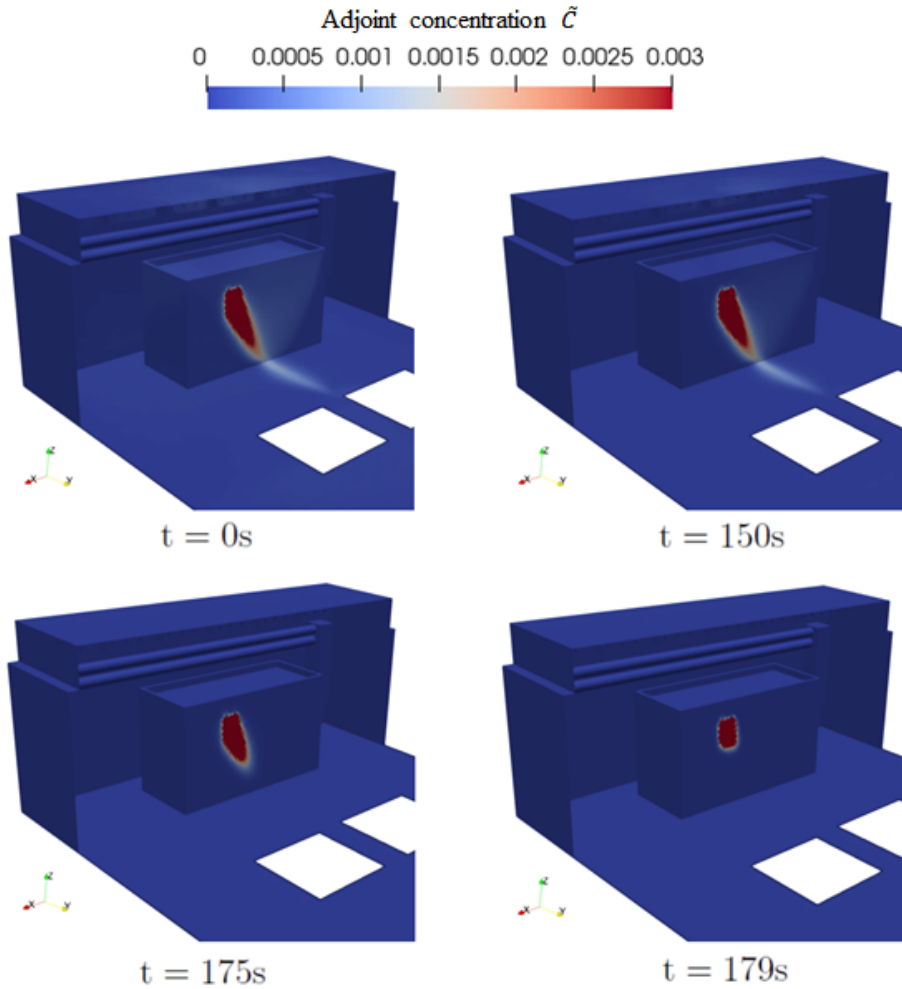


Figure 4.16: Adjoint solution represented at the surfaces of Sense-City district - Quantity of interest \mathcal{J}_2 associated to the pollutant concentration at the vicinity of the window building.

that depolluting panels have to be positioned on the bottom of the building surface, and on a restricted part of the sidewalk and on the road to reduce the quantity of interest \mathcal{J}_1 (sidewalk pollutant concentration). Concerning the pollutant concentration at the building window \mathcal{J}_2 , air pollution exposures can be decreased by placing panels below the window on the building facade, and on a portion of the sidewalk and on the road. We recall that the placement of depolluting panels is determined

thanks to the knowledge of the pollutant dispersion via the airflow.

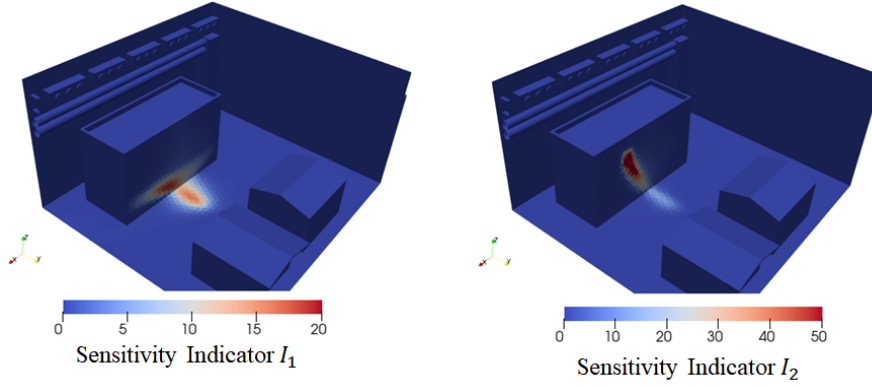


Figure 4.17: Sensitivity indicator maps I_1 associated to the pollutant concentration at the building sidewalk \mathcal{J}_1 (at left) and I_2 associated to the pollutant concentration at the building window \mathcal{J}_2 .

In conclusion, we propose to smartly placed depolluting panels to decrease the pollutant concentrations for both quantities of interest \mathcal{J}_1 and \mathcal{J}_2 using the spatial sensitivity indicators I_1 and I_2 . In Fig. 4.18, the two sensitivity indicators are displayed on the most influential surfaces, *i.e.* the building walls, the building sidewalk, and the road. Three depolluting panel areas, noted DP1, DP2, and DP3, are determined by taking the sensitivity threshold value to 5. The lowest is the sensitivity threshold value, highest is the deployment surface of the panels. In practice, the threshold value can be chosen to get a deployment surface of panels strictly less than the maximum deployment surface allowed by the urban planner. In the Sense-City application, the total surface of depolluting panels corresponds to $29.7m^2$. Let us give more details about the three optimal depolluting areas represented in Fig. 4.18:

- “DP1” is located on the building wall above the window. It is defined by $\{x \in [-0.3m, 2.7m], y = -5.5m, z \in [2m, 3.7m]\}$. As shown in Fig. 4.17, panels in “DP1” allow mainly to improve the air quality at the building window and thus to reduce outdoor/indoor transfer of pollutant;
- “DP2” is located on the bottom building wall. It is given by $\{x \in [-3.4m, 4m], y = -5.5m, z \in [0m, 2m]\}$. Panels in this area contribute to improve both quantities of interest;

- “DP3” is placed on a part of the sidewalk and the road, and it is defined by $\{x \in [-1.9\text{m}, 1.3\text{m}], y \in [-2.5\text{m}, -5.5\text{m}], z = 0\text{m}\}$. As for “DP2”, panels in “DP3” can reduce the pollutant concentrations on the building sidewalk and window.

For operational urban purposes, we preferred rectangular areas to more complex shapes.

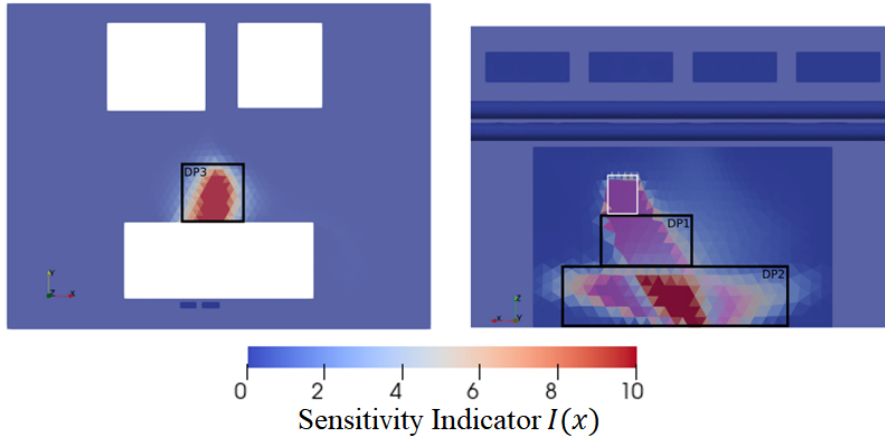


Figure 4.18: Smart placement of depolluting panels, indicated by black rectangles, in Sense-City district on the road and the sidewalk (at left) and on the building facade (at right) to improve the quantities of interest \mathcal{J}_1 and \mathcal{J}_2 - White rectangular denotes the window position.

4.2.3.4 Numerical validation of the optimized placement of depolluting panels

In the previous section, we determined smart placement of depolluting panels to improve both quantities of interest \mathcal{J}_1 and \mathcal{J}_2 using the spatial sensitivity indicator defined in Eq. (3.11). To validate numerically the relevance of the predicted position of panels, the pollutant concentration in Sense-City and the QoIs are evaluated by solving the advection-diffusion direct problem (see Eq. (3.6)) in three different configurations of deployed panels:

- “no depolluting panel” - it corresponds to the initial district urban planning, *i.e.* in the absence of depolluting device. It was detailed in Sections 4.2.2.2 and 4.2.3.1;

- “optimal depolluting panel placement” - the depolluting panels DP1, DP2 and DP3, determined from the smart placement strategy in Section 4.2.3.3, are integrated in the Sense-City district;
- “bad depolluting panel placement” - depolluting panels are massively deployed on all the district roads of Sense-City district (see Fig. 4.4) except in the sensitive area DP3.

For these three urban planning configurations, we compute the quantities of interest \mathcal{J}_1 (mean pollutant concentration at the building sidewalk) and \mathcal{J}_2 (mean concentration at the building window). The numerical results are summarized in Table 4.5. In the case of “optimal depolluting panels placement”, different values of the reaction rate $k(m/s)$ of the depolluting panels are investigated for all the panels DP1, DP2, and DP3. If the reaction rate $k(m/s)$ of the depolluting panels is less or equal to $0.01(m/s)$, the reduction of the pollutant concentration in the areas of interest is not significant, *i.e.* less than $2\mu g/m^3$. As predicted from the sensitivity indicator in Fig. 4.17, the smart placement of depolluting panels has more impact on the improvement of the air quality at the building window (\mathcal{J}_2) than the one on the building sidewalk (\mathcal{J}_1). Table 4.5 confirms this expectation. Indeed, when considering depolluting panels (DP1,DP2,DP3) with $k = 1(m/s)$, the quantity of interest \mathcal{J}_2 decreases by about $10 \mu g/m^3$ (-59% variation) whereas the decrease is less than $5 \mu g/m^3$ (-14% variation) for the quantity of interest \mathcal{J}_1 . According to the study of the airflow in the Sense-City district [124], the pollutant may pass closer to the district surfaces (road, sidewalk, and building surfaces) for the trajectory between the source and the building window than the one between the source and the sidewalk. In summary, depolluting panel strategy will not be efficient if the pollutant does not pass close to district surfaces.

In the last configuration noted as “bad depollution placement”, the panels are largely deployed on all the road surfaces of the Sense-City district except the area DP3. Hence, it represents $172m^2$ of depolluting panels over a total ground surface of $328m^2$. Even for a high value of depolluting panel reaction rate $k(m/s)$, *i.e.* $k = 1(m/s)$, Table 4.5 shows that a massive deployment of panels can result in no improvement of the air quality in the areas of interest when the panels are badly positioned. In conclusion, the use of district airflow in numerical strategies can allow the design of efficient urban planning to improve the air quality in critical areas with a reduced surface area of depolluting panels.

Configuration		\mathcal{J}_1 ($\mu\text{g}/\text{m}^3$)	\mathcal{J}_2 ($\mu\text{g}/\text{m}^3$)
“No depolluting panel”	-	33.0	17.9
“Optimal depolluting panel placement”	$k = 0.01(\text{m}/\text{s})$	32.5	16.6
	$k = 0.1(\text{m}/\text{s})$	30.4	11.4
	$k = 1(\text{m}/\text{s})$	28.3	7.3
“Bad depolluting panel placement”	$k = 1(\text{m}/\text{s})$	33.0	17.9

Table 4.5: Numerical values of the quantities of interest in different urban planning configurations for Sense-City district, k denotes the reaction rate of the depolluting panels.

4.3 Study of the interaction between outdoor and indoor air quality through simulation and experiment

In this section, the interaction between outdoor and indoor air quality within Sense-City is investigated using simulations and full-scale measurements. As the pollutant dispersion largely depends on the airflow field, firstly I focus on the comparison between the simulation and measurements for airflow. An outdoor airflow comparison in Sense-City has already been done in [124], which shows a satisfactory agreement between the simulation and the measurement. Therefore, in my Ph.D., I explore the indoor airflow induced by natural ventilation in the Sense-City concrete building. Additionally, the study compares and discusses the accuracy and limitations of the coupled and decoupled approaches for the interaction between outdoor and indoor airflow. Finally, a pollutant dispersion experiment was designed and conducted in Sense-City to measure CO_2 concentration and to compare with the simulations.

4.3.1 Airflow validation

4.3.1.1 Experimental set-up for indoor airflow measurement with 3D anemometer

In the full-scale experiment conducted on 21st June 2022, a 3D anemometer “CSAT3B” from Campbell Scientific company is used to measure the flow velocity inside the room on the first floor of the concrete building. Two windows (the green and red color in Fig. 4.19) are opened, through which airflow enters the room from the outdoors. The forced ventilation, heating and cooling systems of the concrete building are turned off during the experiment to only study natural ventilation phenomena.

Let us recall that airflow is forced by the climatic chamber of Sense-City. The ventilation system settings of the climatic chamber remain the same as those used in [124]. The climatic chamber’s ventilation system of the Sense-City was activated few hours before starting the measurement to allow the airflow in the climatic chamber and indoor environment to be fully developed. We recall that inside the rooms on the first floor, there is a removable wall with an approximately 1 m opening that separates the two rooms. There are three desks and one locker in the room. Only the two windows serve as connections between the indoors and outdoors, while all other doors and ventilation systems remain closed. The outdoor air temperature during the measurements is maintained at a constant 20°, and the humidity is 60 ~ 70 % using Sense-City climatic chamber. Sun and rain are not taken into account.

Airflow speeds are measured at a total of 14 points on the first floor (Fig. 4.19 (c)). Table 4.6 provides the coordinates of these measurement points, with the origin located at the top left bottom corner of the room (see Fig. 4.19 (c)). The measurement duration with the 3D anemometer lasts for 30 minutes, but I utilize 20 minutes of data for analysis, starting from 5 minutes after the activation of the sensor to ensure that our presence does not influence the airflow.

Point	x	y	z	Point	x	y	z
P1	-2.8	3.6	1.55	P8	-4.8	1.8	1.55
P2	-3.1	3.1	1.55	P9	-1.3	0.1	1.55
P3	-4.3	3.5	1.55	P10	-4.1	0.5	1.55
P4	-0.1	1.8	1.55	P11	-5.8	2.6	1.55
P5	-1.6	1.8	1.55	P12	-6.2	3.1	1.55
P6	-2.7	1.8	1.55	P13	-6.8	3.5	1.55
P7	-3.5	1.8	1.55	P14	-7.8	1.8	1.55

Table 4.6: Coordinates of Points for 3D anemometer position.

4.3.1.2 CFD modeling

In this subsection, I compare the coupled and decoupled approach. Afterward, I select the more suitable one for airflow simulation that is compared with airflow experiments.

In both cases, the governing equations used for the CFD simulation are the same as those used in the previous section. Solver is "Code_Saturne".

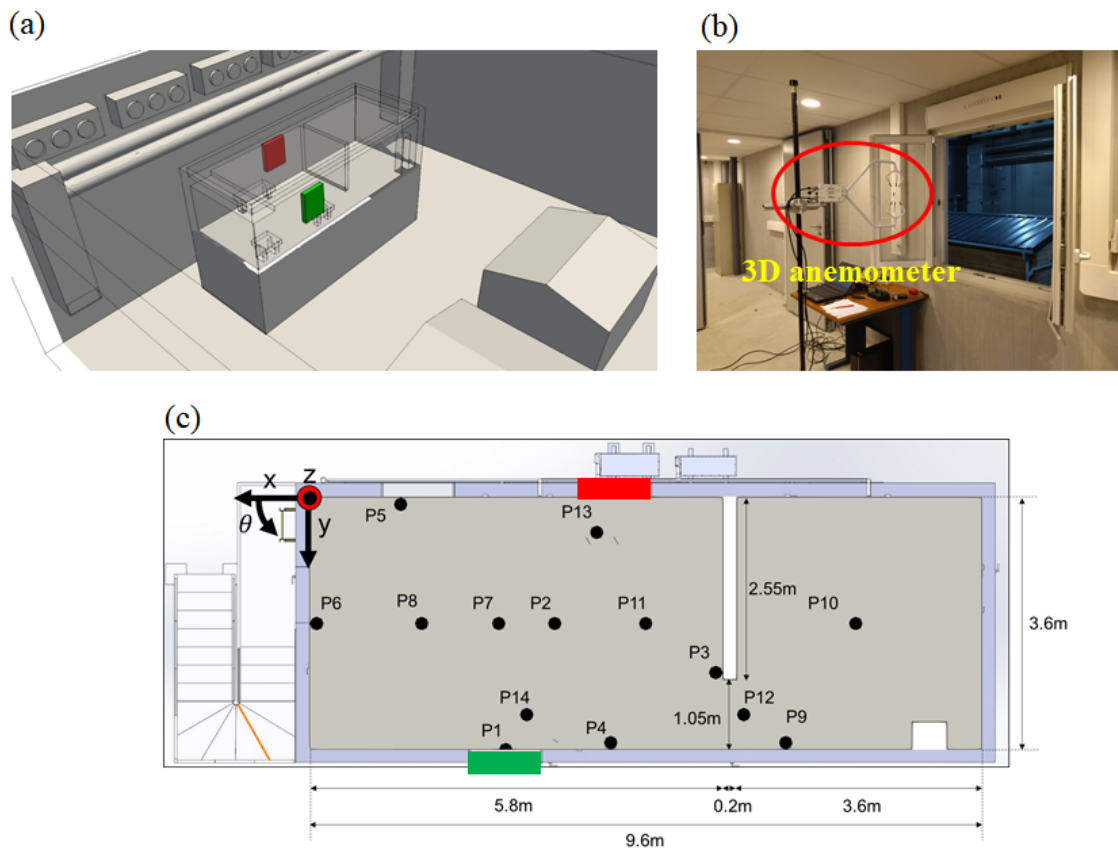


Figure 4.19: 3D anemometer set-up: (a) virtual geometry of Sense-City with the indoor environment at the 1st floor of the concrete building, (b) Picture of 3D anemometer and (c) Location of 3D anemometer for airflow measurement.

• Geometry

In the coupled approach, the numerical mock-up is created by adding the indoor geometry to the mock-up used in the previous section (see Fig. 4.20 (a)). Fig. 4.21 shows the actual picture of the room and the indoor area of the new mock-up; the TV on the desk has not been created in the mock-up; the thickness of the desks was made thicker than the actual ones to reduce the number of cells. Once again, let me note that the detailed geometry of the inside of the climatic chamber's ventilation system has not been created, and thereby airflow inside the ventilation system is not calculated.

In the decoupled approach, as already described, two mock-ups are required; one outdoor and one indoor (Fig. 4.20 (b)). The outdoor mock-up is identical to that used in the previous section for the depolluting panels. Therefore, the results of [124] are reused here to get pressure boundary conditions for the indoor simulation. The indoor mock-up has the same geometry as the indoor geometry of the coupled approach.

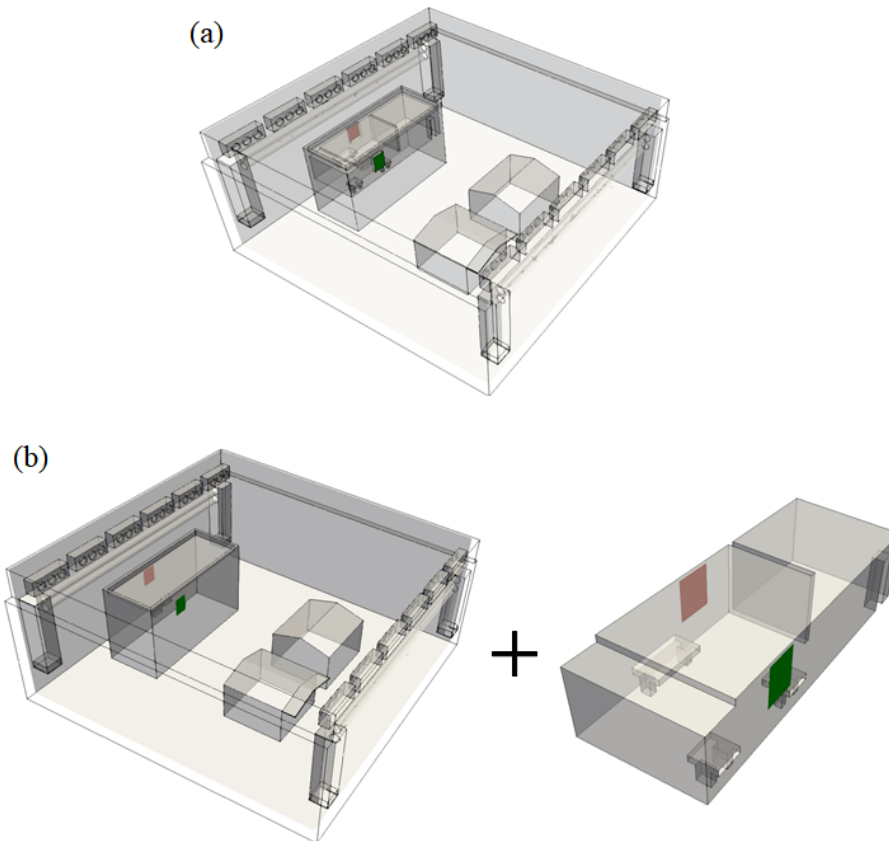


Figure 4.20: Numerical mock-up: (a) coupled approach and (b) decoupled approach.

- **Mesh configuration**

In the coupled approach, the unstructured mesh is used. The total number of cells is 1,442,169. As we discussed, outdoor airflow rises along the concrete building's front surfaces (as shown in Fig. 4.7). Hence, once the outdoor airflow reaches the opening window, outdoor airflow separates at the window frame and enters the indoor room. To precisely capture the flow separation at the window, smaller meshes



Figure 4.21: Indoor geometry: (a) actual geometry (picture) and (b) numerical mock-up.

with 0.05 m are employed on the concrete building’s front surfaces than the mesh used in the previous section (Fig. 4.22 (a)).

In the decoupled approach, the outdoor simulation conducted of [124] utilized unstructured meshes. The number of cells was 910,157 and the mesh size on the concrete building’s front surface was around 0.3 m. For the indoor simulation, the same mesh as in the previous Subsection 4.2.2.3 is used: the number of cells is 255,270. As mentioned, hexa meshes are employed in proximity to the windows with 0.1 m mesh (the green area in Fig. 4.22 (b)), while unstructured meshes are used with 0.12 m in the main room and 0.16 m in the side room.

• **Boundary condition**

In the coupled approach, the boundary conditions are equivalent to what was presented in Subsection 4.2.2.1 for the numerical study of the depolluting panels. They are taken from the ventilation system setting. No boundary conditions are needed for the indoor environment.

In the decoupled approach, the time histories of pressures at the windows are extracted from the outdoor simulation carried out in [124]. (Note that in the previous section, time-average pressure was imposed at the windows.) Time histories of the pressures for 20 minutes extracted at the building’s front and rear window areas are given to the window areas of the indoor simulation as Dirichlet conditions. In the pressure-drive flow, the important aspect is the pressure difference. Fig. 4.23 shows the time history of the pressure difference between the front and rear window areas. It is found that, overall, the pressure difference tends to be positive; the pressure at the front window area of the building is generally higher than at the rear area. As a result, it can be expected that airflow mainly enters from the front window towards

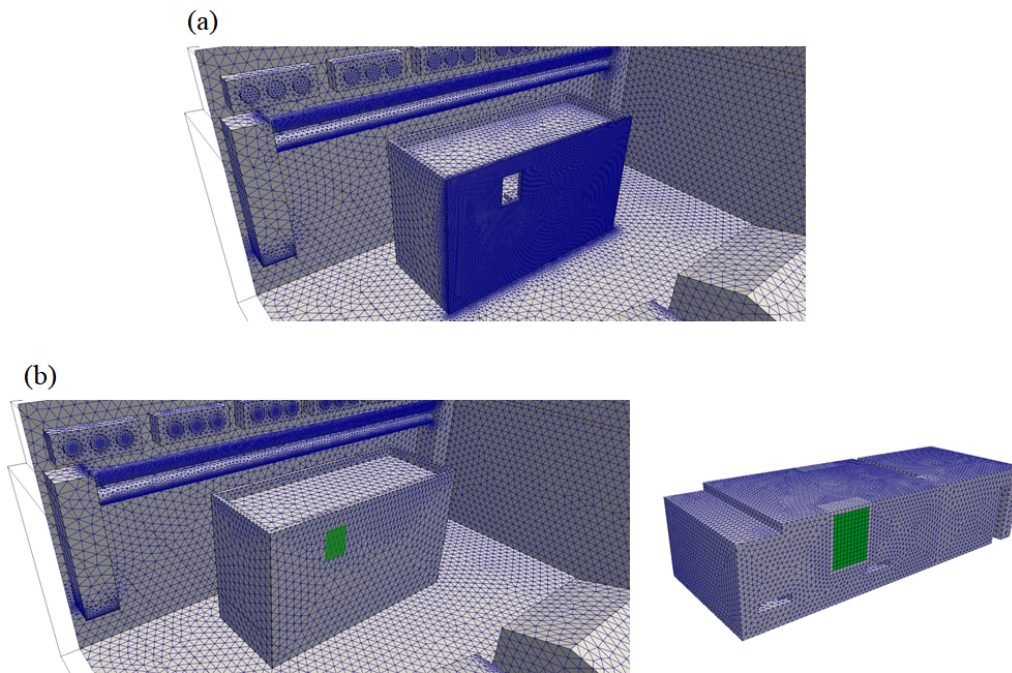


Figure 4.22: Surface mesh: (a) coupled approach and (b) decoupled approach.

the rear window, but sometimes the pressure is higher at the rear. In addition, Neumann conditions (zero gradients) are imposed for the velocity at the building windows.

- **Result comparison between coupled and decoupled approach**

Fig. 4.24 shows the average flow velocity in the indoor environment obtained with the coupled and decoupled approaches. Fig. 4.24 (a) is a vertical section at the front window, Fig. 4.24 (b) is a vertical section at the rear window and Fig. 4.24 (c) is a horizontal section at a height of 1.55 m from the floor. Overall, we can observe different velocity magnitudes and wind directions when comparing the numerical results of the two approaches. As can be seen in Fig. 4.24 (a), in the coupled approach, one has a significant vertical component at the entering of the room (front window) due to the airflow ascending along the concrete building surface outdoors. Then it reaches the indoor ceiling and circulates along the room's perimeter. In the coupled approach, the velocity magnitude is around 0.3 m/s at the window. On the other hand, in the decoupled approach, there is no vertical component at the front window. Rather, some airflow is downwards after entering. The

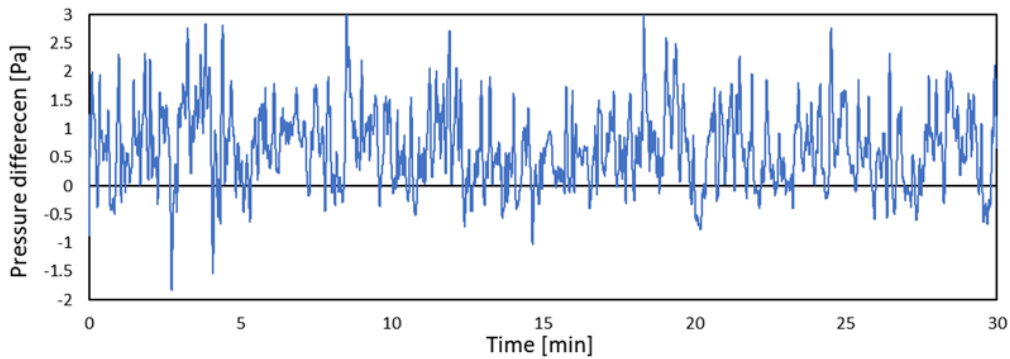


Figure 4.23: Time history of the pressure difference between inlet and outlet (inlet pressure - outlet pressure).

velocity at the window exceeds 1 m/s. This is obviously an overestimation, given that the velocity at the vicinity of the concrete wall surface in the outdoor simulation is approximately 0.6 m/s. This kind of overestimation is also observed at the rear window (Fig. 4.24 (b)). Looking at Fig. 4.24 (c), in the coupled approach, the wind direction has a slight leftward component with a main upward direction at the front window, contrary to the decoupled approach. These differences in wind speed and direction are attributed to the limitations of the decoupled approach. In fact, this overestimation is pointed out in a guidebook for indoor air quality design [139] when using decoupled approach with pressure conditions. Also, as some studies, e.g., [82, 140] explained, the decoupled approach cannot take into account the flow momentum and turbulence kinematic energy of the outdoor airflow at the window for the indoor simulation, causing the overestimation. Moreover, in pressure-driven flows, it is inevitable that the wind direction is normal to inlet surfaces. [83] notes that there are both normal and tangential pressures at the window and that only the normal pressure is converted to surface pressures when windows are being closed, implying only the normal contributes to an inflow ventilation rate. However, it is difficult to determine the normal and tangential components of pressures on the window modeled by walls from outdoor simulations. The only advantage of the decoupled approach in this study is that the velocity direction and distribution in the horizontal section (Fig. 4.24 (c)) has similar trends with the coupled approach contrary to the vertical sections. The two large circulations in the main room and the low-velocity airflow circulation in the side room are similar in both cases. It should be noted again, however, that the velocity magnitude is still overestimated in the decoupled approach.

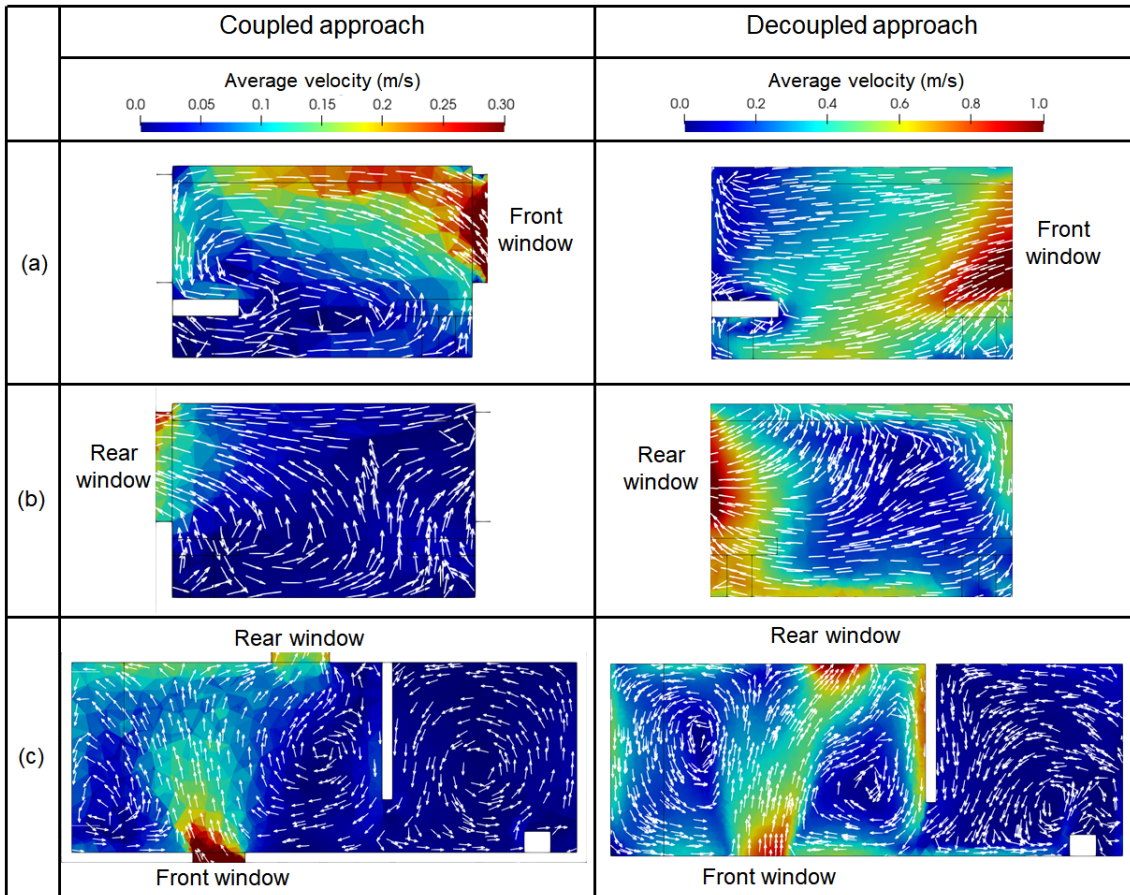


Figure 4.24: Average velocity comparison between coupled and decoupled approach: (a) vertical section at the front window ($x = -2.9m$), (b) vertical section at the rear window ($x = -3.9m$) and (C) horizontal section at a height of 1.55 m.

Based on this comparison, it seems that the decoupled approach has many limitations in the Sense-City case. Hence, I have chosen to employ the coupled approach to compare with the measurement and to use it for predicting indoor pollutant dispersion in Sense-City case. However, in real and complex urban scenarios, where the number of cells can be extremely large and the repetition of the outdoor simulation is demanding, the decoupled simulations can serve as an alternative to roughly investigate the propagation of pollutants into the indoor environment, despite the significant mismatch in vertical flow velocities.

4.3.1.3 Airflow comparison between measurement and coupled approach

To begin, let me note that in the experiment the average values are calculated using 20 minutes of measured data from 5 minutes after the start of data acquisition with the 3D anemometer. Similarly, for the simulation, 20 minutes of data are used for the data analysis after a 10-minute preliminary calculation. The measurement interval was 0.02 s for the experiment and 0.1 s for the simulation. To compare the experiment and measurement, the moving average was applied to the measurement data on a length of 0.1s.

Let me start with the analysis at P1 (see Fig. 4.19 and Table 4.6), the main inlet of the airflow, which is the most important for indoor airflow. Fig. 4.25 shows time histories on 20 min time intervals for each velocity component of the experiment and simulation with $\Delta t = 0.1$ s. Note that

See Fig. 4.19 (c) for the definition of the direction of each velocity component (U_x , U_y , U_z). Due to the nature of URANS, tiny fluctuations observed in the measurement are not captured in the simulation. Table 4.7 summarized statistical values (average velocity components (U_x , U_y , U_z) (m/s), horizontal flow direction θ , turbulent kinetic energy (TKE) (m^2/s^2) and standard deviation σ_i (m/s)) for the time histories of Fig. 4.25. TKE is defined as: $TKE = \frac{1}{2} (\sigma_u^2 + \sigma_y^2 + \sigma_z^2)$, where σ_i^2 (m^2/s^2) represents the variance of the velocity component i . At P1 (front window), the three velocity components are of the same order of magnitude in both experiment and simulation. From the horizontal flow direction θ defined in Fig. 4.19 (c), it is found that airflow entering the room is not purely normal to the front window for both experiment and simulation, as can be seen in the coupled approach result in Fig. 4.24. Accordingly, the simulated airflow at the front window has a higher tangential component than the experiment, but this kind of 10° difference is an acceptable gap. The error in the velocity magnitude, $U_{magnitude}$, between the experiment and the simulation is about 5%. For TKE, the simulation overestimates it compared to the experiment. The magnitude of the TKE indicates the degree of airflow mixing, where a bigger TKE corresponds to increased diffusion of airflow. Overall, at P1, the simulation is in good agreement with the experiment, which is one of the important factors in getting accurate indoor airflow prediction.

Next, Fig.4.26 shows comparisons at all the measurement points inside the concrete building (a total of 14 points including P1) in terms of average U_x , U_y , U_z and TKE. Regarding the average velocity components and TKE, the results demonstrate

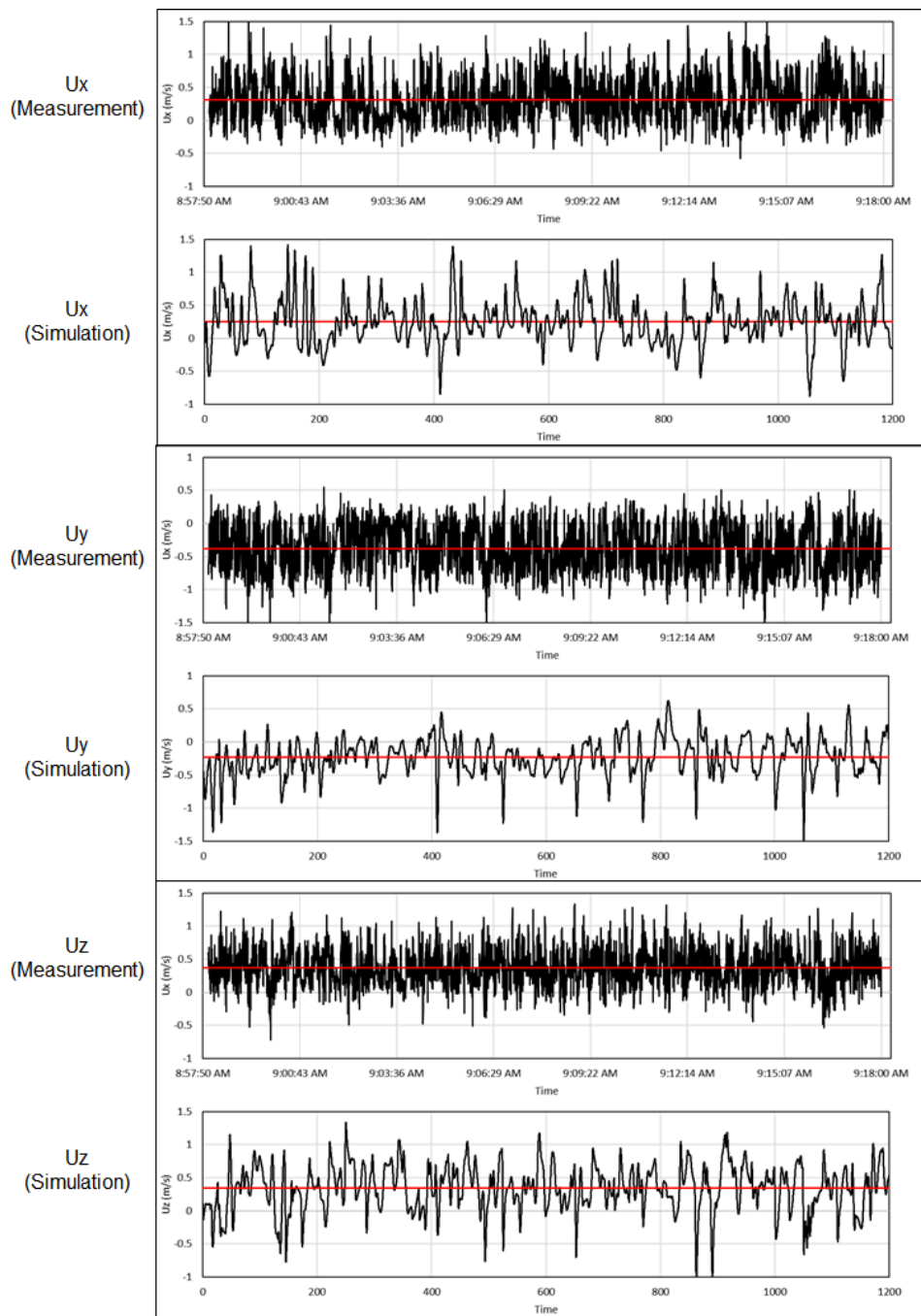


Figure 4.25: Time history of U_x , U_y , U_z with $\Delta t = 0.1s$ at P1 of experiment and URANS simulation. The red lines show the average of each velocity component. The moving average is applied to the measurement data on a length of 0.1s.

	Experiment	Simulation
Ux (m/s)	0.31	0.25
Uy (m/s)	-0.38	-0.23
Uz (m/s)	0.37	0.34
Horizontal flow direction θ ($^\circ$)	-28	-17
$U_{magnitude}$ (m/s)	0.72	0.69
TKE (m^2/s^2)	0.13	0.16

Table 4.7: Comparison of average velocity, TKE, and standard deviation at P1 (front side window).

a high level of agreement with the experimental data. In most of the points, velocity directions are correct, but some points have opposite directions of the velocity components, i.e., Ux and Uy at P6, and Uy at P3. At P6, the simulated value differs from the experimental value for all the velocity components, and, as mentioned, Ux and Uy have opposite velocity directions. One possible reason for this is that in reality, there are a door, ceiling and step near P6, which add complexity to the airflow. However, these geometrical features are not considered in the numerical mock-up. This difference may result in the difference between the experiment and the simulation at P6. A further reason is that the mesh on the indoor wall surface is too coarse to capture the fluctuations near the wall. At P8, Uy difference between the experiment and the simulation looks proportional to the difference of P1. At both points, measurement Uy is about two times higher than the simulation. In fact, this is because the airflow at the front window (P1) goes directly towards P8 due to the slight leftward wind direction at the front window as discussed in Table 4.7. It also can be seen in Fig. 4.24 (c) of the coupled approach. Therefore, the underestimation at P8 of the Uy of the simulation can be due to the underestimation of Uy of the simulation at P1. With regard to TKE in Fig. 4.26, values at almost all measurement points except for P1 are small. The order of magnitude is in good agreement at every sensor. As discussed at P1, P14 located near the front window also shows the overestimation of the TKE.

Statistical metrics, including BIAS, RMSE, and NRMSE, are employed to evaluate the simulation's performance compared to the experimental results. Each metric is defined as follows:

$$BIAS = \frac{1}{N} \sum_{i=1}^N (y_i - \hat{y}_i) \quad (4.24)$$

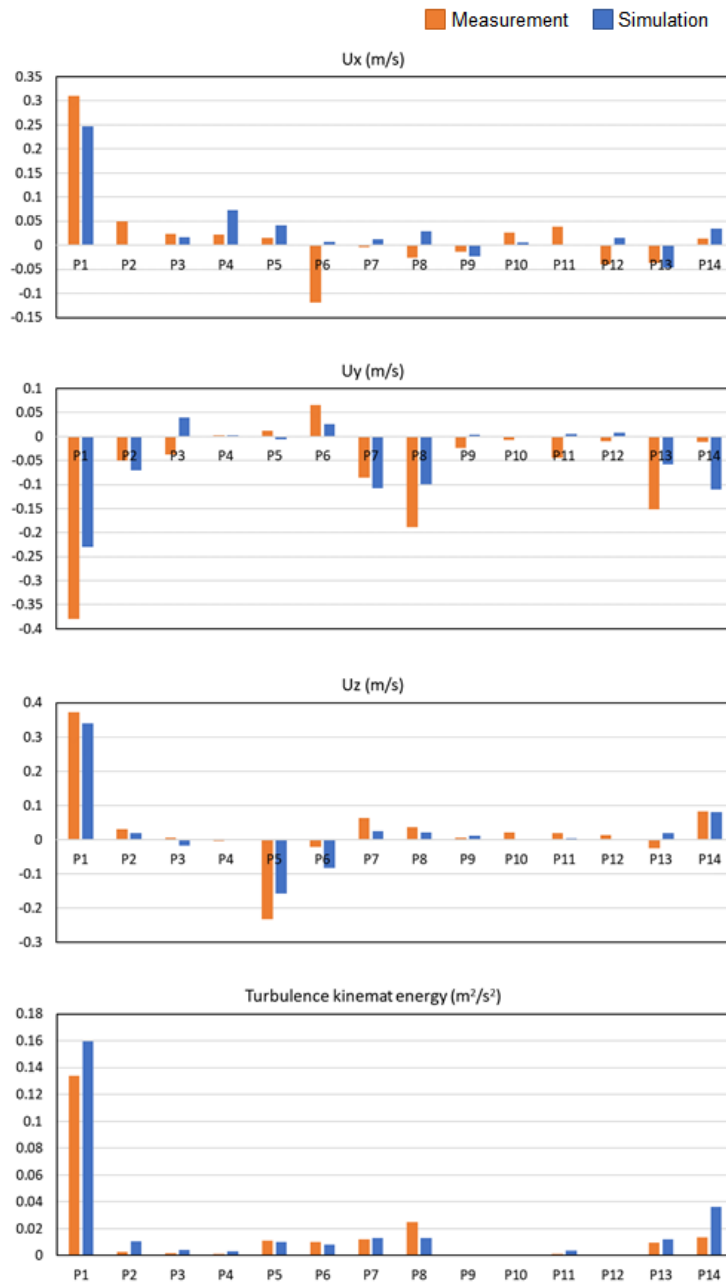


Figure 4.26: Velocity and TKE comparison at 14 points between the experiment and the coupled approach inside the concrete building in Sense-City.

$$RMSE = \sqrt{\frac{1}{N} \sum_{i=1}^N (y_i - \hat{y}_i)^2} \quad (4.25)$$

$$NRMSE = \frac{RMSE}{\frac{1}{N} \sum_{i=1}^N \hat{y}_i} \quad (4.26)$$

where y_i and \hat{y}_i represent simulated and measured values and N is the number of measurements. BIAS can be used to assess how much simulation over/underestimates results compared to experiments. RMSE is useful to evaluate the quality of simulations. NRMSE is a normalized RMSE that evaluates the quality of simulations in a normalized way for the different physical quantities i.e., flow direction *vs* velocity magnitude.

Fig. 4.8 summarizes the results of each metric. Based on BIAS, we note that the simulation is very accurate for the horizontal flow direction. However, RMSE shows a value of 23.6° in the airflow direction. By examining the differences of the airflow direction at all points between the experiment and the simulation, differences of approximately 50° are found at P3 and P8, and a difference of 30° is seen at P11 where the velocity is almost null, i.e., less than 0.05 m/s . Concerning the magnitude of the velocity and TKE, BIAS and RMSE values are very small and seemingly very accurate, but this is because the average wind velocity in the room is below 0.1 m/s at many points. From NRMSE values, we can conclude that the accuracy of the simulations is acceptable, i.e., $NRMSE < 0.3$ for airflow magnitude and Horizontal flow direction θ .

	BIAS	RMSE	NRMSE
Horizontal flow direction θ	1.9°	23.6°	0.26
$U_{magnitude}$	-0.01 m/s	0.05 m/s	0.3
TKE	$0.004 \text{ m}^2/\text{s}^2$	$0.01 \text{ m}^2/\text{s}^2$	0.64

Table 4.8: Statistical metrics comparing the simulation with the experiment at 14 points in the concrete building of Sense-City.

To sum up, in the simulation, various assumptions are included, such as simplification of the geometry of buildings and obstacles, simplification of boundary conditions, etc. Furthermore, one has discretization and modeling errors in the numerical calculations. Considering these factors, the accuracy of the present airflow simulations is acceptable. Although some points (e.g., P8 and P11) have a significant gap of airflow directions, but they have a tiny velocity (less than 0.1 m/s). Therefore, they should not have a significant impact on the main indoor pollutant

dispersion phenomena. Accordingly, in the following section, based on the airflow field of the coupled approach, the advection-diffusion equation for pollutant dispersion is solved. The results are then compared with the full-scale CO₂ dispersion experiments.

4.3.2 CO₂ dispersion validation

4.3.2.1 Experimental set-up for CO₂ dispersion measurement in Sense-City

Full-scale pollutant dispersion experiments are designed and conducted for CO₂ concentrations in Sense-City. NO₂ is the main pollutant from vehicles that is my focus in my Ph.D., but CO₂ is chosen here as it is a non-reactive pollutant easier to study and also for the safety of the experiment. This experiment is the first pollutant dispersion experiment with a fully controlled pollutant source conducted in Sense-City at Université Gustave Eiffel.

• Set-up for experimental equipment

In this experiment, a gas emission device (Fig. 4.27) is used to release CO₂. The gas emission device is positioned at 1 m above the road, between the concrete building and the two houses (see Fig. 4.28), following the same placement defined in the simulation (see Subsection 4.2.2.1) for the study on the optimal placement of the depolluting panel. The gas emission device has dimensions of 0.5 m x 0.5 m and a thickness of 5 cm (Fig. 4.27). Pollutants are released from the top surface of this device. To control the emission volume of pollutants ($\mu g/s$), the device is connected to a CO₂ bottle located in a technical room outside the climatic chamber (Fig. 4.29). A tube connects the bottle to the gas emission device, allowing us to control CO₂ emissions by adjusting the pressure at the outlet of the bottle. The tube runs from the bottles outside the climatic chamber, along the outside wall, over the concrete building, returns to the ground, and lastly to the gas emission device (Fig. 4.29). In the present experiment, CO₂ emission rate from the gas emission device remained constant at 256 mg/s , which is the combination of the CO₂ bottle at 50,000 ppm (= 90,000 mg/m^3) and airflow bottle emission at 171 L/min (= 0.00285 m^3/s) when using a pressure of 5.5 *bar* at the outlet of the bottle.

To measure CO₂ concentration, ETHERA CO₂ sensors are used (Fig. 4.30), whose detection method is NDIR (see Subsection 1.3.1.1). The measuring range is 0 to 5000 ppm with a resolution of 1 ppm. The accuracy of the detection is ± 50 ppm $\pm 3\%$ of the reading value. The total of the twelve CO₂ sensors is deployed outdoors and indoors, as indicated by pink circles in Fig. 4.28. The sensors are

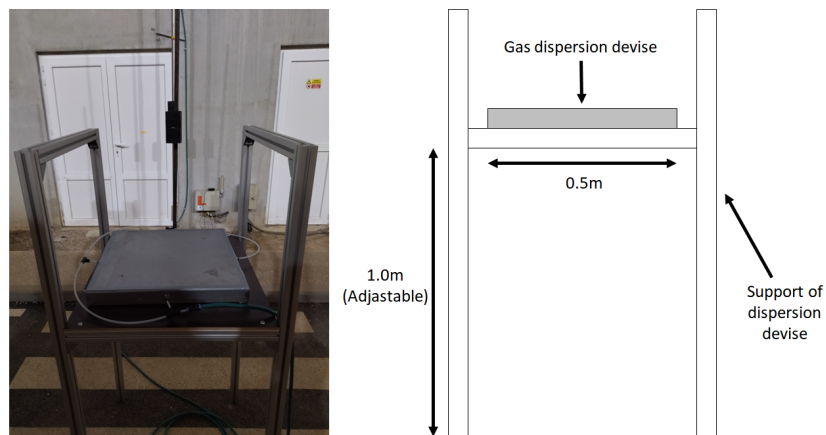


Figure 4.27: Gas dispersion device.

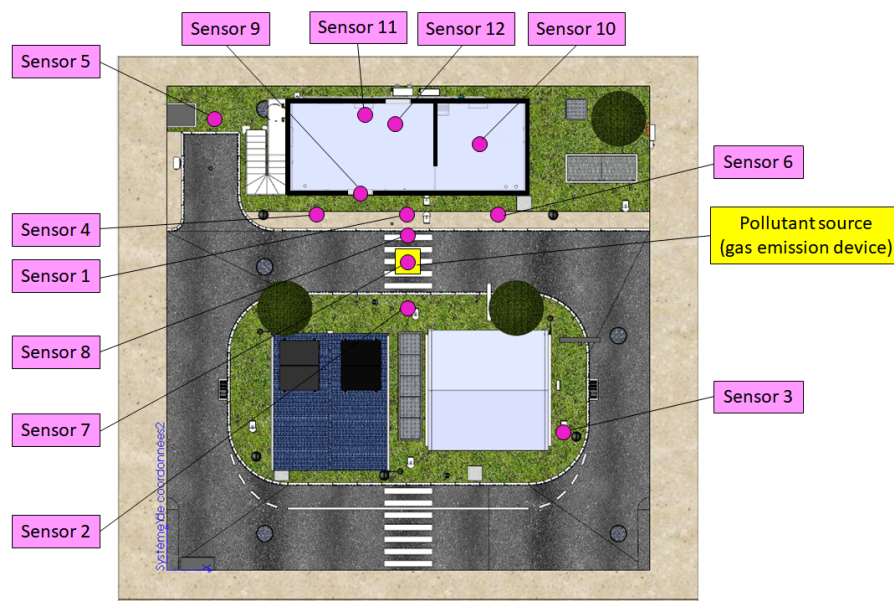


Figure 4.28: Position of the pollutant source and CO_2 sensor in the CO_2 controlled dispersion experiment.

placed at a height of 1.5 m. Through the airflow and pollutant dispersion simulations conducted in the previous section, it has been revealed that pollutants tend to be transported toward the concrete building and the top left extraction duct from

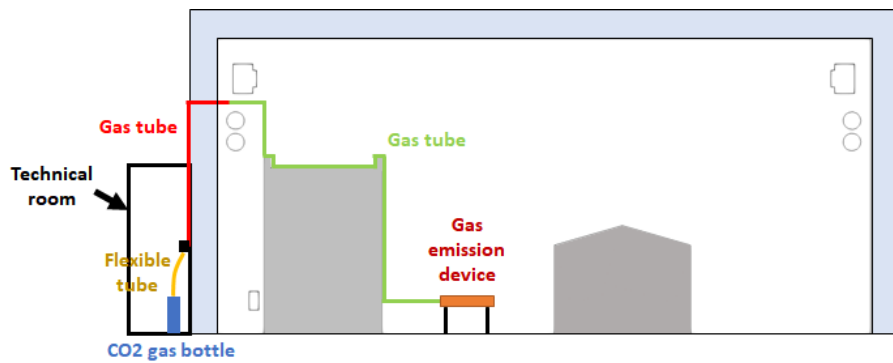


Figure 4.29: Diagram for connection of the gas emission device and gas bottles in Sense-City.

the source, as can be seen in Fig. 4.8. Accordingly, most of the sensors are installed close to the concrete building. In particular, since the pollutants are carried by the airflow directed from the pollution source to the top left extraction duct, sensor 5 is placed near the duct to investigate when the pollutant starts recirculating through the duct and the air-forced duct of the climatic chamber. In fact, the CO₂ pollutants measured near sensor 5 are expected to be drawn in and recirculated by and through ducts and fans and discharged back into the climatic chamber, leading to an increase in the ambient concentration in the climatic chamber. Let us recall that the Sense-City climatic chamber ensures a closed-cycle airflow circulation. To measure the ambient concentration in the climatic chamber, only sensor 3 is located away from the pollution source in the opposite direction to the building. To see the propagation of outdoor pollutants into the indoor environment, four sensors are installed on the 1st floor of the concrete building: one is located at the front window, enabling direct measurement of the interaction between outdoor and indoor air quality. The coordinates of the sensors are provided in Table 4.9, where the origin is on the ground at the center of Sense-City district. Fig. 4.31 shows some sensor placements.

• Experimental condition

In this experiment, the two windows on the 1st floor of the concrete building are consistently kept open throughout the entire duration of the experiment. The ventilation systems within the climatic chamber are activated few hours before to ensure that the airflow develops adequately before the release of CO₂. I consider two experimental scenarios: short and long duration of CO₂ dispersion. The short-duration CO₂ dispersion scenario is designed to avoid the re-circulation of pollutants



Figure 4.30: ETHERA CO₂ sensor [141].

Point	x	y	z	Point	x	y	z
S1	0	-4.7	1.5	S7	0	-2.75	1.1
S2	0	-0.75	1.5	S8	0	-3.75	1.5
S3	-6.8	4	1.5	S9	2	-5.5	4.65
S4	3.5	-4.7	1.5	S10	-3.025	-7.5	4.65
S5	8	-8.3	1.5	S11	2.5	-8	4.65
S6	-3.5	-4.7	1.5	S12	0.5	-8	4.65

Table 4.9: Coordinates of CO₂ sensor position.

via the climatic chamber’s ventilation system; this numerical scenario is similar to the pollutant dispersion simulation in the smart placement of depolluting panels in Sense-City (see Section 4.2). From the pollutant dispersion simulation in Section 4.2, it was found that the pollutants from the center of Sense-City reach the left suction duct in few minutes. Concerning the long-duration CO₂ dispersion scenario, the objective is to observe more elevated levels of CO₂ concentration, which can be easily detected by the CO₂ sensors. Needless to say, in this long scenario, the measurement takes into account the pollutants recirculated through the climatic chamber’s ventilation system. CO₂ is released for 3 minutes for the short-duration case and 55 minutes for the long-duration case. Humidity in the climatic chamber is about 60 - 70% and the temperature is maintained at 20°.

As a matter of fact, two measurement campaigns were conducted in September 2022 and January 2023, where three and six experimental tests respectively were carried out. In the first measurement campaign in September 2022, CO₂ emission rate was too low to be detected by CO₂ sensors. More specifically, the CO₂ emission

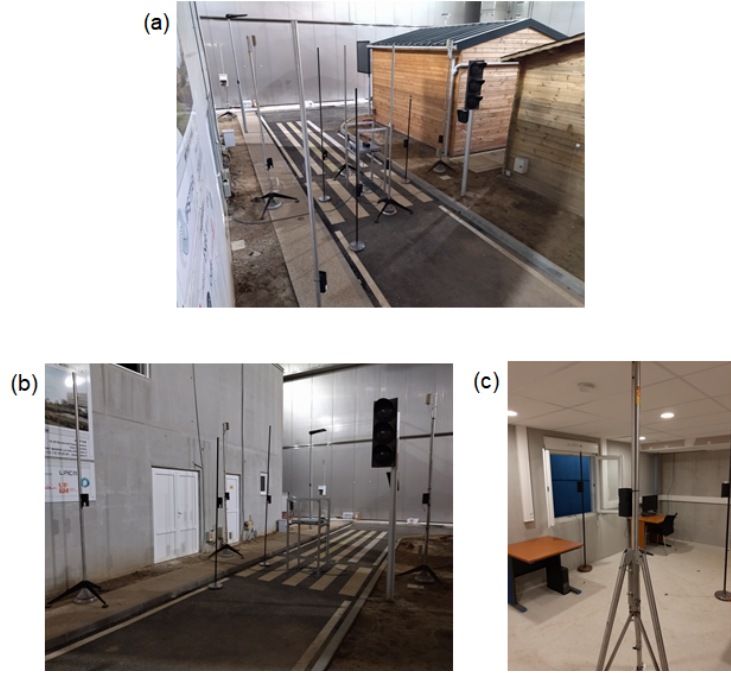


Figure 4.31: CO₂ sensor arrangement; (a) ~ (b) around the gas dispersion device from the 1st floor and (c) inside the 1st floor.

rate was 40 mg/s , which was the combination of the CO₂ bottle at 10,000 ppm (= 18,000 mg/m^3) and air bottle emission at 133 L/min (= 0.00222 m^3/s). Therefore, a new campaign was conducted in January 2023 with stronger CO₂ emissions: 256 mg/s .

- **Calibration of CO₂ sensor**

Before the experimental campaign, calibration was performed to obtain correct experimental results. As said, I used 14 sensors, five of which were purchased just before the experiment and the remaining seven were purchased approximately one year before the experiment. Calibration was performed using linear regression based on three or two measurement points. Assuming C_{ref} as a known reference concentration, C_{corr} as the calibrated sensor concentration and C_{old} as the sensor concentration before calibration, C_{corr} is obtained as follows:

$$C_{corr} = \alpha C_{old} + \beta \quad (4.27)$$

where α is called "gain" and β "offset". Now this calibration is done by minimizing

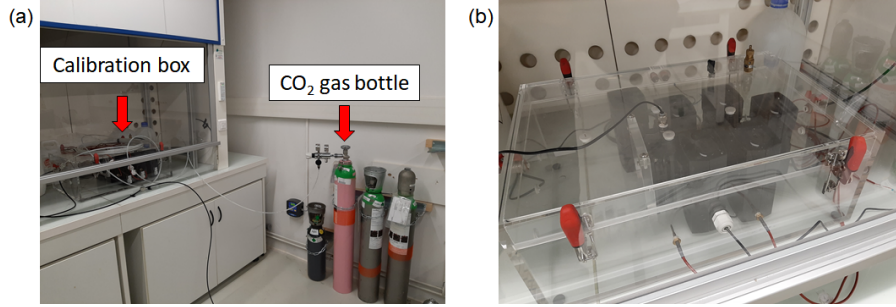


Figure 4.32: Picture of the calibration (a) overview and (b) CO₂ sensors in the calibration box.

the sum of the square of the difference between C_{corr} and C_{ref} :

$$\min_{\alpha, \beta} Y \text{ where } Y = \sum_{n=1}^{Nm} (C_{corr}^i(\alpha, \beta) - C_{ref}^i)^2 \quad (4.28)$$

where i represents the number of reference concentrations and Nm is the number of measurement points (in this case 2 or 3). The minimum is obtained when the derivative Y , $\frac{\partial Y}{\partial \alpha}$ and $\frac{\partial Y}{\partial \beta}$ are null. Hence, we get:

$$\alpha = \frac{N_m \cdot \sum_i (C_{ref}^i \cdot C_{old}^i) - (\sum_i C_{ref}^i) \cdot \sum_i C_{old}^i}{N_m \cdot \sum_i (C_{old}^i)^2 - (\sum_i C_{old}^i)^2} \quad (4.29)$$

$$\beta = \frac{(\sum_i (C_{ref}^i \cdot C_{old}^i)) \cdot (\sum_i C_{old}^i) - (\sum_i C_{ref}^i) \cdot \sum_i (C_{old}^i)^2}{(\sum_i C_{old}^i)^2 - N_m \cdot \sum_i (C_{old}^i)^2} \quad (4.30)$$

When considering in my calibration, the number of reference points i is three; reference CO₂ concentrations are at 500 ppm, 1000 ppm and 2,000 ppm. They are obtained from a CO₂ gas bottle which are connected to the calibration box, respectively (see Fig. 4.32). Concerning the calibration conditions in the laboratory, the temperature was 22°C and the humidity 60 was $\sim 70\%$. The calibration protocol is described below:

1. Activate the sensors
2. Clean air inside the box by venting with compressed air for 5 minutes
3. Emit 500 ppm reference CO₂ concentration for 13 minutes
4. Stop emissions, close the box inlet/outlet and leave for 5 minutes to stabilize and save the measured concentration

5. Open box inlet/outlet and clean air inside the box by venting with compressed air for 5 minutes
6. Repeat the procedures from Step 3 for 1000 ppm and 2000 ppm reference concentrations respectively

Note that due to a lack of CO₂ gas in the bottle, some sensors were calibrated based only on the two reference points C_{ref} at 500ppm and 1000ppm. The obtained calibration factors α and β for each sensor are summarized below:

Sensor position	Calibration factor		Number of measurement point
	α	β	
Sensor 1 (new)	1.05	-1.16	2
Sensor 2 (new)	1.01	-4.81	3
Sensor 3 (new)	1.01	-5.63	3
Sensor 4 (new)	1.04	-4.27	3
Sensor 5 (new)	1.01	-26.00	3
Sensor 6	0.99	19.06	2
Sensor 7	1.01	71.31	2
Sensor 8	1.01	15.83	2
Sensor 9	1.02	94.76	3
Sensor 10	1.02	42.45	2
Sensor 11	1.05	74.26	2
Sensor 12	0.98	60.68	3

Table 4.10: Calibration factor determined in laboratory.

Sensor 1 ~ 5 are newer sensors than the others. According to Table 4.10, the offset β is higher for old sensors, but the gain α is almost 1 for every sensor.

4.3.2.2 CFD modeling

As discussed in the flow validation, the coupled approach is retained. The numerical conditions for the pollutant are chosen to mimic the experiments. In fact, I consider a volumic source of dimension $0.5\text{ m} \times 0.5\text{ m} \times 0.5\text{ m}$ (0.125 m^3) placed at the center of Sense-City road at 1 m height. The magnitude of the source in the simulation is 1141 ppm/s (CO₂ emission rate $256\text{ mg/s} \times 0.125\text{ m}^3$). The studied times of the simulations are 3 min for the short case and 55 min for the long case with $\Delta t = 0.1\text{ s}$, during which the pollutant emission magnitude is constant at 1141

ppm/s. In the previous study of the smart placement of depolluting panels in Section 4.2.3.1, I solved the advection-diffusion equation based on the average velocity field. I continue that here, but I also consider solving an unsteady solution for both airflow and pollutant dispersion. Namely, both airflow (Eq. (4.7)) and scalar transport (Eq. (4.16)) are solved with coupling. In total, four pollutant dispersion simulations are carried out;

- Case I-a : Short duration with the average velocity;
- Case I-b : Short duration with the instantaneous velocity;
- Case II-a : Long duration with the average velocity;
- Case II-b : Long duration with the instantaneous velocity;

For the cases of solving pollutant dispersion with average velocity (Case I-a and Case II-a), a total 20 min calculation was carried out, and the last 10 min was used to obtain the average flow field. For the unsteady case (Case I-b and Case II-b), 10 min pre-calculation was carried out to develop airflow in Sense-City enough. Subsequently, 55 min simulation is started. SOLU (second-order linear upwind) scheme is used for the advection term of the advection-diffusion PDE (Eq. (4.16)). CO₂ pollutant is regarded as a passive scalar.

For the short-duration pollutant simulation (Case I), all the numerical settings are identical to the airflow validation except for the setting of pollutant dispersion.

For the long-duration pollutant dispersion simulation (Case II), new boundary conditions for airflow and pollutants should be introduced to simulate long-term trends in pollutant dispersion in the climatic chamber with the closed-cycle airflow circulation. In fact, in the short-duration simulation, the recirculation of pollutants in the climatic chamber was not reproduced. Consequently, for the long-duration pollutant dispersion simulation, a new numerical mock-up is created that considers the inside of the climatic chamber's ventilation system. When dealing with scalar transport inside the ventilation system, pollutants should be drawn in the extraction duct and outlet fans and then re-exhausted from the inlet fan and upper-lower forced-air ducts (see Fig. 4.5). In order to take into account the scalar transport inside the ventilation systems while keeping the same boundary condition for airflow, I introduce "mapped" boundary conditions in Code_Saturne for boundaries inside the ventilation systems. In this way, variables such as velocity and pollutant concentrations at outlet boundary faces of the ventilation systems, Γ_o , i.e., the outlet extraction duct, outlet fan and outlet forced-air duct are re-mapped to inlet boundary faces of the ventilation systems, Γ_i , i.e., the inlet extraction dust, inlet fan and

inlet forced-air duct (see Fig. 4.33).

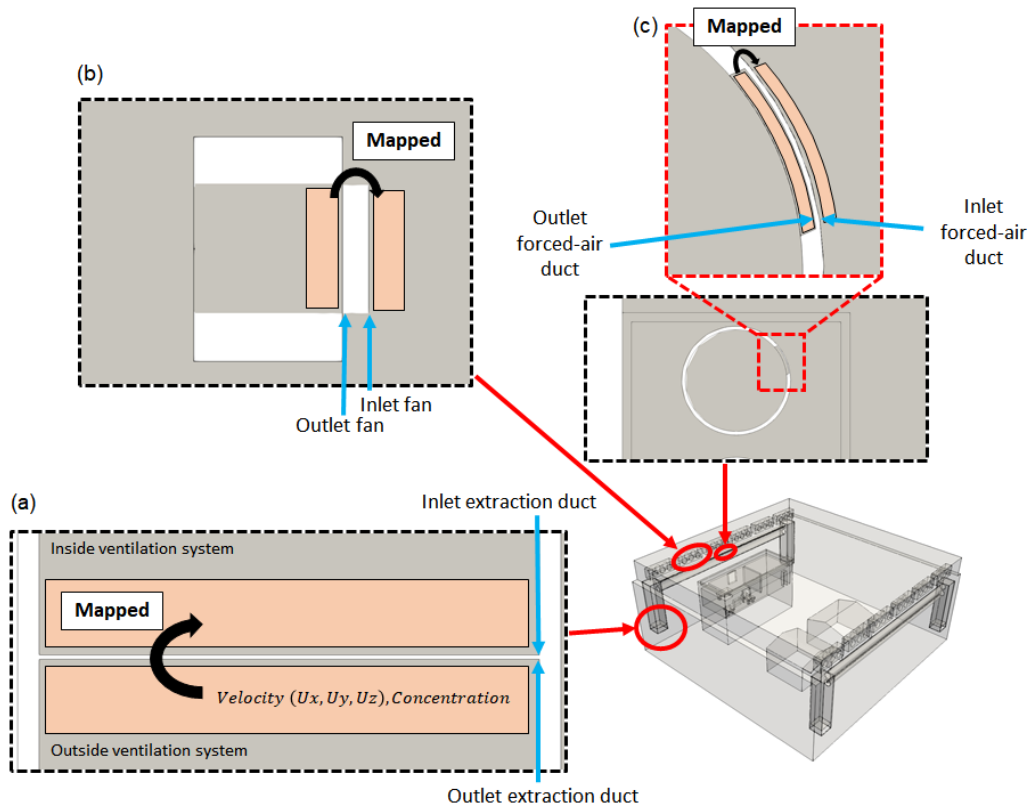


Figure 4.33: Mapped boundary conditions for the inside of the climatic chamber's ventilation systems: (a) extraction duct, (b) fan and (c) forced-air duct.

4.3.2.3 Result comparison between experiment and simulation

- **Short-duration cases**

Fig. 4.34 illustrates a comparison of pollutant concentrations at six sensors' points over three minutes between sensors' measurements (C_{exp}), simulated pollutant dispersion using the average airflow (C_{ave}) and simulated pollutant dispersion using the instantaneous airflow (C_{ins}). As the sensors in the experiment measured concentration every 10 seconds, the simulation results were also applied with a 10-second moving average. Sensor 1 is located immediately on the leeward of the source and must show the highest pollutant concentration. The numerical results show that C_{ave} increases sharply in the first 30 seconds and then remains constant; for C_{ins} and C_{exp} , the concentrations fluctuate. From this, it is worth noting that in the three-minute experiment, there is no significant increase in pollutant concentration in Sensor 1, even when close to the pollution source. Sensors 4 and 6 are symmetrically located from the source. Looking at those results, C_{ave} is more elevated at Sensor 4 than at Sensor 6. This is due to the airflow in Sense-City being mainly directed from the source to the left extraction duct. However, it is not clear from the variations shown by C_{ins} and C_{exp} that more pollutants are flowing toward Sensor 4. Sensors 3 and 10 are located away from the source. From C_{ave} and C_{ins} , it can be concluded that no pollutants reached those sensors in the first three minutes of the simulations. Concerning the measurement, C_{exp} shows fluctuations that can be due to sensor measurement errors. Sensor 9 is located on the window surface and measures pollutant concentrations at 3 m higher than the other sensors. The result of Sensor 9 shows that the fluctuation in C_{exp} is lower than that of the ground-based sensors (e.g., Sensor 1, 4, 6), and the measured pollutant concentration values are stable at around 510 ppm. The degree of increase of C_{ave} is less than that of the ground-based sensors. The increasing rate of C_{ave} can be sorted in the order of Sensor 1 > 4 > 6 > 9, implying that the C_{ave} simulations suggest that pollutants flow predominantly horizontally rather than vertically within Sense-City.

In summary, pollutant concentrations using the average airflow tend to be over-estimated in short-time simulations, particularly for sensors located on the leeward side of the source. This is attributed to the fixed average wind direction where pollutant diffusion due to variation of airflow direction is not considered. Despite constant CO₂ pollutant emissions during the measurements, there was no significant difference in pollutant concentrations before and after for all sensors. Regardless of the distance from the source, there was no noticeable difference in the degree of variation between the sensors. This might be partly due to the sensors' error margin, which encompasses the measured pollutant concentration fluctuations in the 3-minute CO₂ emission period. Consequently, it remains uncertain whether the

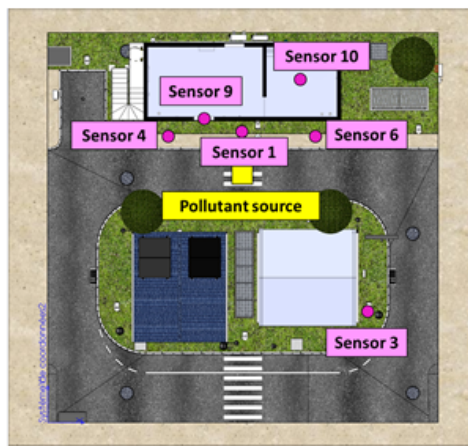
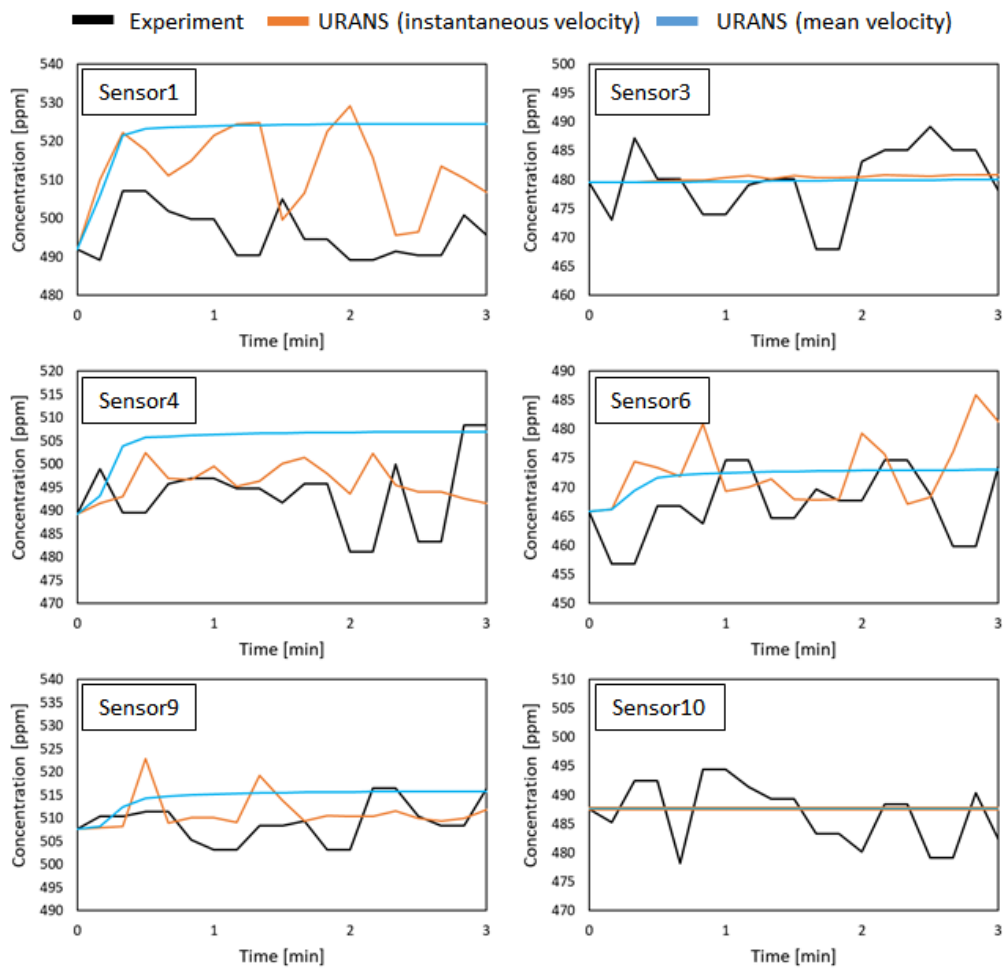


Figure 4.34: Time history of the pollutant concentration (CO_2 for the experiment and passive scalar for the simulations) in long-term simulation for 3 min.

concentration fluctuations reflect true pollutant concentration fluctuations or stem from measurement uncertainty. However, as we have seen in the previous airflow validation, the airflow is constantly fluctuating, which can lead to significant pollutant concentration fluctuations in short-duration dispersion cases. To capture these fluctuations, I recommend using URANS model for short-duration dispersion cases, instead of average velocity. In the future, by increasing the intensity of the CO₂ emissions during measurements to make it exceed the sensor's error range, differences in pollutant concentrations between sensors could become noticeable even for short-time scenarios. Furthermore, differences in the initial concentration between sensors were seen even before the CO₂ emission. For example, Sensor 9 shows around 510 ppm from the beginning, exceeding the value observed at Sensor 1 closest to the source. Although it was not shown here, such initial elevated CO₂ concentrations have also been observed by some sensors, e.g., near the extraction ducts and in the room closer to the ventilation system (near the rear window). One potential explanation is that CO₂ emissions could also originate from the ventilation systems themselves.

- **Long-duration cases**

Here I study the time history of pollutant concentrations in the long-duration scenario. Let me note that two different CO₂ measurements were conducted before the start of this experiment, and thereby air extraction system of the climatic chamber was activated for 40 min to renew the air inside Sense-City. As Fig. 4.35 shows, pollutant concentrations in the long scenario increase linearly through the measurement and simulation for many sensors, indicating that the recirculation of pollutants through the ventilation system (closed-cycle airflow circulation) can be reproduced in the simulation. Overall, similar to the results of the short scenario, for Sensors 1, 4, 6 and 9, C_{ave} increases sharply immediately after the start of the simulation and then it increases linearly, while C_{ins} and C_{exp} increase gradually from the beginning.

Table 4.11 presents the slope α of the linear regression line α for C_{ave} , C_{ins} and C_{exp} , along with statistical metrics (BIAS and RMSE) comparing the simulated and measured pollutant dispersion for C_{ave} , C_{ins} based on the data after 5 minutes at Sensors 1, 4 and 6. It is observed from all the slope α that the rate of increase in pollutant concentration at the leeward side sensors (Sensors 1, 4 and 6) at the pedestrian level is comparable for C_{exp} , C_{ins} and C_{ave} . When arranged in descending order of magnitude, the sequence remains consistently at every sensor: C_{ave} , C_{ins} , and C_{exp} . Considering the diffusion of pollutants by the fluctuation of airflow direction, it is easy to expect that C_{ave} , which does not account for such fluctuation, has

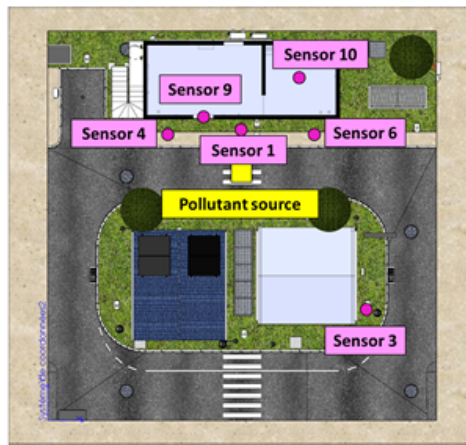
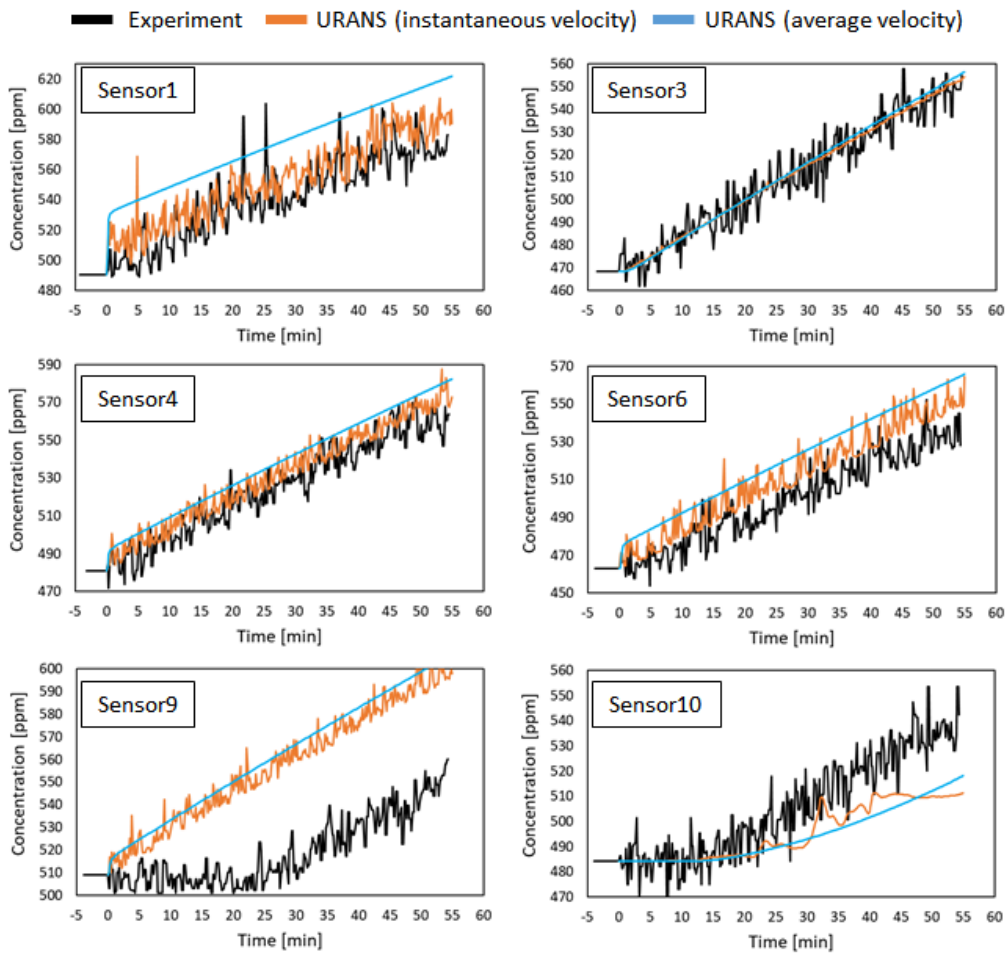


Figure 4.35: Time history of the pollutant concentration (CO₂ for the experiment and passive scalar for the simulations) in long-term simulation for 55 min.

the highest slope α . Nevertheless, despite differences in gradients, Fig. 4.35 does not exhibit significant changes in the gap between the experiments (C_{exp}) and each URANS model (C_{ins} and C_{ave}). Regarding BIAS in Table 4.11, C_{int} outperforms C_{ave} . The maximum BIAS value is obtained at Sensor 1 for C_{ave} , which is 34.4. These gaps in C_{ave} are primarily attributed to the initial rapid increase. RMSE also shows similar trends. Based on the slope, BIAS, and RMSE, therefore, we can conclude that both URANS models are capable of capturing the pollutant concentration on the leeward side of the pollutant source.

	Sensor1			Sensor4			Sensor6		
	C_{exp}	C_{ins}	C_{ave}	C_{exp}	C_{ins}	C_{ave}	C_{exp}	C_{ins}	C_{ave}
Slope α	1.5	1.62	1.64	1.52	1.58	1.64	1.42	1.58	1.63
BIAS [ppm]	-	10.3	34.4	-	6.3	12.5	-	12.1	21.6
RMSE [ppm]	-	18.3	36.8	-	10.5	14.4	-	15.7	23.0

Table 4.11: Accuracy validation: slope α of the linear regression line of the pollutant concentration and statistical metrics (BIAS and RMSE) comparing the simulated and measured pollutant dispersion at Sensor 1, 4, 6 in Sense-City.

Now let me move on Sensor 9. It is important to note that Sensor 9 is also on the leeward side of the pollutant source (like Sensor 1, 4, 6) but is located few meters higher from the ground. As can be seen in Fig. 4.35, C_{exp} starts to rise after 25 minutes of CO₂ emission start. Contrary to the simulation results showing a linear increase from the beginning, C_{exp} represents a completely different trend. Even the measured CO₂ concentration at Sensor 10, placed in the side room, starts increasing before Sensor 9. From flow validation, the pollutants in the Sense-City district are expected to enter predominantly from the front window, so Sensor 9 should start to increase earlier than Sensor 10. There are several possible reasons for these differences:

1. Airflow difference between the simulation and the experiment during this experiment;
2. Sensor accuracy;
3. Density of CO₂.

Airflow is the first possible explanation. Table 4.12 compares the flow velocity components at the front window (Sensor 9) in the airflow experiment and the present long-term simulation, which includes the inside modeling of the ventilation system.

	Experiment	Simulation with inside ventilation modeling
U_x (m/s)	0.31	0.18
U_y (m/s)	-0.38	-0.47
U_z (m/s)	0.37	0.36
$U_{magnitude}$ (m/s)	0.72	0.61
TKE (m^2/s^2)	0.13	0.19

Table 4.12: Velocity comparison at Sensor 9 between the experiment and the long-term simulation with the insider modeling of the ventilation systems.

According to this, the present long-term simulation shows higher U_y than in the experiment, where U_y is the velocity component normal to the front window now. Let me recall that negative values of U_y mean airflow enters the room from outside through the front window. Previously, I have pointed out that the Sense-City's street canyon causes airflow from the ground traveling along the building wall to enter the concrete building through the front window. The pollutants that enter the room are transported along the air currents along the outdoor building wall. In other words, only pollutants flowing near the building wall can enter the room. However, the current higher $|-U_y|$ (increased perpendicular velocity to the front window) also makes pollutants slightly further away from the building wall enter the room.

The second reason could simply be attributed to a deficiency in Sensor 9. In fact, in other experiments conducted after this long-term experiment, only Sensor 9 showed an abnormal trend of CO_2 concentration, where pollutant concentration was late to start increasing.

Lastly, the reason would be the density of CO_2 . CO_2 is heavier than air. Therefore, CO_2 tends to accumulate from the bottom, and thus the concentration increases from the bottom. However, in the simulation, the pollutants are passive scalar, and they do not accumulate from the ground, resulting in a different pollutant concentration time evolution at Sensor 9.

Finally, let me examine the pollutant dispersion characteristics in Sense-City. Fig. 4.36 illustrates pollutant concentration of URANS using instantaneous velocity at $t = 55, 80, 90$ s in the vertical cross-section at the front window ($x = 2m$) (Fig. 4.36 (a)) and contour surface at $C = 501$ ppm (Fig. 4.36 (b)). In Fig. 4.36 (b), the background concentration is considered 490 ppm. First, the time evolution of

the contour surfaces shows that pollutant dispersion fluctuates from left to right (at $t=55$ s towards the right extraction duct, at $t=80$ s during the movement from right to left and at $t=90$ s towards the left extraction duct). From the pollutant concentration in the vertical sections, it is shown that at $t=55$ the pollutant concentration is below 492 ppm in many parts of Sense-City, but at $t=90$ s, the pollutant concentration becomes higher in the whole Sense-City. Therefore, as mentioned, the increased flow velocity normal to the window $| - U_y |$ may have allowed more outdoor pollutants to enter the room (see the red arrow in Fig. 4.36 (c)). Therefore, the pollutant concentration in the simulation has been overestimated compared to the experiment (see again Sensor 9 in Fig. 4.35). Looking at Fig. 4.36 at $t = 80$ s, it can be seen that the pollutants emitted from the source enter the room after ascending along the building wall surface. Due to the inertia of the rising airflow, after entering the room, the pollutants firstly pass along the ceiling and wall (and finally floors but not presented here), and thereby high pollutant concentration is observed around the perimeter of the room. (The problem of the decoupled approach is that this kind of influence of outdoor airflow cannot be taken into account.) Based on these results, it is advisable to improve indoor air quality by placing depolluting panels just below the window as proposed in the study on the smart placement of depolluting panels (Section 4.2) to remove pollutants before they enter the room. Moreover, placing depolluting panels on surfaces of rooms' perimeters (ceiling, walls and floor) is promising to improve indoor air quality.

In summary, in the long-time scenario of about 1 hour, the slopes of pollutant concentrations of both URANS on the average and instantaneous airflow were very close to that obtained in the experiment, with the exception of observations on the 1st floor (Sensors 9 and 10). However, when the average airflow was used, there was a sharp increase in pollutant concentrations immediately after the start of the simulation (Sensors 9 and 10) because of the failure to consider the fluctuation of airflow direction. Overall, URANS on the instantaneous airflow is superior to the one on the average airflow in terms of accuracy, but URANS on the average airflow is a good compromise to get pollutant concentration increase trends at a lower computational cost and lower usage of storage in memory. An important finding on the interaction between outdoor and indoor air quality in Sense-City is that indoor pollutant concentrations increase from the perimeter, as pollutants travel along the perimeter of ceilings, walls and floors once they enter the room. Therefore, to effectively remove indoor pollutant concentrations using depolluting panels, it may be effective to place them below the window and/or on the room perimeter. Further detailed studies are needed in the future, taking into account different densities of pollutants and also Schmidt numbers in simulations and other

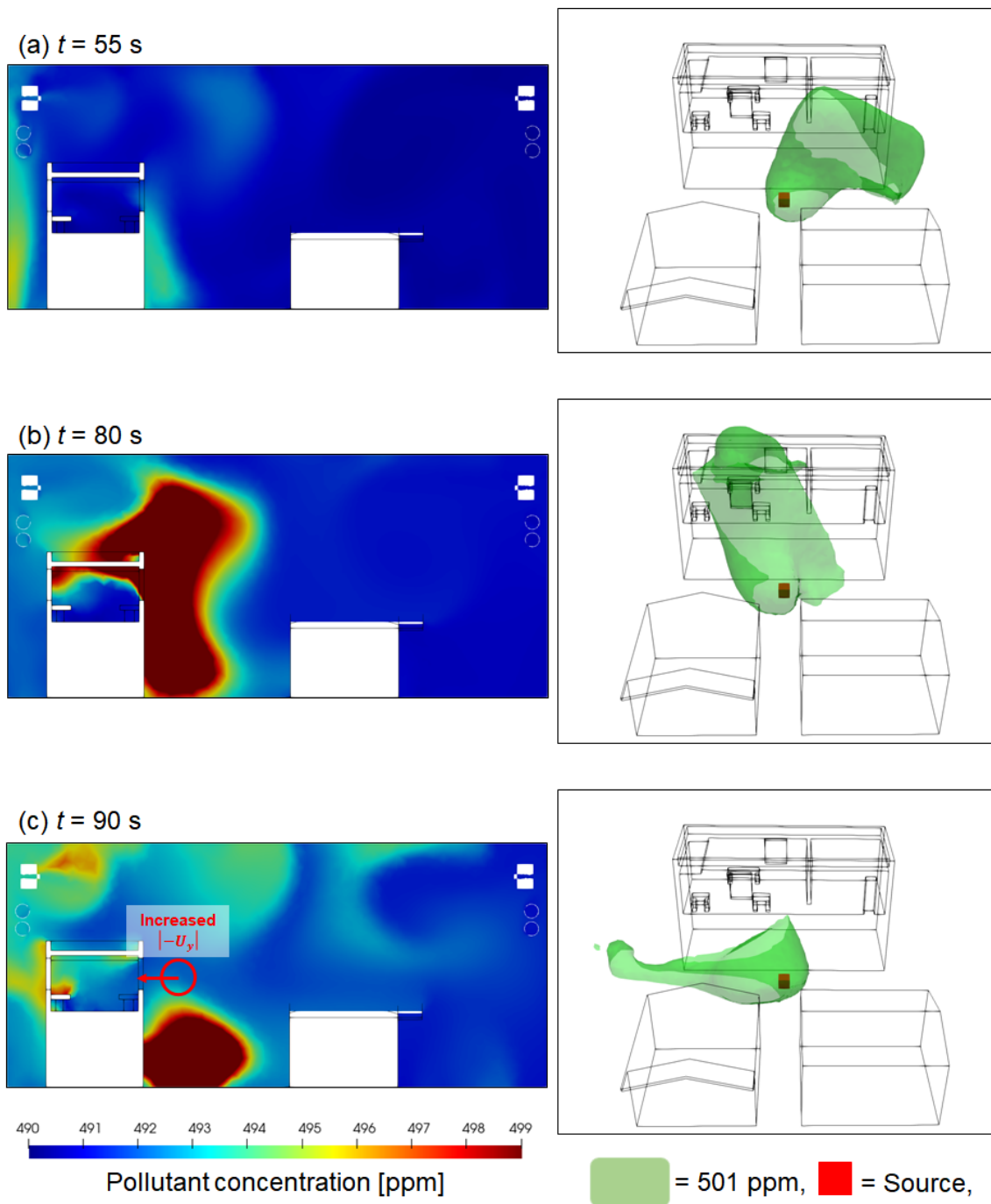


Figure 4.36: Time evolution of pollutant dispersion of URANS using instantaneous velocity in Sense-City at $t = 55, 80, 90$ s: (left) pollutant concentrations in the vertical cross-section at the front window at $x = 2$ m and (right) contour surface at $C = 501$ ppm. Background concentration is 490 ppm.

experiments to better predict the pollutant concentration evolution on the 1st floor of the concrete building.

4.4 Conclusion

In this chapter, the novel proposed numerical strategy is used for the first time. An example of an application is the Sense-City, a full-scale experimental city with controlled conditions, e.g., airflow. Subsequently, the interaction between outdoor and indoor air quality in Sense-City was investigated through the simulation and experiment. At the same time, appropriate numerical simulation approaches for the interaction between outdoor and indoor air quality were investigated. The key findings are outlined below:

- **Outdoor-Indoor Airflow and Air Quality Interaction:** When simulating the interaction between outdoor and indoor airflow and pollutants within Sense-City, the decoupled approach proved inaccurate as in Sense-City real airflow travels along the wall surface before entering indoors and airflow direction is not normal to an inlet window;
- **URANS Accuracy on Short Duration Pollutant Dispersion Simulation:** The accuracy of URANS on instantaneous and average airflow was compared in the short-term pollutant dispersion in Sense-City. In this case, the increase in measured pollutant concentrations was not noticeable and pollutant concentrations only showed fluctuations. In order to capture this variability, it is necessary to use URANS on the instantaneous airflow;
- **URANS Accuracy on Long Duration Pollutant Dispersion Simulation:** When simulating long-term pollutant dispersion in the Sense-City, whether URANS on the instantaneous or average airflow should be used depends on the location and distance from the source, and on how much initial increase of concentration can be compromised. Overall, URANS on instantaneous airflow demonstrated higher accuracy. Nevertheless, URANS on average velocity is still a good compromise to get pollutant concentration increase trends at a lower computational cost;
- **CO₂ Dispersion Experiment Insights:** From the CO₂ dispersion experiment, noteworthy observations were made regarding pollutant density and the ventilation period prior to the experiment. In addition, there were significant variations in the initial pollutant concentration values of the sensors, suggesting CO₂ emissions from within the ventilation systems of the climatic

chamber. These remarks will be beneficial in designing future pollutant dispersion experiments;

- **Comparative Assessment of Effectiveness of Smart Panel Placement:** The usefulness of the proposed numerical strategy was demonstrated by comparing the degree of pollutant removal in different depolluting panel placement scenarios. Arbitrary massive panel deployment did not improve air quality at all;
- **Smart Placement of Depolluting Panel:** The numerical strategy was employed to enhance air quality on the pedestrian level and indoors, suggesting some recommended panel placement: part of the road, of the sidewalk and of the building façade.

Chapter 5

Application to real conditions in Paris 8 district

In Section 4, the numerical strategy for the smart placement of depolluting panels was applied to Sense-City, where geometry is simple and weather conditions can be controlled. Accordingly, we demonstrated its effectiveness with regard to airflow. However, in most real-world scenarios, airflow is constantly changing, and urban geometry is complex. Considering the practical use of the proposed numerical methodology, it is important to validate its applicability to natural environments. In this section, therefore, I examine the suitability of the numerical strategy to a real urban district in Paris under different wind conditions and pollutant emissions from traffic. Realistic weather conditions and pollution situations in Paris are considered using the two most dominant wind directions encountered in Paris and actual measured data of NO_x concentrations on the roads from Airparif agency.

This chapter is organized as follows. First, the interaction between outdoor and indoor air quality in a realistic environment is investigated through experiments and simulations. To validate the outdoor simulation results, we compare them with data obtained from a monitoring station in Paris. Additionally, indoor air quality measurements for NO_2 are conducted in an apartment in Paris 8 arrondissement. A subsequent section is devoted to the smart placement of depolluting panels to improve outdoor air quality and to prevent indoor pollution deterioration due to the transfer of outdoor air quality indoors.

5.1 Description of Paris 8 arrondissement

The studied area in this chapter is a part of the 8th arrondissement of Paris, France (hereafter called the 8th district), located on the west side of Paris (see Fig. 5.1 (a)). This area includes residential, commercial, and political buildings and many tourist spots such as Avenue des Champs-Élysées (the green line in Fig. 5.1 (a)). Many streets in this area are known to be highly polluted because of the heavy traffic, e.g., Avenue des Champs-Élysées.

5.2 Study on the interaction between outdoor and indoor air quality in natural conditions in Paris via measurement and simulation

This section explores the interaction between outdoor and indoor air quality via measurements and simulation. In the measurement, indoor pollution concentrations are measured using multiple NO₂ microsensors placed inside an actual apartment. The decoupled approach is adopted in order to perform operational simulations. Indeed, the computational domain of Paris covers a huge area compared to Sense-City, leading to the difficulty of making a numerical mock-up including both outdoor and indoor domains.

5.2.1 Indoor NO₂ measurement in an apartment in Paris

This subsection describes the measurement of indoor NO₂ concentration in an apartment in the 8th district under natural ventilation. Two indoor NO₂ measurement campaigns, three days each, were conducted in October 2021 and November 2022. From them, I select one specific day (15th November 2022) to perform simulations and comparisons. This selection was based on several factors: the ambient NO₂ concentration in Paris was higher than the used NO₂ microsensor detection limit, and the flow direction and magnitude observed were more stable than other measurements. The other measurement results are given in Appendix A.

5.2.1.1 Target apartment in Paris

The target apartment is located in the north part of the 8th district in Paris, as indicated by the yellow circle in Fig. 5.1 (b); the exact address is 15 rue de Naples, 75008 Paris. It is located on the first floor of a Haussmann building (typical Paris

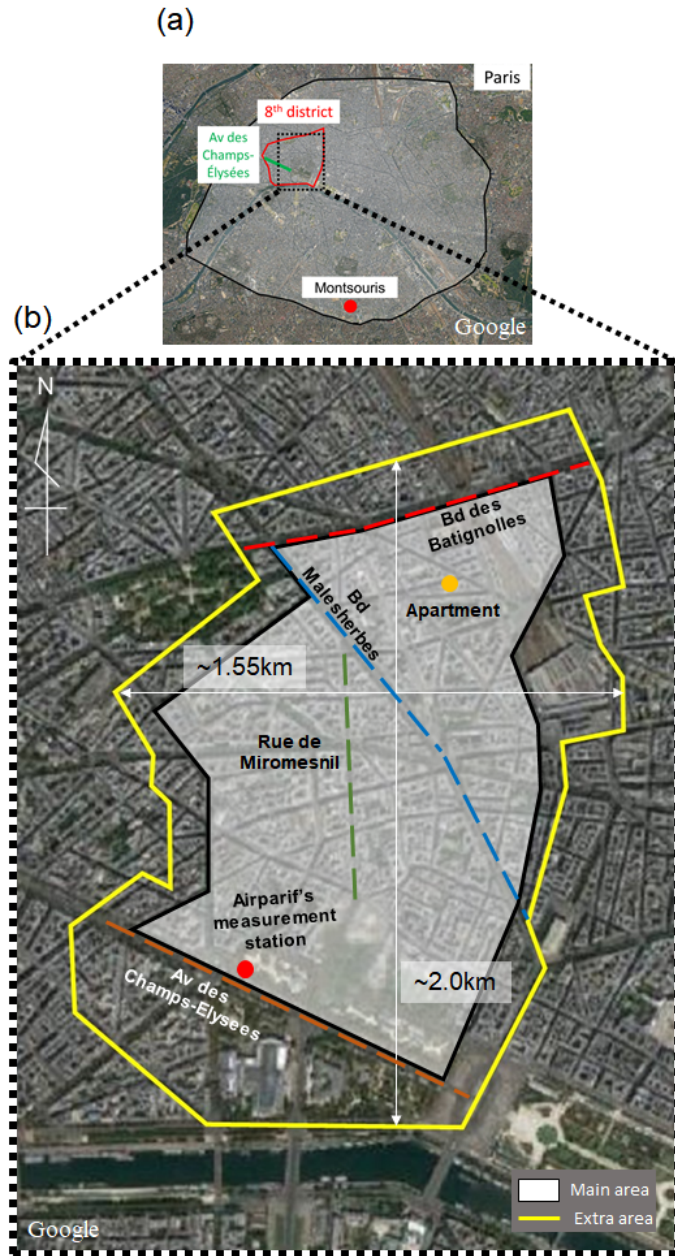


Figure 5.1: Paris 8 district: (a) overview of Paris and (b) studied domain in Paris 8 arrondissement.

building) and features various rooms, including a living room, a kids' room, a corridor, a kitchen, a bedroom, and a bathroom (see Fig. 5.2). The north side of the apartment faces a one-way road, and the south side faces a courtyard enclosed by neighboring buildings. It is worth mentioning that the apartment is being currently occupied by residents, and thus all furniture is in place, although no one is inside the apartment during measurements

5.2.1.2 NO₂ microsensor

For indoor NO₂ measurement, "Cairsens" microsensor, an electrochemical microsensor from "Envea," is used to measure NO₂ concentration (ppb). The sensor employs an aerometric technology, which measures current response as a result of an electroactive substance losing (oxidation) or gaining (reduction) an electron while undergoing an electrochemical reaction. The sensor consists of three electrodes: the working electrode, the counter electrode and the reference electrode. The electro signal generated between the working and counter electrodes is proportional to the pollutant concentration. NO₂ is captured by a controlled micro-fan at the bottom (Fig. 5.3). Regarding sensor accuracy, it is important to note that the sensor's minimum detection limit stands at 20 ppb although the sensor's measurement range spans from 0 to 250 ppb. Measurement values typically encompass a maximum 30% error of NO₂ concentration. The minimum sampling frequency is 1 min. Measurement data can be stored in the sensor directly. Once a measurement is finished, the data can be extracted in "Cairsoft," free software.

5.2.1.3 Experimental set-up for the indoor NO₂ measurement in the apartment

• Experimental condition

The selected day of the measurement is, as mentioned, November 15th, 2022, from 8:30 AM to 10:00 AM, a day with high ambient NO₂ concentration. In this experiment, two windows are considered as pathways for outdoor pollutants to enter the indoor environment: one window in the living room (see Fig. 5.2, referred as the "road-side" window) and one window in the bedroom (see Fig. 5.2, referred as the "courtyard-side" window); the dimensions of the road-side windows is 1.3 m wide × 1.8 m height and the courtyard-side windows 1.3 m wide × 1.6 m height. The windows remain closed from the previous night of the experiment's day until the experiment starts. Then at the start of the measurement, both windows are opened to study outdoor and indoor pollutant transfer by natural ventilation, and they remain open during the experiment. All internal pathways (doors) connecting the rooms are kept open throughout the experiment except for the entrance door.

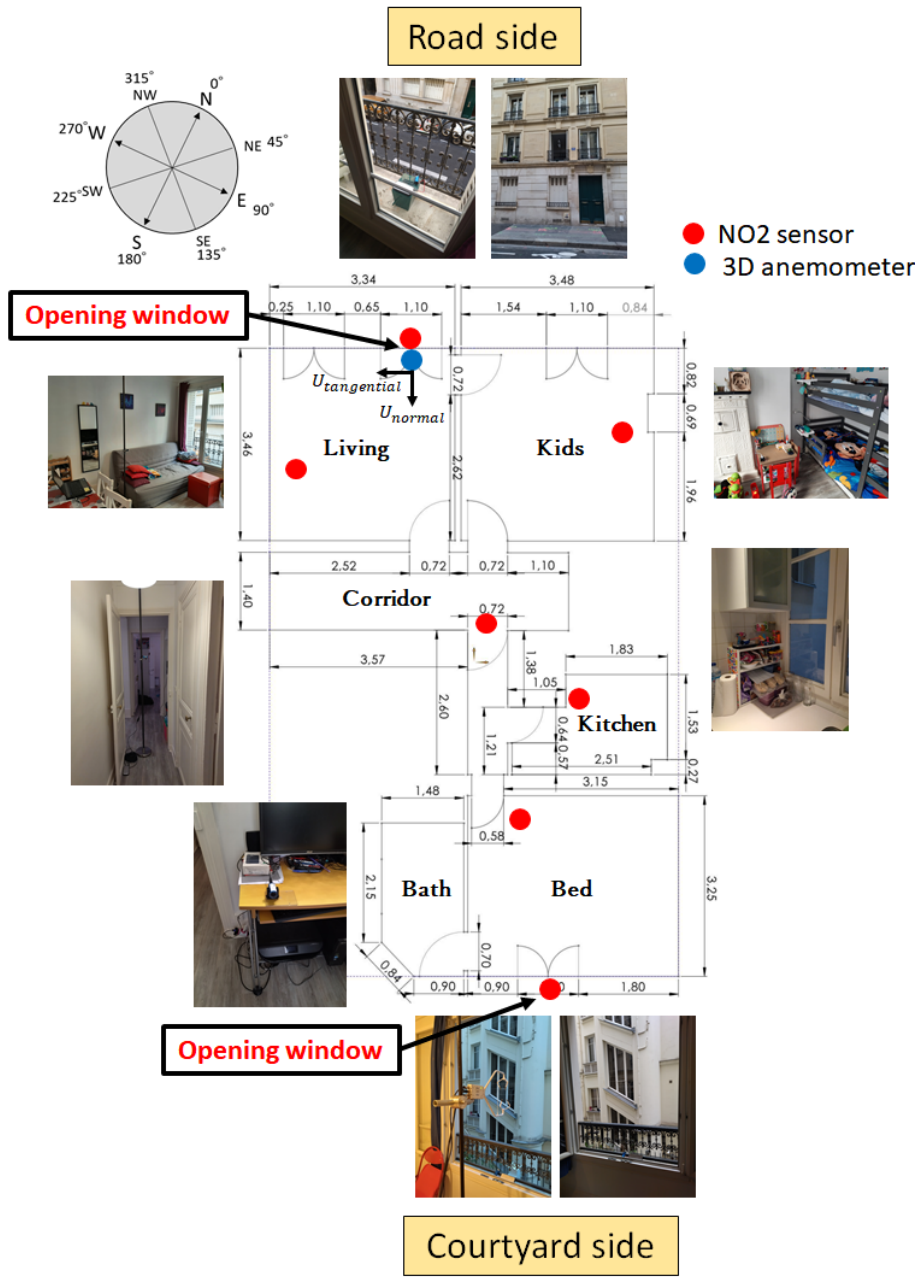


Figure 5.2: Floor map of the 1st floor of the target apartment and NO₂ microsensors location.

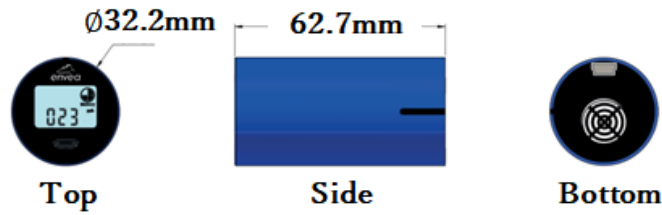


Figure 5.3: Cairsens NO₂ microsensors.

All heating and ventilation systems are turned off. No one is in the room for the duration of the measurement.

- **Position of NO₂ microsensors and 3D anemometer**

A total of seven NO₂ microsensors are installed; one sensor is allocated to each room, excluding the bathroom. Furthermore, a sensor is placed at the road-side window and also at the courtyard-side window to measure outdoor pollutant concentrations at the windows. The positions of each sensor are indicated by the red circles in Fig. 5.3. Specifically, the sensors in the living room and corridor are mounted on masts at a height of 1 m and 1.5 m respectively. Sensors within the other rooms are placed on furniture items like desks. To measure flow velocity, a 3D anemometer is used at the road-side window where airflow was predicted to enter based on the weather forecast in advance. According to a monitoring station at the height of 10 m at Montsouris station in Paris (see the red circle in Fig.5.1 (a)) on November 15th, 2022, from 8:30 AM to 10:00 AM, averaged velocity and direction were 180° and 3.9 m/s. However, note that this information was only available after the experiment.

- **Verification of NO₂ microsensors accuracy**

To verify the accuracy of the seven NO₂ microsensors used in my Ph.D. experiment, I compared NO₂ concentrations between the microsensors and analyzer (reference sensor) of the Sense-City equipment. The microsensors were placed outdoors for 9 days in Sense-City (Chapms-sur-Marne). A tube from the analyzer was extended near the microsensors so that the analyzer measured the same air quality as the microsensors (see Fig. 5.4). The individual microsensors' numbers and their corresponding placement in the indoor measurement campaign in the Paris apartment are listed in Table 5.1. Fig. 5.5 illustrates the time series of the concentrations recorded with the seven microsensors and analyzer over the 9 days. Generally, the trends are similar. During the period from February 8th to 12th, when high pollu-

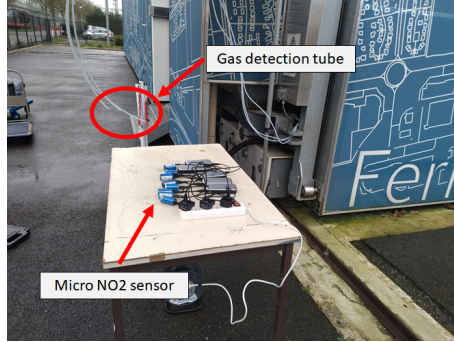


Figure 5.4: Picture of the NO₂ analyzer and NO₂ microsensors for sensors' validation.

No.	Number	Position
1	9425	Living room
2	9426	Kids room
3	9433	Corridor
4	9431	Kitchen
5	9427	Bedroom
6	9432	Road-side window
7	9434	Courtyard-side window

Table 5.1: Sensor numbers and placement in indoor measurement campaign.

tant concentrations were observed, the microsensors underestimated some very big peaks compared to the analyzer. However, concerning other peaks, the microsensors captured them. At very low pollutant concentrations, particularly less than 5 ppb, the analyzer captured those lower concentrations, but the microsensors did not. As the detection limit of the NO₂ microsensor given by the manufacturer is 20 ppb. Nevertheless, a good agreement between the microsensors and the analyzer is obtained for NO₂ concentration in the range 10 ppb \sim 20 ppb.

In addition, three validation metrics are calculated to evaluate the accuracy, BIAS, MAE and RMSE:

$$BIAS = \frac{1}{N} \sum_{i=1}^N (y_i - \hat{y}_i) \quad (5.1)$$

$$MAE = \frac{1}{N} \sum_{i=1}^N |y_i - \hat{y}_i| \quad (5.2)$$

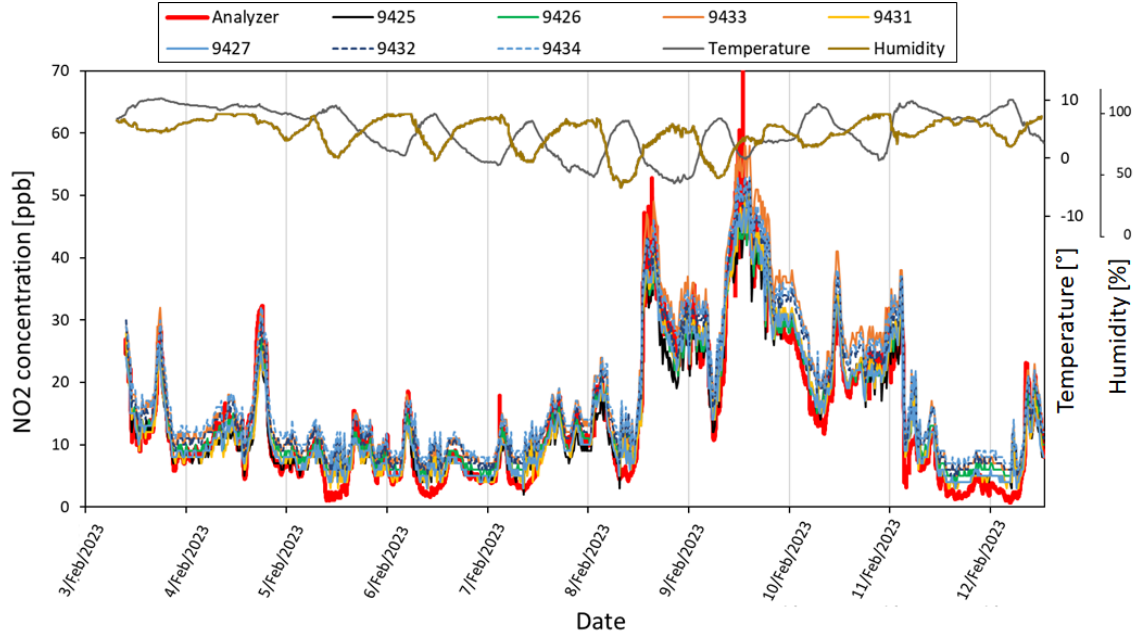


Figure 5.5: Time history of NO₂ concentration for the analyzer and microsensors for 9 days in February 2023.

$$RMSE = \sqrt{\frac{1}{N} \sum_{i=1}^N (y_i - \hat{y}_i)^2} \quad (5.3)$$

where N represents the number of sampling points (herein 919 points measured every 15 min), y_i is the concentration of the NO₂ microsensors, and \hat{y}_i is the concentration of the analyzer. All the indicators show the same trend where microsensors 1, 2, 4, and 5 have better scores than the remaining sensors. Indeed, microsensors 1, 2, 4, and 5 exhibit BIAS below 1 ppb. In contrast, microsensors 3, 6, and 7 show BIAS above 3 or 4 ppb. Looking at MAE and RMSE, they show similar score trends. In summary, from the results of validation metrics, the maximum RMSE is about 4 ppb, but this can be considered in an acceptable error range. Assuming 20 ~ 40 ppb as an outdoor pollutant concentration, ± 8 ppb ($= 2 \times RMSE$) corresponds to 40 ~ 20 % errors, which is an acceptable error range. Consequently, I use the NO₂ microsensors without a calibration phase.

	No.1	No.2	No.3	No.4	No.5	No.6	No.7
BIAS	-0.16	0.91	4.18	0.31	0.41	3.10	4.35
MAE	2.20	2.12	4.25	1.95	2.03	3.34	4.44
RMSE	2.93	2.73	4.84	2.60	2.71	3.95	4.93

Table 5.2: Validation metrics in ppb for the NO₂ microsensors in comparison with NO₂ analyzer (reference sensor) in Sense-City: BIAS, MAE and RMSE.

5.2.1.4 Result and discussion of apartment measurement

Fig. 5.6 illustrates the NO₂ concentration during the first 30 minutes of the measurement in the apartment in Paris on 15th November 2022, along with the normal U_{normal} , horizontal tangential $U_{tangential}$, and vertical wind velocities recorded by the 3D anemometer positioned at the road-side window. For the definition of the wind directions, see Fig. 5.2. The window was opened at 8.40 a.m. and measurements were taken over two hours. Only the results of the first 30 minutes are shown in Fig. 5.6 because the pollutant concentrations reached a stable state after 30 minutes.

Fig. 5.6 (a) reveals that the pollutant concentration increased rapidly within the first 5 minutes. After 15 minutes, it reached an almost steady level around 15 ppb. The two sensors placed at the windows (the road-side and courtyard-side windows) constantly show outdoor pollutant values between 15 ppb and 20 ppb. It indicates that the indoor pollutant level reaches the outdoor pollutant level within about 15 minutes following the window’s opening. Let me underline that, from the experimental observations, the outdoor NO₂ concentration at the windows can be considered as constant on the measurement duration (about 1 hour). It also justifies the choice of a constant outdoor pollutant level on a 3-minute time interval at the inlet window in Sense-City simulations (Section 4.2.2.4). In the Paris apartment, the order of the pollutant concentration increase is as follows: living room, corridor, kids’ room, bedroom, and kitchen.

Upon examining the velocities (Fig. 5.6 (b) and (c)), U_{normal} , $U_{tangential}$, and $U_{vertical}$, they show non-changing wind directions especially during the first 15 minutes. This is one of the reasons why I chose this day as the target day for outdoor and indoor simulation. After 15 minutes, the airflow has higher fluctuations, but these fluctuations are unlikely to pose an issue in the indoor pollutant concentration’s behavior as the indoor pollutant levels had already stabilized.

Table 5.3 provides the average velocities in each direction during the first 15 minutes. The average normal component to the window surface, U_{normal} , is measured

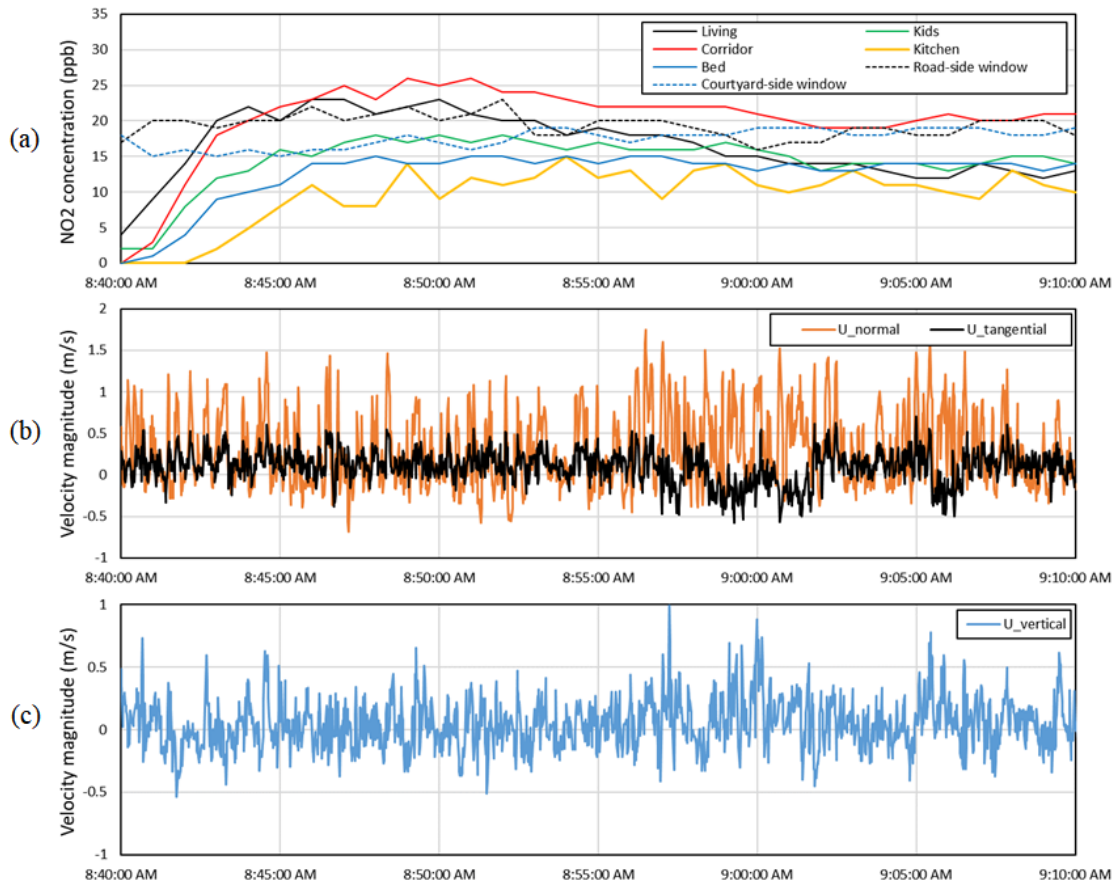


Figure 5.6: Measurement results in the Paris apartment: (a) NO₂ concentration at each sensor, (b) Normal and horizontal tangential velocity at the road-side window, (c) vertical velocity at the road-side window.

at 0.23 m/s, meaning that the airflow entered (not leave) the living room through the road-side window. Furthermore, the horizontal tangential component, $U_{tangential}$, displays a positive value at 0.15 m/s, which indicates that the airflow entering from the window surface has some SW directional component (opposite to the children’s room direction). $U_{vertical}$ is very small and can be neglected.

Average velocity (m/s)	
U_{normal}	0.23
$U_{tangential}$	0.15
$U_{vertical}$	0.01

Table 5.3: Average velocity at the road-side window for the first 15min.

In summary, from the order in which the NO_2 concentrations increase at the sensors and each velocity component, it becomes apparent that the pollutants entering through the road-side window were initially directed towards the sensor in the living room. Subsequently, it dispersed into the corridor and kids’ room. The kitchen is situated along the corridor and on the way to the bedroom. Nevertheless, as the primary airflow direction in the corridor is oriented towards the bedrooms, the pollutant levels increase in the bedrooms first, followed by the subsequent increase in the kitchen. The details of the outdoor pollutant transfer into the apartment and how to disperse indoors will be clarified by the indoor simulation in Subsection 5.2.3. In the next subsection, at first, the outdoor velocity and pollutant concentration are simulated, which are used as the boundary conditions for the indoor simulation.

5.2.2 CFD modeling for outdoor air pollutant dispersion

This subsection describes the simulation for outdoor pollutant dispersion. After extracting the weather conditions on November 15th, 2022, from 8:30 AM to 10:00 AM (period of indoor NO_2 measurement), the outdoor NO_x air pollutant concentrations in the 8th district are reproduced using CFD. In Paris simulation, the hourly average outdoor pollutant concentration is calculated instead of the transient solution. Let me recall that once NO_x is obtained, NO_2 concentration is deduced by Derwent and Middleton function [120] that is a polynomial-logarithmic function linking hourly averaged NO_x and NO_2 concentrations for NO_x concentrations in the range of 9.0 – 1145.1 ppb. By using Derwent and Middleton function (Eq. (3.43)), hourly averaged NO_2 concentration in $\mu\text{g}/\text{m}^3$ is obtained. Based on the information on NO_x concentrations provided by Airparif, volumic pollutant sources are placed only

on 44 major roads in the considered simulation domain, not all the roads (see Sub-section 5.2.2.2). Then, the simulated NO_x and NO₂ concentrations are compared with the monitoring station on Av des Champs-Élysées and the indoor measurement campaign.

5.2.2.1 Numerical mock of Paris 8 arrondissement

- **Considered domain**

The studied area is a part of the 8th district, as outlined with the yellow lines in Fig. 5.1 (b). The white area in Fig. 5.1 (b) represents the main area of study, encompassing the apartment and the monitoring station on Av des Champs-Élysées of Airparif agency (see the red circle in Fig. 5.1 (b) and 5.7) to validate simulation results with the measurement values. To replicate incoming airflow affected by the neighboring structures, an extra region is introduced, depicted through the yellow lines within Fig. 5.1 (b). The domain's dimensions are approximately 2 km in the NS (North-South) direction and 1.55 km in the EW (East-West) direction. Notably, several streets within this area, such as Av des Champs-Élysées, Bd Malesherbes, Rue de Miromesnil, and Bd Batignoiles, are known to be significantly polluted due to substantial traffic congestion.

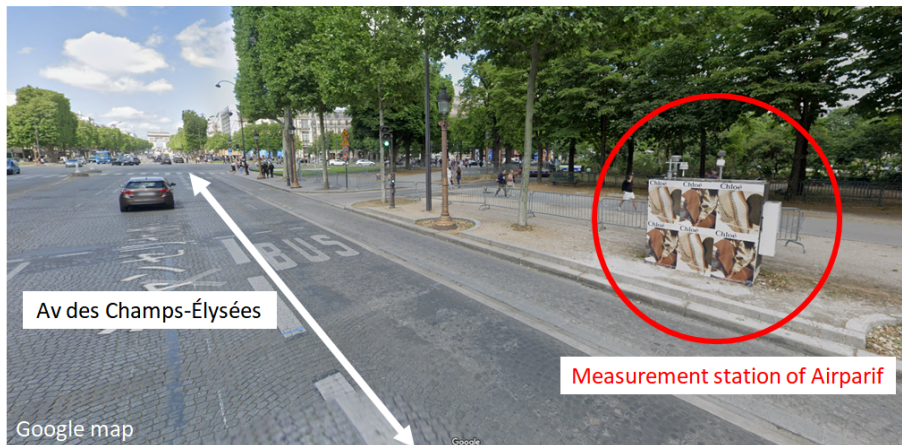


Figure 5.7: Measurement station of Airparif in Av des Champs-Élysées.

- **Software chain for Paris' numerical mock-up**

Herein, my objective is to propose a semi-automatic software chain to minimize manual intervention for making numerical mock-ups of real urban districts. The numerical mock-up of the considered area is generated *via* a dedicated software chain,

as shown in Fig. 5.8. From "IGNMap" [142], 2D shapes with height information of each building are exported as shape files. Then, 3D geometry is obtained by the automatic extrusion process in "CityEngine" [143]. The building plane information obtained from IGNMap may contain some minor errors, such as overlapping building corners or missing buildings. These errors should be corrected manually in "CityEngine", and the corrected data is then imported into "Solidworks" [144] as object files. This step in Solidworks is critical. In this step, adjacent buildings extruded in CityEngine must be combined. Otherwise, the building cannot be made to be solid in the next step, or objects with zero thickness are created that cause errors in meshing. Once the neighboring building groups are successfully combined, the data is imported into Fusion360 [145] as STL files and converted to a solid as STEP files, making it available in the meshing software "SALOME" [136].

• Numerical mock-up and computational domain for outdoor and indoor simulation

Fig. 5.9 (a) shows an overview of the numerical mock-up in the computational domain. The wind direction is 180 degrees (coming from the south), which was obtained from a meteorological station at Montsouris station in Paris on November 15th, 2022, between 8:00 AM and 9:00 AM. Let me note that, in the main area (white area in Fig. 5.1 (b)), the buildings have their actual height and courtyards, even though small gaps of the height between adjacent buildings are smoothed and small courtyards are removed (see the main area in Fig. 5.9 (b)). On the other hand, the buildings in the extra area (yellow line in Fig. 5.1 (b)) are simplified; the height of each building block is constant, and courtyards are eliminated (see the extra area in Fig. 5.9 (b)). In addition, the elevation differences in the terrain are not taken into account because the actual terrain has a height difference of only approximately 20 m between the northern and southern ends of the main zone. The dimensions of the domain are 2500 m x 3500 m x 500 m. Each distance from the outer buildings to the boundary of the domain is determined by reference to a CFD guidebook from Architectural Institute of Japan [56], suggesting maintaining enough length to avoid the interaction between flow and the domain boundary except for the inlet face where the distance between them should be small enough to let the inflow keep its inlet profile until the main domain. Vertical length is more than $10H_{max}$. Here, H_{max} equals 42.5 m, corresponding to the maximum building height.

5.2.2.2 CFD modeling and numerical set-up

As with Sense-City case, the direct simulation for flow and pollutant dispersion in Paris is performed with Code_Saturne. In order to compromise between computational stability and cost, we consider the pseudo-steady-state incompressible RANS

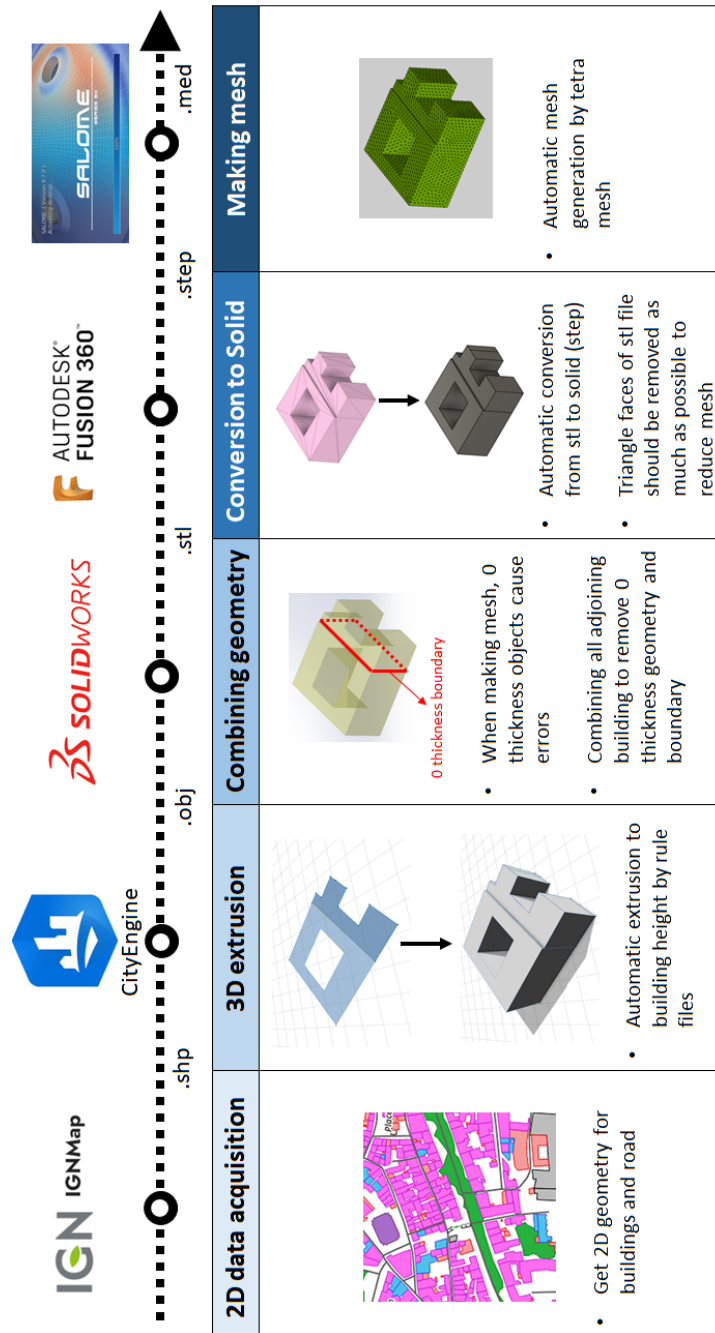


Figure 5.8: Proposition of a dedicated software chain for making numerical mock-ups of urban districts.

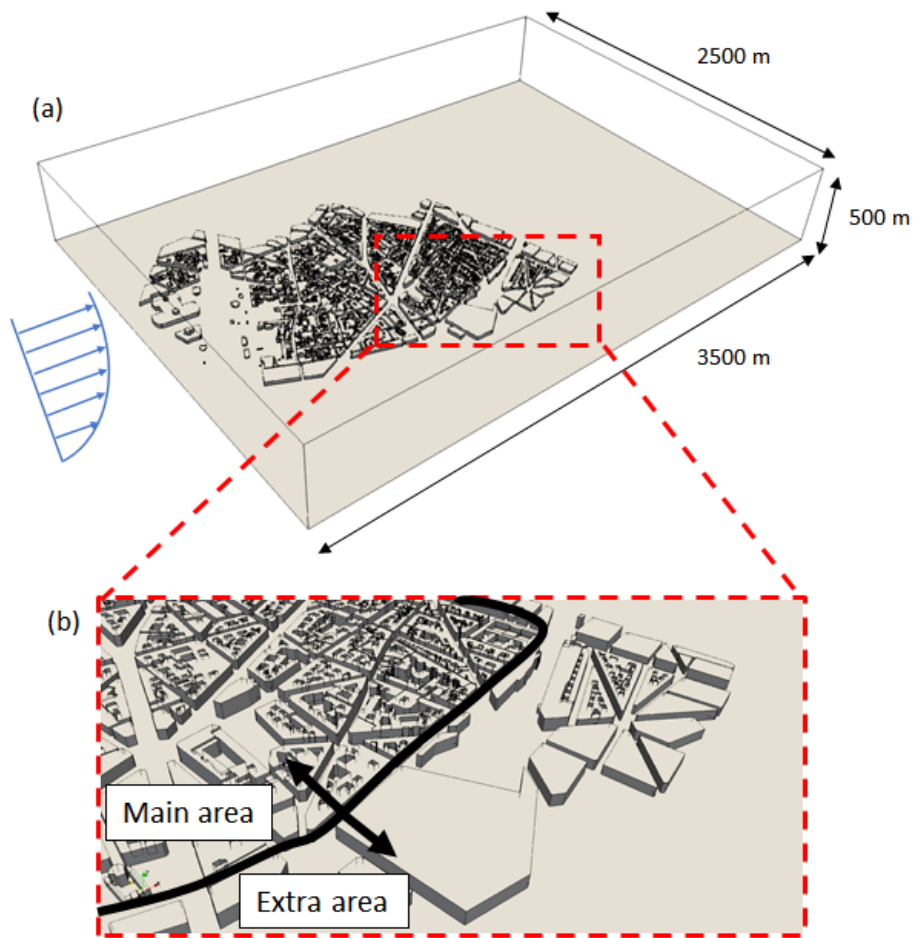


Figure 5.9: Computational domain: (a) overview and (b) detailed view.

with $k - \omega$ SST turbulence model. The key difference between the pseudo-steady-state solvers and the unsteady-state solvers used in the previous chapter is that in the pseudo-steady-state method, an artificial transient term ($\frac{\partial u_i}{\partial t_p}$) is used instead of the time derivative term ($\frac{\partial u_i}{\partial t}$) to march forward in time;

$$\frac{\partial \langle u_i \rangle}{\partial t_p} + \frac{\partial \langle u_i \rangle \langle u_j \rangle}{\partial x_j} = -\frac{1}{\rho} \frac{\partial \langle p \rangle}{\partial x_i} + \frac{\partial}{\partial x_j} \left[(\nu + \nu_t) \left(\frac{\partial \langle u_i \rangle}{\partial x_j} + \frac{\partial \langle u_j \rangle}{\partial x_i} \right) \right] \quad (5.4)$$

$$\frac{\partial C}{\partial t_p} + \langle u_i \rangle \frac{\partial C}{\partial x_i} - D \frac{\partial^2 C}{\partial x_i \partial x_i} = S \quad (5.5)$$

It looks similar as the unsteady-state equations (Eq. (4.7 and 4.16)), but notably the magnitude of time step Δt_p varies for each cell depending on chosen Courant number (CFL, $CFL = u \Delta t / \Delta x$). For example, when one defines $CFL = 1$ as a CFL threshold in the pseudo-steady-state simulation, Δt_p is adjusted in each cell in order to satisfy $CFL \leq 1$ as much as possible within a designated change limit of Δt_p . Thus, Δt_p changes in each cell locally in the pseudo-steady-state method. For this reason, the transient solution has no physical meaning in the pseudo-steady-state method. Only final and convergent enough solutions can be interpreted as a result. Herein, CFL is set to be 10, and thereby Δt_p varies in a way that CFL is less than 10. In my Ph.D., after 4,000 iterations where the solution reaches a sufficiently steady state, the average values of airflow and pollutants are calculated from another 1,000 additional iterations. Here, the airflow and pollutant dispersion are simultaneously solved by coupling Eq. (5.4 and 5.5). Concerning other numerical aspects, the same numerical settings are employed as with Sense-City case: $k - \omega$ SST turbulence modeling; implicit Euler scheme for time integration, the second-order linear upwind scheme for the convective term of the velocity $\langle u_i \rangle$, turbulence kinetic energy k , and specific dissipation ω and pollutant concentration C , SIMPLE algorithm, turbulent Schmidt number Sc_t at 0.7.

5.2.2.3 Boundary conditions

At the inlet faces, as shown in Eqs. (5.6-5.8), I impose a logarithmic profile for velocity, a constant value for kinematic energy and a height-dependent profile for specific dissipation assuming fully developed inflow conditions [146].

$$U = \frac{u_*}{\kappa} \ln \left(\frac{z + z_0}{z_0} \right) \quad (5.6)$$

$$k = \frac{u_*^2}{\sqrt{C_\mu}} \quad (5.7)$$

$$\omega = \frac{u_*}{\sqrt{\beta'} \kappa_{k-\omega} z} \quad (5.8)$$

where u_* , z_0 , and κ are the friction velocity, the roughness length, and Von Karman constant. The roughness length is taken to 1 m. To define u_* for the inlet velocity profile, I use velocity measurement data at 10 m height at Montsouris station in Paris. It corresponds to 3.9 m/s, and thereby u_* is 0.67 deduced from Eq. 5.6. The details of the coefficients $C_\mu = 0.09$, $\beta' = 0.09$ and $\kappa_{k-\omega} = 0.408$ can be found in [146]. On the outlet face, zero-gradient conditions are imposed. Wall function is used on the bottom face and all the building surfaces. For other boundaries, symmetry conditions are given on laterals and upper faces. As mentioned, the wind direction is constant at 180° (south direction).

5.2.2.4 Model of traffic pollutant: NOx emission data from Airparif

Concerning NOx emission from traffic, almost all the roads inside the domain can be considered as traffic pollutant sources in reality. However, we consider 44 main roads (Fig.5.10) as pollutant sources which are modeled using the volumic source term in the advection-diffusion equation (Fig. 5.5). According to Airparif agency, those roads have the highest significant contribution to air pollution in this area. On these 44 roads, one-hour average NOx values are estimated every hour by Airparif agency using emission factors from COPERT [135] and data assimilation, which combines observed data and a traffic model. These one-hour average NOx values are used as the magnitude of the 44 pollutant sources. The magnitude of NOx emissions on each road are given in $\mu\text{g}/\text{m}^3/\text{s}$. The details of NOx magnitude are shown in Table 5.4. The pollutant volumic sources are defined on the roads from 0 m to 1 m height to mimic traffic emissions. The width of the pollutant is determined based on the number of lanes, with each lane of the road considered to be 3.5 m wide. For instance, for a road with one lane, the width of the pollutant source is 3.5 m; if the road has two lanes, the width of the source is 7 m.

5.2.2.5 Mesh configuration

To construct a mesh efficiently, the computational domain is divided into four parts: Vol.1 is near the building, Vol.2 is defined from the inflow surface to the area at the vicinity of the building, Vol.4 is the area close to the outlet, and Vol.3 is the remaining other parts of the domain (see Fig. 5.11 (a) and (b)). The maximum and minimum mesh sizes in each of these regions are given in Table 5.5. The minimum mesh size is 2 m at the pollution sources (Fig. 5.11 (c)) and the surface of the target apartment, and 3 m for the other buildings' surface and the ground surface in Vol.1

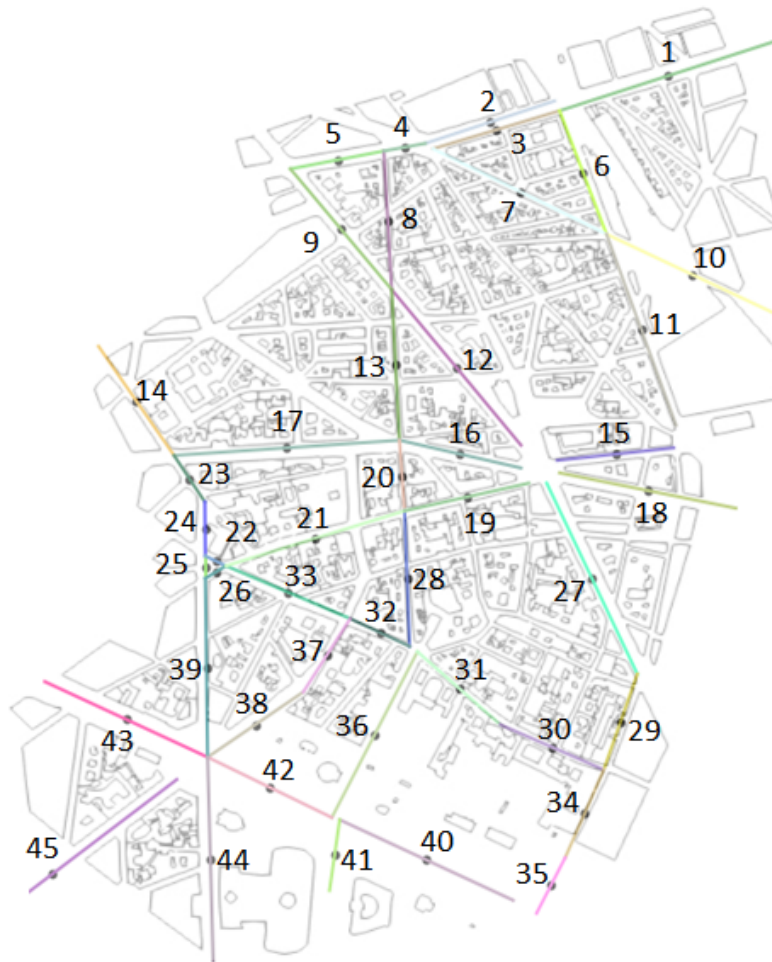


Figure 5.10: Position of NO_x pollutant source on the 44 main roads in Paris 8 district.

~ 3. From the smallest mesh on each surface, the size gradually increases as one moves further inside the domain, up to a maximum of 3 m within Vol 1. In Vol 2, the size gradually increases from 3 m on the ground to a maximum of 10 m. In other areas, even larger meshes are placed. Consequently, the total number of cells is 22,825,760. An overview is given in Fig. 5.11 (d).

$(\mu\text{g}/\text{m}^3/\text{s})$					
No. road	NOx	No. road	NOx	No. road	NOx
1	13.2	16	12.9	31	6.0
2	9.9	17	5.1	32	23.2
3	17.4	18	31.2	33	0.0
4	21.8	19	24.9	34	4.9
5	16.1	20	4.7	35	32.3
6	43.7	21	14.2	36	14.5
7	3.4	22	7.7	37	18.9
8	10.5	23	16.0	38	12.6
9	24.4	24	16.0	39	14.8
10	3.5	25	9.7	40	10.8
11	34.5	26	11.9	41	28.9
12	12.3	27	10.1	42	13.8
13	27.5	28	8.2	43	17.7
14	21.8	29	3.3	44	15.0
15	14.8	30	6.0	45	7.5

Table 5.4: Magnitude of NOx pollutant sources on the roads ($\mu\text{g}/\text{m}^3/\text{s}$) on 15th November 2022 8 AM \sim 9 AM.

Volume	Min (m)	Max (m)
Vol.1	2	3
Vol.2	3	10
Vol.3	3	25
Vol.4	3	30
Traffic pollutant source	2	
Bottom of Vol.1 \sim 3	3	
Surface on the target apartment	2	

Table 5.5: Mesh size of the Paris 8 domain discretization when wind direction at 180° (south direction).

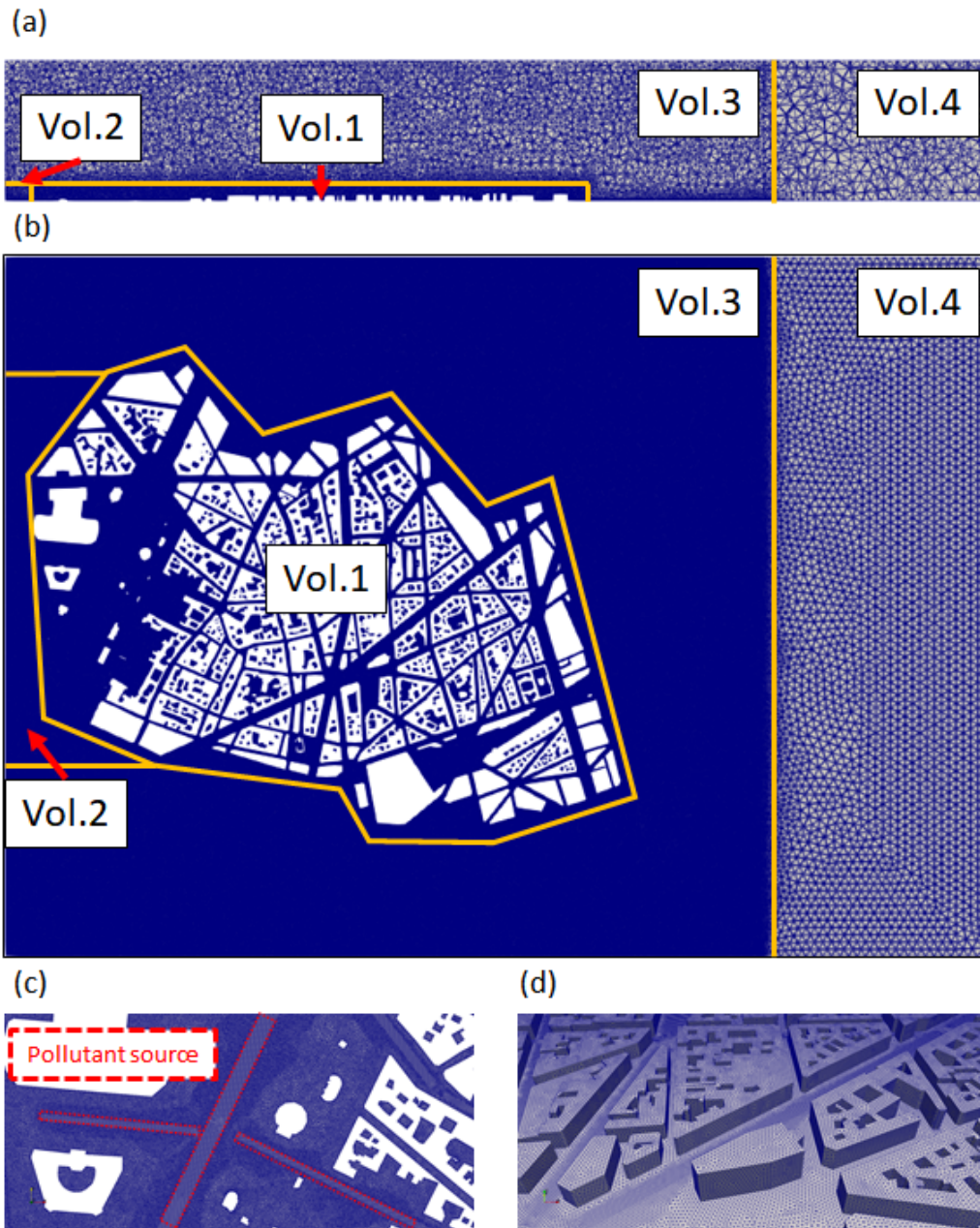


Figure 5.11: Mesh configuration: (a) vertical section, (b) horizontal section at $z = 1.5$ m, (c) mesh near the pollutant sources and (d) overview.

5.2.2.6 Simplifications and limitations for simulations of Paris study

Some assumptions are made to simplify the simulations of Paris study case in terms of geometry, airflow, pollutant dispersion, and chemical modeling as follows;

- *Wind direction*: wind direction is always constant at 180° from the south so the real fluctuation of wind direction is not considered;
- *Estimated traffic pollution emission*: as mentioned, the pollutant sources are estimated from a traffic model and pollutant emission factors. The type of fleet and the vehicle speeds not being well-known, these input data are subject to significant uncertainties;
- *No height variation in the geometry*: in the present Paris domain, the elevation is about 20 m lower from north to south in reality. which can influence the airflow. Nevertheless, I do not consider the height variation of the terrain;
- *Airflow disturbance induced by urban equipment, trees, traffic, and temperature*: trees and vehicles can increase turbulence and air mixing in urban areas. Thereby, they may facilitate the dispersion of pollutants and reduce pollutant accumulations. However, for simplicity, they are not considered in my Ph.D. In the same way, some geometrical details, such as urban equipment, are not included in the digital twin. Furthermore, I do not consider the buoyancy effects caused by temperature-induced density changes and the atmospheric stability caused by temperature differences between the ground and the atmosphere;
- *Chemical reaction of traffic pollutants*: from NO_x traffic emissions data, background concentration and the detailed velocity field, I compute the cartography of NO_x concentration in the Paris domain using advection-diffusion PDE without reaction terms. I neglected the possible reaction with other chemical species like COV;

5.2.2.7 Result and discussion for outdoor airflow and NO_x dispersion in Paris 8 district.

Fig. 5.12 and 5.13 illustrate the average velocity and average NO_x pollutant concentration at a height of 1.5 m, on November 15th, 2022, between 8:00 AM and 9:00 AM. With regard to the average velocities, high velocities with a maximum magnitude of approximately 4 m/s can be seen around Av des Champs-Élysées (e.g., see ①). These high velocities gradually diminish upon entering the inside of the urban district. Nevertheless, some big roads have high velocities even inside the urban area (e.g., see ②). Furthermore, airflow is accelerated in some roads even

though they have narrow widths and perpendicular orientation to the wind direction (e.g., see ③). Otherwise, airflow is frequently accelerated within the urban area, particularly at intersections where airflow converges (e.g., see ④). Courtyards surrounded by buildings also experience higher velocities, especially when the area is large (e.g., see ⑤). Concerning low-velocity regions, large areas of reduced velocities are found behind large dimension buildings (e.g., see ⑥). In addition, we can identify some low-velocity regions; many portions of Rue de Miromesnil (e.g., see ⑦), at the intersection of Rue de Miromesnil and Bd Malesherbes (see ⑧), and at complex intersections formed by multiple roads (see ⑨). As well as acceleration areas in many parts of the city, deceleration areas are observed in many places (e.g., see ⑩). Moreover, street canyon flows are seen on roads situated close to perpendicular angles relative to the wind direction of 180° (e.g., see ⑪).

Regarding pollutant concentrations, in Fig. 5.13, the upper limit of the NOx concentration range is set at $200 \mu\text{g}/\text{m}^3$. Let me note that the pollutant concentration of $26.3 \mu\text{g}/\text{m}^3$ observed at the air quality subway station *Chatelet-Les Halles* was added across all areas as a background concentration. In most of the regions far from the 44 main emission roads, the pollutant concentrations remain below $60 \mu\text{g}/\text{m}^3$, indicating generally moderate pollution levels. Simulated pollutant concentrations exceeding $200 \mu\text{g}/\text{m}^3$ are confined to specific, limited areas, particularly around the several main roads where the pollutant sources of high concentration magnitude are placed, such as Bd Batignolles and Bd Malesherbes (see ①). Furthermore, poor air quality is evident along Rue de Miromesnil, characterized by its considerable traffic volume despite its small width (see ②). In Rue de Miromesnil, it was noted that it has a large portion of the low-velocity regions in Fig. 5.12 ⑦, preventing the pollutant from dissipating. It can also be observed at the intersection of Rue de Miromesnil and Bd Malesherbes (see ③), which is identified as the place having low-velocity in Fig. 5.12 ⑧. Looking at the roads identified as having street canyon flows in Fig. 5.12 ⑪, the pollutants accumulate predominantly on the leeward side of the road, which is characteristic of street canyons, instead of the homogeneous pollutant concentrations (see ④). Typical street canyon's pollutant distribution can also be seen on many roads, e.g., Bd Batignolles (⑤). Moreover, several other regions also exhibit locally high pollutant concentrations (see ⑥). The common feature of these areas is the presence of the low-velocity, which is pointed out in Fig. 5.12. On the contrary, the high-velocity regions tend to have lower concentrations. For instance, Av des Champs-Élysées has very high traffic volumes leading to big pollutant emission magnitude but benefits from high velocities that aid in pollutant dispersion, resulting in few areas with high pollutant concentrations (see ⑦). High pollutant concentrations are generally not observed in any courtyards surrounded

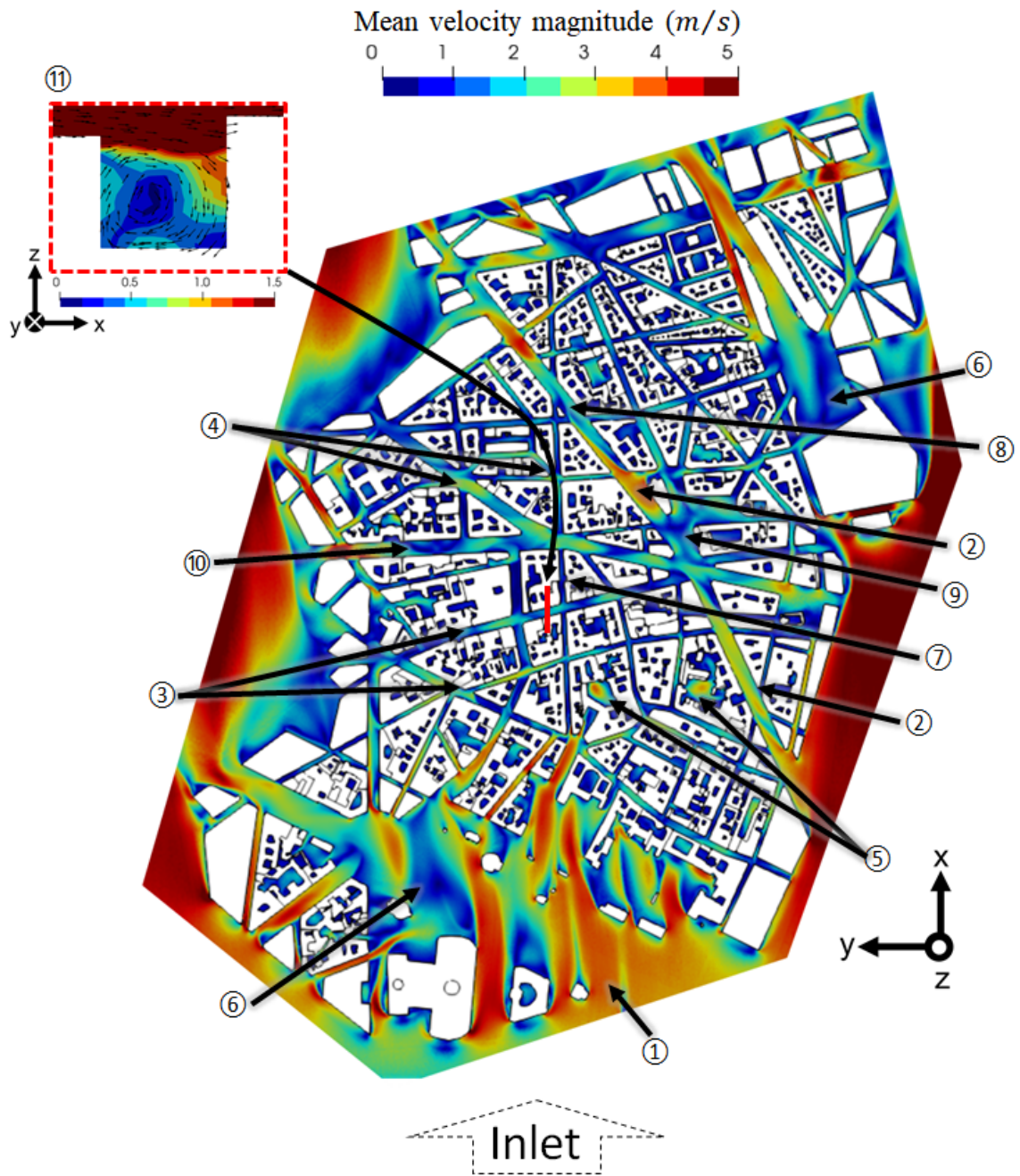


Figure 5.12: Image of the horizontal average velocity (U_x , U_y) at a height of 1.5 m. ⑪ is the vertical average velocity (U_x , U_z).

by buildings (e.g., Fig. 5.12 ⑧), as these structures act as barriers against pollutant transport (see ⑥). In summary, flow velocity and pollutant concentration are closely linked; pollutant concentration tends to be higher in the low-velocity region.

Table 5.6 compares the pollutant concentrations of NOx obtained using CFD with the measurement value taken by Airparif agency at the monitoring station on Av des Champs-Élysées (see the red circle in Fig. 5.1 (b)). NO₂ is obtained using Derwent and Middleton formula (Eq. 3.43). As a result, CFD overestimates the NOx and NO₂ pollutant concentrations compared to the measurement. This monitoring station is located a few meters away from the road edge of Av des Champs-Élysées. Several factors that were not considered in the simulation, such as air disturbances caused by vehicles and the presence of vegetation, could have contributed to the overestimation of CFD. Subsequently, Table 5.7 provides a comparison between the measured NO₂ pollutant concentrations at the road-side window of the apartment during the indoor NO₂ measurements (15 Rue de Naples, indicated by the yellow circle in Fig. 5.1 (b)) and the results obtained from the simulation. As shown in Fig. 5.6 (a) in Subsection 5.2.1.3, in the measurement, the NO₂ pollutant concentration at the road-side window is generally around 28 ~ 37 $\mu\text{g}/\text{m}^3$ (= 15 ~ 20 ppb). In the same way, CFD with Derwent and Middleton formula also shows a similar level of NO₂ concentration at 30.8 $\mu\text{g}/\text{m}^3$, indicating very good agreement.

	($\mu\text{g}/\text{m}^3$)	
	NOx	NO ₂
Background concentration at <i>Chatelet-Les Halles</i> station	26.3	-
CFD simulation (traffic-derived emission)	32.4	-
Total predicted concentration (background + CFD)	58.7	35.8
Measurement station at Av des Champs-Élysées	32.8	21.7

Table 5.6: Comparison of NOx concentration between CFD and the measurement station at Av des Champs-Élysées. Note that the total NO₂ simulated concentration is deduced from Derwent and Middleton formula.

To conclude, I have made outdoor NOx comparisons at two points (Av des Champs-Élysées and 15 Rue de Naples). It would have been even better if more sensors could be placed permanently in the district during the experimental campaigns to validate the result of CFD. Unfortunately, this was not done in my Ph.D. Instead, a mobile measurement with a "Cairsens" NO₂ microsensor was carried out on the same day by walking within the 8th district. However, this mobile measurement is

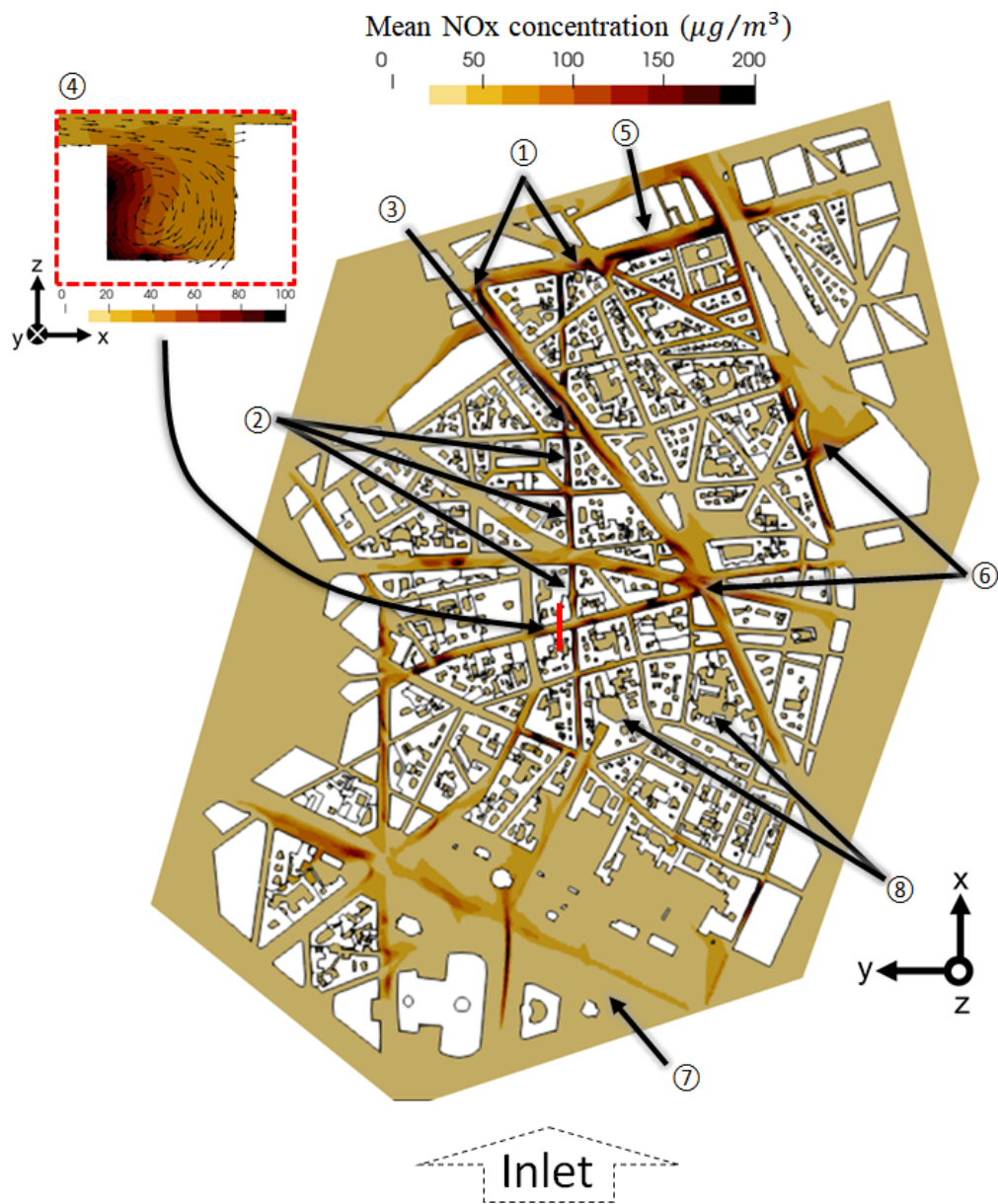


Figure 5.13: Image of average NOx concentration at a height of 1.5 m.

	($\mu\text{g}/\text{m}^3$)	
	NO _x	NO ₂
Background concentration at <i>Chatelet-Les Halles</i> station	26.3	-
CFD simulation (traffic-derived emission)	21.6	-
Total predicted concentration (background + CFD)	47.9	30.8
Concentration at roadside window during experiment	-	[28 , 37]

Table 5.7: Comparison of NO₂ concentration between CFD and the measurement from the indoor NO₂ experiment at 15 Rue de Naples. Note that, for CFD simulations, total NO₂ concentration is deduced from Derwent and Middleton formula.

only qualitatively useful. Indeed, the mobile measurements were conducted at different locations (roads) for a few minutes from 8:45 AM to 10:40 AM resulting in one or two-hour time lag compared to the time that the simulated NO₂ concentration deduced from Derwent and Middleton formula with 1-hour averaged NO_x concentration around 9 AM. Thus, a rigorous comparison between the mobile measurements and the simulation is not possible. Fig. 5.14 represents the route during the mobile measurements. At the eight points marked with red circles, concentrations were measured by stopping for 1 ~ 2 minutes. Fig. 5.15 shows the concentrations obtained through the mobile measurements. The red dotted lines correspond to the time I stopped at the eight points. It shows that, overall, the concentrations in Paris 8 district on the morning of November 15th, 2022 were between 20 ppb and 40 ppb, except for notably high pollutant concentrations from 9:40 AM to 10:10 AM. These elevated concentrations were measured when walking along around Av des Champs-Élysées. The highest pollutant concentrations occurred around 10:05 AM, likely attributed to the presence of a nearby construction site at Av. Matignon.

Table 5.8 presents a comparison between the measured and the simulated concentrations at eight stop measurement points; the CFD results use the Middleton formula to estimate NO₂. This shows that pollutant concentrations at No.1 and No.2 are in reasonably good agreement. However, these points are far from the main polluted roads, and consequently, both measured and simulated are dominated by background concentrations. For the other points, CFD overestimates pollutant concentrations by about 1.5 times more than the experimental ones. As mentioned, the measurements were taken one to two hours later than the time covered by the CFD; the CFD analyzed the peak commuting period when the highest number of vehicles are present, while the measurements were not. Therefore, pollutant concentrations can be lower in the measurements. The constant wind direction in CFD also leads

to higher local pollutant concentrations, as it underestimates pollutant dispersion.

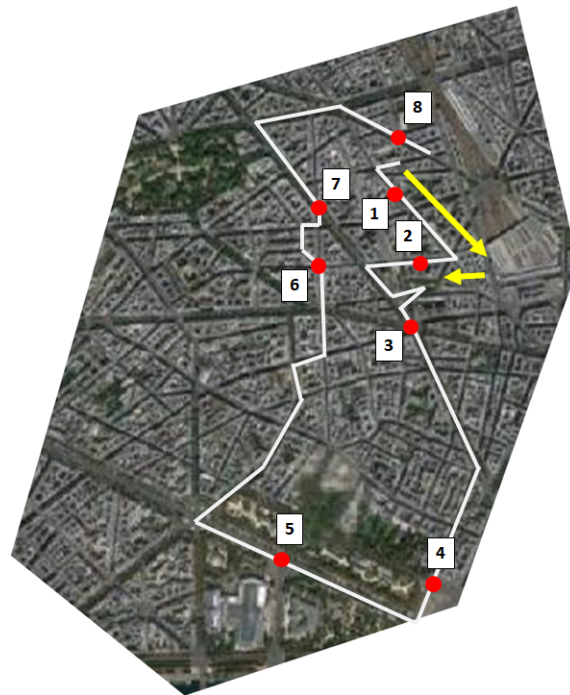


Figure 5.14: NO₂ mobile measurement route in Paris 8: starting from Rue de Naples.

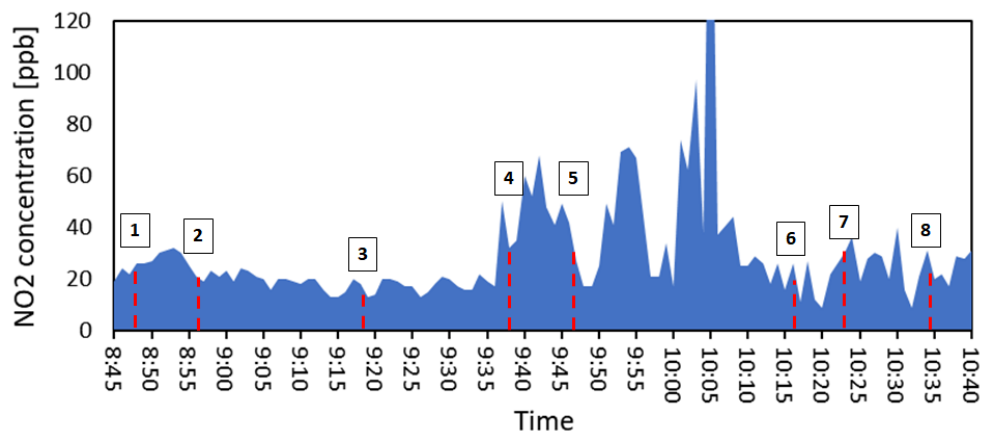


Figure 5.15: NO₂ concentration in the mobile measurement campaign in Paris 8.

No.	Road name	Time	Measurement NO ₂ [ppb]	Simulation NO ₂ [ppb]
1	61 Rue du rocher	8:45 - 8:48	23	20
2	Rue Bienfaisance	8:54 - 8:58	24	20
3	Intersection bd Haussman and Malesherbes	9:17 - 9:20	16	40
4	Hôtel Crillon Place concorde	9:36 - 9:39	34	19
5	Pavillon Elysee	9:47 - 9:49	20	23
6	Cèdre rouge Rue Treilhard - Miromesnil	10:16 - 10:17	19	31
7	Intersection bd Malesherbes Miromesnil	10:22 - 10:24	31	53
8	Place Jean Pierre Levy Chaptal	10:33 - 10:36	24	36

Table 5.8: Comparison of NO₂ concentration on 15th November 2022 between the mobile measurement and the CFD using Derwent and Middleton formula at 8 points marked by the red circles in Fig. 5.14.

5.2.3 CFD modeling of outdoor/indoor pollutant transfer

This subsection describes the indoor simulation using the decoupled approach.

As observed in Sense-City study, outdoor airflow runs along the buildings' surface until entering the building indoors. This implies that in the Paris apartment, as in Sense-City, airflow entering the room would have tangential (parallel) components with respect to the window surface. Since Paris case has a huge computational domain, it is not operational to calculate the interaction between outdoor and indoor airflow with the coupled approach as in Sense-City. In response to this challenge in Paris case, as [139] suggests, I consider a method of creating a numerical mock-up that includes indoor domains and part of outdoor domains. Then, the kind of velocity Dirichlet conditions are imposed. Hereafter, I referred to this method as "Additional Domain Approach". In this subsection, I first compare the accuracy of the pressure-driven approach and the additional domain approach to select a more appropriate one regarding airflow distribution. Then, the numerical result will be compared with the indoor air quality measurement campaign.

5.2.3.1 Numerical mock-up and mesh of the apartment

Fig. 5.16 shows the numerical mock-ups of the apartment for the pressure-driven approach and additional domain approach, respectively. Refer to Subsection 5.2.1 for the detailed plan view of the apartment. According to the 3D anemometer and NO_2 measurements, it was found that the airflow entered the apartment from the road-side window on 15th November 2022 around 9 AM. Also, from the outdoor simulation, I see that pressure is higher on the road-side window than on the courtyard window. Therefore, in the additional domain approach, a new domain is added at the road-side window, to mimic an inlet velocity condition. The angle of this domain is determined based on the wind direction near the road-side window simulated in the outdoor simulation (Fig 5.12) so that the wind direction near the road-side window of the outdoor simulation can be reproduced. In practice, I have extracted from the outdoor simulation the velocity components from coordinates located approximately 1 m away from the window wall surface. Then I found that the velocity has a tiny normal velocity component to the window wall surface. As a result, the domain has a small oblique angle in the mock-up of the additional domain approach. The dimensions of the additional domain are 5 m width, 8 m long and 5m height.

Fig. 5.17 displays mesh configurations for both approach. As in the Sense-City case, the pressure-driven approach employs hexa-mesh near the inlet and outlet boundaries for computational stability. The size of the hexa-mesh is 0.1 m. In other areas, mesh size of 0.1 m is used on the wall surfaces and up to 0.2 m for the other regions. The total number of cells is 241,069. For the additional domain approach, a minimum mesh size of 0.05 m is employed at the road-side window. This enhances the accuracy of flow separation at the window frame. In the new outdoor additional volume, the maximum mesh size reaches 0.5 m. Within the indoor domain, the minimum and maximum mesh sizes are 0.1m and 0.25m respectively. It is noted that all cells are tetra mesh in the additional domain approach. The total number of cells is 302,624.

5.2.3.2 Numerical set-up and boundary conditions

From the indoor NO_2 measurements, it was found that the observed constant outdoor pollutant concentration on 1-hour time period leads to a gradual increase of indoor pollutant concentration by natural ventilation followed by stabilization at the outdoor pollutant level. Hence, this is a transient phenomenon. To capture this unsteady trend, the indoor CFD simulation employs URANS based on the instantaneous airflow (as with Sense-City, see Section 4.2.2.1). It should be noted that although transient simulations are performed using URANS, the pressure and

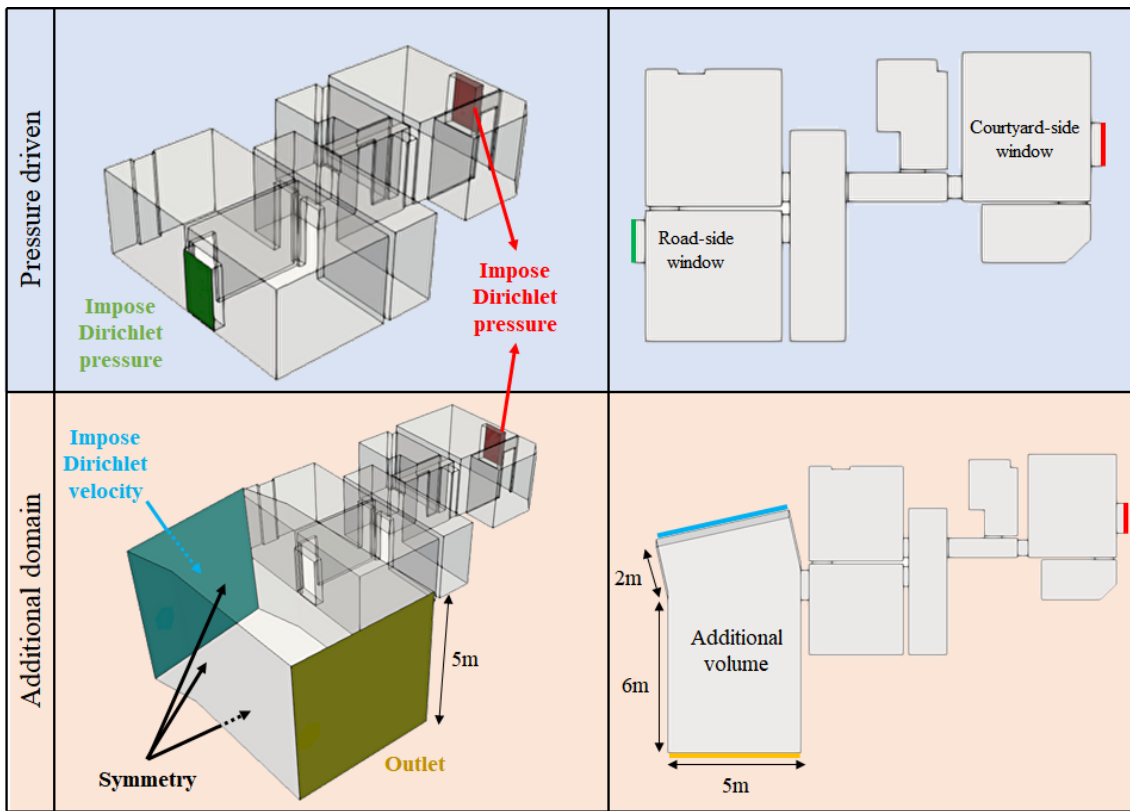


Figure 5.16: Numerical mock-up for the pressure-driven and additional domain approaches.

velocity given as the boundary conditions are time-average values from the outdoor simulation on 15th November 2022 around 9 AM.

Regarding the pressure-driven approach, the pressure difference between the road-side and courtyard-side windows is 0.3 Pa, obtained from the outdoor simulation.

Regarding the additional domain approach, the new inlet boundary (see the blue face in Fig. 5.16) is given a velocity magnitude of 1.93 m/s as a Dirichlet condition and a Dirichlet scalar of magnitude 20 ppb as a passive scalar. At the courtyard-side window, "imposed pressure outlet" condition is given. According to the outdoor simulation, the pressure difference between the road-side and courtyard-side windows is 0.3 Pa. Therefore, I imposed 101324.7 Pa at the courtyard-side

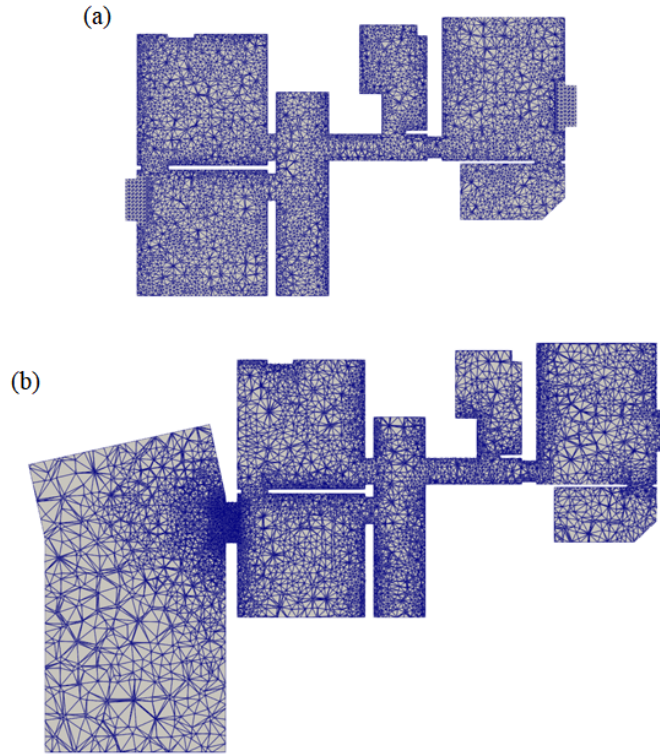


Figure 5.17: Mesh configuration of the apartment from top view at a height = 1.33 m from the floor of the rooms: (a) pressure-driven approach and (b) additional domain approach.

window in the additional domain approach, which is 0.3 Pa lower pressure than the default atmospheric pressure Code_Saturne; the default atmospheric pressure is 101325.0 Pa. The outlet condition is imposed on the new additional volume's outlet face (the yellow face in Fig. 5.16), and the symmetry conditions are given to the other three faces on the new additional volume's faces (see Fig. 5.16). The other walls have wall condition with wall function. All the Dirichlet conditions (pressure, velocity, scalar magnitude) are considered in time on the simulation interval of 30 min. Table 5.9 summarized important boundary conditions for the additional domain approach.

All other computational settings are the same as the outdoor simulations (i.e., $k - \omega$ SST turbulence modeling; implicit Euler scheme for time integration, the second-order linear upwind scheme for the convective term of the velocity $\langle u_i \rangle$, turbulence kinetic energy k , and specific dissipation ω and pollutant concentration C , SIMPLE algorithm, turbulent Schmidt number Sc_t at 0.7).

Boundary face		Velocity	Pressure	Scalar concentration
Inlet on the additional volume	Γ_i	1.93 m/s	-	20 ppb
Courtyard-side window	Γ_o	Neumann	101324.7 Pa	Neumann

Table 5.9: Boundary conditions for the additional domain approach.

5.2.3.3 Result and discussion for the outdoor/indoor pollutant transfer simulation

Prior to comparing the simulation with the NO₂ measurements, the airflow of the pressure-driven approach and the additional domain approach are compared to determine the better appropriate simulation approach. Once more, the coupled approach was not simulated for Paris due to practical considerations. Therefore, herein, its accuracy is evaluated by comparing them with the airflow measured with the 3D anemometer placed on the road-side window during the indoor measurement campaign. Fig. 5.18 (a) and (b) exhibit the averaged velocity fields at a height of 1.5 m from the floor, corresponding to the height of the 3D anemometer. The averaged simulated velocities are obtained from the last 20 minutes of the total 30-minute simulation. In Fig. 5.18 (c), the plan view is presented alongside the average magnitude of U_{normal} , $U_{tangential}$ obtained from the first 15min by the 3D anemometer.

The comparison between Fig. 5.18 (a) and (b) reveals noticeable differences, especially in the living room where the airflow enters. In the pressure-driven approach, the airflow from the inlet boundary travels along the wall separating the living room and kids' room, and subsequently, it circulates near the perimeter of the living room. Airflow also enters the kids' room directly from the inlet boundary. On the other hand, in the additional domain approach, the outdoor airflow passes across the center of the living room and then collides with the wall and is divided into left and right directions. The divided airflow passes along the wall separating the living room and the kids' room before entering the kids' room. The airflow in the corridor, kitchen and bedrooms are similar to each other, although the velocity magnitude differs between them. In terms of airflow direction, the additional domain approach and measurement have positive tangential velocity components, whereas the pressure-driven driven has an opposite airflow direction. Concerning the magnitude of each velocity component, the additional domain approach, $(U_{normal}, U_{tangential}) = (0.19m/s, 0.15m/s)$ is found to be more accurate when compared to the 3D anemometer results, $(U_{normal}, U_{tangential}) = (0.23m/s, 0.14m/s)$. It is evident that the wind direction at the road-side window can significantly change the indoor

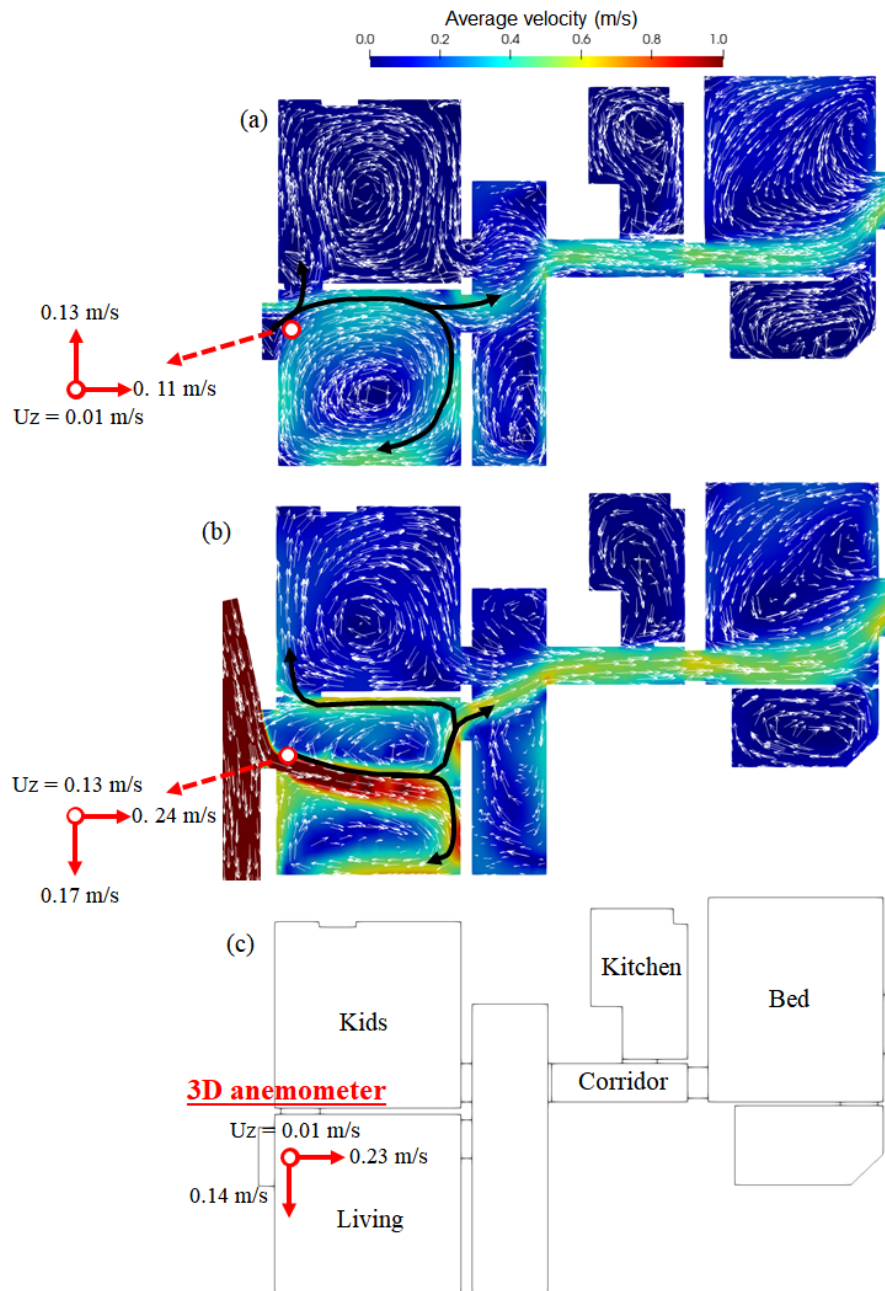


Figure 5.18: Comparison of averaged velocity at height of 1.5m (measurement height of the 3D anemometer): (a) pressure-driven approach, (b) additional domain approach and (c) floor plan and the average velocity components of 3D anemometer.

airflow distribution, which thus influences the NO_2 dispersion. Therefore, from this comparison with the 3D anemometer result, I select the additional domain approach for subsequent comparisons for NO_2 concentration.

Fig. 5.19 depicts the time evolution of the pollutant concentration at a height of 1.33 m (corresponds to the center of the road-side window) at $t = 5\text{s}$, 10s , 25s , 45s , 300s (5min) and 900s (15min). It shows that pollutants entering the living room are dispersed to the corridor and kids' room via different pathways (see Fig. 5.19 (b) and (c)). In the corridor, the pollutants come directly from the living. In the kids' room, the pollutants enter the kids' room through a door between the living room and the kids' room (see the yellow circle in Fig. 5.19 (a)) just next to the road-side window, and then the pollutants are transported along the wall due to the airflow. At $t = 25\text{s}$ (Fig. 5.19 (c)), the pollutant reaches the bedroom. Looking at the kids' and bedroom in Fig. 5.19 (d), the pollutant concentrations initially increase from the perimeter of the rooms. After five minutes (Fig. 5.19 (e)), pollutant concentration levels are comparable to outdoor pollutant concentration levels at 20 ppb in most of the indoor areas, except for the kitchen, but finally, the indoor pollution levels are homogeneous after 15 minutes (Fig. 5.19 (f)).

Fig. 5.20 shows a comparison of the time history of NO_2 pollutant concentration between the measurement and the simulation. Overall, the simulation results are very similar to the measured trends: the rapid increase in pollutant concentration in the first 5 minutes and the indoor pollutant concentration level reaching the outdoor pollutant level after 15 minutes. The order of the increase is also generally the same between the experiment and the simulation (Living room, Corridor & Kids room, Bedroom, Kitchen). Nevertheless, in Fig. 5.20 (a), it can be seen that the simulated pollutant concentration in the kids' room and corridor are similar, whereas the measurement concentration in Fig. 5.20 (b) shows that pollutant concentrations increase slightly faster in the corridor than in the kids' room. This discrepancy can be due to the opened road-side window's frame blocking the passage between the living room and the kids' room during the measurement (Fig. 5.21), which is not modeled in the geometry for the numerical simulation. It reduces the propagation of NO_2 into the kids' room from the living room, resulting in the concentration in the kids' room to rise slower than in the corridor. Moreover, let me recall that for practical purposes, the indoor numerical mock-up was simplified omitting details such as furniture. From the results, we conclude that these details are not so important for capturing the global trend of indoor pollutant dispersion, as the differences between the measured and simulated concentrations trends are small.

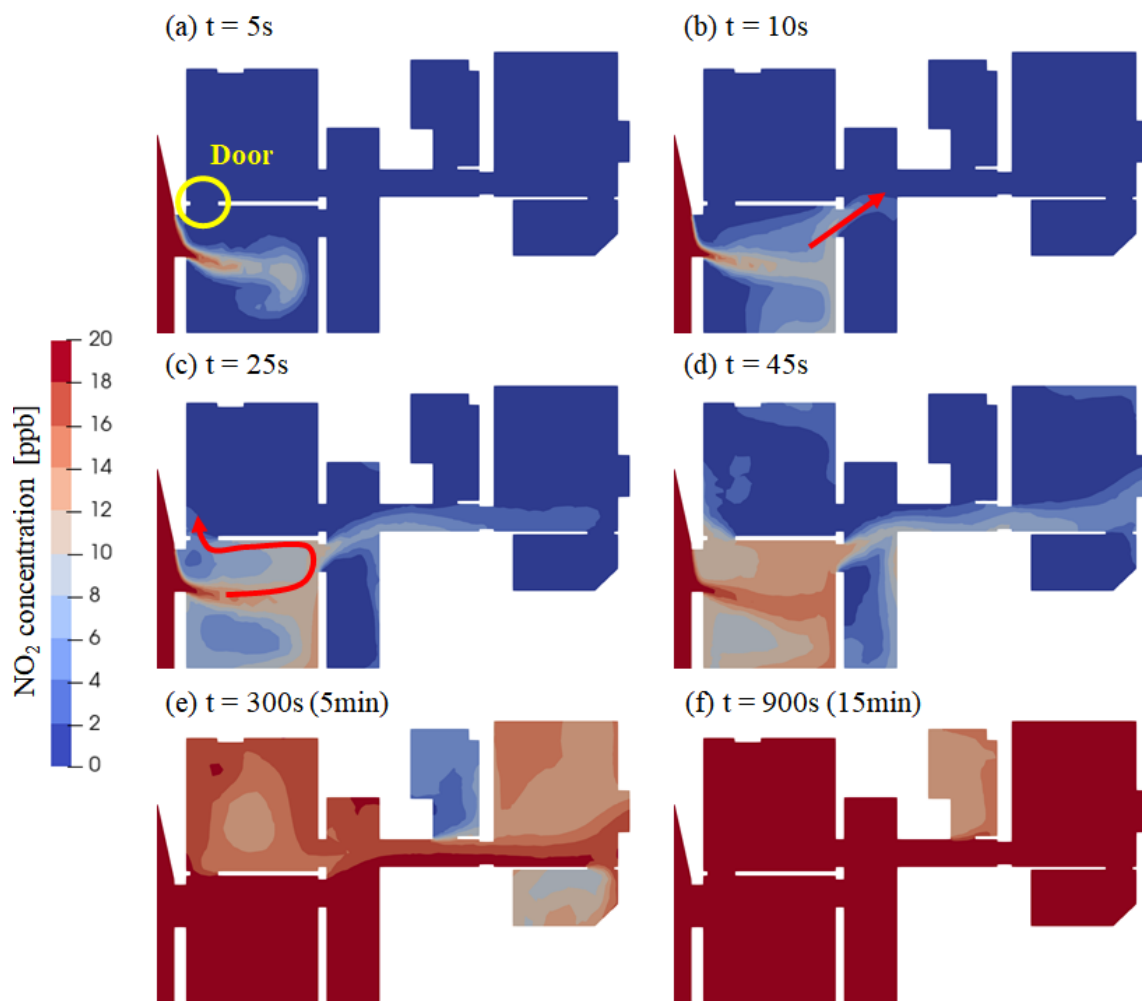


Figure 5.19: Time evolution of NO_2 concentration at a height of 1.33 m (corresponds to the center of the road-side window): (a) $t = 5\text{s}$, (b) $t = 10\text{s}$, (c) $t = 25\text{s}$, (d) $t = 45\text{s}$ (e) $t = 300\text{s}$ (5min) and (f) $t = 900\text{s}$ (15min).

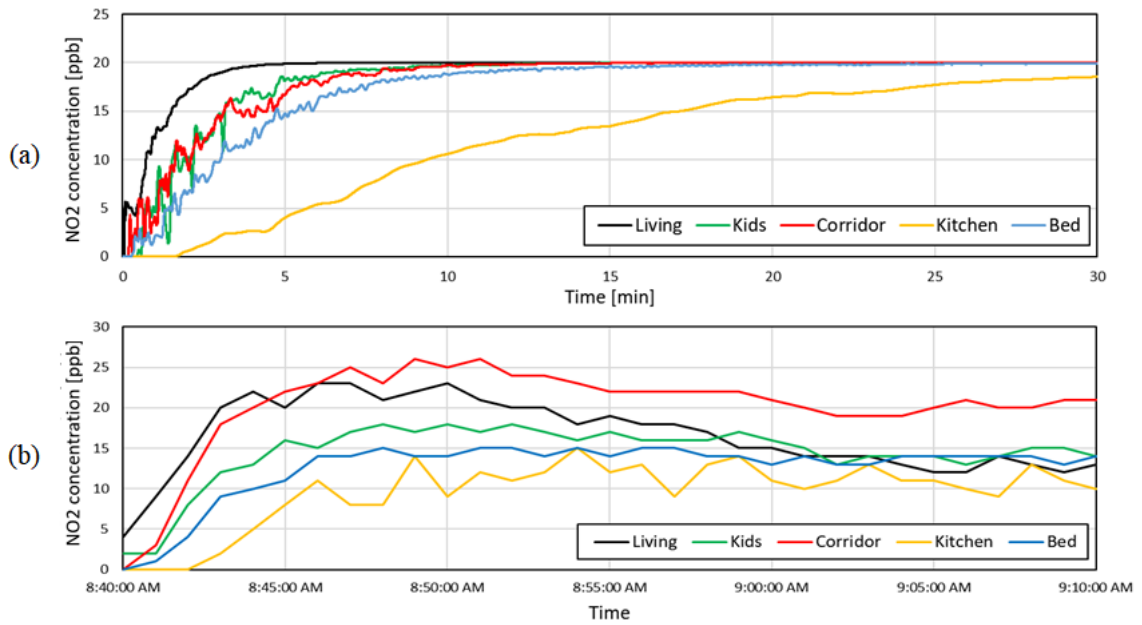


Figure 5.20: Time evolution of NO₂ concentration: comparison between the simulation (a) and measurement (b). Note that (b) is the same figure as Fig. 5.6 (a).



Figure 5.21: Window frame in the passage between the living room and the kids' room.

5.2.4 Summary on the interaction between outdoor and indoor air quality in the apartment in Paris

A small summary of the interaction between outdoor and indoor air quality in the Paris apartments is proposed here. The key points of the study on the interaction between outdoor and indoor air quality are summarized based on three aspects: appropriate simulation approach, characteristics of physical phenomenon and how to mitigate indoor air pollution from traffic.

• Appropriate simulation approach

- The additional domain approach outperforms the pressure-driven approach in accurately replicating real airflow directions measured in the experiment. This advantage arises from the additional domain approach's ability to predict the complex interaction between indoor and outdoor airflow at windows. In contrast, the pressure-driven approach lacks the capability to consider the tangential component of the window;
- When the pressure-driven approach was adopted for the apartment, the numerical velocity distribution at the inlet boundary was not in agreement with the measurement. This could potentially be attributed to the fact that the area of the window is large. It is unclear whether giving a single pressure value for the entire large window surface is appropriate, especially when the window balcony thickness is 30 cm, as in the present apartment, which causes flow separations at the edge of the balcony and therefore inhomogeneous pressure distribution on the window;
- Airflow direction at the window has a significant influence on the behavior of indoor pollutant dispersion. Therefore an appropriate method that can accurately reproduce the indoor airflow should be applied to ensure reliable simulation outcomes.

• Physical characteristics of the interaction between outdoor and indoor air quality

- Both measurement and simulation results demonstrate that indoor pollutant concentrations become comparable to outdoor levels within approximately 15 minutes of window opening. Notably, there is a rapid increase in pollutant concentrations during the initial 5 minutes;
- Pollutant concentrations increase from the room closer to the inlet window, but this is not the case in the kitchen, which lies tangentially to the corridor's airflow and has very low airflow velocity;

- Except in the room with inlet windows (here, i.e., the living room), the pollutant concentrations increase from the perimeter of the rooms because the airflow mainly travels along the room's perimeter, and therefore the pollutants are mainly transported along the perimeter's airflow.

• **Proposition of mitigation strategies to reduce people's exposure to air pollutants within indoor environments**

- According to the typical flow characteristics traveling along rooms' perimeters, we should place depolluting devices (panel, paint, tile) on the surface (wall).;
- To reduce the transfer of outdoor pollutants into indoor spaces, we should reduce pollutant concentration at windows from which pollutants enter indoors. This is studied in the next section.

5.3 Numerical study for smart placement of depolluting panel in Paris 8 district

The interaction between outdoor and indoor air quality in the Paris apartment was examined in the previous section. It found that the indoor pollution levels reaches the outdoor pollution levels within 15 minutes after opening the windows. Nevertheless, people are also exposed to NO_2 (often emitted by cars) outdoors. In this context, depolluting panels can be a very practical solution to those problems. In the previous chapter, the method for the smart placement of depolluting panels was applied to simpler urban districts under the controlled conditions in Sense-City. Herein, in this section, it is applied in a real Paris urban area considering common wind directions with highly realistic polluted scenarios. The results of this section are presented in [138] and [147].

5.3.1 Wind direction and target dates

Wind directions are constantly changing and the state of pollutant dispersion varies from time to time. Yet, it is difficult to simulate all wind directions from the point of view of computational cost and time limitations. Accordingly, herein, I consider the optimal placement of depolluting panels in some dominant wind directions in Paris. Fig. 5.22 shows a wind rose from one year of measured data in 2021 at Aéroport Roissy-Charles-de-Gaulle (CDG) that is located in the North of Paris. It shows that there are two well-known dominant wind directions in Paris: North-East (NE) and South-West (SW). These two wind directions are considered in the present study.

To apply my numerical strategy for the smart placement of depolluting panels, specific dates and times characterized by these two dominant wind directions with high pollutant concentrations were selected based on the data provided by the Airparif agency and the meteorological station at 10 m height in Montsouris.

- 4th December 2021 at 7 pm with wind direction (South-West) of 230 degrees with 2 m/s at 10 m height (SW case);
- 16th December 2021 at 11 am with wind direction (North-East) of 70 degrees with 2.5 m/s at 10 m height (NE case).

As already said, my methodology does not consider chemical reactions of pollutants due to UV radiation. Therefore, I deliberately selected winter days, i.e., outside of the intensive photochemical period.

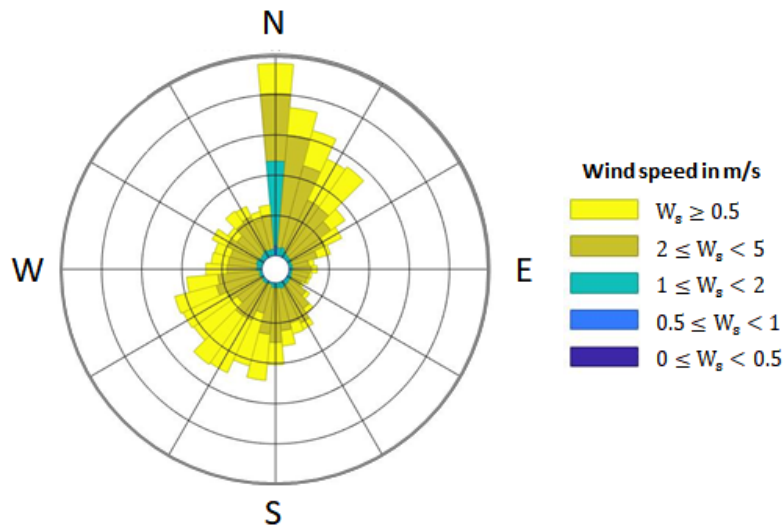


Figure 5.22: Wind rose obtained at CDG airport in 2021.

5.3.2 Diagnosis stage: making pollutant cartography

5.3.2.1 Computational setting of direct (CFD) simulation

All CFD settings (i.e., turbulence modeling, numerical schemes and boundary conditions) are the same as in Section 5.2.2. It only differs in the wind characteristics (directions and velocities) and NOx ($\mu\text{g}/\text{m}^3/\text{s}$) pollutant sources magnitude on the roads. Table 5.10 presents the NOx pollutant sources magnitude in the SW and NE

cases, which are provided by Airparif agency. For the road locations corresponding to the respective numbers, see Fig. 5.10.

(Unit : $\mu\text{g}/\text{m}^3/\text{s}$)

No. road	SW	NE	No. road	SW	NE
1	17.5	15.6	24	16.9	15.2
2	13.3	17.1	25	8.9	6.5
3	27.2	18.5	26	18.7	21.5
4	20.8	27.7	27	16.5	23.4
5	14.2	18.2	28	8.6	8.4
6	39.7	52.8	29	7.9	11.8
7	11.2	8.4	30	10.6	14.1
8	12.2	20.2	31	10.6	14.1
9	38.8	41.1	32	13.6	31.5
10	11.5	8.9	33	0.7	1.0
11	33.5	34.8	34	10.6	12.3
12	22.1	24.3	35	31.0	41.2
13	20.9	33.7	36	17.7	24.3
14	24.3	43.5	37	11.3	24.8
15	15.5	16.2	38	7.5	16.5
16	12.0	12.6	39	20.2	16.5
17	7.3	5.8	40	13.6	15.4
18	34.4	43.6	41	24.0	35.3
19	19.9	34.2	42	15.5	18.2
20	13.5	10.4	43	21.8	27.7
21	18.4	20.4	44	12.1	18.1
22	9.1	9.6	45	9.9	8.8
23	16.9	15.2			

Table 5.10: Magnitude of NOx emission on 44 main roads for NE and SW case.

5.3.2.2 Numerical mock-up and mesh configuration

The numerical mock-up of the 8th district is the same as in Subsection 5.2.2.1, but it is rotated according to the wind directions to generate the new numerical mock-ups. The dimension of the computational domain is also identical to that in Subsection 5.2.2.1. Fig. 5.23 shows each numerical mock-up.

For the mesh, as in Subsection 5.2.2.5, the computational domain is divided into four areas, where different sizes are considered. The mesh size is basically identical to that of Subsection 5.2.2.5, but a finer mesh size of 1 m is employed at the vicinity of the pollution sources (see Table 5.11).

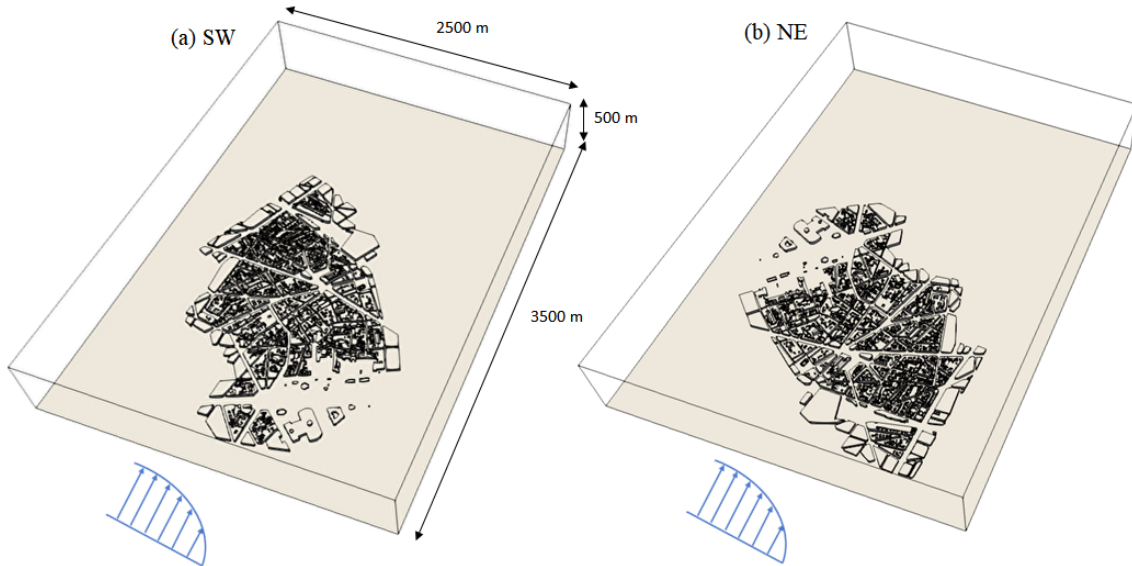


Figure 5.23: Overview of the numerical Paris 8 district mock-ups for (a) SW case and (b) NE case.

Volume	Min (m)	Max (m)
Vol.1	1	3
Vol.2	3	10
Vol.3	3	25
Vol.4	3	30
Traffic pollutant source	1	
Bottom of Vol.1 ~ 3	3	

Table 5.11: Mesh size of the Paris 8 domain for the study on the smart placement of depolluting panels.

5.3.2.3 Result and discussion: outdoor pollutant cartography

The first step of the proposed numerical strategy for the optimal placement of depolluting panels developed in Section 3 is to make a detailed cartography of pollutant concentration. Fig. 5.24 shows the mean velocity and NO_x concentration at 1.5 m height for the SW and NE cases. Concerning the numerical estimation of NO_x concentrations, measurement values of the air quality subway station *Chatelet-Les Halles* (in the center of Paris) are used as background concentrations: $45.5 \mu\text{g}/\text{m}^3$ and $164.5 \mu\text{g}/\text{m}^3$ for SW and NE cases, respectively. In my Ph.D., CFD is used to compute the cartography of NO_x concentration resulting only from traffic emissions. Hence, the total NO_x concentration is obtained by adding the background concentration to the traffic-derived concentration predicted by CFD as it was done in Subsection 5.2.2. In the NE case, since the background concentration is high, the overall pollutant concentration looks high in Fig. 5.24. Note that the upper limit of the range of concentrations in the figure is now set at $300 \mu\text{g}/\text{m}^3$, which is higher than in the previous section's result (Fig. 5.13). Herein, there are many areas with high pollutant concentrations, but this is not surprising as I have chosen two critical days with very high pollutant concentrations.

First of all, to validate the accuracy of the CFD results, a comparison is made with the measurements at the monitoring station of Av des Champs-Élysées. Table 5.12 compares the numerical NO_x concentration with the measured concentration at the air quality station of Airparif agency located at Av des Champs-Élysées (see the red circle in Fig. 5.1 (b)). As shown in Table 5.12, the traffic-derived pollutant concentration at the air quality station at Av des Champs-Élysées is lower in NE case than in SW case. This is due to the position of the measurement station at Av des Champs-Élysées. In NE case, few traffic emissions from Av des Champs-Élysées are conveyed to the measurement station as the wind direction is from NE and the air quality station is placed on the NE sidewalk of Av des Champs-Élysées. In this case, pollutants are carried away from the road in the opposite direction of the measurement station. Furthermore, there is a large green park on the upwind side of the monitoring station, leading to reduced traffic-derived pollution in NE case. Therefore, the concentration at the measurement station for NE case corresponds mainly to the background concentration. In contrast, in SW case, the measurement station observes the high traffic pollutant emissions from Av des Champs-Élysées. Overall, in both simulated cases, an acceptable gap, *i.e.* less than 25%, is obtained between the simulated and measured NO_x concentrations at Av des Champs-Élysées.

CFD results in Fig. 5.24 highlight that the pollutant concentration is inhomogeneous at the district and street scales. As expected, high pollutant concentrations

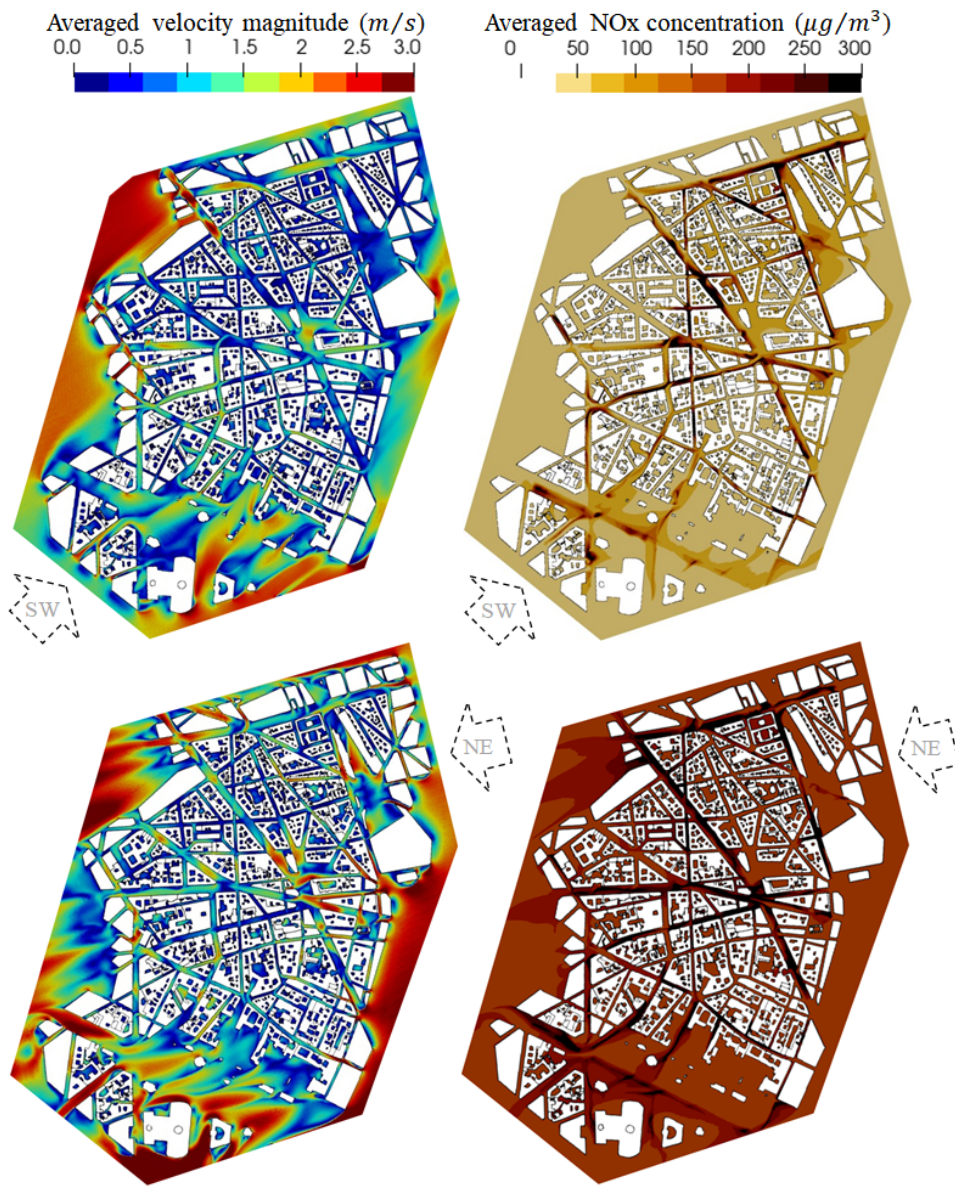


Figure 5.24: Mean velocity and mean NOx concentration on 1 hour-interval at 1.5 m height: SW case (top) and NE case (bottom) in Paris 8 district.

are predicted on the 44 main streets where volumic sources are placed e.g., Av des Champs-Élysées, Bd Malesherbes and Bd Batignoles, (to see the position of each road, see Fig. 5.1 (b)). Low velocities in some areas result in pollutant accumula-

	($\mu\text{g}/\text{m}^3$)	
	SW	NE
Background concentration at <i>Chatelet-Les Halles</i> station	45.5	164.5
CFD simulation (traffic-derived emission)	52.3	5.4
Total predicted concentration (background + CFD)	97.8	169.9
Measurement station at Av des Champs-Élysées	123.0	154.1

Table 5.12: Comparison of NOx concentration between CFD and measurement station.

tion such as in Rue de Miromesnil, which was already shown in the previous section. Also, it is observed on many streets that the pollutant concentrations are high only on one side of the roads. As explained earlier, this is due to the typical pollutant distribution in street canyons where the highest concentrations are noticed on the leeward side of roads, as the street primary vortex [148] conveys pollutants leeward. For example, Fig. 5.25 shows the averaged pollutant concentration and wind direction vector on a street's cross section at 58 Bd Malesherbes for the SW case. Note that the scale range; the upper value of the range is $500 \mu\text{g}/\text{m}^3$ here. On the left side (leeward), the NOx concentration is much higher than the right side and above $500 \mu\text{g}/\text{m}^3$ at the pedestrian level, with decreasing concentration as height increases. This really high concentration can be attributed to the limitations of CFD calculations such as fluctuating wind direction, which was not considered. Moreover, the presence of vehicle-induced turbulence was not modeled here, but it enhances pollutant dissipation and removal in reality. Let me note that the other simplifications given in Section 5.2.2.6 also cause some overestimation of the predicted NOx concentration, e.g., no tree effect, no buoyancy effect, etc. On Av des Champs-Élysées, pollutant concentrations are higher on the south side of the street in SW case and on the north side in the NE case, but these are attributed to the wind directions, not the street canyon effect.

5.3.3 Remediation stage: smart placement of depolluting panel

5.3.3.1 Selecting QoI (NOx pollutant concentration in highly polluted areas)

The next step is to select critically polluted areas where the air quality should be improved. From the pollutant maps of the two wind directions (Fig. 5.24), four

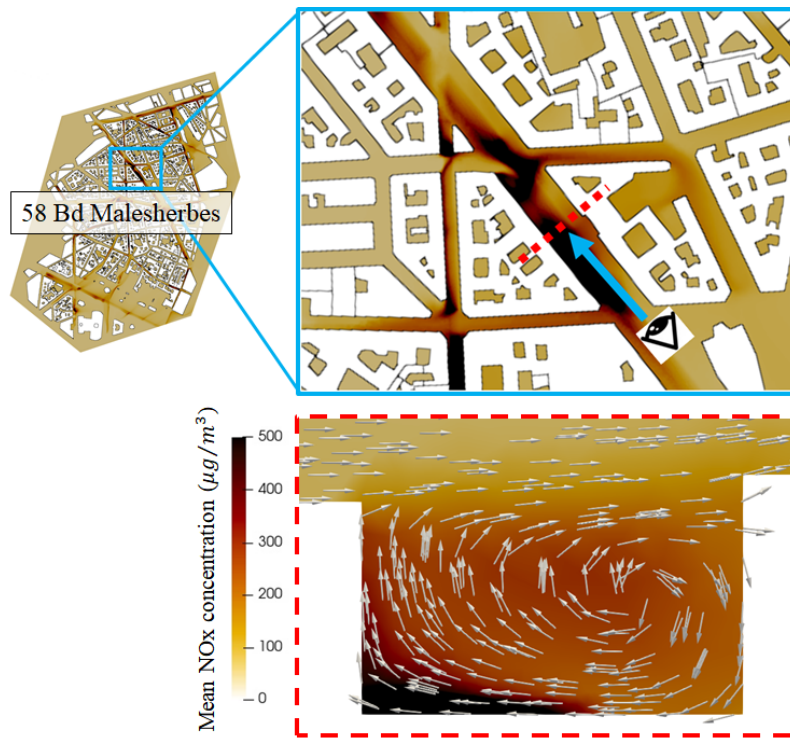


Figure 5.25: Average NOx concentration and wind direction on the vertical direction in SW case at 58 Bd Malesherbes.

areas of interest are selected:

- Ω_{q1} : southwest sidewalk from 69 to 85 Bd Malesherbes represented in the red box in Fig. 5.26 (a) and in Fig. 5.27 (a), for SW case. Dimension of the area is 5 m width, 140 m length, and height belongs to [0.5 m, 2 m]. The associated mean pollutant concentration \mathcal{J}_1 is $627 \mu\text{g}/\text{m}^3$.
- Ω_{q2} : building facade of the lower floors on the southwest side from 69 to 81 Bd Malesherbes represented in Fig. 5.26 (a) in blue and in Fig. 5.27 (a), for SW case. The dimension of the area is 0.5 m width, 110 m length, and height belongs to [4 m, 9.2 m]. The associated mean NOx concentration \mathcal{J}_2 is $427 \mu\text{g}/\text{m}^3$.
- Ω_{q3} : sidewalks at the intersection of Rue de Miromesnil and Rue la Boétie represented in Fig. 5.26 (b) and in Fig. 5.27 (b), for SW case. The dimension

of the area is 1 ~ 2.5 m width, 20 ~ 50 m length, and height belongs to [0.5 m, 2 m]. The associated mean NOx concentration \mathcal{J}_3 is 252 $\mu\text{g}/\text{m}^3$.

- Ω_{q4} : north-east sidewalk from 48 to 60 Bd Malesherbes represented in Fig. 5.26 (c) and in Fig. 5.27 (a), for NE case. Dimension of the area is 4 m width, 140 m length, and height belongs to [0.5 m, 2 m]. The associated mean NOx concentration \mathcal{J}_4 is 326 $\mu\text{g}/\text{m}^3$.

The quantities of interest \mathcal{J}_1 , \mathcal{J}_3 and \mathcal{J}_4 have been selected in order to improve the air quality on sidewalks frequented by pedestrians. \mathcal{J}_3 is also of particular interest as it is located at a road intersection having the crowded metro station entrance “Miromesnil” and many city shops. Lastly, reducing air pollution on the building facade, *e.g.* \mathcal{J}_2 at Bd Malesherbes, is important in order to decrease the transfer of traffic pollutants from the outdoors to the indoors, which was studied in the first part of this chapter (Section 5.2).

5.3.3.2 Computational setting of Adjoint simulation

To obtain adjoint concentration for Paris case, OpenFOAM [149], a finite volume open-source software, is used to solve the pseudo-steady-state adjoint advection-diffusion equation:

$$-\frac{\partial \tilde{C}}{\partial t_p} - \langle u_i \rangle \frac{\partial \tilde{C}}{\partial x_i} - D \frac{\partial^2 \tilde{C}}{\partial x_i \partial x_i} = f_q \xi \quad \text{in } \Omega \times [0, T] \quad (5.9)$$

where Δt_p is a pseudo time step that, which changes locally according to the specified CFL number threshold. Herein, the CFL threshold is set to be 10, and thereby Δt_p varies in order to satisfy $\text{CFL} \leq 10$. The other settings are almost the same as in Sense-City’s depolluting panel study (Section 4.2.3.2), but note that the first-order upwind scheme is chosen to discretize the advection term for the numerical stability. The average of the velocity $\langle u_i \rangle$ (m/s) and turbulent diffusion D_t (m^2/s) are imported from the direct simulation. In the iterative solver process, the calculation stops once the residual reaches 10^{-6} .

5.3.3.3 Adjoint concentration and sensitivity indicator

To smartly place the depolluting panels on the surfaces of the urban domain, the final phase is to calculate the adjoint concentration and the sensitivity indicator for each selected quantity of interest defined in the previous subsection. As explained before, the sensitivity indicator becomes significant when both direct and adjoint concentrations are high. Fig. 5.28 shows the cartography of the NOx concentration (solution of the direct problem), the adjoint concentration, and the resulting

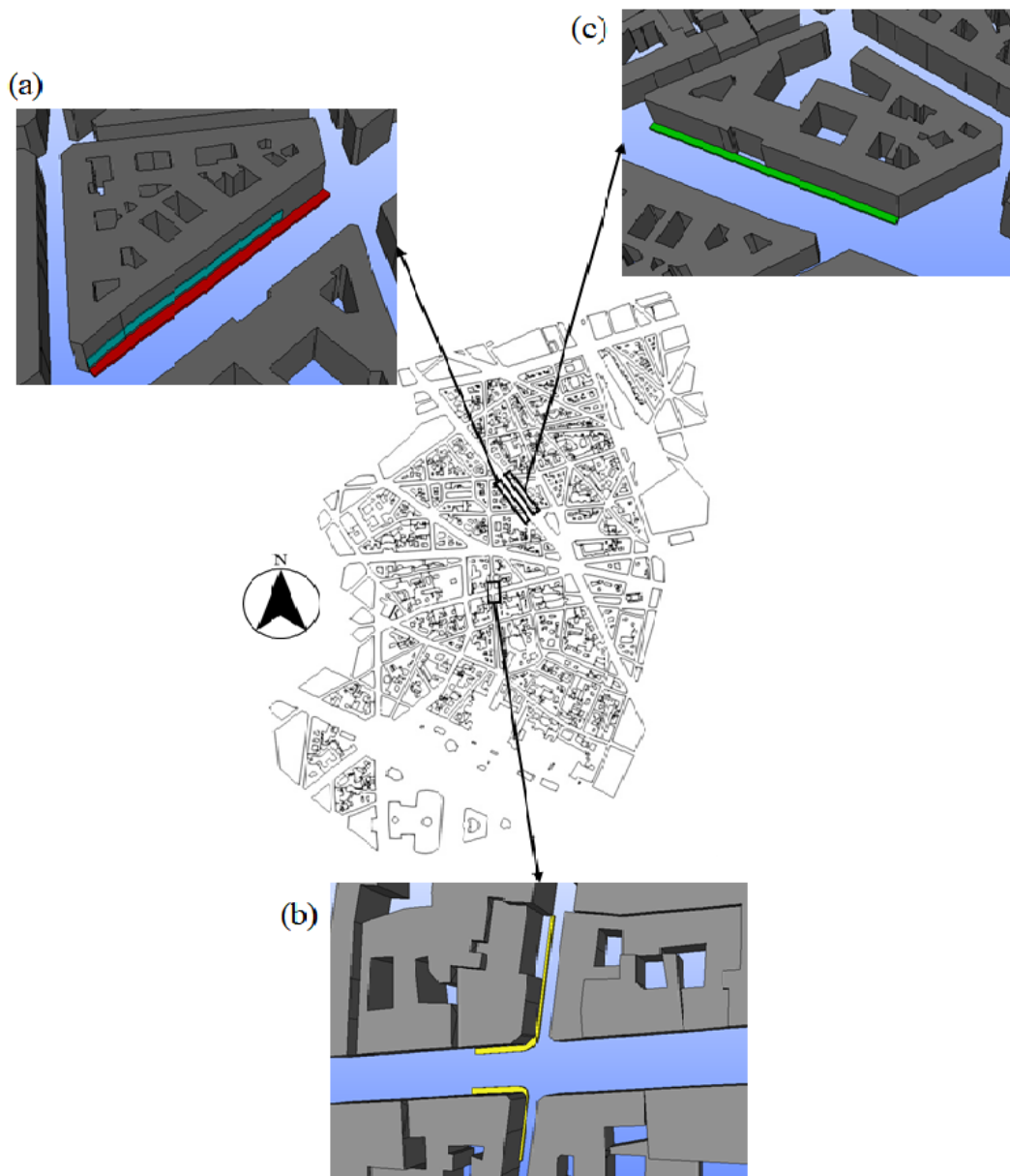


Figure 5.26: Selected areas of interest in the Paris district where air quality should be improved: (a) the south-west sidewalk in red and the lower floors of the building facade in blue from 69 to 81 Bd Malesherbes, (b) sidewalks at the intersection of Rue de Miromesnil and Rue de Boétie, (c) the north-east sidewalk from 48 to 60 Bd Malesherbes.

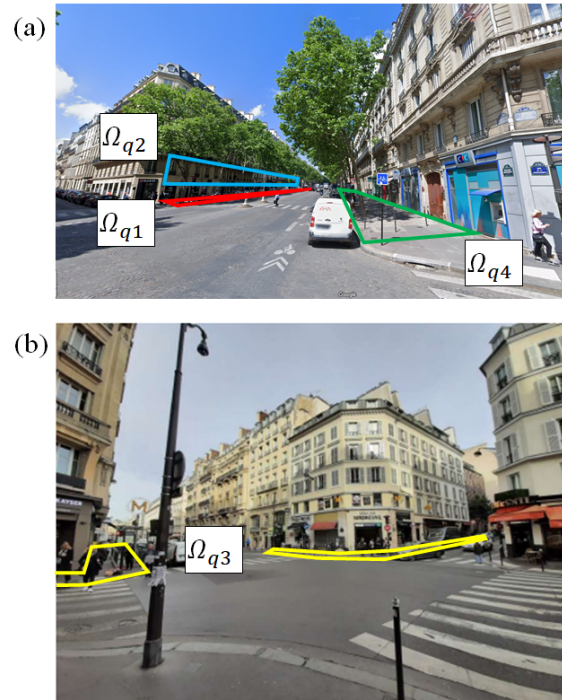


Figure 5.27: Pictures of the selected areas of interest in the Paris district: (a) 58 Bd Malesherbes and (b) 43 Rue de Miromesnil.

sensitivity indicator on the surfaces of the domain for each quantity of interest. As mentioned, since panels can only be placed on the surface of the urban district e.g., the ground and building surfaces, the figure shows the values only on the ground and on the building surface. The bold yellow lines in the sensitivity indicator map denote the contour lines of the sensitivity indicator at 0.1 for both the south-west sidewalk and the lower floor building facade at Bd Malesherbes, at 0.2 at the intersection of Rue de Miromesnil and at 0.003 for the north-east sidewalk at Bd Malesherbes. This value is used as a threshold for determining the panel placement areas. Herein, the thresholds have been selected such that the area of depolluting panels does not exceed 300m^2 , which will be finally described in Subsection 5.3.3.4.

On the southwest sidewalk at Bd Malesherbes, I define the north and south parts of the sidewalk (see Fig. 5.29). Firstly, concerning the quantity of interest \mathcal{I}_1 , the sensitivity indicator reaches the highest values on the ground of the north part as shown in Fig. 5.28 (a). It corresponds to a part of the sidewalk, of the road and of

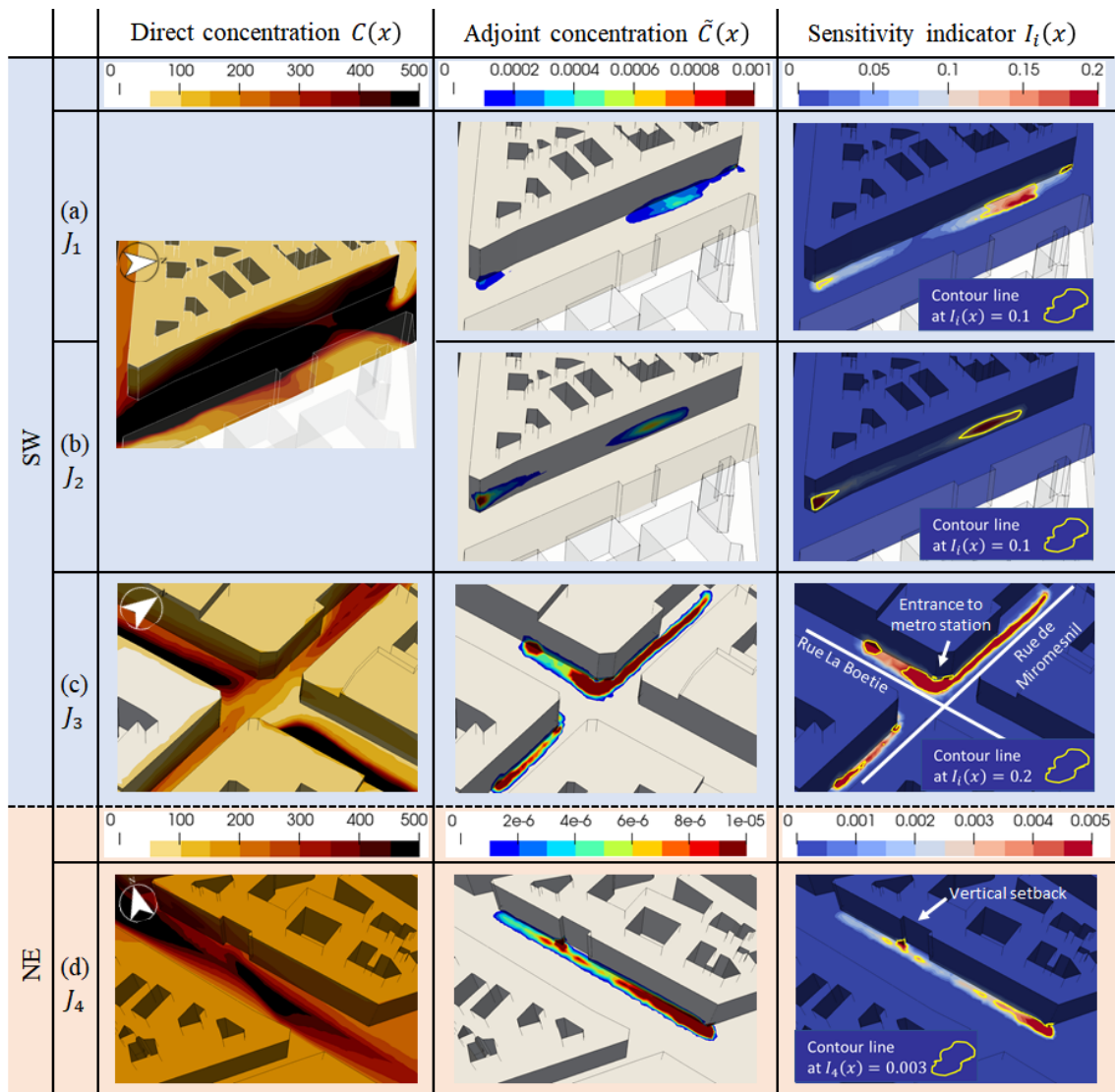


Figure 5.28: Direct concentration, adjoint concentration, and sensitivity indicator associated with each quantity of interest: (a) \mathcal{J}_1 , the south-west sidewalk from 69 to 85 Bd Malesherbes, (b) \mathcal{J}_2 , the building facade at the lower floor on south-west side from 69 to 81 Bd Malesherbes, (c) \mathcal{J}_3 , the subway station and shops at the intersection of Rue de Miromesnil and Rue la Boétie, (d) \mathcal{J}_4 , the north-east sidewalk from 48 to 60 Bd Malesherbes.

the lower floor's building facade (for the definition of the position for the sidewalk and road, see Fig. 5.30). Similarly, for the quantity of interest \mathcal{J}_2 , significant sensi-

tivity indicator values are mainly located on the north part of Bd Malesherbes on the lower floor building facade (Fig. 5.28 (b)). In the other regions, the indicator is relatively low. For \mathcal{J}_1 and \mathcal{J}_2 , I observe inhomogeneous sensitivity indicators even on a given sidewalk and building facade. This is mainly attributed to the magnitude of adjoint concentration. Here, let me detail the airflow characteristics that affect the adjoint magnitude. Looking at the airflow characteristics in Bd Malesherbes (Fig. 5.29), a typical street canyon flow occurs in the north part. Hence, in this region, the virtual pollutant source of the adjoint problem defined on Ω_{q1} and Ω_{q2} are backwardly transported along and near the ground and building facade by the primary vortex of the street canyon flow. It leads to high adjoint concentration on the sidewalk, road and building facade in the north part of Bd Malesherbes. On the other hand, in the center and south parts (except for the south corner), the adjoint concentration is low on the ground and building facade because the vertical velocity is tiny compared to the north part, and the airflow direction near the building surfaces is oriented parallel to the road (Fig. 5.29). This airflow does not transport the adjoint pollutant concentration close to the ground and building facade, resulting in low indicator values in these regions. To sum up, urban airflow plays a major role in the sensitivity indicator level and in determining the smart placement of depolluting panels. The amount of adjoint concentration passing close to the ground or the building surface is a major contributor to the dimension of depolluting panels (location and size).

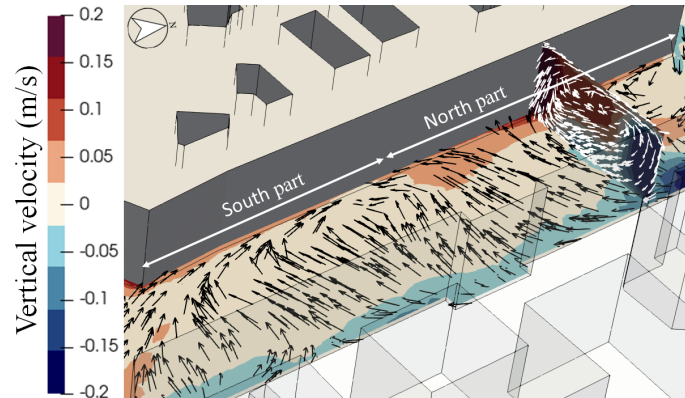


Figure 5.29: Vertical velocity and wind direction on the southwest sidewalk at Bd Malesherbes at 1m height.

For the quantity of interest \mathcal{J}_3 dealing with the NOx concentration at the street

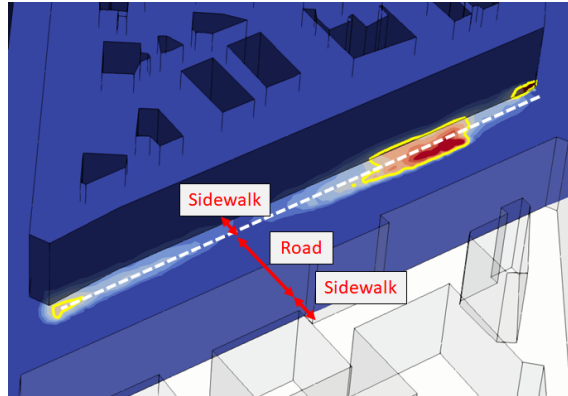


Figure 5.30: Definition of the position for the sidewalk and road in Bd Malesherbes (on the sensitivity map of Fig. 5.28 (a)).

intersection of Rue de Miromesnil and Rue la Boétie, Fig. 5.28 (c) shows that high sensitivity indicator values are obtained on the sidewalk surfaces, especially in Rue de Miromesnil, a well-known road having heavy traffic, and also on lower floor's building facades. Moreover, the sensitivity indicator is significant at the entrance to the subway station particularly due to the high adjoint concentration. In this intersection, complex airflow is created as winds come from many directions and merge. Hence, this air mixing favors the direct and adjoint concentrations to reach the ground surfaces and building facades. It is noted that the direct concentration is not significant in this corner compared to the center of the road and the north part of the sidewalk. From this observation, thus, I can confirm that the adjoint concentration plays an essential role in determining the magnitude of the sensitivity indicator.

Concerning the quantity of interest \mathcal{J}_4 on the north-east sidewalk of Bd Malesherbes for NE case, Fig. 5.28 (d) indicates significantly high sensitivity indicators locally at the building corner on the south part mainly due to high adjoint concentrations. In addition, high indicators are obtained around the center of the sidewalk near the vertical setback. [99] pointed out that vertical setbacks increase airflow and enhance pollutant dispersion in the vertical direction. Its effect contributes to the high adjoint concentration in this region, thereby the high indicator. This finding implies that combining measures to facilitate airflow mixing with depolluting panels can be a more efficient way to improve air quality. However, in this northeast sidewalk case, note that the magnitude of the adjoint concentration and the sensitivity indicator is much smaller than in the other cases. Therefore, putting depolluting panels on

the northeast sidewalk can be less efficient.

5.3.3.4 Practical recommendation on the depolluting panel placement as regards of urban airflow in Paris 8 district

To conclude, for the improvement of the air quality at Bd Malesherbes (69-85 and 48-60) and at the intersection of Rue de Miromesnil and of Rue la Boétie under the considered wind conditions, the recommended panel placements are finally represented in Fig. 5.31. The black squares in the figure represent the approximate size and position of the depolluting panels. The recommended placement of depolluting panels based on the chosen sensitivity lines (defined thresholds) in Fig. 5.28 are the following:

- Bd Malesherbes - panels should be placed on the north part of the south-west sidewalks (4 m wide \times 30 m long, Fig. 5.31 (a) DP1) and of the road adjacent to the sidewalk (3.5 m \times 30 m, Fig. 5.31 (a) DP2), on the building facade in the north part (height \in [2.5m, 9.5m] \times 35 m, Fig. 5.31 (a) DP3) and in the south part (height \in [2m, 9m] \times 10 m, Fig. 5.31 (a) DP4). Although the placement of panels can be less effective on the north-east sidewalk due to the low sensitivity indicator in comparison with the south-west sidewalk, candidate positions are on the sidewalk at the south corner (6 m \times 35 m, Fig. 5.31 (b) DP5) and in the center of the sidewalk close to the setback (4 m \times 30 m, Fig. 5.31 (b) DP6).
- Intersection of Rue de Miromesnil and of Rue la Boétie - panels should be placed on a part of the sidewalk and road on the north side of Rue de Miromesnil (1.5 m wide \times 50 m long, Fig. 5.31 (c) DP1) and (1.5 m \times 50 m, Fig. 5.31 (c) DP2) respectively, at the entrance of the metro station (6 m \times 15 m, Fig. 5.31 (c) DP3) and at the part of the sidewalk on Rue la Boetie (6 m \times 5 m, Fig. 5.31 (c) DP4). The other candidate position is a part of the south sidewalk on Rue de Miromesnil (1.5 m \times 12 m, Fig. 5.31 (c) DP5).

The total areas (m^2) enclosed by each contour line $I_i(x)$ for each quantity of interest are summarized in Table 5.13. Let us recall that $I_i(x)$, the contour lines of the sensitivity indicators for chosen thresholds, are used to identify the smart placements. In my Ph.D., the sensitivity indicator thresholds are chosen empirically to ensure a limited and reasonable deployment of depolluting panels. This is done in such a way that the total area of depolluting panels does not exceed 300 m^2 . In practice, the threshold can be chosen depending on how much urban planners want to improve air quality and the cost that can be afforded.

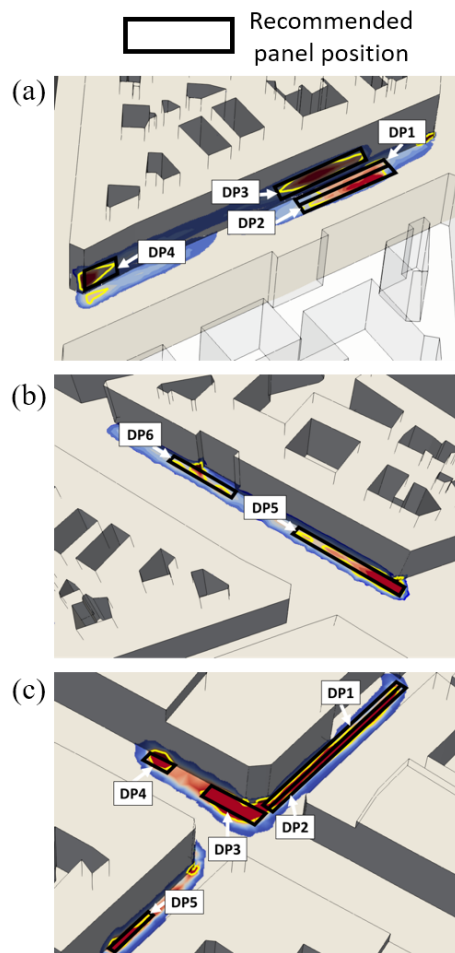


Figure 5.31: Recommended depolluting panel placement as regards of urban airflow in Paris 8 district

5.3.3.5 Summary on optimal placement of depolluting panel in a real urban district

I applied the numerical strategy for the optimal placement of depolluting panels to a real urban area in Paris. A brief summary is provided here. The key points are the applicability of our proposed numerical method to real urban areas and the factors that determine the magnitude of the sensitivities indicator, which is important when determining the depolluting panel placement.

	(m^2)
South-West sidewalk and road at Bd Malesherbes (I_1)	255.7
SW South-West building facade at Bd Malesherbes (I_2)	236.2
Sidewalk and road at the intersection of Rue de Miromesnil (I_3)	252.3
NE North-East sidewalk at Bd Malesherbes (I_4)	239.6

Table 5.13: Area of depolluting panel enclosed by $I_1(x) = 0.1$, $I_2(x) = 0.1$, $I_3(x) = 0.2$ and $I_4(x) = 0.003$.

• Practical operational applicability

- The numerical strategy is beneficial in realistic cities. In real urban areas, airflow varies from time to time depending on factors such as weather conditions and urban geometry. In such a complex flow field, it is difficult for urban planners to determine the relevant deployment of depolluting panels. The proposed numerical strategy can narrow from the potential locations to restricted relevant areas;
- In the present study, the numerical strategy was applied to the two dominant wind directions in Paris, but in practice, more efficient panel placement can be obtained by also considering days with high pollutant concentrations in many other wind directions;
- The numerical strategy was utilized to improve air quality on sidewalks, lower floors of building surfaces and station entrances, etc. In the present study, I selected areas of interest from high pollutant concentration, but they should be chosen with local authorities who have a good knowledge on important and crowded areas frequented by people. For example, it can also be applied to parks and marches along roadsides, as well as to the outdoor grounds of primary schools and nurseries;
- The current numerical strategy does not consider the chemical reactions of pollutants, and it was applied to periods of low UV radiation. If the numerical strategy is applied for summer days with high UV radiation, chemical reactions need to be incorporated into the numerical strategy;
- Setting the threshold value of sensitivity indicator is very important with respect to determining the panel size. Indeed, the panel size can vary significantly depending on the threshold value. Needless to say, the larger the panel

size, the more air quality will be improved, but the threshold should be determined in agreement with the local authorities, considering installation and maintenance costs.

- **Factors determining the magnitude of the sensitivity indicator**

- Urban airflow plays a major role regarding the pollutant concentration distribution, the adjoint concentration and ultimately the sensitivity indicator;
- In particular, the sensitivity indicator tends to be significant when the airflow path is on a line connecting the quantity of interest downwind and the buildings and ground surface windward;
- Although direct concentration is an important factor in determining the magnitude of the sensitivity indicator, the magnitude of adjoint concentration is even more important;
- Although it was not examined in this study, combinations with other air pollutant mitigation actions, especially actions that enhance airflow mixing, may enable the panels to be placed more efficiently.

5.4 Conclusion

In this chapter, firstly I investigate the interaction between outdoor and indoor air quality through measurements and simulations in an apartment in Paris 8 district. An appropriate numerical simulation approach for the interaction between outdoor and indoor air quality was selected, i.e., additional domain approach. Based on the measurements and simulations, the physical characteristics of the outdoor transfer into indoor space are analyzed. Subsequently, the proposed numerical strategy for smart placement of depolluting panels is applied for the first time to a real urban district in Paris as regards to two common wind directions in Paris. Then the effectiveness of the numerical strategy was investigated in a real urban district.

- **Indoor Pollutant Concentrations and Airflow:** With natural ventilation, indoor concentrations increased rapidly in the first five minutes and then stabilized. After 15 minutes, pollutant concentrations in most of the indoors reached levels comparable to outdoors. Due to the characteristics of the indoor airflow, indoor pollutant concentration increases from the perimeter (wall) of the room as pollutants are carried along the perimeter of the room. This highlights that people are exposed to traffic air pollution even indoors, as outdoor pollutants transfer into indoor spaces;

- **Mitigating Indoor Exposure:** To mitigate people’s indoor exposure to outdoor pollutants, it is advisable to reduce pollutant concentrations near windows. Once outdoor pollutants enter indoors, placing depolluting devices on perimeters of the room (ceiling, wall and floor) can be effective in reducing indoor air pollution;
- **Appropriate Numerical Approach to Study the Interaction between Outdoor and Indoor Air Quality:** As airflow at the inflow boundary significantly influences the nature of indoor pollutant dispersion, it is preferable to use an approach that can adequately reproduce the wind direction at the inflow boundary. When simulating the interaction between outdoor and indoor air quality, the accuracy of the additional domain approach is superior to the pressure-driven approach because the additional domain approach can consider the interaction between outdoor and indoor airflow;
- **Outdoor optimal Depolluting Panel Placement:** By applying the numerical strategy to Paris 8 district, the optimal placement of depolluting panels can be determined within a huge urban area. The thresholds affecting the dimensions and size of the depolluting panels should be determined with the local authority;
- **Sensitivity Indicator and Urban Airflow:** Sensitivity indicator for optimal depolluting panel placement is closely related to urban airflow. In particular, the sensitivity indicator tends to be significant when the airflow path is on a line connecting the quantity of interest leeward to the surfaces of the buildings and grounds windward;
- **Enhancing Panel Effectiveness by Combination with other Measures:** It is important that pollutants are transported in the vicinity of depolluting panels to enhance the panel’s effectiveness. This implies that the effectiveness of the depolluting panels can be improved by combining the depolluting panels with measures to encourage air mixing.

Conclusions and Perspectives

In my Ph.D. work, there are two main focuses. The first is to develop a practical numerical strategy for the optimal placement of depolluting panels to reduce human exposure to traffic pollution in urban areas using detailed outdoor and indoor air quality cartography. The second is to apply the strategy to realistic urban areas to verify its effectiveness.

Concerning the first aspect, I proposed a numerical strategy for the smart placement of depolluting panels to improve the air quality in critical highly-polluted urban areas. The proposed strategy encompasses a comprehensive series of steps; from the automatic creation of 3D urban geometry, the computation of detailed outdoor and indoor pollutant cartography using CFD to the generation of sensitivity indicator maps that pinpoint relevant placement for depolluting panel installation through adjoint-based sensitivity analysis. These considered panels can adsorb and degrade a part of traffic pollutants provided that the pollutants pass near these depolluting surfaces. Hence, I focused on the efficient placement of panels as regards to urban airflow. The numerical strategy can be decomposed into two steps. Firstly, in the diagnosis stage, detailed airflow and pollutant cartography are computed using CFD at the district scale to identify critical highly-polluted areas. The pollutant concentrations in these areas are designed as "quantities of interest". Then, in the remediation stage, local sensitivity analysis is performed through the adjoint framework to determine a relevant and limited placement of depolluting panels with the aim of reducing the pollutant concentration in localized critical areas. Indeed, the adjoint concentration shows the areas of the domain having an impact on the chosen quantities of interest. As shown in the studied cases, Sense-City and Paris, the adjoint advection-diffusion problem can be solved using finite volume or finite element method-based CFD software. To smartly place the depolluting panels, a spatial sensitivity indicator was introduced. The proposed indicator is the product of the pollutant concentration field and the adjoint concentration field. To summarize, I prove that the depolluting panels should be deployed on surfaces having high pollutant concentration and significant impact on the chosen quantities of interest (high

adjoint concentration).

Concerning the second aspect, the numerical strategy for the smart placement of depolluting according to urban airflow was illustrated in two real cases. The first application deals with a small full-scale district named “Sense-City” under controlled airflow and environmental conditions provided by a huge climatic chamber. In this case, I considered a scenario with a localized source of pollutants on the road. Then, in the second application, a real district of Paris was studied. In this case, two representative wind conditions of Region Ile de France and realistic NO_x source emissions given by the Airparif agency were considered. In both cases, inhomogeneous, highly polluted areas were observed on the sidewalks, road and building facades. In the cartography-making phase, I also studied the interaction between outdoor and indoor air quality through the measurement and CFD simulation in both Sense-City and Paris. Obviously, indoor air quality was deteriorated with increasing outdoor pollutant concentrations. When outdoor pollutant concentrations were almost constant on 1 hour time period, indoor air quality became comparably harmful to outdoor air quality within about 15 minutes after opening the windows. This clearly demonstrates the need for mitigation measures indoors by limiting the pollutant concentration at the inlet windows. In order to improve outdoor air quality in critical areas and to prevent outdoor air pollutant transfer into the indoor environment, smart placements of depolluting panels were proposed using the numerical strategy. It was shown that depolluting panels should be placed on a part of the sidewalks, of the lower floor building facades and of the roads adjacent to the sidewalks. By comparing improvement effectiveness in two scenarios of panel deployment in Sense-City: smart and non-smart placements, it revealed that extensive aleatory deployment of depolluting panels can not be efficient. In addition, I proved that urban airflow plays a major role in pollutant concentration distribution, in the adjoint concentration and ultimately in the sensitivity indicator for the smart placement of depolluting panels. In particular, the sensitivity indicator tends to be significant when the airflow path is on a line connecting the quantity of interest leeward to the surfaces of the buildings and grounds windward. By fixing a threshold value on the sensitivity indicator, one can determine the areas of depolluting panels to be deployed. In practice, the local authorities can select the threshold value by considering the balance between the objective of air quality improvement and the financial cost of depolluting panels.

In my strategy, understanding the interaction between outdoor and indoor air quality was an important part of the strategy for making pollution cartography. As mentioned, there are coupled and decoupled approaches available for studying

this interaction. In general, the decoupled approach is preferable for its practicality, thanks to its ease in generating numerical models and in reducing computational demands. However, their accuracy and scope of application still need to be studied. Hence, I compared their accuracy for Sense-City and Paris cases, which revealed that the decoupled approach fails to reproduce the correct indoor wind direction at the inlet boundary. As an alternative, I considered the "additional domain approach." In this kind of decoupled approach, a small outdoor domain around the inlet boundary is added. This approach allows the interaction of outdoor and indoor airflow to be taken into account more efficiently at a reduced computational cost. In fact, the pollutant dispersion simulation in Paris showed a time evolution of the numerical pollutant concentrations close to the measurement. However, as there are few previous works on the accuracy and guidelines for the additional domain approach, further studies are necessary in the future.

Regarding the scenarios in Paris case, I considered only two dominant wind directions and realistic NO_x pollutant emissions (averaged on 1 hour) on roads given by Airparif agency. Then, depolluting panel placements were discussed with respect to two main wind directions and traffic pollutant emissions. The sensitivity indicators obtained for each wind direction were used to suggest the smart panel placements for each case separately. In reality, wind directions vary; however, in the considered 1-hour time interval, this variability is not taken into account, and simulating all wind directions is challenging for practical urban design. Consequently, one needs to choose a limited number of representative wind directions to simulate as long as computational time and cost permit. Nevertheless, provided that many wind directions can be considered, e.g., at 5 or 10-degree pitch, alternative options for determining the optimal panel placements may also be available. For example, panel placements could be determined based on the sum of sensitivity indicators on each surface on the buildings or ground obtained from many different wind directions' simulations. This would allow optimal panel placements to be considered for many wind directions. Although considering many wind directions is challenging, the use of reduced order models such as reduced-basis techniques is an interesting solution. In this way, one can save the computational time and cost. Also, data-driven technique would be advantageous in terms of computational limitations. Nevertheless, further study for the accuracy of these alternative techniques should be required in the future.

Smart placement of depolluting panels was the main topic of my research. In my thesis, I considered deploying depolluting panels near buildings' windows to prevent outdoor pollutants from entering indoors and improve indoor air quality.

According to my research, it was found that once outdoor pollutants enter indoors, pollutants are firstly carried along the periphery (walls) of the room. Then, pollutant concentration is increased from the periphery of the rooms to the center of the room. In addition, indoor environments also have various pollutant sources. Consequently, placing photocatalysis devices on target indoor surfaces determined by the proposed numerical strategy is promising. In such cases, my numerical strategy could be extended to paint, building materials and furniture indoors incorporating photocatalytic technologies.

Although it was not examined in my Ph.D. work, the results showed that combinations with other outdoor air pollutant mitigation actions may enable the panels to be placed more efficiently. The current strategy only takes airflow into consideration. Depending on the airflow, pollutants can be transported closer to the panels. Hence, there might be a possibility that a combination with mitigation measures that encourage airflow mixing strategies can be more effective. For example, it may be possible to promote airflow mixing through changes in urban density and heterogeneity. This is also true with regard to other factors that are currently simplified. When considering solar radiation, urban planning should incorporate designs that locally reduce shading at the position of the depolluting panels. If the buoyancy effect is to be considered, one can deliberately create dead zones where air movement is limited, trapping heat and pollutants. In this case, putting depolluting panels in these zones could be efficient. Therefore, urban planning can be designed to maximize the effectiveness of the panels.

Before discussing perspectives, I would like to summarize some practical aspects of the simulations and experiments performed in my study. With regard to simulations, I proposed a software chain for creating numerical mock-ups used in simulations, which is semi-automatic, using existing software from the creation of the 3D geometry to the creation of the mesh. This makes it easy to create 3D geometry of real urban areas. Regarding the experiments, the full-scale CO₂ pollutant dispersion experiment in Sense-City conducted in my Ph.D. was the first Sense-City experiment under controlled CO₂ emissions. Previously, a former Ph.D. student worked on the outdoor airflow of Sense-City. In my Ph.D., the objective was to continue with the study of outdoor and indoor pollutant dispersion in Sense-City. These works have contributed to get a better understanding of the airflow and pollutant dispersion in Sense-City district covered by its huge climatic chamber with a specific ventilation system. These efforts will help to design future pollutant experiments within Sense-City. Besides, in my research, airflow and pollutant concentrations were measured using 3D anemometers and gas sensors in both controlled and realistic environments.

This gave pointwise airflow and pollutant concentrations. Although it was not presented in this manuscript, I participated in the first test using PIV in Sense-City district to get a large flow-field measurement. In future works, more details of airflow and pollutant dispersion in Sense-City will be revealed using PIV, and compared with CFD results. Lastly, concerning air quality sensors, I calibrated and verified the micro-sensors in laboratory in order to ensure their accuracy. Hence, I was made aware of the need to calibrate air quality sensors before conducting the experiments.

The goal of my Ph.D. was to propose a simple and preliminary operational numerical strategy for a better deployment of depolluting panels in urban areas, which is useful in the urban design phase. In the presented results, the first recommendations on depolluting panel placement are essentially given regarding the transport of pollutants via the urban air flows. Herein, many simplifications have been considered for easier practical use. Even though the pollution scenarios in Paris were studied in the winter period (outside of the intensive photo chemical period: April \sim September) on small time intervals of 1 hour, I did not consider buoyancy effects, traffic-induced turbulence terms, and tree vegetation which can modify the airflow and the pollutant dispersion. Moreover, to limit the complexity and the time computation, the pollutant was modeled as passive (multiple pollutant reactions not considered). Indeed, after simulating NO_x concentration as a passive scalar, NO₂ concentration in Paris district was simply deduced using Derwent and Middleton formula. Lastly, the degradation of the pollutant by the depolluting system is described in a simple way using a Robin boundary condition with a first-order reaction. Despite these simplifying assumptions, it can be underlined that the actual proposed method can distinguish “useless panel placement areas” corresponding to surfaces having no impact on the improvement of the quantities of interest and “promising panel placement areas”. In future works, a more sophisticated strategy can be developed to account for the above limitations and to get a more precise quantitative evaluation of the “promising panel placement areas”. For that, we can move toward multi-pollutant reactions and multi-physics simulations as the pollutant degradation mechanism of the panels is based on photocatalysis; the panels’ efficiency depends on the solar irradiance, the temperature, and many other physical parameters. Research work still has to be conducted on both experimental and numerical aspects. An extensive experimental characterization of the ZnO depolluting panels at the material scale in controlled conditions in the laboratory is required. From these experiments, a constitutive law can be obtained and implemented in multi-physics simulation at the district scale. The coupled-problem solutions providing notably airflow, solar irradiance, temperature, and pollutant cartography will allow an improved prediction of panel pollutant degradation and thus an enhanced evaluation

of the panel placement. At Université Gustave Eiffel, forthcoming controlled air pollution experiments are to be conducted in the district of the Sense-City equipment to validate the proposed numerical strategy for the smart placement of ZnO depolluting panels.

Appendix A

NO₂ measurements in Paris apartment - 2021&2022 campaigns

Fig. A.1 shows additional NO₂ concentration measurements conducted in the Paris apartment on October 19th and 22nd, 2021, and November 8th and 14th, 2022. Here, U_n represents the normal component of velocity at the courtyard-side (a) and at the road-side window (b) (c) (d). A positive value of U_n indicates airflow movement from outdoors to indoors. Let me recall that the road-side window is in the living room and the courtyard-side window is in the bedroom. As U_n has positive and negative values in (a), it indicates that airflow moves in and out at the courtyard-side window. When moving out (U_n negative), airflow enters the living room from the road-side window. When moving in (U_n positive), airflow enters the bedroom from the courtyard-side window. As a result, NO₂ concentrations first increase in the living room and the bedroom, and after it propagates to the other rooms. In these changing wind direction conditions (positive/negative U_n), it should be noted that this order of NO₂ concentration increase differs from what was presented in Chapter 5 with only positive U_n values, namely, living room, corridor, kids room, bedroom, and kitchen. In (b), the negative U_n values measured at the road-side window just after the window opening lead to an initial increase of NO₂ concentration in the bedroom. Concerning the remaining two days (c) (d) with dominant positive airflow (without U_n negative values) measured at the road-side window, we observe that NO₂ pollutants enter from the road-side window, propagate in the apartment, and finally reach the bedroom and kitchen. This order of NO₂ increasing trend is similar to the one shown in Chapter 5 as we are in similar wind conditions (only positive U_n values). In summary, the trend of increase in NO₂ concentration depends on airflow conditions at the windows (U_n positive/negative values or strictly positive values).

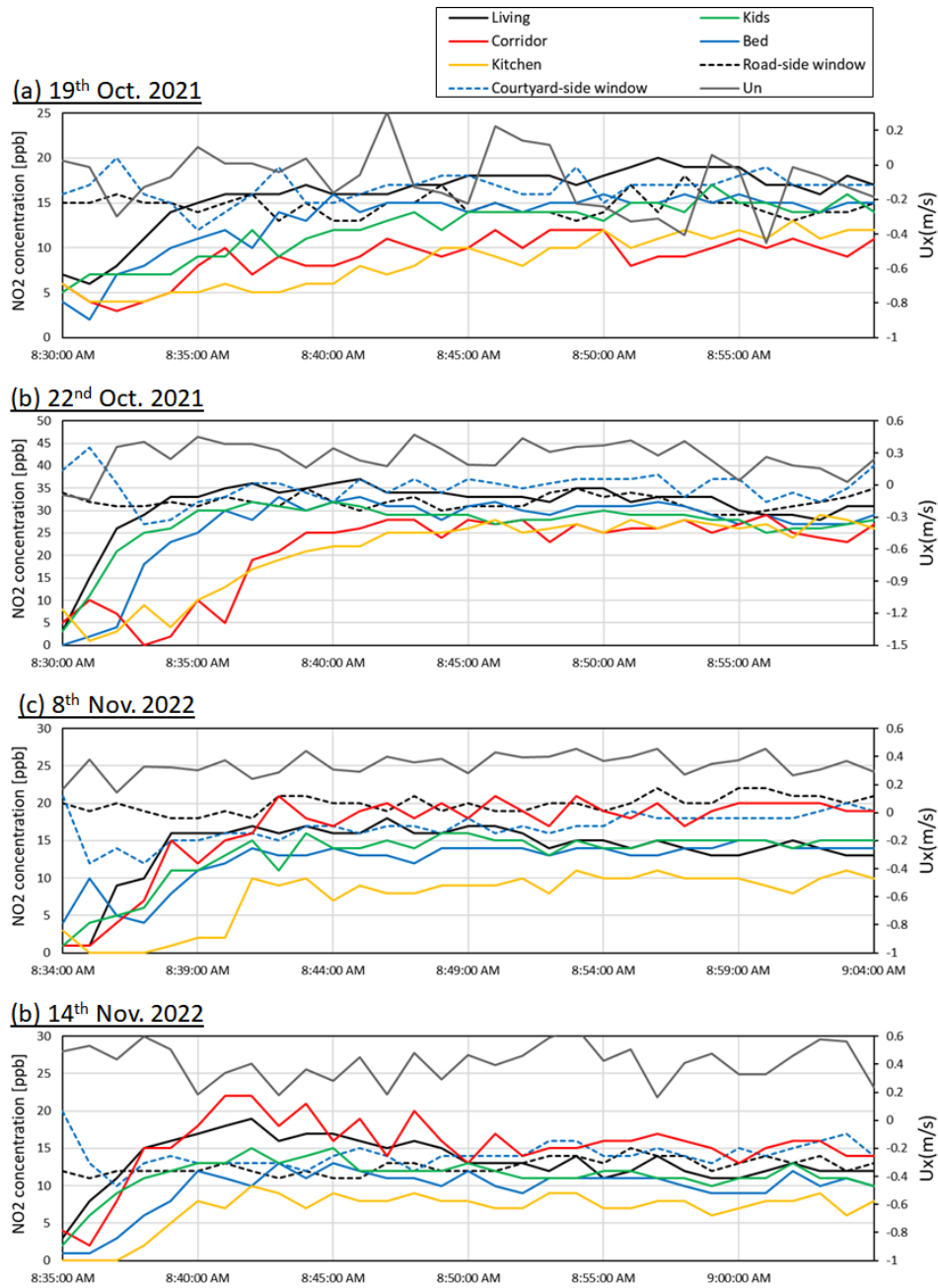


Figure A.1: Results of other NO₂ measurement in the Paris apartment: (a) 19th October 2021, (b) 22nd October 2021, (c) 8th November 2022 and (d) 14th November 2022. Results of first 30 min. U_n denotes the normal velocity component at the window.

Bibliography

- [1] World Health Organization. Air pollution. https://www.who.int/health-topics/air-pollution#tab=tab_1. Accessed: 2023-04-03.
- [2] Avril Challoner and Laurence Gill. Indoor/outdoor air pollution relationships in ten commercial buildings: Pm2.5 and no2. *Building and Environment*, 80:159–173, 2014.
- [3] Silvana Di Sabatino, Riccardo Buccolieri, Beatrice Pulvirenti, and Rex Britter. Simulations of pollutant dispersion within idealised urban-type geometries with cfd and integral models. *Atmospheric Environment*, 41(37):8316–8329, 2007.
- [4] C. Peng, C. Li, Z. Zou, S. Shen, and D. Sun. Improvement of air quality and thermal environment in an old city district by constructing wind passages. *Sustainability*, 7(9):12672–12692, 2015.
- [5] Muhammad Yazid, Nor Azwadi Che Sidik, Salim M. Salim, and Khalid Saqr. A review on the flow structure and pollutant dispersion in urban street canyons for urban planning strategies. *Simulation*, 90, 04 2014.
- [6] Hong Kong Buildings Department. Practice Notes for Authorized Persons, Registered Structural Engineers and Registered Geotechnical Engineers, No. APP-152 – Sustainable Building Design Guidelines, 2011.
- [7] Yaxing Du and Cheuk Ming Mak. Improving pedestrian level low wind velocity environment in high-density cities: A general framework and case study. *Sustainable Cities and Society*, 42:314–324, 2018.
- [8] P.A. Mirzaei and F. Haghghat. A novel approach to enhance outdoor air quality: Pedestrian ventilation system. *Building and Environment*, 45(7):1582–1593, 2010.

- [9] M Humayun, F Raziq, A Khan, and W Luo. Modification strategies of tio2 for potential applications in photocatalysis: a critical review. *Green Chemistry Letters and Reviews*, 11(2):86–102, 2018.
- [10] Seunghyun Weon, Fei He, and Wonyong Choi. Status and challenges in photocatalytic nanotechnology for cleaning air polluted with volatile organic compounds: Visible light utilization and catalyst deactivation. *Environmental Science: Nano*, 6(11):3185–3214, 2019.
- [11] Di He, Yongli Li, Junshu Wu, Yilong Yang, Qier An, et al. Carbon wrapped and doped tio2 mesoporous nanostructure with efficient visible-light photocatalysis for no removal. *Applied Surface Science*, 391:318–325, 2017.
- [12] Isabel Garrido, Marta Pastor-Belda, Natalia Campillo, Pilar Viñas, María José Yañez, Nuria Vela, Simon Navarro, and José Fenoll. Photooxidation of insecticide residues by zno and tio2 coated magnetic nanoparticles under natural sunlight. *Journal of Photochemistry and Photobiology A: Chemistry*, 372:245–253, 2019.
- [13] Marie Le Pivert, Olivier Kerivel, Brahim Zerelli, and Yamin Leprince-Wang. Zno nanostructures based innovative photocatalytic road for air purification. *Journal of Cleaner Production*, 318:128447, 2021.
- [14] Ajeet Kumar Kaushik and Jaspreet Singh Dhau. Photoelectrochemical oxidation assisted air purifiers; perspective as potential tools to control indoor sars-cov-2 exposure. *Applied Surface Science Advances*, 9:100236, 2022.
- [15] Airparif. Inventaire des émissions 2015, 2019. Accessed: August 23, 2023.
- [16] World Health Organization. Ambient air pollution: A global assessment of exposure and burden of disease, 2016.
- [17] Michal Krzyzanowski and Aaron Cohen. Update of who air quality guidelines. *Air Quality, Atmosphere & Health*, 1:7–13, 2008.
- [18] World Health Organization. Household air pollution. <https://www.who.int/news-room/fact-sheets/detail/household-air-pollution-and-health>, 2022. Accessed: September 13, 2023.
- [19] Otto Hänninen, Isabell Rumrich, and Arja Asikainen. Challenges in estimating health effects of indoor exposures to outdoor particles: Considerations for regional differences. *Science of The Total Environment*, 589:130–135, 2017.

- [20] Dennis Leung. Outdoor-indoor air pollution in urban environment: Challenges and opportunity. *Frontiers in Environmental Science*, 2, 01 2015.
- [21] Vinh Van Tran, Duckshin Park, and Young-Chul Lee. Indoor air pollution, related human diseases, and recent trends in the control and improvement of indoor air quality. *International Journal of Environmental Research and Public Health*, 17, 2020.
- [22] Department of the Environment and Energy, Australian Government. Air pollutants. <https://www.environment.gov.au/protection/air-quality/air-pollutants>, Accessed on 2023-04-04.
- [23] European Lung Foundation. Outdoor air pollution and the lungs. <https://europeanlung.org/en/information-hub/factsheets/outdoor-air-pollution-and-the-lungs/>. Accessed on September 13, 2023.
- [24] Paul Lioy and Panos Georgopoulos. New jersey: A case study of the reduction in urban and suburban air pollution from the 1950s to 2010. *Environmental health perspectives*, 119:1351–5, 05 2011.
- [25] Vermont Department of Environmental Conservation. Criteria air pollutants. <https://dec.vermont.gov/air-quality/pollutants-health/criteria-air-pollutants>. Accessed: April 4, 2023.
- [26] U.S. Environmental Protection Agency. Timeline of major accomplishments in transportation, air pollution, and climate change. <https://www.epa.gov/transportation-air-pollution-and-climate-change/timeline-major-accomplishments-transportation-air>, 2022. Accessed on September 13, 2023.
- [27] Kai Chen, Susanne Breitner, Kathrin Wolf, Francesco Sera, Ana Vicedo-Cabrera, Yuming Guo, Shilu Tong, Eric Lavigne, Patricia Correa, Nicolas Valdes Ortega, Haidong Kan, Jouni Jaakkola, Niilo Rytty, Veronika Huber, Matteo Scortichini, Árpád Farkas, Masahiro Hashizume, Yasushi Honda, and Diogo Vidal. Ambient carbon monoxide and daily mortality: a global time-series study in 337 cities. 5, 04 2021.
- [28] Andreas PseftogkasNG2014429. *Comparison of inferred S5P/TROPOMI NO₂ surface concentrations with in-situ measurements over Central Europe*. PhD thesis, 10 2020.

- [29] Hui Yu, Qianqian Liu, Nana Wei, Mingfeng Hu, Xuezhe Xu, Shuo Wang, Jiacheng Zhou, Weixiong Zhao, and Weijun Zhang. Investigation of summertime ozone formation and sources of volatile organic compounds in the suburb area of hefei: A case study of 2020. *Atmosphere*, 14(4), 2023.
- [30] World Health Organization. Regional Office for Europe. *Air quality guidelines: global update 2005: particulate matter, ozone, nitrogen dioxide and sulfur dioxide*. World Health Organization. Regional Office for Europe, 2006.
- [31] Robert B Hamanaka and G”okhan M Mutlu. Particulate matter air pollution: Effects on the cardiovascular system. *Frontiers in endocrinology*, 9:680, 2018.
- [32] Sumedha M Joshi. The sick building syndrome. *Indian journal of occupational and environmental medicine*, 12(2):61–64, 2008.
- [33] World Health Organization. *WHO handbook for guideline development*. World Health Organization, 2nd edition, 2014.
- [34] European Union. Directive 2004/107/EC of the European Parliament and of the Council. <https://eur-lex.europa.eu/legal-content/FR/TXT/HTML/?uri=CELEX:32004L0107>, 2004.
- [35] European Union. Directive 2008/50/EC of the European Parliament and of the Council. <https://eur-lex.europa.eu/legal-content/EN/TXT/HTML/?uri=CELEX:32008L0050#d1e89-30-1>, 2008.
- [36] European Environment Agency. Air quality standards. <https://www.eea.europa.eu/themes/air/air-quality-concentrations/air-quality-standards>. Accessed on April 5, 2023.
- [37] European Environment Agency. Exceedance of air quality standards. <https://www.eea.europa.eu/ims/exceedance-of-air-quality-standards>, 2023. Accessed: Apr. 5, 2023.
- [38] World Health Organization. Regional Office for Europe. *Air quality guidelines for Europe*. WHO Regional Office for Europe, Copenhagen, 1987.
- [39] French Agency for Food, Environmental and Occupational Health & Safety. French agency for food, environmental and occupational health & safety: Maximum levels of contaminants considered safe for various environments. https://www.anses.fr/fr/system/files/Tableau_VGAI_Juillet2018EN.pdf, 2018.

- [40] Emily Snyder, Timothy Watkins, Paul Solomon, Eben Thoma, Ronald Williams, Gayle Hagler, David Shelow, David Hindin, Johnathan Kilaru, and Peter Preuss. The changing paradigm of air pollution monitoring. *Environmental science & technology*, 47, 08 2013.
- [41] John Roy Garratt. The atmospheric boundary layer. *Earth-Science Reviews*, 37(1-2):89–134, 1994.
- [42] Peng-Yi Cui, Yan Zhang, Wei-Qiu Chen, Jin-Hao Zhang, Yang Luo, and Yuan-Dong Huang. Wind-tunnel studies on the characteristics of indoor/outdoor airflow and pollutant exchange in a building cluster. *Journal of Wind Engineering and Industrial Aerodynamics*, 214:104645, 2021.
- [43] Francisco Toja-Silva, Jia Chen, Stephan Hachinger, and Frank Hase. Cfd simulation of co2 dispersion from urban thermal power plant: Analysis of turbulent schmidt number and comparison with gaussian plume model and measurements. *Journal of Wind Engineering and Industrial Aerodynamics*, 169:177–193, 2017.
- [44] Salim Mohamed Salim, Riccardo Buccolieri, Andy Chan, and Silvana Di Sabatino. Numerical simulation of atmospheric pollutant dispersion in an urban street canyon: Comparison between rans and les. *Journal of Wind Engineering and Industrial Aerodynamics*, 99:103–113, 2011.
- [45] Zheming Tong, Yujiao Chen, Ali Malkawi, Gary Adamkiewicz, and John D. Spengler. Quantifying the impact of traffic-related air pollution on the indoor air quality of a naturally ventilated building. *Environment International*, 89-90:138–146, 2016.
- [46] Airparif. Air quality monitoring in the city of paris, esa webinar, space for twin cities air quality, November 2020. Available at https://commercialisation.esa.int/wp-content/uploads/2020/11/Air-quality-monitoring-in-the-City-of-Paris_Basthiste.pdf.
- [47] Chi Vuong Nguyen and Lionel Soulhac. Data assimilation methods for urban air quality at the local scale. *Atmospheric Environment*, 253:118366, 2021.
- [48] Ron Petersen, Brad Cochran, and John Carter. Specifying exhaust and intake systems. *ASHRAE Journal*, 44:30–37, 08 2002.
- [49] Yoshihide Tominaga and Bert Blocken. Wind tunnel experiments on cross-ventilation flow of a generic building with contaminant dispersion in unsheltered and sheltered conditions. *Building and Environment*, 92:452–461, 2015.

- [50] Adam Leelossy, Ferenc Molnár, Ferenc Izsák, Ágnes Havasi, István Lagzi, and Róbert Mészáros. Dispersion modeling of air pollutants in the atmosphere: a review. *Central European Journal of Geosciences*, 6:257–278, 08 2014.
- [51] R.F. Lee. AERMOD - the development evaluation. In *Proceedings from the 21st International Conference on Air Pollution Modeling and Its Application*, Baltimore, Maryland, USA, November 2004.
- [52] Leonard Ortolano. Estimating air quality impacts. *Environmental Impact Assessment Review*, 5:9–35, 1985.
- [53] Laurent Menut, Bertrand Bessagnet, Dmitry Khvorostyanov, Matthias Beekmann, Blond Nadège, Augustin Colette, Isabelle Coll, Gabriele Curci, Gilles Foret, Alma Hodzic, S. Mailler, Frederik Meleux, Jean-Louis MONGE, I. Pison, Guillaume Siour, Solene Turquety, Myrto Valari, Robert Vautard, and Marta García Vivanco. Chimere 2013 : a model for regional atmospheric composition modelling. 6, 01 2014.
- [54] Airparif. Airparif - la modélisation. <https://www.airparif.asso.fr/la-modelisation>. Accessed: June 22, 2023.
- [55] Jörg Franke and Alexander Baklanov. *Best Practice Guideline for the CFD Simulation of Flows in the Urban Environment: COST Action 732 Quality Assurance and Improvement of Microscale Meteorological Models*. 01 2007.
- [56] AIJ. *Guidebook for CFD Predictions of Urban Wind Environment*. Architectural Institute of Japan, 2020.
- [57] Yoshihide Tominaga. Implementation of the RANS-based CFD method reproducing organized unsteady flow fluctuation in wind environment around buildings. Grants-in-aid for scientific research, report on the research achievements, 2016.
- [58] Idealsimulations. Turbulence Models in CFD. <https://www.idealsimulations.com/resources/turbulence-models-in-cfd/>. Accessed on September 13, 2023.
- [59] Kaoru Iwamoto, Nobuhide Kasagi, and Yuji Suzuki. Direct numerical simulation of turbulent channel flow at $re\tau=2320$. In *Proc. 6th Symp. Smart Control of Turbulence*, pages 327–333, 2005.
- [60] Yoshihide Tominaga and Ted Stathopoulos. Cfd modeling of pollution dispersion in a street canyon: Comparison between les and rans. *Journal of Wind Engineering and Industrial Aerodynamics*, 99(4):340–348, 2011.

- [61] T. van Hooff, B. Blocken, and Y. Tominaga. On the accuracy of cfd simulations of cross-ventilation flows for a generic isolated building: Comparison of rans, les and experiments. *Building and Environment*, 114:148–165, 2017.
- [62] Yoshihide Tominaga and Ted Stathopoulos. Numerical simulation of dispersion around an isolated cubic building: Comparison of various types of k–e models. *Atmospheric Environment*, 43:3200–3210, 06 2009.
- [63] Bert Blocken, Ted Stathopoulos, and Jan Carmeliet. Cfd simulation of the atmospheric boundary layer: wall function problems. *Atmospheric Environment*, 41(2):238–252, 2007.
- [64] Florianr Menter. Zonal two equation kw turbulence models for aerodynamic flows. In *23rd fluid dynamics, plasmadynamics, and lasers conference*, page 2906, 1993.
- [65] Maxence Mendez, Nadège Blond, Patrice Blondeau, Coralie Schoemaeker, and Didier A. Hauglustaine. Assessment of the impact of oxidation processes on indoor air pollution using the new time-resolved inca-indoor model. *Atmospheric Environment*, 122:521–530, 2015.
- [66] Nina Szczepanik-Scislo and Lukasz Scislo. Comparison of cfd and multizone modeling from contaminant migration from a household gas furnace. *Atmosphere*, 12(1), 2021.
- [67] Wangda Zuo and Q. Chen. Validation of fast fluid dynamics for room airflow. 09 2007.
- [68] S.-J. Cao and J. Meyers. On the construction and use of linear low-dimensional ventilation models. *Indoor Air*, 22(5):427–441, 2012.
- [69] Brett Stephens. Infiltration of outdoor pollutants: How building airtightness and pollutant characteristics affect the transport of outdoor air pollution into the indoor environment. *Home Energy*, 2015.
- [70] Mohammad Sadegh Hassanvand, Kazem Naddafi, Sasan Faridi, Mohammad Arhami, Ramin Nabizadeh, Mohammad Hossein Sowlat, Zahra Pourpak, Noushin Rastkari, Fatemeh Momeniha, Homa Kashani, et al. Indoor/outdoor relationships of pm10, pm2. 5, and pm1 mass concentrations and their water-soluble ions in a retirement home and a school dormitory. *Atmospheric Environment*, 82:375–382, 2014.

- [71] Chun Chen and Bin Zhao. Review of relationship between indoor and outdoor particles: I/o ratio, infiltration factor and penetration factor. *Atmospheric environment*, 45(2):275–288, 2011.
- [72] Ying Hu and Bin Zhao. Relationship between indoor and outdoor no₂: a review. *Building and Environment*, 180:106909, 2020.
- [73] W. Physick, Powell Jennifer, Martin Cope, K. Boast, S. Lee, William Lilley, R. Gillett, and G. Edgar. Assessment of different approaches for determining personal exposure. 01 2008.
- [74] Andrew Hornery. The sky’s the limit: developers and councils transforming sydney into manhattan. *The Sydney Morning Herald*, October 19 2019. Accessed on April 13, 2023.
- [75] Japan Property Central. More details on kyoto’s new building height rules. <http://japanpropertycentral.com/2022/10/more-details-on-kyotos-new-building-height-rules/>, October 2022. Accessed on April 13, 2023.
- [76] T.R. Oke. Street design and urban canopy layer climate. *Energy and Buildings*, 11(1):103–113, 1988.
- [77] Cheng-Hsin Chang and Robert N. Meroney. Concentration and flow distributions in urban street canyons: wind tunnel and computational data. *Journal of Wind Engineering and Industrial Aerodynamics*, 91(9):1141–1154, 2003.
- [78] Zheming Tong, Yujiao Chen, and Ali Malkawi. Defining the influence region in neighborhood-scale cfd simulations for natural ventilation design. *Applied Energy*, 182:625–633, 2016.
- [79] Walter F. Dabberdt, F.L. Ludwig, and Warren B. Johnson. Validation and applications of an urban diffusion model for vehicular pollutants. *Atmospheric Environment (1967)*, 7(6):603–618, 1973.
- [80] Elena Boldo, Cristina Linares, Nuria Aragonés, Julio Lumbreras, Rafael Borge, David de la Paz, Beatriz Pérez-Gómez, Pablo Fernández-Navarro, Javier García-Pérez, Marina Pollán, Rebeca Ramis, Teresa Moreno, Angeliki Karanasiou, and Gonzalo López-Abente. Air quality modeling and mortality impact of fine particles reduction policies in spain. *Environmental Research*, 128:15–26, 2014.

- [81] Yoshihide Tominaga and Ted Stathopoulos. Ten questions concerning modeling of near-field pollutant dispersion in the built environment. *Building and Environment*, 105:390–402, 2016.
- [82] R. Ramponi and B. Blocken. Cfd simulation of cross-ventilation for a generic isolated building: Impact of computational parameters. *Building and Environment*, 53:34–48, 2012.
- [83] Takashi Kurabuchi, Masaaki Ohba, Tomoyzaki Endo, and Yoshihiko Akamine. Local dynamic similarity concept and underlying wind tunnel tests prediction accuracy of flow rate of cross-ventilated buildings (part 1). *Transactions of AIJ. Journal of Environmental Engineering*, 607:37–41, 2006. In Japanese.
- [84] Robert Meroney. Cfd prediction of airflow in buildings for natural ventilation. *Proceedings of the 11th Americas Conference on Wind Engineering*, pages 1–11, 01 2009.
- [85] L James Lo, David Banks, and Atila Novoselac. Combined wind tunnel and cfd analysis for indoor airflow prediction of wind-driven cross ventilation. *Building and environment*, 60:12–23, 2013.
- [86] Ting Xia, Monika Nitschke, Ying Zhang, Pushan Shah, Shona Crabb, and Alana Hansen. Traffic-related air pollution and health co-benefits of alternative transport in adelaide, south australia. *Environment international*, 74:281–290, 2015.
- [87] Susan C Anenberg, Joshua Miller, Ray Minjares, Li Du, Daven K Henze, Forrest Lacey, Christopher S Malley, Lisa Emberson, Vicente Franco, Zbigniew Klimont, et al. Impacts and mitigation of excess diesel-related no x emissions in 11 major vehicle markets. *Nature*, 545(7655):467–471, 2017.
- [88] Francisco Posada, Zifei Yang, and Rachel Muncrief. Review of current practices and new developments in heavy-duty vehicle inspection and maintenance programs. 2015.
- [89] M. Andre, K. Sartelet, S. Moukhtar, J.M. Andre, and M. Redaelli. Diesel, petrol or electric vehicles: What choices to improve urban air quality in the ile-de-france region? a simulation platform and case study. *Atmospheric Environment*, 241:117752, 2020.
- [90] M. André, A. Pasquier, and M. Carteret. Experimental determination of the geographical variations in vehicle fleet composition and consequences for

- assessing low-emission zones. *Transportation Research Part D: Transport and Environment*, 65:750–760, 2018.
- [91] D Sofia, F Gioiella, N Lotrecchiano, and A Giuliano. Mitigation strategies for reducing air pollution. *Environmental Science and Pollution Research International*, 27(16):19226–19235, Jun 2020.
- [92] Yuhan Huang, Chengwang Lei, Chun-Ho Liu, Pascal Perez, Hugh Forehead, Shaofei Kong, and John L. Zhou. A review of strategies for mitigating roadside air pollution in urban street canyons. *Environmental Pollution*, 280:116971, 2021.
- [93] Tetsu Kubota, Masao Miura, Yoshihide Tominaga, and Akashi Mochida. Wind tunnel tests on the relationship between building density and pedestrian-level wind velocity: Development of guidelines for realizing acceptable wind environment in residential neighborhoods. *Building and Environment*, 43(10):1699–1708, 2008.
- [94] Man Lin, Jian Hang, Yuguo Li, Zhiwen Luo, and Mats Sandberg. Quantitative ventilation assessments of idealized urban canopy layers with various urban layouts and the same building packing density. *Building and Environment*, 79:152–167, 2014.
- [95] Jian Hang and Yuguo Li. Ventilation strategy and air change rates in idealized high-rise compact urban areas. *Building and Environment*, 45(12):2754–2767, 2010.
- [96] F.T. da Silva, N. Costa Reis, J.M. Santos, E.V. Goulart, and C.E. de Alvarez. Influence of urban form on air quality: The combined effect of block typology and urban planning indices on city breathability. *Science of The Total Environment*, 814:152670, 2022.
- [97] J. Yang, B. Shi, Y. Shi, S. Marvin, Y. Zheng, and G. Xia. Air pollution dispersal in high density urban areas: Research on the triadic relation of wind, air pollution, and urban form. *Sustainable Cities and Society*, 54:101941, 2020.
- [98] Yuan-dong Huang, Wen-rong He, and Chang-Nyung Kim. Impacts of shape and height of upstream roof on airflow and pollutant dispersion inside an urban street canyon. *Environmental Science and Pollution Research*, 22:2117–2137, 2015.
- [99] Wai-Yin Ng and Chi-Kwan Chau. A modeling investigation of the impact of street and building configurations on personal air pollutant exposure in

- isolated deep urban canyons. *Science of The Total Environment*, 468-469:429–448, 2014.
- [100] P. Vos, B. Maiheu, J. Vankerkom, and S. Janssen. Improving local air quality in cities: To tree or not to tree? *Environmental Pollution*, 183:113–122, 2013.
- [101] A.P.R Jeanjean, G. Hinchliffe, W.A. McMullan, P.S. Monks, and R.J. Leigh. A cfd study on the effectiveness of trees to disperse road traffic emissions at a city scale. *Atmospheric Environment*, 120:1–14, 2015.
- [102] A. Issakhov and P. Omarova. Modeling and analysis of the effects of barrier height on automobiles emission dispersion. *Journal of Cleaner Production*, 296:126450, 2021.
- [103] C. Gromke, N. Jamarkattel, and B. Ruck. Influence of roadside hedgerows on air quality in urban street canyons. *Atmospheric Environment*, 139:75–86, 2016.
- [104] J Gallagher and C Lago. How parked cars affect pollutant dispersion at street level in an urban street canyon? a cfd modelling exercise assessing geometrical detailing and pollutant decay rates. *Science of the Total Environment*, 651:2410–2418, 2019.
- [105] F.F. Daghistani. Solar chimney street-lighting pole for ventilating polluted urban areas. *Sustainable Cities and Society*, 72:103057, 2021.
- [106] Teresa M. Mata, António A. Martins, Cristina S. C. Calheiros, Florentina Villanueva, Nuria P. Alonso-Cuevilla, Marta Fonseca Gabriel, and Gabriela Ventura Silva. Indoor air quality: A review of cleaning technologies. *Environments*, 9(9), 2022.
- [107] Meera A Sidheswaran, Hugo Destailats, Douglas P Sullivan, Sebastian Cohn, and William J Fisk. Energy efficient indoor voc air cleaning with activated carbon fiber (acf) filters. *Building and Environment*, 47:357–367, 2012.
- [108] S Mohammad Darvish, A Morteza Ali, and S Ramezani Sani. Designed air purifier reactor for photocatalytic degradation of co2 and no2 gases using mwent/tio2 thin films under visible light irradiation. *Materials Chemistry and Physics*, 248:122872, 2020.
- [109] Marie Le Pivert, Brahim Zerelli, Nathan Martin, Martine Capochichi-Gnambodoe, and Yamin Leprince-Wang. Smart zno decorated optimized engineering materials for water purification under natural sunlight. *Construction and Building Materials*, 257:119592, 2020.

- [110] Vassilios Binas, Danae Venieri, Dimitrios Kotzias, and George Kiriakidis. Modified tio₂ based photocatalysts for improved air and health quality. *Journal of Materiomics*, 3(1):3–16, 2017.
- [111] MS Zuraimi, RJ Magee, DY Won, G Nong, CD Arsenault, W Yang, S So, G Nilsson, L Abebe, and C Alliston. Performance of sorption-and photocatalytic oxidation-based indoor passive panel technologies. *Building and Environment*, 135:85–93, 2018.
- [112] Airparif. Inventaire 2018 des émissions atmosphériques en Île-de-france. <https://www.airparif.asso.fr/actualite/2021/inventaire-2018-des-emissions-atmospheriques-en-ile-de-france>, 2021. Accessed: May 30, 2023.
- [113] Y. Tominaga and T. Stathopoulos. Turbulent schmidt numbers for cfd analysis with various types of flowfield. *Atmospheric Environment*, 41(37):8091–8099, 2007.
- [114] X. Wang and K.F. McNamara. Evaluation of cfd simulation using rans turbulence models for building effects on pollutant dispersion. *Environmental Fluid Mechanics*, 6:181–202, 2006.
- [115] B. Pulvirenti, S. Baldazzi, F. Barbano, E. Brattich, and S. Di Sabatino. Numerical simulation of air pollution mitigation by means of photocatalytic coatings in real-world street canyons. *Building and Environment*, 186:107348, 2020.
- [116] A. Yusuf, H. Oladipo, L. Yildiz Ozer, C. Garlisi, V. Loddo, M.R.M. Abu-Zahra, and G. Palmisano. Modelling of a recirculating photocatalytic microreactor implementing mesoporous n-tio₂ modified with graphene. *Chemical Engineering Science*, 391:123574, 2020.
- [117] A. Yusuf and G. Palmisano. Three-dimensional cfd modelling of a photocatalytic parallel-channel microreactor. *Chemical Engineering Science*, 229:116051, 2021.
- [118] Julien Waeytens and Sara Sadr. Computer-aided placement of air quality sensors using adjoint framework and sensor features to localize indoor source emission. *Building and Environment*, 144:184–193, 2018.
- [119] Frank Pasquill. The estimation of the dispersion of windborne material. *Meeteoro. Mag.*, 90:20–49, 1961.

- [120] Xavier Jurado, Nicolas Reiminger, José Vazquez, Cédric Wemmert, Matthieu Dufresne, Nadège Blond, and Jonathan Wertel. Assessment of mean annual no2 concentration based on a partial dataset. *Atmospheric Environment*, 221:117087, 2020.
- [121] Peter E.J. Vos, Bino Maiheu, Jean Vankerkom, and Stijn Janssen. Improving local air quality in cities: To tree or not to tree? *Environmental Pollution*, 183:113–122, 2013. Selected Papers from Urban Environmental Pollution 2012.
- [122] J. Gallagher and C. Lago. How parked cars affect pollutant dispersion at street level in an urban street canyon? a cfd modelling exercise assessing geometrical detailing and pollutant decay rates. *Science of The Total Environment*, 651:2410–2418, 2019.
- [123] F. Derkx, B. Lebental, T. Bourouina, F. Bourquin, C.-S. Cojocar, E. Robine, and H. Van Damme. The Sense-City project. In *XVIIIth Symposium on Vibrations, Shocks and Noise*, page 9p, 2012.
- [124] Benjamin Streichenberger, Rachida Chakir, Bastien Jouy, and Julien Waeytens. Simulation and validation of cfd turbulent airflow at pedestrian level using 3d ultrasonic anemometer in the controlled urban area “sense-city”. *Journal of Wind Engineering and Industrial Aerodynamics*, 219:104801, 2021.
- [125] Archambeau Frederic, Mechtoua Namane, and Sakiz Marc. Code saturne: A finite volume code for the computation of turbulent incompressible flows-industrial applications. *International Journal on Finite Volumes*, 1(1), 2004.
- [126] F. Hecht. New development in freefem++. *Journal of Numerical Mathematics*, 20(3-4):251–265, 2012.
- [127] J. Boussinesq. *Essai sur la théorie des eaux courantes*, volume XXIII. 1877.
- [128] Florian Menter, M. Kuntz, and RB Langtry. Ten years of industrial experience with the sst turbulence model. *Heat and Mass Transfer*, 4, 01 2003.
- [129] Clarence Tee, EYK Ng, and George Xu. Analysis of transport methodologies for pollutant dispersion modelling in urban environments. *Journal of Environmental Chemical Engineering*, 8(4):103937, 2020.
- [130] Yoshihide Tominaga and Ted Stathopoulos. Cfd simulations of near-field pollutant dispersion with different plume buoyancies. *Building and Environment*, 131:128–139, 2018.

- [131] Riccardo Longo, Magnus Fürst, Aurélie Bellemans, Marco Ferrarotti, Marco Derudi, and Alessandro Parente. Cfd dispersion study based on a variable schmidt formulation for flows around different configurations of ground-mounted buildings. *Building and Environment*, 154:336–347, 2019.
- [132] Nicolas Reiminger. *Modélisation 3D de la pollution atmosphérique à l'échelle du quartier*. PhD thesis, Université de Strasbourg, 2020. Thèse de doctorat.
- [133] Thomas JR Hughes, Michel Mallet, and Mizukami Akira. A new finite element formulation for computational fluid dynamics: Ii. beyond supg. *Computer methods in applied mechanics and engineering*, 54(3):341–355, 1986.
- [134] Leopoldo P Franca, Sergio L Frey, and Thomas JR Hughes. Stabilized finite element methods: I. application to the advective-diffusive model. *Computer Methods in Applied Mechanics and Engineering*, 95(2):253–276, 1992.
- [135] L. Ntziachristos, D. Gkatzoflias, C. Kouridis, and Z. Samaras. Copert: A european road transport emission inventory model. In *Information Technologies in Environmental Engineering*, pages 491–504. Springer Berlin Heidelberg, 2009.
- [136] André Ribes and Christian Caremoli. Salomé platform component model for numerical simulation. *Proceedings - International Computer Software and Applications Conference*, 2:553 – 564, 2007.
- [137] Tsubasa Hamada, Fatiha Chabi, Rachida Chakir, Delphine Lejri, and Julien Waeytens. Interaction between indoor and outdoor air pollution in natural ventilating building: Application to sense-city urban area. In *15th World Congress on Computational Mechanics (WCCM-XV)*, Yokohama, Japan, July - August 2022. Virtual conference.
- [138] Tsubasa Hamada, Fatiha Chabi, Rachida Chakir, Delphine Lejri, Fabrice Dugay, and Julien Waeytens. Smart placement of depolluting panels in urban areas as regards of the air flow using adjoint framework and district digital twin. *Journal*, 2023. Submitted.
- [139] Air-Conditioning The Society of Heating and Sanitary Engineers of Japan. *Guidebook of computational fluid dynamics: Hajimete no kankyō/setsubi sekkei shimyurēshon CFD gaidobukku [Beginner's Environmental and Facility Design Simulation CFD Guidebook]*. Ohmsha, Ltd, 2017. in Japanese.
- [140] Chao Ding and Khee Poh Lam. Data-driven model for cross ventilation potential in high-density cities based on coupled cfd simulation and machine learning. *Building and Environment*, 165:106394, 2019.

- [141] ETHERA. Indoor air quality measurement. <https://www.etheralabs.com/en/>. Accessed: August 28, 2023.
- [142] IGNMap. <https://ignmap.ign.fr/>. Accessed August 11, 2023.
- [143] ArcGIS CityEngine. <https://www.esri.com/en-us/arcgis/products/arcgis-cityengine/overview>. Accessed August 11, 2023.
- [144] SolidWorks. <https://www.solidworks.com/>. Accessed August 11, 2023.
- [145] Fusion360. <https://www.autodesk.com/products/fusion-360/overview?term=1-YEAR&tab=subscription>. Accessed August 11, 2023.
- [146] S.E. Norris P.J. Richards. Appropriate boundary conditions for computational wind engineering models revisited. *Journal of Wind Engineering and Industrial Aerodynamics*, 99:257–266, 2011.
- [147] Tsubasa Hamada, Rachida Chakir, Fabrice Dugay, Delphine Lejri, and Julien Waeytens. Rans simulation of traffic-related air pollutant dispersion in paris and smart placement of depolluting panels. In *IACM COMPUTATIONAL FLUIDS CONFERENCE (CFC)*, Cannes, France, April 2023.
- [148] Walter F Dabberdt, FL Ludwig, and Warren B Johnson Jr. Validation and applications of an urban diffusion model for vehicular pollutants. *Atmospheric Environment (1967)*, 7(6):603–618, 1973.
- [149] Christopher J Greenshields et al. Openfoam user guide. *OpenFOAM Foundation Ltd, version*, 3(1):47, 2015.